Mathematical modelling of growth, reorganisation and active response in cells and tissues

Politecnico di Torino

UNIVERSITÀ DI TORINO

Doctoral Dissertation
Doctoral Program in *Pure and Applied Mathematics* (XXXV cycle)

Mathematical modelling of growth, reorganisation and active response in cells and tissues

By

Giulio Lucci

Supervisors:
Prof. Luigi Preziosi, Politecnico di Torino
Prof. Chiara Giverso, Politecnico di Torino

Thesis Referees:
Prof. Luciano Teresi, Roma Tre University
Prof. Giuseppe Zurlo, University of Galway

Politecnico di Torino – Università di Torino
2023

Declaration

I hereby declare that the contents and organization of this dissertation constitute my own original work and do not compromise in any way the rights of third parties, including those relating to the security of personal data.

Giulio Lucci
2023

* This dissertation is presented in partial fulfilment of the requirements for **Ph.D. degree** in the Graduate School of Politecnico di Torino and Università di Torino.

Acknowledgements

The last three years have been a journey full of challenges, sacrifices, incredible satisfactions and sometimes also disappointment, which however is fundamental in making good science. Looking at the work carried out and collected together in this Thesis, I can only be grateful for how much I have learnt during this rewarding doctoral experience. In particular, I wish to deeply thank the people that worked with me, that stood by me, or that I simply came across in the last few years.

First of all, I would like to express my full gratitude to my supervisors, Prof. Preziosi and Prof. Giverso – or maybe I should say Luigi and Chiara. Luigi has always been an inspiration and a reference, as well as a valuable advisor: I thank him for all the discussions and the thoughtful comments, which made me grow as a researcher. Moreover, I would like to thank him for the support during the very first part of the PhD, when the pandemic outbreak rather destabilized me: he helped me a lot and guided my work despite the non-trivial logistic difficulties of that period.

I probably cannot thank Chiara enough for all she has done for me: she has been always present, a constant and precious support that was simply fundamental at all stages. I want to thank her for the patience she always had, answering my emails and opening her office door whenever I knocked, and for helping me to overcome all the difficulties with her helpful advice. Working with her has been incredibly stimulating and a pleasure.

I also want to thank Prof. Paola Nardinocchi and Prof. Jacopo Ciambella, who cordially welcomed me in Rome during my visiting period. We had numerous insightful discussions, from which I learned a lot, and they introduced me to a different viewpoint in Mechanics that I found fascinating.

A heartfelt thanks goes to all my family, always believing in me: we have been physically far for many years, but I constantly felt your support and unconditional love. Thanks to my mother and father, mamma Elena and babbo Alessandro, who kept believing in my dreams probably more than I did. Thanks to Eleonora, who always stood by my side and by my heart, walking with me towards unexplored lands with her reassuring and

empathic presence. Thanks to my brother Elia, with whom I always have a good time. Thanks to my grandmother, nonna Nadia, whose support made of food, recipes, and love was essential.

Thanks to all the people I met at conferences and schools, from young researchers to recognized Professors, and thanks also the people who collaborated with me. A special thanks to the past residents of office number 30, who kindly welcomed me when I began, and to the current office mates, with whom I spent the last months and shared some freezing office days when the heating decided to break.

Abstract

The understanding of biological systems like cells and tissues is increasingly taking advantage of tools from quantitative sciences, which can provide powerful instruments to unravel complex mechanisms. In this respect, the emerging field of mechanobiology, that aims at analysing how mechanics affects the cellular and sub-cellular processes, represents a prominent example in which a combination of efforts from several disciplines is fundamental. The contribution of mathematical models to the description of biomedical phenomena can provide a notable support to the research process: indeed, they can be fruitfully employed to reproduce physiological and pathological conditions *in silico*, and to perform simulations to support clinical observations. Stimulated by these facts, in this Thesis we introduce some models to capture reorganisation, growth, and active processes in cells and tissues, with particular emphasis on their mechanical behaviour. First of all, we deal with the response of cells to external mechanical stimuli, motivated by experimental evidence showing that cells are able to reorganise their cytoskeleton as a reaction to external forces or deformations. Indeed, if cells are placed on a substrate that is cyclically stretched, a reorientation of the cytoskeletal fibres is observed, until a stable configuration is reached. To get insight into such a reorganisation process, which is relevant in tissue engineering and in the understanding of some diseases, we propose different types of models grounded on Continuum Mechanics. After a review of the experimental and modelling literature, we employ tools from nonlinear elasticity, active remodelling, and linear viscoelasticity to capture some relevant experimental observations. We find that strain energies belonging to a very general class all give rise to the same preferential orientations of cells on two-dimensional substrates, corresponding to the observed ones. Moreover, a remodelling framework for an anisotropic material with two fibre families is introduced and applied to the problem of cytoskeletal alignment. Viscoelastic effects are then considered to capture the effect of the deformation frequency on the cell realignment process.

Then, we consider another problem related to the cellular response to mechanical stimuli, which is the active contractility of axons. In fact, experimental evidence suggests

that the axonal cortex, i.e., the external coating of axons, is able to actively contract and to exert compression on the inner part. This capability seems related to the active regulation of the axon diameter which is observed in some experiments. We describe these phenomena by following an active strain approach, in which both the circumferential and axial contractility of the axonal cortex are considered. A model is derived on a thermodynamically consistent basis and used to simulate the stretching of axons and drug-induced alterations of their cytoskeletal structure, showing a good agreement with experiments.

Finally, at the tissue scale, we address the problem of providing a mechanical description of brain tumour growth inside the brain. In fact, the effect of solid stresses in addition to fluid pressure has been proved to be harmful for patients. These negative repercussions are also amplified in brain tissue, which is extremely soft and confined by the skull. To study these issues, we propose a mathematical model of tumour growth based on mixture theory, to account for solid and fluid components, and morphoelasticity, to describe growth-related distortions. Both the healthy brain tissue and the tumour are treated as hyperelastic solids, so as to quantify the displacement and stress induced by cancer growth. Moreover, we perform simulations on a realistic brain geometry, reconstructed from patient-specific data, to underline the importance of a detailed mechanical description of brain tumour growth.

Related Publications

- G. Lucci and L. Preziosi. A nonlinear elastic description of cell preferential orientations over a stretched substrate, *Biomechanics and Modeling in Mechanobiology* 20:631–649 (2021).
- G. Lucci, C. Giverso, and L. Preziosi. Cell orientation under stretch: Stability of a linear viscoelastic model, *Mathematical Biosciences* 337:108630 (2021).
- J. Ciambella, G. Lucci, P. Nardinocchi, and L. Preziosi. Passive and active fiber reorientation in anisotropic materials, *International Journal of Engineering Science* 176:103688 (2022).
- G. Lucci, A. Agosti, P. Ciarletta, and C. Giverso. Coupling solid and fluid stresses with brain tumour growth and white matter tract deformations in a neuroimaging-informed model, *Biomechanics and Modeling in Mechanobiology* 21:1483–1509 (2022).
- D. Andrini, V. Balbi, G. Bevilacqua, G. Lucci, G. Pozzi, and D. Riccobelli. Mathematical modelling of axonal cortex contractility, *Brain Multiphysics* 3:100060 (2022).
- C. Giverso, N. Loy, G. Lucci, and L. Preziosi. Cell orientation under stretch: A review of experimental findings and mathematical modelling, *Submitted*.

Contents

List of Figures

List of Tables

Chapter 1

Introduction

1.1 Biological Background and Motivation

In the last sixty years, dramatic advances have been made in the fields of biology and biomedical sciences. The development of modern imaging techniques, sophisticated instruments, and effective drugs consistently improved our understanding of biological systems both in physiological and pathological conditions at all scales, and especially at the microscopic one.

Nevertheless, the study of biological organisms still faces a number of complex and intriguing challenges, which require a combination of efforts from several disciplines to be addressed. In this respect, the emerging field of *mechanobiology*, that aims at analysing how mechanics affects cellular and sub-cellular processes, involves the interaction of mathematics, physics, engineering, and chemistry [180, 186]. Furthermore, mathematical models and their computational counterparts started to be increasingly more involved into the understanding of biomedical issues, since they can provide tools to speed up the research process. As life sciences become more quantitative, the support of models can be of help to identify the most relevant mechanisms, to recreate physiological and pathological conditions *in silico*, to perform realistic simulations, and possibly to tailor effective therapies to patients.

In particular, within the modelling context, the importance of mechanics at all scales has been underscored in recent years. At the cell level, we already mentioned the increasing development of mechanobiology, which allowed to get a deeper insight into how a cell reacts to external forces and mechanical stimuli. Indeed, the key role of electro-chemical signals in cellular processes had been known for many years, but more recently the interplay

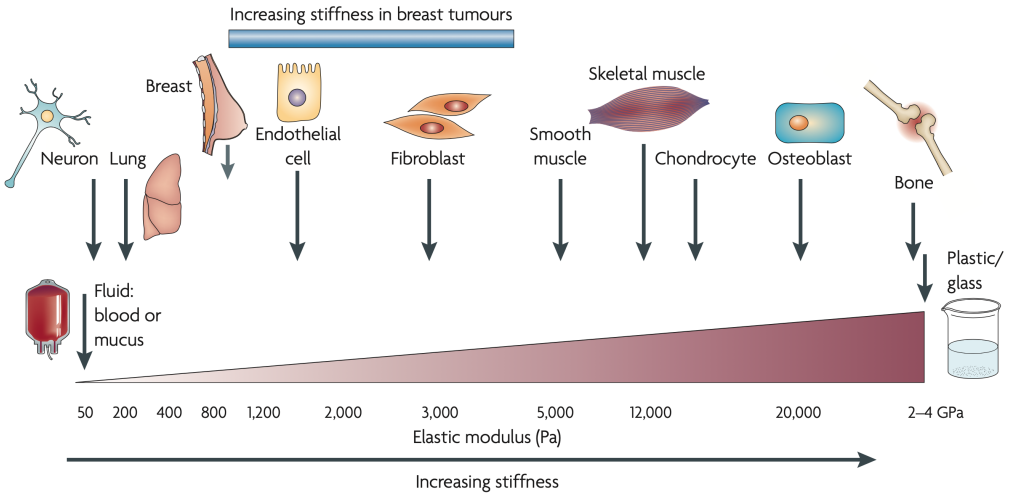

Fig. 1.1 In physiological conditions, cells in different tissues and organs are tuned to the specific mechanical properties of their environment. For instance, given that the brain is much softer than bone tissue, neurons are found to grow and survive preferentially in very soft matrices. However, pathological situations like the occurrence of tumours might alter the stiffness of the tissue, and in turn affect the correct functioning of its cells. Figure taken from [56].

with mechanics has been put in evidence and attracted substantial research interest [56, 147]. The cell was shown to be able to react to imposed forces and to mechanical alterations of its environment, through a process named *mechanotransduction*. For instance, the cell can adapt its structure to changes in the substrate or matrix stiffness [56, 149] and can in general respond to mechanical cues which may result in cellular differentiation [271, 305, 382], proliferation [123, 366], and reorientation [226]. As shown in Fig. 1.1, given that different tissues in the body exhibit different stiffnesses, each cell type is tuned to the material properties of the tissue in which it is found. For instance, neurons and neural-type cells show optimal growth and differentiation in very soft environments, coherently with the extreme softness of the brain. Instead, differentiation and survival of osteoblasts is favoured by a rigid matrix mimicking bone tissue. However, changes in rigidity may happen as a consequence of pathologies like tumours, leading to alterations in the optimal mechanical environment of a cell, that in turn provokes a change in its phenotype [56]. Moreover, in addition to cancer, several diseases like atrial fibrillation, intimal hyperplasia, and liver fibrosis appear to be related to alterations in the mechanotransduction process [180]. Therefore, it is fundamental to obtain insights into the cell behaviour following a mechanical alteration, and mathematical models can provide important clues.

Mechanics is however crucial also at the tissue and organ scale, as highlighted in Fig. 1.1. Indeed, the knowledge of their material properties turns out to be necessary in

tissue engineering applications, where artificial constructs must be designed as realistically as possible. In this respect, there exists a feedback between the properties of a tissue and the orientation of the cells inside it, which can be altered thanks to mechanical cues, as we will extensively discuss in this Thesis. Then, in the context of tumour growth, recent discoveries suggest that a relevant role is played by solid stresses in the cancer micro-environment, in addition to fluid pressure [269, 317]. Advances in Magnetic Resonance Elastography techniques [262, 339] may allow to get detailed information on tissue stiffness, though the field is currently under investigation. A realistic reproduction of tissue properties is also mandatory to perform simulations which aim at building personalised therapeutic strategies.

Motivated by these observations, in this Thesis we focus on the mathematical modelling of cells and tissues, with particular emphasis on their mechanical behaviour in physiological and pathological processes. Specifically, we firstly deal with the cell cytoskeletal reorganisation that happens as a consequence of external forces or deformations, which is a relevant issue in tissue engineering and in the understanding of some diseases, like neurodegeneration. Then, we move to the macroscale and investigate tumour growth happening in the brain from a mechanical perspective. The mathematical description of such phenomena poses several modelling challenges, since biological materials exhibit nonlinear and active behaviours that should be taken properly into account. We will therefore deal with structural reorganisation and active responses of cells, as well as with growth and remodelling subsequent to tumour proliferation.

1.2 Mechanical Framework and Notation

Before moving to the main body of the Thesis, we collect in this Section some basic notions of Continuum Mechanics that will be widely used in the following, alongside with the employed notation. Additional instruments will be introduced in subsequent Chapters, whenever needed.

1.2.1 Kinematics and Balance Equations

We denote by Ω_0 a region of the three-dimensional Euclidean space $\mathcal{E}$ which identifies the *reference configuration* of a body. We refer to a point $\mathbf{X} \in \Omega_0$ as a *material point*, and its coordinates will be called material or *Lagrangian* coordinates. For an open time interval $\mathcal{T}$, we consider the time-dependent smooth map $\boldsymbol{\chi} : \Omega_0 \times \mathcal{T} \to \mathcal{E}$, called *motion*. Such a map

assigns to each point $\mathbf{X} \in \Omega_0$ and each time instant $t \in \mathcal{T}$ a point $\mathbf{x} = \boldsymbol{\chi}(\mathbf{X},t)$, determining the *current configuration* $\Omega = \boldsymbol{\chi}(\Omega_0,t)$ of the body at time t. We will sometimes refer to $\mathbf{x}$ as the *spatial* or *Eulerian coordinate* of the point $\mathbf{X}$.

As a notational convention, we will distinguish between differential operators in material and spatial coordinates. In particular, we will denote by Grad and Div the material gradient and material divergence, respectively. Instead, ∇ and $\nabla\cdot$ will be employed for the spatial gradient and spatial divergence, respectively.

With this notation, we indicate by $\mathbb{F} = \mathrm{Grad}\,\boldsymbol{\chi}$ the *deformation gradient*. Its determinant, also called *Jacobian*, is denoted by $J := \det\mathbb{F} > 0$ and needs to be strictly positive for physical consistence. The deformation of a continuum can be equivalently described using the *displacement field* $\mathbf{u}:\ \Omega_0 \times \mathcal{T} \to \mathcal{V}$, with $\mathcal{V}$ the translation space of $\mathcal{E}$, such that $\mathbf{x} = \mathbf{X} + \mathbf{u}(\mathbf{X},t)$. Hence, the deformation gradient can be rewritten as

$$\mathbb{F} = \mathbb{I} + \mathrm{Grad}\,\mathbf{u}\,, \tag{1.1}$$

where $\mathbb{I}$ denotes the second order identity tensor. By definition, the deformation gradient maps material vectors to spatial vectors, that is, if $d\mathbf{X}$ is an infinitesimal vector in the tangent space at $\mathbf{X} \in \Omega_0$, the corresponding infinitesimal vector in the deformed configuration is

$$d\mathbf{x} = \mathbb{F}d\mathbf{X}. \tag{1.2}$$

Moreover, the Jacobian of the deformation is related to local volume changes in the body, so that

$$dV = JdV_0\,, \tag{1.3}$$

where dV and dV_0 denote volume elements in the current and reference configurations, respectively. Finally, the deformation of surface elements from the reference to the current configuration is described by *Nanson's formula*:

$$\mathbf{n}\,d\Sigma = J\mathbb{F}^{-\mathrm{T}}\mathbf{n}_*\,d\Sigma_0\,, \tag{1.4}$$

in which $d\Sigma$ is an element of area in the current configuration, with outward normal $\mathbf{n}$, and $d\Sigma_0$ is an element of area in the reference configuration, with outward normal $\mathbf{n}_*$. We also introduce the *right Cauchy-Green tensor* $\mathbb{C} := \mathbb{F}^{\mathrm{T}}\mathbb{F}$, which represents the metric tensor of

the embedding of Ω_0 onto $\mathcal{E}$, and the *Green-Lagrange tensor*

$$\mathbb{E} := \frac{1}{2}(\mathbb{C} - \mathbb{I}) \,. \tag{1.5}$$

The *invariants* of $\mathbb{C}$, which will be widely employed in the next Chapters, are defined as [327]

$$\begin{aligned}
&\mathrm{I}_1 := \mathrm{tr}\,\mathbb{C}\,, && \mathrm{I}_2 := \frac{1}{2}\left[(\mathrm{tr}\,\mathbb{C})^2 - \mathrm{tr}\,\mathbb{C}^2\right], && \mathrm{I}_3 := \det\mathbb{C}\,,\\
&\mathrm{I}_4 := \mathbb{C} : \mathbf{N}\otimes\mathbf{N} = \mathbf{N}\cdot\mathbb{C}\mathbf{N} && \mathrm{I}_5 := \mathbb{C}^2 : \mathbf{N}\otimes\mathbf{N} = \mathbf{N}\cdot\mathbb{C}^2\mathbf{N}\,,\\
&\mathrm{I}_6 := \mathbb{C} : \mathbf{M}\otimes\mathbf{M} = \mathbf{M}\cdot\mathbb{C}\mathbf{M}\,, && \mathrm{I}_7 := \mathbb{C}^2 : \mathbf{M}\otimes\mathbf{M} = \mathbf{M}\cdot\mathbb{C}^2\mathbf{M}\,,\\
&\mathrm{I}_8 := (\mathbf{N}\cdot\mathbf{M})(\mathbf{M}\cdot\mathbb{C}\mathbf{N})\,,
\end{aligned} \tag{1.6}$$

where $\mathbf{N}\otimes\mathbf{N}$ and $\mathbf{M}\otimes\mathbf{M}$, with $\mathbf{N},\mathbf{M}$ unit vectors, are the line fields representing the preferential directions of anisotropy in the reference configuration of the material, whereas $\otimes$ stands for the dyadic product, $(\cdot)$ for the standard scalar product between vectors, and $:$ for the double contraction between second-order tensors. We notice that two different definitions of the invariant I_8 are found in the literature. In particular, the definition $\mathrm{I}_8 := \mathbf{M}\cdot\mathbb{C}\mathbf{N}$ is sometimes employed instead of the one reported in Eq. (1.6) [168, 276]. The definition of I_8 in Eq. (1.6) turns out to be automatically invariant under change of sign of either direction vector, which might be a desired property when working with fibres that do not have a directional orientation. On the other hand, if the definition of Eq. (1.6) is adopted, then $\mathrm{I}_8 \equiv 0$ if $\mathbf{N}$ and $\mathbf{M}$ are orthogonal, which might be a drawback. In Chapter 3 we will use both definitions, specifying which one we are dealing with whenever needed and showing that the derived results do not change.

As regards the balance equations, we will consider continuum bodies whose mass is described by a density field ρ in the current configuration. The conservation of mass in local form can be written as

$$\frac{\partial\rho}{\partial t} + \nabla\cdot(\rho\mathbf{v}) = 0\,, \tag{1.7}$$

where $\mathbf{v}$ is the velocity of the body. The corresponding material law is

$$\dot{\rho}_0 = 0\,, \tag{1.8}$$

with ρ_0 the density field in the reference configuration. As a consequence of mass conservation Eqs. (1.7)–(1.8) and the volume transformation Eq. (1.3), the following relation

between densities holds:

$$\rho_0 = \rho J\,. \tag{1.9}$$

As regards the balance of linear momentum in the current configuration, let $\mathbf{t}(\mathbf{n})$ be the surface force per unit area of normal vector $\mathbf{n}$, including both contact forces between different portions of the body and contact forces exerted on the boundary of the body by the environment, while $\mathbf{b}$ denotes the external body forces per unit volume. Then, according to Cauchy's theorem [150, 151], the balance of linear momentum is satisfied if and only if the contact force density is a linear function of $\mathbf{n}$, that is,

$$\mathbf{t}(\mathbf{n}) = \mathbb{T}\mathbf{n}\,, \tag{1.10}$$

where $\mathbb{T}$ is the *Cauchy stress tensor*, and

$$\nabla\cdot\mathbb{T} + \mathbf{b} = \mathbf{0}\,, \tag{1.11}$$

neglecting inertial effects. Therefore, the Cauchy stress provides a measure of the contact force acting on an element of area in the current configuration. In addition, the balance of angular momentum requires that $\mathbb{T}$ be symmetric, that is, $\mathbb{T} = \mathbb{T}^{\mathrm{T}}$. Another relevant measure of stress, which unlike the Cauchy stress tensor is related to the reference configuration, is the *first Piola-Kirchhoff stress*:

$$\mathbb{P} := J\mathbb{T}\mathbb{F}^{-\mathrm{T}}\,. \tag{1.12}$$

Thus, $\mathbb{P}$ is a tensor-valued flux representing a surface stress density per unit of referential area, whereas $\mathbb{P}\mathbf{n}_*$ is a material vector field such that, recalling Eq. (1.4) and omitting time,

$$\mathbb{P}(\mathbf{X})\mathbf{n}_*(\mathbf{X})d\Sigma_0(\mathbf{X}) = \mathbb{T}(\mathbf{x})\mathbf{n}(\mathbf{x})d\Sigma(\mathbf{x})\,, \quad \text{when} \quad \mathbf{x} = \boldsymbol{\chi}(\mathbf{X})\,. \tag{1.13}$$

The local form of the linear momentum balance in reference coordinates therefore reads

$$\mathrm{Div}\,\mathbb{P} + J\mathbf{b} = \mathbf{0}\,. \tag{1.14}$$

We remark that the first Piola-Kirchhoff stress tensor is not symmetric in general. In fact, the balance of angular momentum, expressed in the reference configuration, only prescribes that

$$\mathbb{P}\mathbb{F}^{\mathrm{T}} = \mathbb{F}\mathbb{P}^{\mathrm{T}}\,. \tag{1.15}$$

Finally, we introduce the *second Piola-Kirchhoff stress* $\mathbb{S}$, which is related to the other stress measures by

$$\mathbb{S} = \mathbb{F}^{-1}\mathbb{P} = J\mathbb{F}^{-1}\mathbb{T}\mathbb{F}^{-\mathrm{T}}. \tag{1.16}$$

1.2.2 Growth and Remodelling

The biological materials that we will consider in this Thesis, like cells and tissues, are constantly subject to processes like growth and remodelling of their structure. The mechanical description of such phenomena requires an appropriate extension of the kinematics, since the reorganisation of the material structure following these processes might lead to the development of residual stresses. In their seminal work, Skalak and collaborators [323] were among the first to propose the idea that growth is accompanied by geometrical incompatibilities in the body, which in turn generate residual stresses. A formalisation of such an idea was provided by Rodriguez et al. [307], who suggested to employ a multiplicative decomposition of the deformation gradient into an inelastic part, related to growth and leading to the development of incompatibilities, and an elastic part, which restores the compatibility and from which residual stresses arise. The use of a multiplicative decomposition was inspired by the theory of plasticity, where it was introduced by Bilby et al. [37], Kröner [208], and Lee [216] in the 1960s.

Afterwards, several theoretical extensions and improvements for the mathematical modelling of growth and reorganisation have been proposed. The work by DiCarlo and Quiligotti [107] introduced the concept of accretive forces, which have to satisfy additional balance equations. Then, Ambrosi et al. [9, 10, 15] applied these concepts to the growth of biological tissues, deriving evolution laws for growth related with the stress state of the body. Several other groups in subsequent years contributed to the refinement of the mathematical description of growth, reorganisation, and instabilities in active and biological matter (see, for instance, [35, 74, 136, 140, 232, 241, 265, 301]).

Nowadays, the theory of *morphoelasticity* [140], which aims at understanding how a body changes dynamically as a consequence of growth and remodelling, has become an established tool for the investigation of these processes.

In mathematical terms, the theory of morphoelasticity assumes that residual stresses are due to local growth or remodelling processes, described by a specific deformation tensor $\mathbb{G}$. Then, the elastic deformation $\mathbb{F}_{\mathrm{e}}$, which is the one determining the stress response of the body, is defined as the difference between the visible deformation $\mathbb{F}$ and the distortion

$\mathbb{G}$ in the sense of multiplicative decomposition [9, 10, 140, 265]:

$$\mathbb{F}_e = \mathbb{F}\mathbb{G}^{-1} \qquad \Longrightarrow \qquad \mathbb{F} = \mathbb{F}_e\mathbb{G}\,, \tag{1.17}$$

where the tensor $\mathbb{G}$ describes the local change of shape and/or volume due to remodelling or growth. In particular, remodelling is often characterised by isochoric processes, for which $\det\mathbb{G} = 1$, while growth is accompanied by volume changes, so that $\det\mathbb{G} > 1$.

Hence, the multiplicative decomposition allows to separate the inelastic distortions related to growth or remodelling from the purely elastic contribution. The state defined by $\mathbb{G}$, often called *natural state*, is not in general compatible, or in other words $\mathbb{G}$ need not be the gradient of any deformation. In such natural state, which by definition is stress-free, each material particle is allowed to grow or remodel freely and independently of all the others. The subsequent elastic accommodation in the material, described by the tensor $\mathbb{F}_e$, restores the compatibility of the body and leads therefore to the development of residual stresses. The time evolution of tensor $\mathbb{G}$ has to be prescribed according to the phenomenon at hand, as we will do in Chapters 4 and 5.

1.2.3 Elastic Constitutive Equations

The balance equations hold for any type of continuum body, but are not sufficient to determine its motion following a prescribed loading. It is therefore necessary to complement the balance laws with appropriate *constitutive equations*, which describe the relation between deformation and stress for a specific class of bodies accounting for the mechanical characteristics of the material which composes such bodies.

Since in Chapters 3–5 we will mostly deal with *elasticity*, we recall here some basic definitions. An elastic body is characterised by a stress which depends on the deformation only through the deformation gradient, i.e.,

$$\mathbb{T} = \mathbb{T}(\mathbf{X}, \mathbb{F}_e(\mathbf{X}))\,. \tag{1.18}$$

Thus, coherently with Eq. (1.17), the stress state of an elastic body is determined by the elastic deformation $\mathbb{F}_e$, which accounts for both local length changes due to external loads and for the deformation required to restore compatibility. If $\mathbb{G} = \mathbb{I}$ we have $\mathbb{T} = \mathbb{T}(\mathbf{X}, \mathbb{F}(\mathbf{X}))$ and all the classical results of finite elasticity without distortions are recovered. In addition, a continuum is said to be *hyperelastic* if there exists a function $\mathcal{W}(\mathbb{F}_e)$, called *strain energy*

density function, such that

$$\mathbb{P}_e(\mathbb{F}_e) = \frac{\partial \mathcal{W}}{\partial \mathbb{F}_e} \qquad \text{and} \qquad \mathbb{T}(\mathbb{F}_e) = J_e^{-1} \frac{\partial \mathcal{W}}{\partial \mathbb{F}_e} \mathbb{F}_e^T . \tag{1.19}$$

where $\mathbb{P}_e$ is the first Piola-Kirchhoff stress in the natural state.

In order to satisfy the frame indifference principle, which states that a constitutive equation must not depend on the adopted reference frame, it can be shown [151] that the strain energy density function has to depend on the deformation through $\mathbb{C}_e$:

$$\mathcal{W}(\mathbb{F}_e) = \widehat{\mathcal{W}}(\mathbb{C}_e) . \tag{1.20}$$

Moreover, if the material is isotropic, as in Chapters 4 and 5, then the energy density can be written as a function of the first three invariants in Eq. (1.6), namely,

$$\widehat{\mathcal{W}} = \widehat{\mathcal{W}}(I_1, I_2, I_3) . \tag{1.21}$$

Instead, for anisotropic materials which exhibit preferential directions due for instance to reinforcements, additional invariants have to be included in the strain energy to describe the mechanical behaviour. In particular, if a material is *transversely isotropic*, i.e., there exists a preferential direction identified by a vector $\mathbf{N}$ in the reference configuration, the energy becomes a function of five invariants [327]:

$$\widehat{\mathcal{W}} = \widehat{\mathcal{W}}(I_1, I_2, I_3, I_4, I_5) . \tag{1.22}$$

Finally, if there are two preferential directions denoted by two unit vectors $\mathbf{N}$ and $\mathbf{M}$, as in Chapter 3, the energy can be written as a function of all the eight invariants in Eq. (1.6), so that [225, 327]:

$$\widehat{\mathcal{W}} = \widehat{\mathcal{W}}(I_1, I_2, I_3, I_4, I_5, I_6, I_7, I_8) . \tag{1.23}$$

1.3 Outline of the Thesis

In detail, the structure of the Thesis is as follows. We begin in Chapter 2 with a thorough review of the literature concerning cell reorientation under mechanical stimuli. In fact, numerous experiments showed that, if cells are seeded on a substrate which is periodically deformed, they will realign their cytoskeleton along a certain direction, in order to relieve the sensed stress. The understanding of this phenomenon is important in applications rang-

ing from mechanotransduction to tissue engineering, as we mentioned above. Therefore, we firstly provide a summary of the available experimental results, so as to capture the fundamental mechanical and biological features involved in the cell reorientation process, and present an overview about previous mathematical models on this topic.

In Chapter 3 we propose three types of mechanical models to address different issues about cell reorientation under periodic stretching. First of all, by using a strain energy minimisation approach that was shown to be effective in the literature, in Section 3.1 we analyse the impact of nonlinear elasticity. In fact, previous models mainly relied upon linear theories, which however might be inadequate to describe some experiments performed with considerable deformations. Afterwards, in Section 3.2 we address the problem of cytoskeletal remodelling within a fibre reorientation framework for anisotropic materials, to investigate the dynamics of cell alignment in more detail. We derive a thermodynamically consistent model for the reorganisation of two fibre families and we analyse its stationary solutions, that exhibit interesting properties of coaxiality between stress and strain, before applying it to cell reorientation experiments. Finally, in Section 3.3 we introduce linear viscoelasticity to model the effect of the cyclic deformation frequency in cellular realignment.

Then, in Chapter 4 we consider another problem related to cell reorganisation and active response, that is, the contractility of axons. Indeed, experiments have demonstrated that these neural components own the ability of actively regulating their diameter as a consequence of external stretching or drug-induced alterations. We propose a model, grounded on Continuum Mechanics, to investigate the interplay between active contractility in the circumferential and axial directions, as suggested by recent experimental evidence.

In Chapter 5, we study the problem of brain tumour growth in a mechanical and computational framework. Specifically, we consider brain tissue as a biphasic mixture, in order to distinguish between solid and fluid components, and we describe the proliferation of a tumour mass thanks to the theory of morphoelasticity. Since we are mostly interested in the impact of solid stresses subsequent to cancer growth, we describe both the healthy and diseased tissues as nonlinearly elastic soft materials: this allows to evaluate the deformations and stress induced by the growth of the solid mass. We test the behaviour of the model by performing simulations on a realistic brain geometry which includes a set of patient-specific data.

Finally, Chapter 6 summarises the main results of the Thesis and provides some concluding remarks, along with open problems on the considered topics.

Chapter 2

Experimental Observations and Mathematical Models of Cell Orientation

After having outlined both the biological and the mathematical framework, in this Chapter we provide a detailed review on the experimental and theoretical findings concerning cell orientation under stretch. Indeed, starting with the very first observations about the mechano-response of cells in the 1980s, a consistent amount of empirical results have been highlighted and the problem attracted increasing research attention in the last years. Given the variety of experiments, performed under very different conditions, it is fundamental to summarise their results, as we do in Section 2.1, in order to capture the relevant aspects to be included in the mathematical modelling process. Afterwards, in Section 2.2 we present and discuss the theoretical works on this topic available in the literature, upon which we will build our models.

The content of this Chapter has been included in a literature review article:

C. Giverso, N. Loy, G. Lucci, and L. Preziosi. Cell orientation under stretch: A review of experimental findings and mathematical modelling, *Submitted*.

2.1 Review of Experimental Findings

The aim of this Section is to provide a thorough review of the experimental literature concerning the reorientation response of cells under periodic mechanical stimuli. Indeed, in the last forty years, a huge amount of experiments have been performed using different

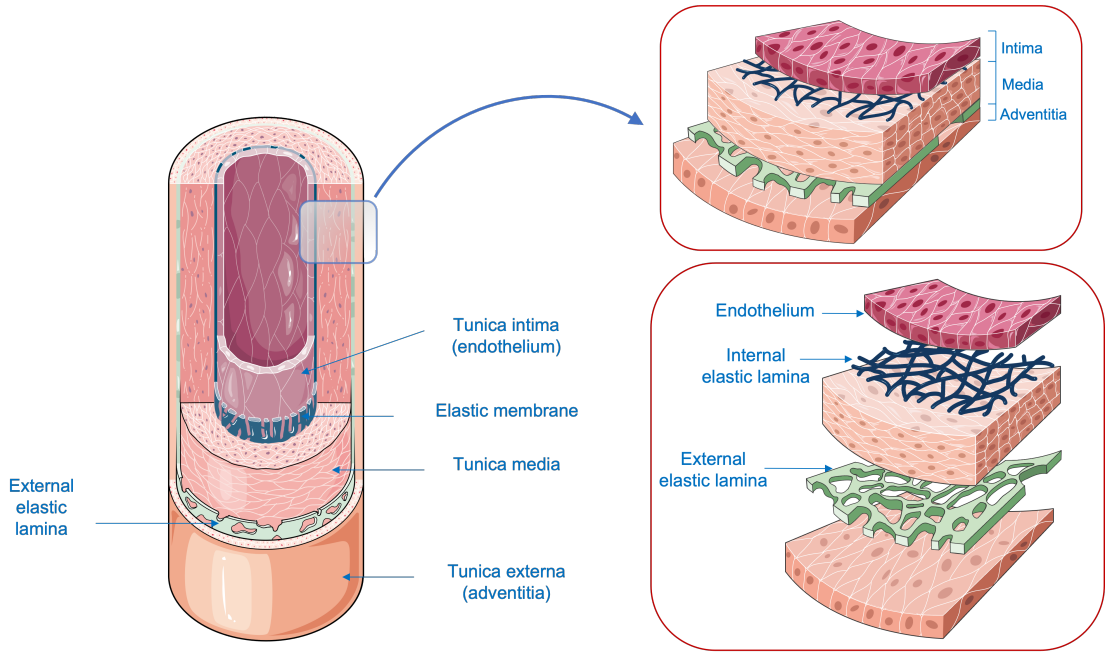

Fig. 2.1 Schematic representation of the inner structure of typical arteries. The innermost layer, whose cells are in direct contact with blood flow, is called *tunica intima*. An internal elastic lamina separates the intima from the *tunica media*, in which the cells appear oriented obliquely or perpendicularly with respect to the flow. Finally, we have an external elastic lamina that divides the media from the *adventitia*, or tunica externa. Adapted from [318].

assays. It is therefore important to summarise all the findings and to identify some common biological mechanisms. In detail, we start with some historical perspective about the first preliminary experiments in Section 2.1.1, which motivated all the subsequent studies. Then, the experimental results are classified in three macro-groups according to the type of substrate employed. Two-dimensional isotropic substrates, that represent the most important group, are discussed in Section 2.1.2. 2D micro-grooved membranes are examined in Section 2.1.3, whereas three-dimensional experiments are considered in Section 2.1.4.

2.1.1 Early Investigations and Experiments

The response of cells to mechanical cues started to attract attention in the 1980s, following the study of cardiovascular patophysiology. In particular, by observing the cellular arrangement in blood vessels, it was found that cells forming the walls of arteries were oriented along specific directions depending on their location, as pictured in Fig. 2.1. Endothelial cells in the innermost layer, in direct contact with blood flow, tended to be aligned in the

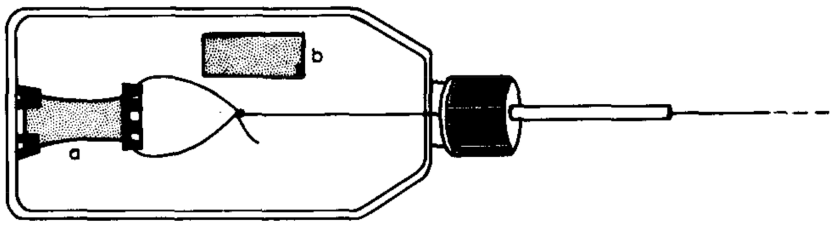

Fig. 2.2 Illustration of the experimental apparatus used for the first investigations about cell reorientation under stretch by Buck, taken from its original article [52]. The substrate *a* is connected to an external device which applies a cyclic stretching, whereas substrate *b* is left as a control.

axial direction of the vessel [50, 387, 390, 403], while smooth muscle cells in deeper layers, e.g., in the intima and in the internal elastic lamina, exhibited an oblique or perpendicular orientation, forming helical-like structures, with cells sometimes disposed at an angle of $20° - 40°$ with respect to the vascular axial direction [168, 300]. The pulsatile behaviour of the heart and the arteries, whose cells are constantly exposed to periodic deformations, stimulated the first investigations *in vitro*, with the aim of gaining a deeper understanding of cell mechanosensitivity and orientation in the circulatory system.

Motivated by his own studies on the orientation of cells in aortic walls [50], Buck was the first to examine the response of cells to mechanical cues *in vitro* [51]. He seeded a cell population on a rubber plastic substrate which was then cyclically stretched, to mimic the periodic vessel inflation during pulsatile flow: an illustration of the original experimental apparatus can be found in Fig. 2.2. Similarly to cells *in vivo*, he found that nearly 81% of fibroblasts tended to reorient between 45° and 90° with respect to the stretching direction. The results attracted some interest since they firstly put in evidence such an alignment behaviour of stimulated cells *in vitro* from the experimental point of view, paving the way for successive investigations.

Later, White and coworkers [387] were among the first to identify the presence of actomyosin fibres in vascular endothelial cells (EC) of mice, even if the function of such filaments was not fully clear at the beginning. In particular, they found that, in the thoracic aorta, cells were mostly oriented along the vessel axis and exhibited the presence of fibres (approximately $0.7\,\mu m$ wide and $4\,\mu m - 25\,\mu m$ long) aligned parallel to the blood flow. Interestingly, in their experimental assays, it is also shown that hypertensive rats displayed a higher proportion of EC containing aligned actin fibres with respect to normal rats. A possible explanation of this result relied upon the sensitivity of the endothelial cell cytoskeleton to external mechanical forces, such as blood pressure and fluid shear stress

on the walls. Indeed, hypertensive rats were characterized by higher arterial pressure, heart rate and flow velocity, leading to stronger hemodynamic forces acting on their vessels. Overall, such findings pointed towards the responsiveness of EC cytoskeleton to environmental mechanical stimuli, caused by anatomical, regional or structural factors, even if the reorientation mechanism following a stimulus was not fully elucidated.

Wong et al. [390] also revealed the presence of actin fibres in endothelial cells of several mammals, all oriented parallel to the blood flow and more prominent in regions where the latter had a higher velocity. It was however unclear which kind of mechanical force was the most relevant in driving the formation and orientation of cellular actin fibres. In this respect, experiments performed under confluent conditions [403] disclosed that a synergistic role was played by both fluid shear stress and circumferential strain in endothelial cells. Specifically, cells in physiological conditions elongated and oriented along the direction of flow and perpendicular to the direction of stretch, showing in all cases the formation of fibres aligned with their long axes. Then, in [403], the authors studied the response of cells to a combination of mechanical stimuli, proving that there is actually an interplay between different forces. In fact, the hoop deformation induced by the pulsatile flow in arteries increased EC sensitivity to shear stresses.

Almost perpendicular orientation of cells and cytoskeletal fibres with respect to the periodic forces was found also by Shirinsky et al. [320] for several types of human endothelial cells, coming both from vein and arterial tissues. The involvement of the cytoskeleton in the orientation process and response of EC was stressed once more and actin fibres were shown to be essential for cell orientation.

Other pioneering works about cell reorientation *in vitro* date back to 1986 and are due to Dartsch and collaborators [88, 89]. Their experiments on confluent monolayers of arterial smooth muscle cells evidenced the reorientation towards an oblique or approximately perpendicular angle, precisely quantified and varying with the amplitude of the cyclic deformation. Moreover, it was already evident that stretches as low as 2% did not succeed in stimulating the alignment of cells. An increase in the amplitude led to an extended degree of alignment and to a faster reorientation. Further studies by the same authors [87] confirmed such findings for vascular smooth muscle cells, which were found to align along two symmetric angles with respect to the perpendicular direction.

Additional investigations dating back to 1986 and 1988 [182, 336, 358] showed a similar behaviour, with cells reorienting towards an almost perpendicular alignment with respect to the direction of the applied cyclic stretch.

To complete the overview upon the preliminary experimental results on cell orientation under mechanical stimuli, it is worth to mention that, differently from the findings discussed so far, a report by Sottiurai et al. [326] claimed that an alignment parallel to the stretching direction was achieved by applying cyclic stretch with 10% amplitude and 0.87 Hz frequency to smooth muscle cells.

2.1.2 Cell over a Two-Dimensional Substratum

Overall, the results found in the experimental settings almost forty years ago were in agreement about some relevant facts, which stimulated subsequent investigations from other groups:

1. In addition to chemical substances, cells appeared to be prone to a response to mechanical cues coming from the environment.
2. The cytoskeleton, and especially the actin fibres, were thought to be involved in the cellular response to an externally applied mechanical force.
3. A reorientation towards a certain preferential direction, still not precisely identified, took place if cells on a substrate were subjected to a cyclic deformation.

Starting from these cornerstones, in the last three decades several attempts to unveil the mechanisms underlying cell alignment and reorientation were performed. Advances in imaging techniques and atomic force microscopy consistently improved the experimental precision, allowing to obtain detailed and high-resolution pictures of cellular and subcellular structures. These improvements in experimental instruments shed light on some relevant common features about the cellular response to external stimuli.

Before reviewing the phenomenological findings obtained in more recent years, we discuss some general features of typical experimental set-ups, so as to facilitate a comprehensive understanding of biological experiments and their outcomes.

The two-dimensional settings that are typically used to test the behaviour of cells under stretch consist of a silicon [159, 171, 215, 258, 268, 377] and/or polydimetylsiloxane (PDMS) substrate [137, 144, 239, 256, 308], very often coated with collagen or fibronectin to favour cell attachment. Cells are then seeded on the membrane at a certain density and, after attachment, the substrate is pulled along one or two perpendicular directions, either statically or periodically with different waveforms. In most of the experiments, a cyclic stretch in only one direction is applied, as this is the case that probably attracted more interest in clinical applications. Indeed, a uniaxial periodic deformation physiologically

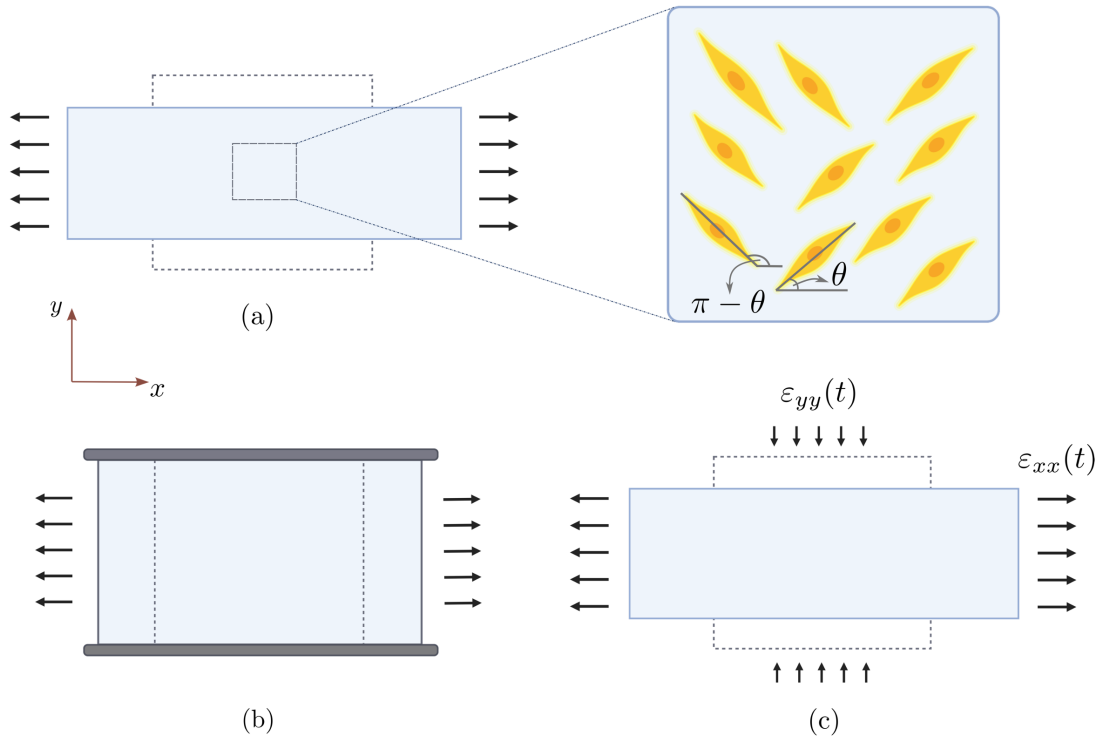

Fig. 2.3 Sketch of typical experimental set-ups for testing cell reorientation on planar substrates. (a): in uniaxial stretching experiments, the substrate is pulled on two sides, while the other two are free to move inwards following the elasticity of the material. In order to observe a homogeneous deformation applied to cells, only a small central region is examined. The angle between the cell major axis and the main stretching direction is denoted by θ. (b): pure uniaxial stretching experiment, in which two sides of the specimen are clamped to avoid deformation in the vertical direction. (c): biaxial experiments, where the strains are controlled in two directions.

happens in several situations: aside from the already cited blood vessels, a number of different tissues and organs undergo periodic strains in physiological conditions, such as the lungs, muscles and tendons, the bladder, and the intestine, to cite but a few.

In general, since the substrate is elastic, a simple pulling of its two lateral sides would naturally lead to a narrowing in the central region, as shown in Fig. 2.3(a). In these cases, experimental data are usually reported for those cells in the central portion of the specimen, highlighted in the Figure, where it can be reasonably assumed that stress and strain are homogeneous, with principal directions along the axis of deformation and its orthogonal. Nevertheless, as we will discuss shortly, the compression of lateral sides relevantly affects the cellular orientation and is one of the main factors that determines the final placement of a mechanically stimulated cell.

In describing the deformation, we will denote by x the direction characterized by the maximum applied stretch. This direction will be also referred to as the *main stretching direction* in what follows. We will then denote by $\varepsilon_{xx}(t) > 0$ and $\varepsilon_{yy}(t)$ the strains along x and y, respectively, and by $\varepsilon_0 := \max_{t\in\mathcal{T}} \varepsilon_{xx}(t)$ the maximum applied strain over the time interval $\mathcal{T}$ of the experiment. Another important quantity that is introduced in the literature and that will be relevant in the mathematical modelling is the so-called *biaxiality ratio*, defined as

$$r := -\frac{\max_{t\in\mathcal{T}} \varepsilon_{yy}(t)}{\max_{t\in\mathcal{T}} \varepsilon_{xx}(t)} = -\max_{t\in\mathcal{T}} \frac{\varepsilon_{yy}(t)}{\varepsilon_0}. \tag{2.1}$$

In static conditions, the parameter r represents the percentage of contraction in the y-direction with respect to the extension applied in the x-direction. If the deformation is uniaxial, as in Fig. 2.3(a), then r can be identified with the Poisson ratio of the elastic material constituting the substrate.

To avoid the central narrowing of the substrate due to the Poisson effect, some countermeasures have been adopted in experimental works, like thickening the borders parallel to the main stretching direction (as done, for instance, in [89]) or attaching the horizontal sides to a more rigid structure or substratum. When these borders are fixed as in Fig. 2.3(b), then $\varepsilon_{yy} = r = 0$ and it is said that the specimen undergoes a *pure uniaxial stretching*.

The uniaxial settings described so far do not allow to have a full control on the deformation along the vertical axis, which instead may be relevant in determining the cellular orientation, as we will discuss later in more detail. To perform broader and more complete experiments, *biaxial tests* – represented in Fig. 2.3(c) – that allow to control both strains in the monolayer plane are sometimes performed [201, 222, 226]. In fact, for biaxial experimental settings, r becomes an externally controlled parameter. However, most of the results presented in the literature do not rely on this kind of mechanical stimulus. The only biaxial case which is investigated in several papers is the *equi-biaxial* deformation, where the tensile strains along the x and y directions are equal to each other [171, 172, 199, 360, 376, 377]. However, such a situation is less interesting from the experimental viewpoint, since it does not trigger the reorientation of cells on a substrate, as put in evidence in all the mentioned references.

Whichever type of deformation is considered, most of the experiments are performed with values of $r \in [0,1]$. We remark however that a negative value of r can be obtained if the substrate is pulled in both directions, as in [201, 222]. In particular, equi-biaxial extension corresponds to $r = -1$. At the other extremum, a value larger than 1 corresponds to a compression along y larger than the pulling along x, which, to our knowledge, has

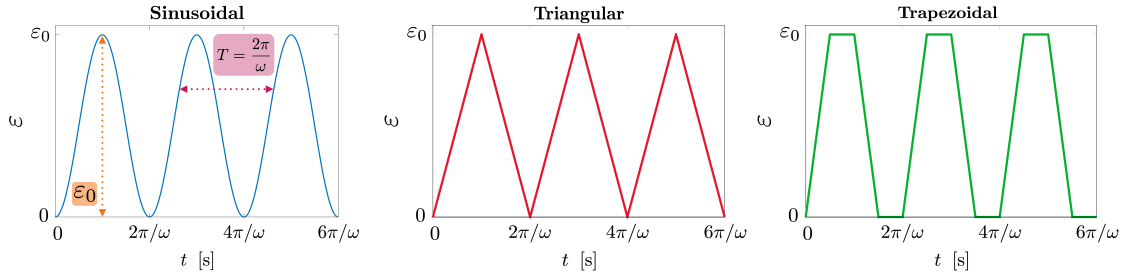

(a) (b) (c)

Fig. 2.4 Typical periodic deformations employed in experimental assays for cell reorientation under cyclic stretching. (a): sinusoidal deformation, with amplitude ε_0 and angular frequency ω, or period $T = 2\pi/\omega$. (b): triangular waveform, with same amplitude and frequency. (c): trapezoidal waveform, which includes a holding period once the maximum and minimum amplitude are reached.

not been done in experiments yet, though it could be interestingly included in the mathematical descriptions discussed later. In addition to the already mentioned case $r = 0$, representing pure uniaxial stretching, other values of interest for the biaxiality ratio are $r = 0.5$, corresponding to $\varepsilon_{yy} = -\varepsilon_{xx}/2$, and $r = 1$ which is equivalent to a deformation such that $\varepsilon_{yy} = -\varepsilon_{xx}$.

As done in the preliminary investigations discussed above, the majority of experiments focus on periodic deformations applied to the substrate, to represent the physiological pulsations *in vivo*. In particular, sinusoidal waveforms defined as

$$\varepsilon(t) = \frac{1}{2}\varepsilon_0\left[1-\cos(\omega t)\right] = \frac{1}{2}\varepsilon_0\left[1-\cos(2\pi f t)\right] \tag{2.2}$$

are often adopted (see for instance [190, 239]), as in Fig. 2.4a, in which ε_0 is the maximum amplitude, ω is the angular frequency in rad/s and $f = \frac{\omega}{2\pi}$ is the frequency in Hz, related to the period by $T = 1/f = 2\pi/\omega$. Alternatively, triangular [268, 362, 388] or trapezoidal [246, 264, 305, 362] waveforms might be employed, like the ones in Figs. 2.4b and 2.4c.

Statistical Description of Experimental Results

Since most of the experimental papers refer to the orientation angle θ of the cell, which is the most natural variable to work with, it is appropriate to firstly comment on the type of data that is usually reported. In particular, almost all investigators define θ as the angle between the cellular stress fibres (or body) and the main stretching direction, as sketched in Fig. 2.3(a). This appears to be the simplest way of defining the orientation of a cell, as

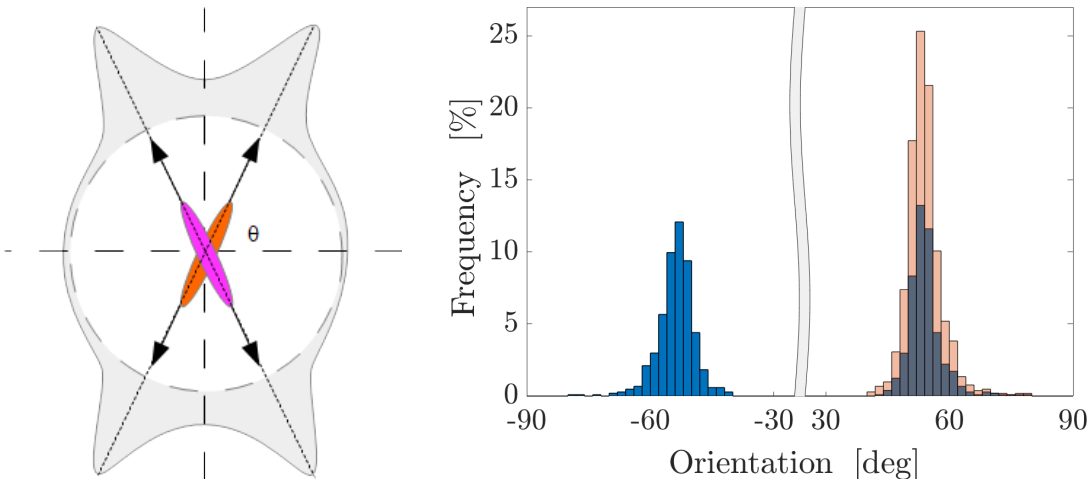

(a) (b)

Fig. 2.5 (a): Symmetric von Mises distribution with 4 symmetric maxima in $[0, 2\pi]$. (b): Distribution function of cell orientation from data by Livne et al. [226] when plotted in $\left[-\frac{\pi}{2}, \frac{\pi}{2}\right]$ in blue and when merged in $\left[0, \frac{\pi}{2}\right]$ in orange. Notice the break of the orientation axis between -30 degrees and 30 degrees.

well as the most effective. However, it is worth to remark that cell orientation experiments present some natural and intrinsic symmetries concerning the angle of alignment. In fact, there is no reason why the cell should prefer the orientation $\pi - \theta$ instead of the one characterised by the angle θ. In addition, as cells do not own a polarisation in the context of reorientation, the angles θ and $\pi + \theta$, as well as $-\theta$ and $\pi - \theta$, turn out to be all equivalent to each other as preferential orientations, as depicted schematically in Fig. 2.3(a). Such symmetries are evident in a wide number of experimental reports [87, 192, 220, 226, 351, 375, 379, 400]. For these reasons, most articles report data about the angle in the interval $\left[0, \frac{\pi}{2}\right]$, or sometimes in $[0, \pi]$, especially if cells are mostly aligned in the perpendicular direction.

In addition, as all biological phenomena, experiments are affected by the random behaviour of cells. For this reason, data are usually given in terms of histograms like those reported in Figs. 2.5b and 2.6, where the angle range of interest is subdivided into a certain number of smaller intervals, and the amount of cells whose orientation falls inside each interval is counted. In conclusion, if we work in $[0, 2\pi]$ the distribution function of orientations exhibits four symmetric peaks as in Figure 2.5a, possibly collapsing in two peaks either in 0 and π, so that most cells are oriented along the main stretching direction,

or in $-\frac{\pi}{2}$ and $\frac{\pi}{2}$, so that most cells are oriented perpendicularly to the main stretching direction.

In this context, let us explicitly discuss some issues that occur when dealing with circular statistics, as the ones regarding cell orientation. Some experimental papers summarise the data about the angle by computing the mean of the alignment distribution over the all sample of cells. However, such a parameter may be misleading and does not convey much information about the preferential orientation of a cell on a stretched substrate. As an example, if we take the distribution in blue in Fig. 2.5b that has two distinct and almost symmetric peaks, the mean of that distribution is close to 0, which is far from precise on describing the preferential arrangement of the cells. On the other hand, if orientations with negative and positive angles are merged as in the distribution in orange, then the mean will probably be nearby the maximum of the distribution. This is closer to the expected value of the favoured direction of cells, which should intuitively fall between 40 and 50 degrees in the Figure. However, such a situation seems particularly lucky, because in Fig. 2.5b the orange distribution is highly peaked in the interior of the interval of orientation angles. This is not the case, for instance, in Fig. 2.6b, which is not rarely observed. In this situation, the mean of the distribution computed in $\left[0, \frac{\pi}{2}\right]$ is 68° [120], but from the histogram it is clear that the distribution function is peaked in the interval $[80^\circ, 85^\circ]$. Going to another extreme case, in control situations where orientations are uniformly distributed, then the mean is trivially $\pi/4$ and several articles refer to this mean (see for instance [1, 100, 192, 217, 246, 330, 396]), which may be misunderstood if not contextualised properly. Indeed, a mean orientation angle of $\pi/4$ does not imply that cells are preferentially oriented along the direction of 45° with respect to the main stretching axis, but rather that the sample exhibits an overall random orientation.

For all these reasons, when considering the preferential orientation of cells, in the following we will refer to the peak of the distribution function (or the mode, in statistical terms) rather than the mean, whenever possible or having the experimental data available.

Given the possible shortcomings of a quantitative description based only on the mean orientation angle, different parameters have been sometimes employed in the experimental literature, which we briefly summarise below. A useful concept that is often used to measure cell orientation in experimental papers is the *order parameter* [143, 144, 190, 362, 363]

$$S := \int_0^\pi g(\theta) \cos 2\theta \, d\theta = \langle \cos 2\theta \rangle \,, \tag{2.3}$$

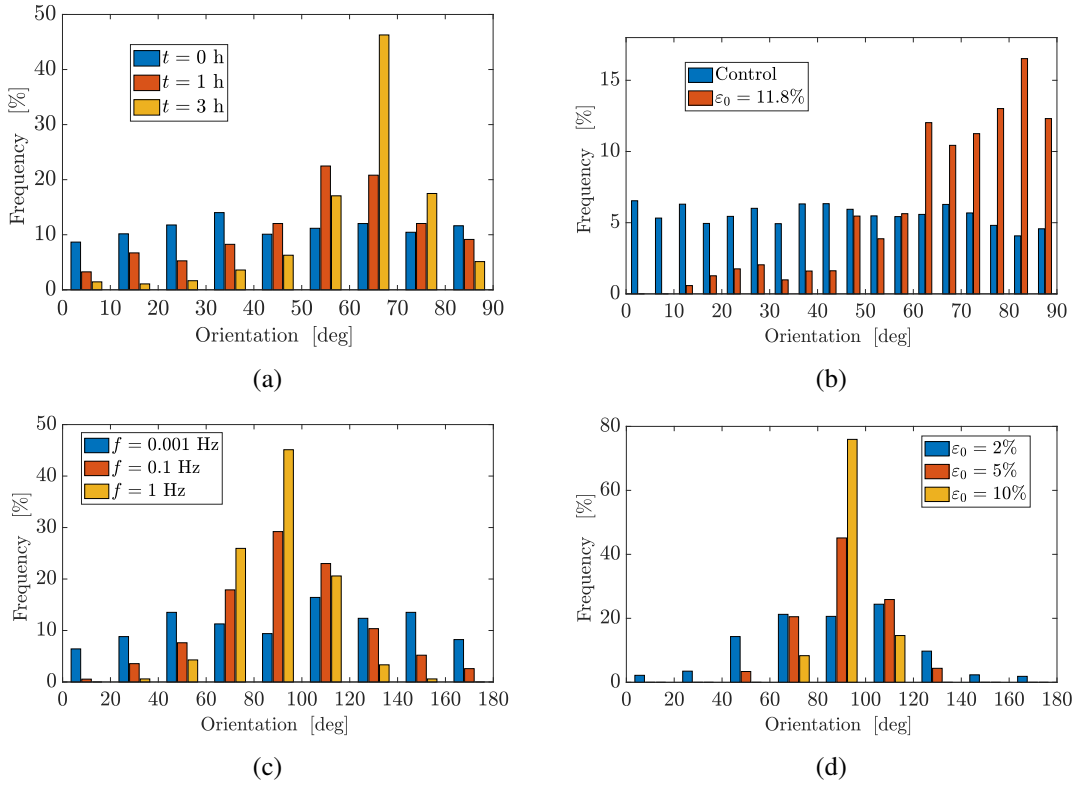

Fig. 2.6 (a): Temporal evolution of orientation angles for the cell body in experiments by Hayakawa et al. [159]. (b): Distribution of final cell orientation for a maximum strain of 11.8% (in red) compared with the control case (in blue). Data taken from Faust et al. [120]. (c): Distribution of final cell orientation for a maximum strain of 5% at different frequencies, specifically, 0.001 Hz in blue, 0.1 Hz in orange, 1 Hz in yellow (data from Mao et al. [239]). (d): Distribution of final cell orientation for a fixed frequency of 1 Hz and maximum strain of 2% (in blue), 4% (in orange), and 10% (in yellow). Data taken from Mao et al. [239].

where $g(\theta)$ is the empirical distribution function of cell angles. Hence, a random orientation of the sample corresponds to $S = 0$, whereas a fully coherent parallel orientation gives $S = 1$ and a fully perpendicular one amounts at $S = -1$. However, unless the distribution function is a deterministic Dirac delta, it is not straightforward to relate this parameter with the mode. In other words, although the order parameter S provides a more meaningful measure of the orientation, it does not give a detailed overview of the preferential direction, unless it corresponds to the parallel or perpendicular one. An oblique orientation, which is found quite often in experimental assays, would not be caught if evaluated using such a parameter.

Another measure of cell alignment that is employed to characterise the dispersion in cell orientation is the *circular variance* [171, 198, 199, 246, 258, 362]:

$$\mathrm{CV} := 1 - \frac{1}{N}\sqrt{\left(\sum_{i=1}^{N}\sin 2\theta_i\right)^2 + \left(\sum_{i=1}^{N}\cos 2\theta_i\right)^2}, \tag{2.4}$$

ranging from 0 to 1. The meaning of such parameter can be easily understood if each cell is associated with a unit vector $\mathbf{N}_i$ of coordinates $\mathbf{N}_i = (\cos\theta_i, \sin\theta_i)$, $i = 1,\dots,N$. The angles are doubled to account for the symmetry in the direction of the vectors, leading to the same cellular orientation as described previously. Then, the square root in Eq. (2.4) represents the norm of the vector obtained by summing all the orientations $\mathbf{N}_i$ of the cells in the experiment. It follows that, if the distribution is uniform and totally random, then $\sum_i \mathbf{N}_i \approx \mathbf{0}$ and $\mathrm{CV} = 1$, i.e. the circular variance is maximized. On the other hand, a perfectly aligned cell population will be characterized by the same orientation vector $\mathbf{N}_i = \mathbf{N}$ for all $i = 1,\dots,N$, leading to $\mathrm{CV} = 0$. In some works, the parameter $R := 1 - \mathrm{CV}$ is instead employed, following the same ideas but with an opposite meaning for the extreme values.

Before presenting the experimental results in isotropic planar conditions, we summarise below the main *in vitro* findings concerning the response of cells to mechanical deformations of their substrate. In particular, we have that:

Summary of experimental findings on 2D planar substrates

- Cells respond to cyclic strain of the substrate by reorienting their stress fibres and bodies towards a preferential orientation. The actin cytoskeletal structure is fundamental for this reorientation process.
- The response of the cytoskeleton can be observed within some minutes and precedes the one of the cell body, which may take some hours to be completed.
- The preferential orientation is *perpendicular or oblique* with respect to the main stretching direction. The biaxiality ratio r, related to the amount of tension and compression transmitted to the substrate and therefore to the cells, seems to play an important role in the precise quantification of the orientation angle.
- The results concerning the preferential equilibrium angle of cells appear to be *robust* with respect to the frequency and the amplitude of the applied cyclic deformation, as well as with respect to the stiffness of the substrate and its coating.

This is true provided that all these mechanical factors are greater than a certain lower threshold, below which no response is triggered. In addition, an increase in frequency and amplitude leads to a more rapid and more pronounced orientation of stress fibres and cells.

- A wide variety of cell types turn out to be mechanically responsive: fibroblasts, endothelial cells, vascular smooth muscle cells, neurons, mesenchymal stem cells, intestinal cells, as evident from Tables 2.1–2.3.
- In the confluent case, the effect of cell-cell contact comes into play and may lead to differences in the preferential orientation. Moreover, if experiments are performed under confluence, reorientation is found to be faster [190].

We now discuss in detail the two-dimensional experiments, both in sub-confluent and confluent conditions. A summary of the main experiments can be found in Tables 2.1–2.3.

Sub-Confluent Cells on 2D Isotropic Substrates

In the majority of experiments on two-dimensional substrates, cells are seeded on the membranes at a sub-confluent density, so that the effect of cell-cell contact and interaction is minimized. Generally speaking, it is found that, under certain conditions that will be discussed in more detail in the following Sections, when the specimen is subject to oscillatory deformations there is a reorganisation of the structure of the cytoskeleton that leads to alignment in a precise direction. In addition, the cell acquires an elongated and clearly oriented morphology [308]. Such a behaviour is evident in Fig. 2.7, which shows some examples of reoriented cells that visibly align along a preferential direction.

In Tables 2.1 and 2.2 we summarise the experimental contributions investigating cell reorientation on flat isotropic substrates in sub-confluent conditions. For each experimental test, we report the relevant parameters (or ranges of parameters in square brackets) characterising the assay, as well as the preferential orientation, whenever available. With regard to the latter, we remark that, in some works, the final configuration of cells is simply referred to as "perpendicular" or "nearly perpendicular", though the observed angle might be oblique. In the Tables we put in evidence this qualitative description by using the symbol $\perp$ (or $\approx\perp$), at variance with those cases where angles can be more precisely specified thanks to the presence of plots and histograms.

Sub-confluent cells on substrates

Cell type	f (Hz)	ε_0 (%)	r	θ_{eq} (max)	Refs.
(m) L strain fibroblasts	0.067	N/A	N/A	$[45°, 90°]$	[51]
(r) aortic SMCs	0.067	$[20, 35]$	N/A	$\approx 90°$	[52]
(r) aortic SMCs	1	20	0.4	$[50°, 70°]$	[159, 160]
(r) aortic SMCs	(0), [0.5, 2]	14	-0.36	$[75°, 90°]$	[222]
(h) bronchial SMCs	0.5	20	0.15	$[65°, 70°]$	[258]
(h) lung alveolar ECs	0.3	5, 10, 15	0.49	76°	[308]
(h) saphenous vein ECs	1	up to 24%	N/A	$\perp$	[179]
(h) umbilical vein ECs	1	10	N/A	$[85°, 90°]$	[256]
(b) aortic ECs	(0.01), 0.1, 1	10	N/A	$\perp$	[171]
(b) aortic ECs	1	(1), [3,10]	0.05	$\perp$	[198]
(h) osteosarcoma	(0.01), 1	10	≈ 0	$\perp$	[215]
(h) osteosarcoma	$0.01, 1$	10	-1	No orient.	[172]
(h) aortic ECs	0.5	5, 10	N/A	72° (median)	[268]
(h) aortic ECs	0.25, 0.5, 1	5, 10	0	$[80°, 85°]$	[377]

(Table Continues)

Sub-confluent cells on substrates

(h) aortic ECs	0.25, 0.5, 1	5, 10	0.34	$[65°, 70°]$	[377]
(h) aortic ECs	0.5	10	0	$[80°, 85°]$	[378]
(h) aortic ECs	$[0.5, 5]$	$[2, 10]$	0	$[63°, 86°]$	[388]
(b) adrenal cortex ECs	1	10	N/A	$[60°, 90°]$	[359]
(h) skin fibroblasts	1	4, 8, 12	N/A	$\approx 60°$	[379]
(h) skin fibroblasts	1	(0), 4, 8, 12	0.38	$[80°, 85°]$	[266, 267]
(m) embryonic fibroblasts	$[0.1, 3]$	8	0.194	$\perp$	[144]
(m) embryonic fibroblasts	1	8	0.194	$\perp$	[137]
(r) embryonic fibroblasts	4	8	0.194	$67.4°$ (mean)	[100]
(h) vaginal fibroblasts	0.1	10	N/A	$\perp$	[383, 384]
(h) lung fibroblasts	$[0.25, 3]$	$(< 1); [2, 25]$	N/A	$[60°, 90°]$	[40]
(h) cortical bone osteoblasts	1	$[0, 12]$	0.38	$[75°, 85°]$	[267]
(m) bone osteoblasts	$0.5, 1$	8	0.52	$[40°, 80°]$	[264]
(m) embryonic fibroblasts	(0.01), 0.1, 1	10	0	$\perp$	[172]
(h) annulus fibrosus cells	1	10, 15, 20	N/A	$86.4°$ (mean)	[1]

(Table Continues)

Sub-confluent cells on substrates

(r) bone marrow MSCs	1	10	0.38	$[70°, 80°]$	[400]
(h) bone MSCs	$[3 \cdot 10^{-5}, 2]$	$(1); [2, 10]$	0	$[80°, 100°]$	[239]
(h) bone marrow MSCs	$(0), 1.2$	10	N/A	64°	[139]
(h) melanocytes	1	4, 8, 12	0.38	$[55°, 60°]$	[375]
(h) umbilical vein ECs	0.5	10	< 0.3	$[80°, 90°]$	[396]
(b) aortic SMCs	0.25, 1, 2	5, 10, 20	N/A	$[80°, 90°]$	[192]
(b) aortic ECs, fibroblasts	1	5	N/A	$[80°, 90°]$	[192]
frog epithelial renal cells	1	20	0.4	Oblique	[160]
(h) umbilical artery SMCs	1	7	N/A	$[80°, 90°]$	[43]
(m) neuron-like cells	0.05, 0.15, 0.25	(2), 5, 10	0	$[60°, 90°]$	[220]
(m) fibroblasts	1	5, 10	≈ 0	$[100°, 110°]$	[63]
(h) aortic SMCs	1	10	N/A	$[60°, 70°]$	[409]

Table 2.1 Summary of the main experiments performed on planar substrates with sub-confluent cells. For each experiment, in addition to the cell type, we report the tested frequencies, amplitudes, biaxiality ratios (whenever available) and preferential orientation. In particular, we use parentheses to address attempted values which however did not give rise to cell reorientation. Instead, square brackets are used to denote a range of values. Abbreviations: N/A = data not available; SMCs = smooth muscle cells; ECs = endothelial cells; MSCs = mesenchymal stem cells; (b) = bovine; (h) = human; (r) = rat; (m) = mouse. We denote by $\perp$ an overall perpendicular orientation, though the precise angle is not specified.

Sub-confluent cells on substrates with specified Young modulus

Cell type	f (Hz)	ε_0 (%)	r	E (kPa)	θ_{eq} (max)	Refs.
(h) coronary artery ECs	(0.01), 0.1, 1	8	0.194	1000	$\perp$	[143]
(h) coronary artery SMCs	$(0.01, 0.1), 1$	8	0.194	1000	$\perp$	[143]
(h) umbilical vein ECs	1	10	0.45	900	$[55°, 60°]$	[32]
(h) dermal fibroblasts	$[0.0001, 20]$; (< 0.1)	(< 2); $[3, 16]$	0.194	1000	$\perp$	[190]
(r) embryonic fibroblasts	$[0.0001, 20]$; (< 0.01)	(< 1); $[2, 16]$	0.194	1000	$\perp$	[190]
(r) embryonic fibroblasts	[1.2, 12]	$[4, 24]$	$[0, 1]$	$20, 1000$	$[45°, 90°]$	[226]
(h) umbilical cord fibroblasts	(0), $[0.009, 0.052]$	(0); $[4.9, 32]$	0.15, 0.29	$(< 3); 11, 50$	$[65°, 85°]$	[120]
(h) osteosarcoma	(0.01), 0.1, 1	10	0.19, 0.43	$\begin{cases} \text{stiff} \\ \text{soft} \end{cases}$	$\begin{cases} \perp \\ \parallel \end{cases}$	[362, 363]
(h) MSCs	1	10	0.43	$\begin{cases} \text{stiff} \\ \text{soft} \end{cases}$	$\begin{cases} \perp \\ \parallel \end{cases}$	[363]
(m) myoblasts	0.5	7	0.5	≈ 1000	$[60°, 70°]$	[5]
pig valvular interstitial cells	1	10	0	0.9, 150	$\perp$	[360]
(h) umbilical vein ECs	0.13	14	0.5	50	78°	[410]

Table 2.2 Summary of the main experiments performed on planar substrates with specified mechanical characteristics in sub-confluent conditions. In particular, for each experiment we report the Young modulus E of the substratum, in addition to the other mechanical variables. Abbreviations: N/A = data not available; SMCs = smooth muscle cells; ECs = endothelial cells; MSCs = mesenchymal stem cells; (b) = bovine; (h) = human; (r) = rat; (m) = mouse. We denote by $\perp$ a perpendicular orientation and by $\parallel$ an overall parallel orientation, though the precise angle is not specified.

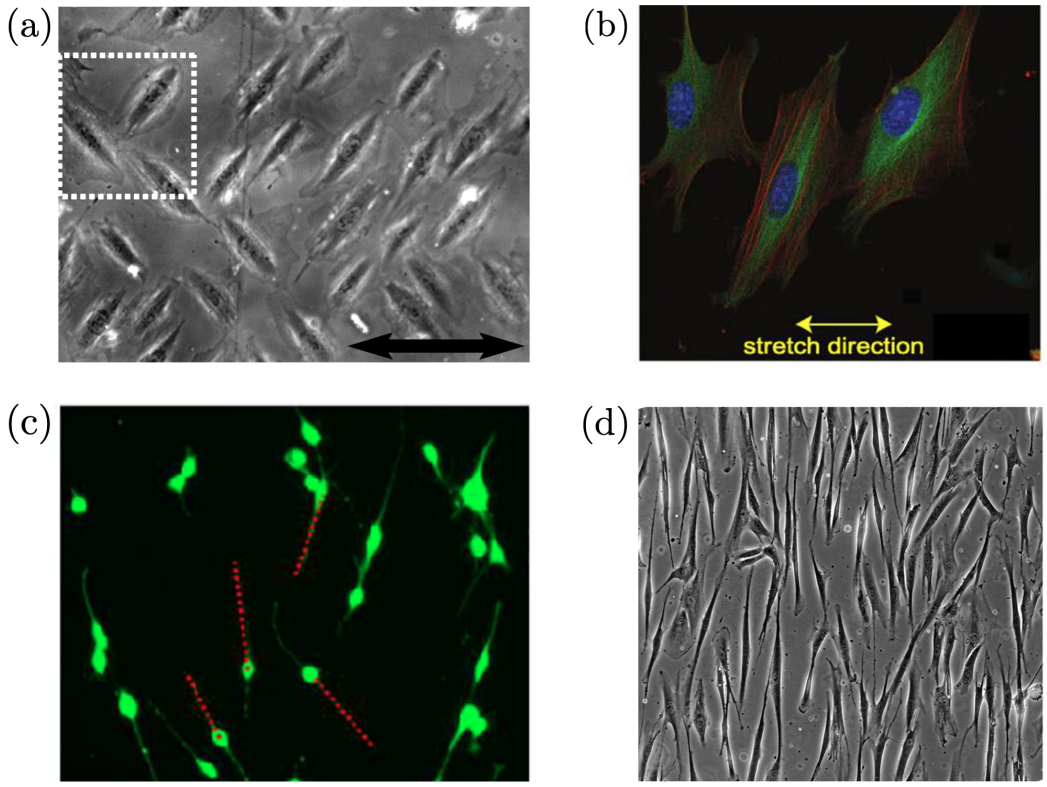

Fig. 2.7 Microscopic representative examples of reoriented cells under stretch. (a): rat fibroblasts oriented in symmetric directions after 6 hours of cyclic stretching at 1.2 Hz and 10% amplitude, with stretching direction highlighted by the double-headed arrows (taken from [226]). (b): rat fibroblasts after 6 hours of cyclic stretching at 1 Hz and 10% amplitude, taken from [63]. Notice the main cell and cytoskeletal components: actin stress fibres (in red), microtubules (in green), and nucleus (in blue). (c): neural-like cells after 72 hours of cyclic stretching at 0.25 Hz and 10% amplitude (taken from [220]). (d): human fibroblasts after 24 hours of cyclic stretching at 0.17 Hz and 20% amplitude. Notice that, in this case, cells are almost in confluence and there might be some cell-cell contacts (taken from [175]).

As a first important remark, we observe that, in addition to the robustness of the experimental results with respect to cell type, the reorientation behaviour appears to some extent almost independent of the applied frequency, amplitude, and of the mechanical characteristics of the substrate. However, in the Tables, we also highlight the values of stretching frequency and amplitude that did not lead to a clear alignment of cells. In what follows, the role of biological components – like the cytoskeleton – and of mechanical parameters – like frequency and amplitude of the deformation, as well as substrate stiffness – will be discussed in more detail, with reference to the Tables that summarise the experimental results.

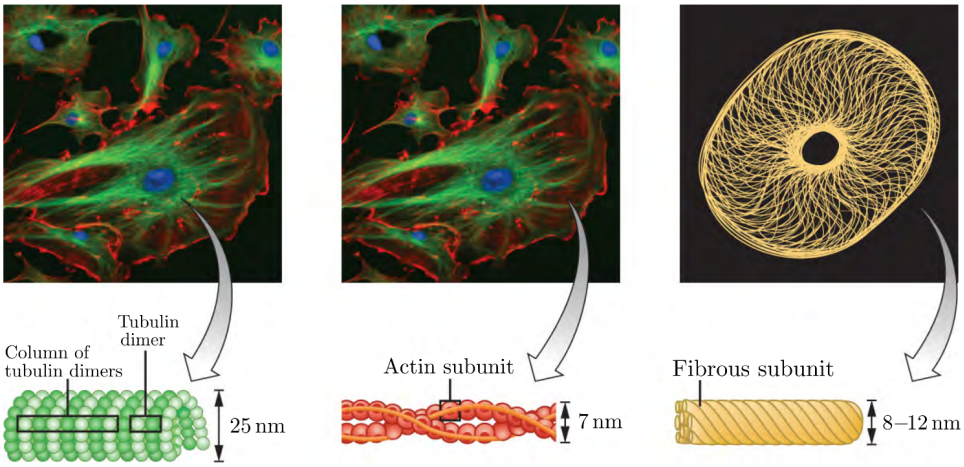

(a) Microtubules (b) Actin filaments (c) Intermediate filaments

Fig. 2.8 Main components of the cell cytoskeleton. (a): Microtubules, which are shown in green in the microscope image. (b): Actin filaments, which appear red in the cell. (c): Intermediate filaments. Adapted from [195].

Role of the Cytoskeleton

As mentioned previously, the cell cytoskeleton, i.e., the network of protein filaments and structures that is found in the cytoplasm, fulfils a fundamental role in sensing the external mechanical stimuli and in driving the subsequent reorientation towards the preferential direction. The relevance was already noticed in the first experimental investigations, though modern imaging techniques allowed to get more insight into its function. We briefly describe here the main components of the cytoskeleton and we discuss their role in the alignment process.

The primary function of the cytoskeleton is to give structural stability to the cell and to maintain its shape [6]. The cytoskeletal network provides a scaffold which keeps all the cytoplasmic components in place. Moreover, the cytoskeleton is able to sustain mechanical deformation as well as to actively contract. These characteristics make it a very relevant part of the cellular mechanical response. In particular, three main types of filaments constitute the typical cytoskeleton of a cell: actin filaments, which may form *stress fibres* (SFs), *microtubules* (MTs), and *intermediate filaments* (IFs), as shown in Fig. 2.8.

The stress fibres are probably the most important structure as far as contractility and reorientation are concerned. They are composed by actin filaments cross-linked together with myosin and other proteins, which form slender rods crossing the cell [6, 361]. These fibres are also able to actively contract and to develop forces as a response to environmental

changes or during cell migration. At the ends of SFs, protein complexes called *focal adhesions* (FAs) connect the cytoskeleton to the external environment, so that the cell is able to sense mechanical changes and to react accordingly. Thus, the interplay of SFs and FAs is crucial in *mechanotransduction*, i.e., the chemical response to mechanical stimuli.

Then, microtubules are hollow cylindrical components that contribute to the maintenance of the cell structure, to the formation of protrusions, and to the building of spindles during cell division. MTs have a typical diameter of about 25 nm and a length ranging from 200 nm to 25 µm.

Finally, intermediate filaments are also involved in the organisation of the spatial structure of the cell, anchoring components in their respective places. IFs have a high tensile strength, which makes them the most stable component of the cytoskeletal architecture.

The role of the cytoskeleton is fundamental in cell reorientation under cyclic stretching. In this respect, a very important work is the one by Hayakawa et al. [160], who studied the relationship between cytoskeletal rearrangement and cytoplasm reorientation. They put in evidence a significant time difference between the reorientation of SFs and the one of the cell body. The former started after 5 minutes of stretching and completed within 15 minutes. Instead, the latter – whose temporal evolution is reported in Fig. 2.6a – was more gradual and took up to 3 hours. These results about the dynamics of reorientation, with a significant delay between stress fibre and cell body alignment, are supported by several other authors (see, for instance, [171, 226, 256, 258, 266, 377]). Moreover, in another work [159], the same group discovered that MTs were not aligned clearly, unlike stress fibres, and did not seem essential for reorientation. Their presence appears to affect mainly the shape of the cell, which was less spindled when MTs were depleted. Instead, if SFs were disrupted, cell reorientation was almost blocked and significantly inhibited, confirming their critical role in the realignment of cells under periodic deformations.

Several other works show similar results about microtubules [63, 137, 144, 377]. The only observation in contrast is put forward by Morioka et al. [258], who demonstrate that a relevant interplay between MTs and actin SFs exists and affects the reorientation of the cytoskeleton. Specifically, their findings show that MTs also aligned along the cell axis under a cyclic stretch. Then, if microtubules are disrupted or stabilized with appropriate drugs, the cells do not seem to orient effectively.

Neidlinger-Wilke et al. [266, 267] provide further evidence supporting the role of the cytoskeleton in that fibroblasts appeared more mechanically responsive in reorientation

than osteoblasts. The former indeed have a stronger cytoskeleton than the latter, given that they exert large traction forces on the extracellular matrix (ECM).

Actually, there appears to be a complex interplay between cytoskeletal deformation and biochemical signalling, as discussed by Kaunas et al. [199]. In particular, the actin cytoskeletal deformation stimulates the production of a molecular signal, whose concentration gradually reduces when SFs reorient to accommodate the sensed strain.

Then, a very relevant and detailed analysis of the role of cytoskeletal components on the reorientation kinetics was performed more recently by Goldyn et al. [137] and by Zielinski et al. [410]. As confirmed by several other investigators, in [137] it was found that actin-disrupting drugs inhibit cellular reorientation, while MTs are not necessary to achieve cell alignment under cyclic stretching. Surprisingly, however, their experiments demonstrate that depletion of MTs reduced the reorientation time, while stabilization of them provoked a 4-fold increase of such time. Hence, even if they are not necessary, MTs might somehow regulate the dynamics of orientation. A possible explanation to this fact could be the sterical hindrance caused by MTs that affects the actin reorganisation: stabilized and fixed tubules might represent a physical obstacle to the reorientation of actin fibres. Alternatively, such influence of MTs on the characteristic time may be due to the cross-linking with actin: if the acto-myosin network needs to drag MTs, the process of reorganisation might overall be slowed down.

In addition to actin SFs and MTs, the dynamics of IFs was studied in [410]. These structures were all found to reorient obliquely or perpendicularly to the strain direction, though their kinetics was different. SFs were in fact the fastest, whereas MTs and IFs reorientation was considerably slower. All the cytoskeletal structures, however, preceded cell body realignment.

Having assessed the importance of the cytoskeletal actin architecture in the reorientation process, a very recent work by Roshanzadeh et al. [308] focused on the mechanoadaptive role of stress fibre subtypes. Indeed, previous experimental analyses concerning the various components of the cytoskeleton were mainly directed to a single type of SFs or MTs, even if, within the cell supporting structure, different types of SFs actually exist, performing different roles. In this regard, the most relevant result of this work lies in the study of the interdependence of different SFs structures. The cytoplasm, whose reorientation was driven by the *peripheral SFs*, oriented at 76° regardless of the strain magnitude, while the nucleus, guided by *perinuclear cap fibres*, showed a lagged dynamics, especially at small strains. The possibly different responsiveness of SFs types to mechanical stimuli

was suggested before by Tamiello et al. [353] in experiments including contact guidance, which will be discussed in Section 2.1.3.

To complete the discussion about the cytoskeletal response and consequent reorientation, an interesting result concerns the only negative example that is reported. Indeed, a cell type that does not appear to respond following a stretch-avoidance mechanism are *immune cells*, like macrophages, neutrophils, or monocytes. The reduced mechanical response of neutrophils on a 2D substrate with anisotropy prescribed by collagen fibres was reported by Haston et al. [155] in 1983. Coherently with a previous work [153], it was suggested that neutrophils are unable to generate sufficient traction forces through their cytoskeleton. This behaviour is probably due to the fact that immune cells do not possess a strong cytoskeleton and they do not adhere firmly to the substrate. Indeed, they have to squeeze while patrolling the body for potential pathogens, which requires an ameboid motion, unlike other types of cells. Following these first experimental suggestions about immune cells, Matsumoto and coworkers [247] carefully analysed their reorientation following a mechanical cue. The results suggest that rat macrophages do not appear to be strongly responsive to the mechanical stimulus, while an alignment slightly parallel to the direction of stretch is reported for human monocytes [247]. This is in contrast with the common behaviour for other cell types, which exhibit an avoidance of cyclic strain and reorient obliquely or perpendicularly to the main stretching direction, as discussed before and summarised in the Tables. Subsequent studies confirmed this behaviour of immune cells [24, 25, 244] for cyclic strain at different amplitudes (10% and 20%) and frequencies (0.25 Hz and 1 Hz), both low and high.

In the following Subsections, we discuss thoroughly the role of mechanical parameters, like the stretching frequency, the stretching amplitude and the substrate stiffness, in the process of cell and stress fibre alignment.

Frequency Effect

The natural frequency to test cell behaviour is a physiological value of 1 Hz, corresponding to normal heart beats [243], or alternatively a value in the range $0.25\,\text{Hz} - 0.3\,\text{Hz}$, corresponding to breathing frequency [350]. The first work to explore the possibility of differences in cell orientation due to the stretching frequency is the one by Kanda and Matsuda [192]. Although they employed only the mean orientation angle of the cell population to quantify the frequency effects, an increase from 0.25 Hz to 1 Hz and to 2 Hz provoked an increase in such an angle, meaning that the alignment of cells was more pronounced

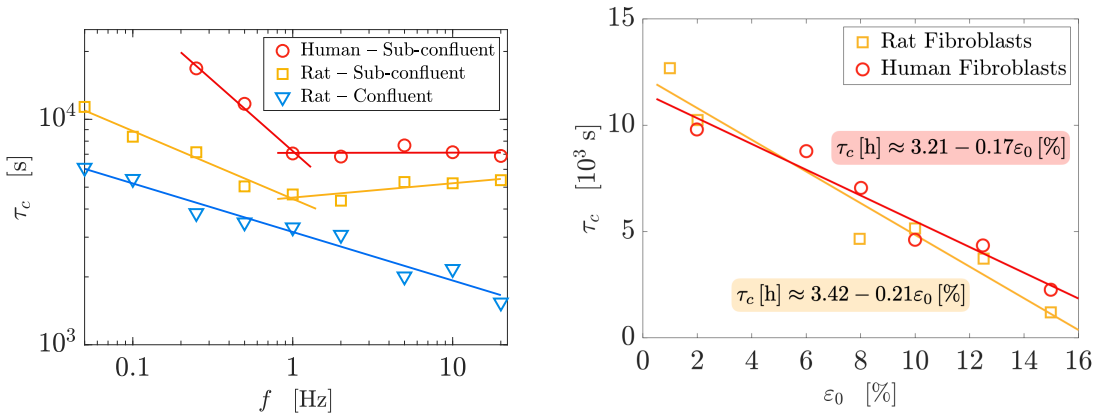

(a) (b)

Fig. 2.9 (a): characteristic time τ_c of reorientation as a function of the applied frequency f, in log-log scale, with data from [190]. In the sub-confluent case, two regimes can be distinguished: a first one in which the characteristic time follows a power law decrease and a second one where, for frequencies above 1 Hz, τ_c remains almost constant. This is not the case for confluent cells, for which the time always decreases with no saturation. (b): characteristic time as a function of the amplitude ε_0.

towards the perpendicular orientation. However, as discussed above, providing the mean angle as a measure is not the most effective way to convey the results.

One of the most detailed works concerning the effects of amplitude and frequency is due to Jungbauer and collaborators [190]. In their work, a wide range of frequencies is tested on rat embryonic fibroblasts (REF) and human dermal fibroblasts (HDF). The results suggest that there is a cell-type-dependent *minimal threshold frequency* needed to induce a significant cellular reorientation: such a threshold amounts at about 0.01 Hz for REF and 0.1 Hz for HDF. Moreover, a linear log-log relationship between the reorientation time and the frequency is observed, with higher frequencies associated with a faster process and a greater alignment in the cellular population, as in Fig. 2.9a. The most relevant finding however is the existence of an *upper threshold frequency* of approximately 1 Hz, above which the reorientation time saturates and the process cannot be accelerated anymore in sub-confluent populations. More specifically, above a threshold value of 0.5 Hz for REF and 1 Hz for HDF, the reorientation time becomes nearly constant and equal to 80 minutes for the former and 120 minutes for the latter (see yellow and red curves in Fig. 2.9a). Below the threshold value, instead, the characteristic time increases and is equal to nearly 3 hours in the case of REF for a frequency $f = 0.05$ Hz and about 5 hours in the case of HDF for $f = 0.25$ Hz. According to the authors, such a result, which was also confirmed later by another group [144], might be due to the saturation of some molecular mechanism

driving the reaction to the stimulus that cannot react faster for periods above 1 second. The hypothesis is corroborated by the results in confluent conditions, where no saturation is observed and the characteristic time is a strictly decreasing function of the applied frequency, as clearly evident from the blue curve in Fig. 2.9a. Indeed, for high cellular densities, the cell-cell contacts through cadherins become relevant and may provide an additional sensing machinery that prevents saturation and speeds up the reorientation. It is also worth to observe that, in general, confluent cells reorient faster than sub-confluent layers, as we will describe later in more detail.

The presence of a lower frequency threshold, pointed out in [190], appears to be a crucial issue to trigger cell response and is confirmed by several experimental reports. In addition, such a threshold seems to be cell-type dependent. For instance, the frequency must be larger than 0.01 Hz for rat embryonic fibroblasts [144, 190], osteoblasts [215, 362], and bovine aortic endothelial cells [171, 215]. Instead, the frequency should be above 0.1 Hz for human dermal fibroblasts [190], human coronary artery endothelial cells [143] and at least 1 Hz for human coronary artery smooth muscle cells [143]. Interestingly, a frequency of 0.05 Hz seems to be enough to induce neuronal alignment away from the stretching direction [220]. However, these differences with the cell type do not affect the cytoskeletal structures, i.e. stress fibres and focal adhesions, which instead are found to be oriented at 0.1 Hz independently of the cell line [143]. Such data support previous findings about the delayed and less sensitive response of the cell body, compared with the mechano-reception of the stimulus by the cytoskeleton.

Very low frequencies in the range of 9–52 mHz applied to human umbilical fibroblasts appeared however to stimulate a cellular reorientation response, though the time span required to observe a steady state was considerably increased [120]. Nevertheless, in the work by Faust and collaborators [120], it is difficult to decouple the effects of frequencies and amplitudes, given that the authors choose to keep a constant strain rate.

Another work pointing out the relevance of the deformation frequency, while providing a possible explanation, is the one by Hsu et al. [171]. Based on a mathematical model of SFs self-adjustment, the authors suggest that if the frequency is too low, then the stress fibres are able to accommodate the changes due to the strain and to maintain an optimal level of extension. Consequently, there is no reorientation if the frequency is below a certain threshold of approximately 0.01 Hz, which is coherent with the experimental findings for some cell types. Then, if the frequency is increased, SFs become less able to compensate the stretch, and therefore reorient away from the deformation until a second threshold is reached, above which the maximal alignment is observed. The same authors also put

in evidence that an increase in the frequency leads to a decrease in the circular variance until a constant value is reached, meaning that the degree of alignment of the cells on the substrate has become more peaked. This is often found in experiments as a frequency increase consequence [144, 171, 190, 239]: for greater frequencies, the distribution of cells becomes more peaked towards the preferential orientation, as shown in Fig. 2.6c.

The effect of cyclic strain frequency was investigated among others by Liu et al. [222]. In particular, an increase in the frequency does not seem to affect the final average orientation of the cells, but the amount of cells falling in the range $[75°, 90°]$ decreases with the frequency. These results are somehow counter-intuitive and contrast with other experimental observations [171, 239], where a frequency increase was associated with a greater perpendicular alignment.

A very relevant work that it is worth to mention is the one by Mao and collaborators [239], whose results are reported in Fig. 2.6c. They studied the frequency effect and observed that, for a 10% strain at 1 Hz, the fraction of orientation angles between 80° and 100° was over 75%, while this value decreased to less than 11% for a frequency of 0.001 Hz, corresponding to that of a uniform distribution. In the same work, it is also found that the critical frequency necessary to observe a reorientation of cells appeared to be amplitude-dependent, namely 0.034 Hz for 2% strain, 0.013 Hz for 5% strain, and 0.004 Hz for 10% strain. Thus, higher frequencies are required for the onset of cellular realignment at low amplitudes, and the combination of these two mechanical parameters is not fully decoupled. Mao and coworkers are the first to observe such an interplay, so they propose a single parameter to summarise the frequency-amplitude threshold, which they call *critical stretching rate* and is defined by $\pi f \varepsilon_0$, or equivalently $\frac{1}{2}\omega\varepsilon_0$. The reciprocal of such value, amounting at 8.3 minutes, correlates well with the turnover time of actin filaments reported in the literature [207, 239].

Other studies analyse variations of the strain rate, which is related to the product between the frequency and the maximum amplitude of the applied strain. For instance, Wille et al. [388] do not find a statistically significant effect of varying the strain rate, whereas, when it is kept constant, higher frequencies appear associated with faster reorientation. It is also found that the median orientation angle does not depend on the strain rate nor on the frequency. However, it is worth to remark that some experiments by Wille et al. [388] are performed varying both the amplitude and the strain rate, which is somehow misleading since it corresponds to variations in both the maximum applied strain and in the frequency. The latter is in fact different from the strain rate and this should be taken into account when interpreting the results.

An evaluation of the strain rate effect is also provided by Nagayama et al. [264], thanks to a detailed analysis of different strain waveforms on reorientation. In particular, it was suggested that alignment was mainly promoted by compressive forces and coherently the trapezoidal waveform, which exhibits the highest such force, led to the most efficient reorientation. However, Tondon et al. [362, 363] proposed an opposite mechanism compared with the results by Nagayama and coworkers [264]. Indeed, in the former work, it emerges that SFs are much more sensitive to the rate of lengthening rather than to the rate of shortening. This is confirmed by a thorough comparison between triangular, square, and asymmetric waveforms: cell subjected to higher strain rates in elongation display a more pronounced oblique orientation. Nevertheless, it is also worth to remark that, for frequencies greater than or equal to 1 Hz, these differences appear less relevant.

To summarise the results about the role of the frequency, the main experimental findings are the following:

- There exists a lower frequency threshold ω_l, below which no reorientation happens.
- There exists an upper frequency threshold ω_u, above which – in sub-confluent conditions – cell alignment cannot become faster. These thresholds might be dependent on the cell type.
- If the frequency falls between ω_l and ω_u, the effect of increasing it is twofold. First of all, the number of cells oriented in the preferential direction increases. Indeed, if ω is low, fewer cells are found to be aligned, while most of the population remains randomly oriented. Conversely, for high frequencies, the probability distribution of oriented cells becomes highly peaked around the preferred orientation angle. Second, higher frequencies are associated with a faster reorientation, and therefore with a lower characteristic time [190]. These effects emerge visibly in Figs. 2.6c and 2.9a.
- The preferential angle at steady state, at least according to some experimental works, does not seem to be affected by a change in the frequency, provided that the latter is above the minimal threshold [120, 239, 270, 362].
- There might be a combined action of frequency and amplitude in determining the thresholds ω_l and ω_u and therefore the onset of cell alignment, with higher amplitudes required at low frequencies and vice versa.

To conclude the discussion about the frequency, a possibly relevant case is the one in which the specimen is subjected to a *step stretch*, which is then sustained without oscillations, corresponding to a null applied frequency. In this situation, however, the

behaviour of cells is not well clarified. Indeed, if the static stretch is regarded as a limit case of low frequency, one would expect that the sample keeps having a uniform distribution of orientation angles. This is observed in some experimental settings [139, 159, 222]. On the contrary, a step deformation provoked an alignment parallel with the stretching direction in other works [68, 362, 363]. Interestingly, Tondon and Kaunas [363] also put in evidence that a static step stretch promoted parallel alignment on soft gels, but not on stiff silicone substrates. Nevertheless, this situation appears more complicated to analyse, due to the interplay between the mechanical stimulus on the cell and the anisotropic changes in the gel stiffness caused by the stretch itself. Indeed, stretching a collagen gel may increase its stiffness along the direction of the deformation, which may consequently affect the cellular orientation. Therefore, the response to a sustained step stretch still needs to be investigated in the two-dimensional case. In 3D matrices, instead, parallel alignment seems to be the preferred response in almost all studies (see Section 2.1.4).

Amplitude Effect

As for the frequency, a minimal strain amplitude needs to be applied in order to induce cell reorientation. Such threshold is generally in the range of few percent of substrate strain. For instance, an amplitude of at least 1% was needed for fibroblasts [40, 190], 3% for bovine aortic ECs [198] , 4.4% for human bone mesenchymal stem cells [259], and 5% for neurons [220]. A similar behaviour is also seen in confluent conditions where, for instance, a strain of at least 2% was needed [89] to reorient rabbit arterial smooth muscle cells. As discussed before, Mao et al. [239] recently observed that the minimum amplitude value decreases for increasing frequencies. This is not surprising, as both of them have the effect of promoting reorientation and lead to more peaked distribution functions, as shown in Figs. 2.6d–2.6c.

In general, an increase in amplitude above the lower threshold leads to a more pronounced orientation towards the preferential direction [120, 171, 192, 330] and to a decrease in the characteristic reorientation time [190]. For instance, as shown in Fig. 2.9b, Jungbauer and coworkers [190] report data showing a linear negative correlation between the reorientation time and the magnitude of applied strain. The fitting suggests an almost linear decrease $\tau_c \approx 3.21 - 0.17\varepsilon_0$ hours for human fibroblasts and $\tau_c \approx 3.42 - 0.21\varepsilon_0$ hours for rat embryonic fibroblasts. Then, unlike the frequency case, no saturation is observed for increasing amplitudes, at least in the tested range.

Of course, a maximum strain bearable by cells also exists, because cell injuries, detachments, and even death may occur if the deformation is too large. For instance, amplitudes greater than 25% might be harmful for the cell population on the substrate [40]. However, some of the most detailed results in terms of cell orientation obtained by Livne et al. [226] and Faust et al. [120] go up to 24% and 32%, respectively. The maximum applied stretch in the experiments by Standley et al. [330] reaches 25% with no reported damage, while Takemasa and coworkers [352] even employed a 110% strain. Hence, the maximum deformation that can be sustained by a cell might be dependent on its type and also on the mechanical properties of the substrate.

Although the amplitude of the cyclic stretch does not seem to alter the preferential orientation of the stress fibres [308, 351, 352], it determines the degree of alignment of the cellular population, with higher amplitudes causing a decrease in the circular variance [171, 198] and therefore a more coherent orientation towards the preferred direction [192].

An anomalous behaviour concerning the amplitude of applied strain is reported for confluent esophageal cells by Ritchie and coworkers [305]. The authors state that an amplitude of 2% favours parallel alignment of cells, while amplitudes of 5% and 10% induce a perpendicular reorientation.

In summary, the effects of the cyclic strain amplitude on the reorientation of cells and SFs are as follows:

- There exists a minimum amplitude necessary to induce a reorientation response. Such a lower threshold appears to be cell-type dependent and probably also frequency-dependent according to recent results [239].
- An increase in amplitude leads to a faster reorientation of cells away from the stretching direction [190], as in Fig. 2.9a.
- Greater amplitudes are associated with a more peaked orientation of the cell population along the preferential direction, as in Fig. 2.6d.

Substrate Stiffness Effect

As mentioned in Table 2.1, most of the experiments do not characterize the substrate from the mechanical point of view. In the majority of cases, silicon or polydimetylsiloxane (PDMS) are used, usually coated with collagen or fibronectin to favour cell attachment and mimic the ECM composition. However, as shown by Moretti et al. [256], reorientation happens also on engineered silicone substrates without precoating, meaning that the cell

response might be independent of any external adhesion promoter. The elastic modulus of the materials employed as substrates is often close to 1 MPa, making them quite stiff and almost impossible to be deformed by cellular traction forces.

On the other hand, the experiments cited in Table 2.2 report the mechanical characteristics of the substratum and some of them focus on what happens when softer materials are used. In particular, as a consequence of substrate softening, the externally applied strain is not completely transferred to the cells attached to its surface. Differently, for stiff environments it is sometimes stated that all the strain is also transferred to the cell [266, 267]. However, Tondon et al. [363] report a difference of 4% between the two. In the experiments performed by Wille et al. [388] and Wang et al. [377], instead, only 77% of the strain of the substrate was actually transmitted to the cell.

Changes in substrate stiffness are also investigated in the work by Faust et al. [120]. Specifically, cells seeded on very soft substrates, with Young moduli of 1-3 kPa, did not respond to cyclic stretches at all. A first, significant reorientation of actin bundles is observed for 11 kPa of substrate rigidity, meaning that a possible stiffness threshold between 3 and 11 kPa exists to induce cell reorientation. According to the authors, for low values of substrate Young modulus, the mechanosensitive apparatus of human umbilical cord fibroblasts was not well established, and so cells were not able to effectively respond to the applied strain.

Conversely, Tondon et al. [362] showed that osteosarcoma epithelial cells and mesenchymal stem cells tend to orient preferentially along the stretching direction, i.e. $\theta_{eq} = 0°$, on softer thick collagen gels, while the prependicular alignment is still found on stiffer collagen-coated silicone substrates (values of Young modulus not explicited, but probably of the order of 1 MPa). Interestingly, such results are consistent with a previous study [198] where SFs in cells with reduced contractility due to treatment with specific inhibitors were found to align parallel to the stretching direction as well. Attenuated contractility may also be a relevant factor in cells adhering to soft substrates, which display a reduced number of SFs [362]. Following the line of thought put forward by the same authors and using a theoretical model [362], it is speculated that, on soft substrates, SFs tension is lower than a certain homeostatic value. Therefore, the stretching increases such tension towards the optimal value, which causes a parallel alignment.

Livne et al. [226] instead did not find significant differences in cell preferential orientations when the substrate stiffness is changed from 1 MPa down to 20 kPa. The parameters they estimate appear rather robust with respect to changes in the mechanical properties of the substrate.

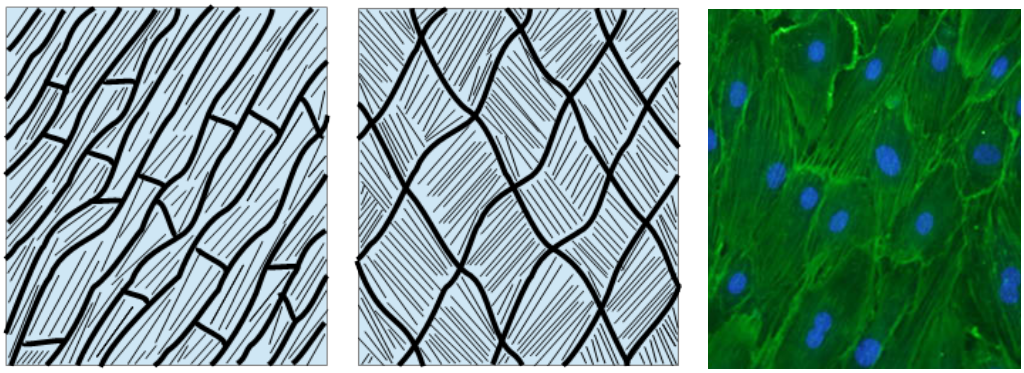

(a) (b)

Fig. 2.10 (a): Sketch of possible stress fibre orientation in confluent cells (redrawn from [352]). (b): Experimental microscopic view of confluent aligned cells, taken from [183]. The stretching direction is horizontal.

The combination of effects due to cyclic stretch and substrate stiffness was investigated by Quinlan and coworkers [360]. Concerning orientation, cells on very soft substrates ($E \approx 0.9$ kPa) showed significantly less alignment than those on stiff substrates ($E \approx 150$ kPa), in accordance with other works.

We also mention that Takemasa and coworkers [351, 352] ruled out the influence of substrate coating (fibronectin, collagen, laminin, vitronectin) on the cell preferential angle.

Confluent Cells on 2D Isotropic Substrates

So far, we have reviewed experimental results performed under sub-confluent conditions, in which the cell density is kept to a lower value in order to reduce the possible effect of cell-cell interaction. However, to more closely reproduce a tissue structure *in vitro*, in some experiments cells are grown until a confluent configuration is achieved. A first consequence of these experimental conditions is that, as depicted in Fig. 2.10a, it may happen that cells and their stress fibres cannot orient at the same time along the directions θ and $-\theta$, because of cell-cell contact and hindrance [89, 383]. Thus, a choice between the two equivalent symmetric orientations has to be made, leading to an advantage from a statistical viewpoint. The distribution of orientations shows therefore only one peak in the interval $[0, \pi]$, so that the problems in statistically describing the outcome of the experiments – discussed before – are often eliminated. In Takemasa et al. [351, 352], instead, cells acquire a romboidal-like shape and so the confluent structure has two symmetric directions, as sketched in the right panel of Fig. 2.10a.

Confluent cells on substrates

Cell type	f (Hz)	ε_0 (%)	r	θ_{eq} (max)	Refs.
rabbit aortic SMCs	0.833	(2), 5	N/A	$[50°, 60°]$	[89]
rabbit aortic SMCs	0.833	10	N/A	$[70°, 80°]$	[89]
rabbit aortic SMCs	1	$[2, 20]$	N/A	$\approx\perp$	[88]
rabbit aortic SMCs	1	$[2, 20]$	N/A	76° at 15%	[87]
pig aortic ECs	1	15	N/A	89°	[87]
(r) aortic SMCs	1	up to 25%	N/A	$[70°, 80°]$	[330]
(b) aortic ECs	1	10	≈ 0.05	$\perp$	[199]
(b) aortic ECs	1	10	≈ 0.05	$\perp$	[198]
(b) aortic ECs	$(0.01), 0.1, 1$	10	≈ 0	$\perp$	[172, 215]
pig esophageal SMCs	0.0725	2, 5, 10	N/A	$\parallel, \perp, \perp$	[305]
(h) pulmonary microvascular ECs	0.833	20	N/A	$\perp$	[183]
(h) umbilical vein ECs	0.867	20	N/A	$[80°, 120°]$	[320]
(h) umbilical vein ECs	$0.5, 1, 2$	$(0), [10, 110]$	$[0.32, 0.7]$	$[61°, 69°]$	[351, 352]

(Table Continues)

Confluent cells on substrates					
(r) aortic SMCs	1	$[10,110]$	$[0.32,0.7]$	$[62°,68°]$	[352]
(h) umbilical vein ECs	0.5	10	< 0.3	$[80°,90°]$	[396]
(h) umbilical vein ECs	1	10	N/A	$90°$	[182]
(b) aortic ECs	1	10	N/A	$\perp$	[182]
(m) osteoblast	$[0.017,0.17]$	$2,4,10$	0.49	$[50°,70°]$	[246]
(r) myocytes, fibroblasts, ECs	0.167	5, 10	N/A	$\perp$	[358]
(h) MSCs	1	5	N/A	$\perp$	[210]
(r) cardiomyocytes	0.5	20	N/A	$[0°,30°]$	[394]
(h) dermal fibroblasts	0.17	20	N/A	$\perp$	[175]
(h) intestinal cells	0.125	10	0.4	$[70°,90°]$	[152]

Table 2.3 Summary of the main experiments performed on planar substrates with confluent cells. For each experiment, in addition to the cell type, we report the tested frequencies, amplitudes, biaxiality ratios (whenever available) and preferential orientation. In particular, we use parentheses to address attempted values which however did not give rise to cell reorientation. Instead, square brackets are used to denote a range of values. Abbreviations: N/A = data not available; SMCs = smooth muscle cells; ECs = endothelial cells; MSCs = mesenchymal stem cells; (b) = bovine; (h) = human; (r) = rat; (m) = mouse. We denote by $\perp$ a perpendicular orientation and by $\parallel$ an overall parallel orientation, though the precise angle is not specified.

We summarise the results about confluent cells in Table 2.3. As in the sub-confluent case, some authors report an oblique angle [89, 246, 351] and others a perpendicular alignment [182, 199, 337, 396]. However, it is worth to advise that the word perpendicular is sometimes used improperly. For instance, Iwaki et al. [183] described the arrangement they observed in this manner, but from their images, reported in Fig. 2.10b, it rather seems that $\theta_{eq} \approx 60^\circ$ is a more appropriate descriptor of the orientation. Similarly, in [383] the term "perpendicular" is used to denote an orientation of nearly 75°. Hence, if a precise estimate of the alignment angle is to be obtained, one should be careful since several experimental reports describe any shift toward 90° as perpendicular.

Differently from sub-confluent conditions, the preferential orientation angle is sometimes found to depend on the imposed stretching amplitude. For instance, Takemasa et al. [351, 352] span from $\varepsilon_0 = 10\%$ to $\varepsilon_0 = 110\%$, measuring a mean inclination $\bar{\theta} \approx 61^\circ$ up to $\bar{\theta} \approx 69^\circ$. A regression line $\bar{\theta} = 30.193 - 0.081\varepsilon_0$ is fitted in [351], whereas the linear relation between the angle and the amplitude becomes $\bar{\theta} = 31.0 - 0.09\varepsilon_0$ in [352]. They also give the biaxiality ratio ranging from $r = 0.7$ when $\varepsilon_0 = 10\%$ to $r = 0.32$ when $\varepsilon_0 = 70\%$ which is known to strongly affect the equilibrium orientation. Moreover, in [352] several other factors possibly influencing the preferential angle are ruled out, including the duration of the stretching, the holding time of the deformation, the frequency, the ECM coating of the substrate (fibronectin, collagen, laminin, vitronectin), and the cell type (human ECs and rat SMCs).

A similar dependence is also found by Dartsch et al. [89] who measured a mean (computed in $[0, \pi]$) of $\bar{\theta} = 61^\circ$ when $\varepsilon_0 = 5\%$ and of $\bar{\theta} = 76^\circ$ when $\varepsilon_0 = 10\%$, and the angle ranges with highest probability are respectively $[50^\circ, 60^\circ]$ and $[70^\circ, 80^\circ]$.

Very recently, Gérémie and collaborators [152] studied the reorientation in a confluent monolayer of intestinal cells undergoing a periodic strain, with parameters mimicking the peristaltic movement *in vivo*. They found a preferential perpendicular alignment, with about 20% of cells aligned orthogonally to the main stretching direction.

It is important to remark that confluent configurations bring into play the relevant and non-negligible role played by cell-cell interactions. As a consequence, both the biological phenomena and the mathematical modelling become more complex. In fact, as mentioned above, most models tend to work in a sub-confluent framework so that each cell can react independently and the dynamics is simplified.

Regarding the speed of reorientation, as before it is found to increase with ε_0. However, compared to the sub-confluent case, Jungbauer et al. [190] report that fibroblasts in

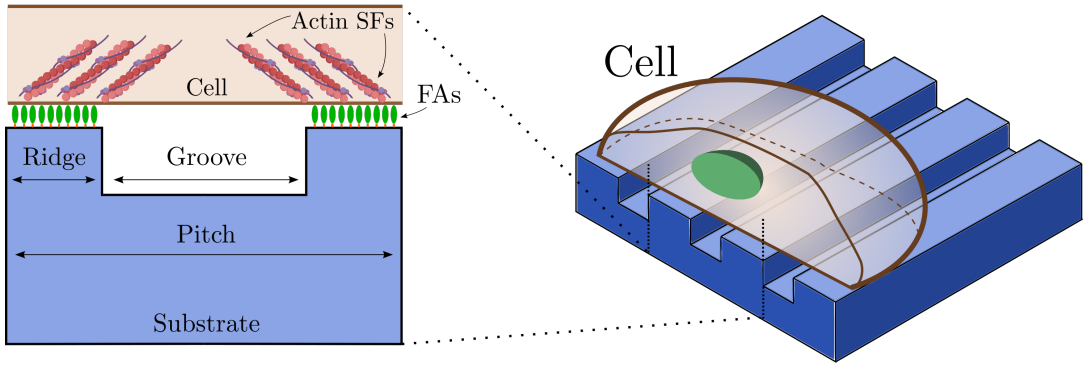

Fig. 2.11 Sketch of a typical experimental setting for cell orientation on micro-patterned substrates. The main parameters that regulate cell adhesion and alignment are the depth of the groove, its width, and the pitch.

confluence take a shorter time to reorient (e.g., 60 minutes at $f = 1$ Hz compared to the 80 and 120 minutes of the sub-confluent cells). Actually, for larger frequencies, the characteristic reorientation time τ_c does not reach a plateau, but continues to decrease following a power law as clearly evidenced in Fig. 2.9a. This suggests an important effect of cell-cell contact, that may avoid the saturation of molecular mechanisms seen in sub-confluent experiments. At variance, Ives et al. [182] state that human umbilical vein endothelial cells in less confluent portions of the membrane aligned more rapidly than the ones in zones with higher cell density.

For the sake of completeness, we have to mention that, differently from all previous experiments, Yamane et al. [394] observed that more than 90% of cardiomyocytes in confluence aligned preferentially along the stretching direction, forming an angle smaller than 30°. A slight tendency to align parallel to the stretch direction is also reported by Collinsworth et al. [81].

2.1.3 Cells on Micro-Patterned Substrates

Summary of experimental findings on 2D micro-patterned substrates

- On micro-grooved substrates, in absence of additional stimuli, cells orient parallel to the grooves due to *contact guidance* mechanisms.
- If a cyclic stretch is applied to the grooved substrates, parallel to the grooves, a competition between contact guidance and stretch avoidance is observed. In fact, the former pushes the cell to align parallel to the patterns, whereas the latter would

induce a perpendicular or oblique alignment. Contact guidance is often found to prevail, but the interplay is not trivial and in some cases stretch avoidance is still observed [283, 294].

- The *geometry and topography* of the patterned substrate, and in particular the groove width and depth, are important to determine the alignment behaviour of cells.

In addition to the effect of an externally applied mechanical stimulus, attention has been paid to the influence of topographic and morphological cues on cells. As a matter of fact, if the substrate is not entirely smooth and planar, the sensing mechanism of a cell is able to feel the changes and to accommodate the cytoskeleton accordingly.

As a prominent example, a series of experiments is performed using 2D substrates suitably coated with stripes or *microgrooves*, whose presence generates an anisotropy that may drive the orientation of cells following the phenomenon of *contact guidance*. A sketch of the experimental setting with grooved substrates is shown in Fig. 2.11.

In absence of any additional stimulus, the cell tends to align along the grooves, by sensing the anisotropic topographical features of the substrate. Then, if the patterned membrane is stretched, a competing effect between directional adhesion promoted by the grooves and stretch avoidance emerges. Indeed, contact guidance pushes cells to orient along the direction of the grooves, whereas a cyclic strain promotes their alignment away from the stretching direction, as discussed in Section 2.1.2. These two forces might be in competition if the grooves are not directed orthogonally or obliquely with respect to the main stretch direction. In most cases, contact guidance is shown to prevail [170, 210, 227, 380–382], but in general the outcome strongly depends on the geometric characteristics of the grooves, in term of width, depth, and spacing (see Fig. 2.11). A role is also played by the adhesion properties of possible stripe coatings, as well as by the stretching amplitude and frequency.

In absence of any external cyclic stimulus, the first detailed investigation of topographical cues on cell alignment was performed by Clark et al. [76–78], both for a single step and for multiply grooved substrates. The major findings of their studies are that, while most cells can overcome a single topographical obstacle, the presence of a pattern of grooves and ridges produces a strong alignment. Specifically, increasing the width of the grooves reduces cell alignment along the texture. Instead, increasing the depth from 0.2 µm to 1.9 µm strongly enhances alignment and ultimately overrules the effect of the

width. Interestingly, the authors also found a similar response for chick neurons, whose growth appears to be aligned along the patterns of a substrate textured with 2 µm deep grooves. Moreover, as a negative example which recalls the one for cyclically stretched isotropic substrates, it is claimed that neutrophil leukocytes, whose cytoskeleton is less responsive, did not react neither to single topographical cues [76] nor to multiple grooves [77]. Later, the same authors analysed the effect of ultrafine topographies [78], reducing the spacing and the depth by an order of magnitude (130 nm of groove spacing, 100-400 nm of depths). This choice was motivated by the will of reproducing the typical length scales of aligned fibrils of ECM, where collagen fibres have a diameter ranging between 20-100 nm. Results were similar to the ones for coarser patterns and showed a parallel alignment to the topographical cues, which was stronger with increasing depth. Only chick embryo neurons appeared unaffected by such fine microgroove textures, suggesting that fibrillar ECM does not have much influence on neural cells [78].

Among the first to investigate the competitive role of cyclic stretch and contact guidance were Wang and Grood [379]. In their setting, fibroblasts grown on a microgrooved substrate without stretching strongly aligned along the direction of microgrooves. Then, after 8% cyclic stretching, cells did not reorient and remained preferentially aligned along the microgrooves. However, the use of smaller microgrooves with a larger strain (12%) managed to change the cellular orientation.

The same group [380–382] grooved a silicon substrate with $1.6\,\mu\text{m} - 2\,\mu\text{m}$ deep grooves and width ranging from 1 to 10 µm, separated by 2 to 10 µm wide ridges. Cells then aligned along the grooves when $\varepsilon_0 = 4\%, 8\%$ and $f = 0.5, 1$ Hz. In most of the experiments, contact guidance prevailed over strain avoidance due to cyclic stretching [380–382], since no changes in alignment were observed after the application of the periodic stimulus. The same results were observed when the microgrooves where aligned at 45 or 90 degrees with respect to the stretching direction [381].

Loesberg et al. [227] similarly explored the combined effects of contact guidance by microgrooves and concurrent cyclic stretching on fibroblasts. Regardless of strain magnitude, cells were found to align along the textures in the substrate, with a secondary role played by mechanical loading. In particular, an enhanced orientation response parallel to the grooves was observed when the latter were positioned perpendicular to the uniaxial strain, coherently with the avoidance reaction observed in smooth membranes. Such an effect is also clearly evidenced by Tamiello et al. [353]. By using a substrate with circular or elliptic micropillars, they observed the typical contact guidance response on the latter, where cells aligned with the major axis of the ellipses in absence of any strain. If the cyclic

deformation was applied perpendicularly to the elliptic micropillars, then the two effects were coherent and cells oriented orthogonally with respect to the stretching direction – which is equivalent to a parallel alignment with the contact guidance cue. Instead, if the applied strain was parallel to the micropillar long axis, no preferential direction was observed: some cells were found to be reoriented, but some were not.

Kurpinski et al. [210] showed as well that the application of a periodic stretch to cells on a patterned substrate did not alter the parallel alignment to the microgrooves promoted by contact guidance. Instead, if the same confluent monolayer was subjected to a cyclic strain on a smooth surface, cells reoriented perpendicularly to the stretching direction, as expected.

Therefore, the results discussed so far point towards a prevalence of adhesion to the grooves over reorientation provoked by cyclic strain, which might also be totally abolished in some cases. However, different observations are sometimes reported, underscoring the non-trivial competitive effects of contact guidance and periodic stretching. For instance, Ahmed et al. [5] found that if cyclic strain is applied to micro-patterns aligned with the stretch direction, the competition between the effects makes cells to align at an average angle of 47.5° with a large standard deviation. These results are in contrast with [210, 227] and point instead towards a combination of effects, though contact guidance still appears to be very relevant. Instead, in coherence with previous works, a combination of periodic deformations with patterns of fibronectin oriented at 45° or 90° with respect to the stretching direction promotes oblique and perpendicular alignment, respectively. It was also noticed that nuclear orientation seems prominently affected by geometric constraints rather than by cyclic stretches, probably because the link between nucleus and outer environment is indirect.

Further support to the competition between microgrooves topographical cues and cyclic stretching is provided by Park and collaborators [283]. In their work, fibroblasts that were aligned with the microgrooves underwent a change in orientation when submitted to cyclic strain, reaching a final oblique alignment. However, their result may be affected by the large groove spacing, up to 50 µm, which can more easily accommodate cell reorientation after initiation of stretching.

Indeed, the dimensions of the grooves might have a role in deciding whether the cell prefers to follow the contact guidance stimulus or to reorient away from the strain. In this respect, the contribution by Prodanov et al. [294] is particularly interesting. Differently from all previous works, which pointed towards a complete dominance of contact guidance or at most to an intermediate response, they observed that strain avoidance can overrule the

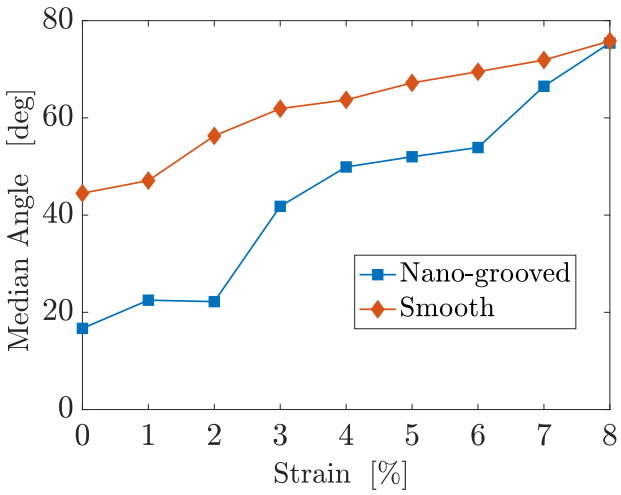

Fig. 2.12 Median angle of cells on a nano-grooved surface (300 nm wide grooves, 600 nm pitch, 150 nm depth) with grooves oriented along the main stretching direction ($\theta = 0°$) as a function of the stretch amplitude (in blue) and on a flat surface (in red). For small strains, cells on a smooth substrate are oriented randomly, as confirmed by a median angle close to 45°. On the contrary, on a nano-grooved surface a parallel alignment is observed. Then, an increase in strain is able to induce a reorientation also on the grooved substrate, and strains greater than 8% overrule the contact guidance effect. Data taken from Prodanov et al. [294].

contact effects when the size of the grooves was reduced to the nanoscale (300 nm wide, 600 nm pitch, 150 nm deep). In particular, a cyclic stretch parallel to the nano-textures above 3% in magnitude is able to reorient the cells toward an oblique or even perpendicular direction. This can be clearly seen in Fig. 2.12, where the median angle as a function of the amplitude is reported. For small strains, below 3%, cells are randomly distributed on smooth surfaces, while they align with the grooves on patterned substrates. However, increasing strains manage to induce a reorientation also on the nano-grooved substrates, which for strains greater than 8% is comparable with the one on smooth surfaces. On the other hand, for a pitch size of 2 µm and a groove size of 1 µm, cells did not respond to mechanical stimuli as high as 8% and persisted in aligning along the grooves. To interpret the results in Fig. 2.12, we advise that in [294] median values of distributions in $[0°, 90°]$ are available and not peak values. So, it should be taken into account that a uniform distribution corresponds to a median value of 45°. Above it, the distribution is skewed towards the perpendicular configuration and below it towards the direction of the nano-grooves.

When analysing the concurrent effects of micropatterns and cyclic strain, groove width appears also to be important, as pointed out by Houtchens et al. [170]. Indeed, they found

that shallow patterns of 15 µm width as well as very large groove widths of 70 µm facilitate a slight cell reorientation away from the stretching direction when both topographical and mechanical stimuli are simultaneously present. Instead, on intermediate groove widths, the influence of the texturing guidance is most effective. This is probably due to the fact that, on the one hand, large spacing allows the cells to better accommodate inside the grooves and therefore to facilitate their stretch avoidance reorientation; on the other hand, for reduced width, the cell is also able to protrude and attaches to the nearby ridges, which may be an helpful support in trying to reorient.

An interesting observation related to the just described behaviours was done by Abbott et al. [1]. They coated a silicon substrate with 40 µm wide stripes of collagen oriented parallel to the main stretching direction, so that they restricted cell reorientation. In this case, many cells became apoptotic (nearly 80% at 20% strain). It was then argued that limitations in the capacity of cells to reorient in response to high strains, due for instance to ageing or degeneration, might lead to apoptosis.

We also mention in this Section two experiments not performed on patterned substrates, which however display results due to some topographical cues. In detail, the experimental outcomes by Liu et al. [223] are probably be due to a mechanical anisotropy induced by stretching. In their work, a coated PDMS membrane is pre-stretched at a constant 10%, 20%, and 30% strain. Then, cells are seeded and it is observed that they reorient along the main stretching direction. The elastic modulus of the material at rest is equal to 268 kPa and is isotropic, but stretching induces an anisotropy. In fact, the ratio of the elastic moduli in the two principal directions becomes 1.33, 1.73, and 2.20, respectively, for the three strains mentioned above. Hence, the reason for parallel alignment is suggested to be the resistance to active cellular pulling. This result is in contrast with the one by Goli-Malekabadi et al. [139], but the differences are likely due to changes in experimental conditions and to the pre-seeding of cells on the substrate.

Finally, another interesting example of topographical orientation is discussed in a recent work by Jin et al. [189], who seeded airway smooth muscle cells on tubular surfaces, either concave or convex. Cells on the concave surface reoriented perpendicular to the cylinder axis, while on the convex one they aligned at a certain oblique angle that appears to be dependent on the radius of curvature.

To conclude this Section, we observe that the use of patterned surfaces in tissue engineering is receiving a lot of attention. Thus, this field appears in rapid development and we here chose to mention only some examples that are closer to the interests of this Thesis, even if the mathematical models will be mainly focused on cells on 2D isotropic

Cells in 3D gels

Cell type	f (Hz)	ε_0 (%)	θ_{eq} (max)	Refs.
(h) bronchial SMCs	0.5	12	0°	[20]
(h) foreskin fibroblasts	0	≈ 40	0°	[217]
(h) dermal fibroblasts	0, 1	10	$\parallel$	[130]
(r) cardiac fibroblasts	$[0.5, 4]$	10	$\begin{cases} 0^\circ \text{ (free)} \\ 90^\circ \text{ for } r = 0 \end{cases}$	[67]
(h) vein myofibroblasts	0.5	10	$\begin{cases} 0^\circ \text{ (core)} \\ 90^\circ \text{ (surface)} \end{cases}$	[124]
(h) vein myofibroblasts	1	5	$\perp$ (cyclic); $\parallel$ (static)	[96]
(h) cardiomyocytes	1	$10 \leftrightarrow 20$	strain aligned	[299]
(h, r) cardiomyocytes	0, 1	5	$\parallel$	[366]
(b) aortic SMCs	0, 1	5	$\parallel$	[193]
(r) bone marrow progenitor cells	0, 1	10	$\parallel$	[271]

Table 2.4 Summary of the main experiments performed in three-dimensional matrices or gels. For each experiment, in addition to the cell type, we report the tested frequencies, amplitudes and preferential orientation. In particular, we use square brackets to denote a range of values. Moreover, in [299] the strain oscillates between 10% and 20%. Abbreviations: SMCs = smooth muscle cells; (b) = bovine; (h) = human; (r) = rat. We denote by $\perp$ a perpendicular orientation and by $\parallel$ an overall parallel orientation, though the precise angle is not specified.

substrates. We refer the interested reader to [354] for a review of other experimental set-ups and further details on topographical contact guidance.

2.1.4 Cells in Three-Dimensional Matrices

Summary of experimental findings in 3D matrices and scaffolds

- Cell alignment in 3D fibrous matrices is not primarily guided by stretch avoidance, as for planar substrates undergoing cyclic strain. An orientation parallel to the deformation is frequently observed, especially in the core of the samples. Instead, at the surface, where contact guidance is less effective, the cells align perpendicularly or obliquely as in 2D substrates.

- Contact guidance due to collagen fibres, which may also be remodelled by cells, competes with cyclic strain avoidance.
- If soft matrices are used, like those composed of collagen, compaction of the tissue sample by the cells due to boundary constraints as well as cellular contractility [299] are suggested to be important in determining cell alignment.
- The interplay of all these factors is not trivial, even if the 3D situation is the one which most faithfully represents the *in vivo* conditions.

The two-dimensional setting with cells adhering on a planar substrate has several advantages, but in some cases might result in a simplification of the real environment experienced by cells *in vivo*. Therefore, experiments culturing cells in three-dimensional matrices and fibre networks (usually made of collagen or fibrin) or in tissue engineered constructs have been performed by numerous groups. In particular, cells in a three-dimensional ECM are surrounded by fibres, and adhesive sites are active all around them. On the one hand, this leads to the fact that cells tend to elongate together with the ECM, due to the phenomenon of contact guidance. On the other hand, the imposed stretch induces both a topological and a mechanical anisotropy. Indeed, cells embedded in a 3D gel may compact the surrounding matrix and also alter its anisotropy by realigning the fibres, thanks to the protrusion of pseudopodia and to exerted traction forces [122]. For instance, collagen gel compaction and contraction by fibroblasts, with development of tension, was already observed in 1982 by Bellows et al. [34]. Then, more recent experiments demonstrate that cells embedded in a matrix, possibly constrained at its boundaries, and left in static conditions tend to compact the sample and to develop stresses [67, 124]. The interplay between contact guidance cues by collagen fibres and mechanical stimuli coming from periodic deformations becomes therefore more complex. Moreover, very soft gels or matrices do not transmit all the applied stretch to the cells [67, 367], and it is more difficult in such cases to precisely quantify the strain sensed by the cells with respect to the externally controlled deformation [96, 303]. Indeed, soft gels mimicking the ECM may undergo alterations in their mechanical properties due to the applied stretches and to cell traction forces.

Overall, as reported in Table 2.4, the result is that cells in 3D structures are more prone to orient along the main stretching direction [20, 67, 96, 124, 130, 217, 271, 299, 305, 366]. In this respect, an interesting comparative study between the 2D and 3D cases for vascular smooth muscle cells undergoing periodic deformations was performed by Bono et al. [43].

In accordance with previous works, the experiments confirmed that in two-dimensional monolayers there was a preference for the perpendicular orientation (80-90 degrees), while in three-dimensional collagen gels parallel alignment (0-10 degrees) was predominant.

In static conditions, cells tend to align with the direction of sustained stretch or with the direction of boundary constraints (see [20, 67, 96, 130, 173, 193, 217, 248, 271, 366, 373]). Specifically, the role of mechanical constraints in 3D tissue constructs was firstly underscored by Nieponice et al. [271], who used two different control groups. The first one, named *unconstrained control*, was made by a scaffold with cells without any clamp and therefore allowed to compact freely. Instead, a second one had two fixed ends and was therefore called *constrained control*: due to cell traction forces and subsequent gel compaction, a stress developed along the axial direction. It was observed that cells in cyclically stretched matrices belonging to the constrained control group reoriented parallel to the direction of stress, while no alignment emerged in the unconstrained control.

Then, the subtle balance between contact guidance, constraints, and stretch avoidance in 3D cultures is vividly highlighted by Foolen et al. [124]. In particular, they performed extensive experimental analyses on myofibroblasts cultured in collagen/matrigel gels. In detail, cells were firstly left free to compact the gel for a few days in pure uniaxial conditions, i.e., with deformation restrained in one direction. In this case, a cell-generated compaction strain emerged in the direction perpendicular to the constraint: cells and SFs orientated towards the direction of the applied constraint. Instead, in static conditions with deformation constrained in two directions, the cells did not show a preferential alignment and oriented in both the constrained directions equally. When cyclic stretch was applied after static culture, to study the combined effect, the results unveiled interesting differences across the gel depth. Cells in the core of the specimen exhibited alignment along the constraint directions, while those at the top and bottom surfaces of the gel strongly aligned perpendicularly to the main stretch direction, as happened for planar membranes. In fact, in the core, the effect of collagen fibres is sterically restrictive, while on the boundary the strain-avoiding mechanism overwhelms the anisotropy induced by ECM fibres. Further confirmation of the prevailing of contact guidance over stretch avoidance is provided by experiments with reduced density of collagen inside the core as well as with perturbed collagen integrity. In these cases, reorientation towards the perpendicular direction is observed throughout the whole tissue sample, since the stretch avoidance response is not inhibited by a restrictive environment and consequent contact guidance mechanism. Later, the same group [125] showed that, even at high collagen densities, activation of protein Rho may result in SFs reorientation away from stretch, as already put in evidence for 2D

settings [198, 215]. Overall, the interplay between matrix density, deformation, and Rho signalling pathway appears therefore important in 3D cell alignment.

Other studies that highlight variations of collagen and cell alignment throughout the depth of 3D tissue constructs are those by Boerboom et al. [41] and by Rubbens et al. [311]. In both of them, when samples were intermittently strained, collagen fibres and cells were found to align perpendicularly or obliquely to the stretch direction at the surface, whereas parallel alignment to the deformation emerged deeper into the 3D matrix.

Chen et al. [67] found slightly different results from Foolen and coworkers [124]. More in detail, they firstly pre-cultured the cells for 24 hours in a 3D gel with deformation restrained in two directions. After that, the gel was subjected to a simple cyclic elongation at 0.5 Hz in one direction, and parallel alignment to the strain was achieved. Instead, if the specimen underwent pure uniaxial stretching (with $\varepsilon_{yy} = r = 0$) no alignment was observed at 0.5 Hz. Increasing the frequency to 2-4 Hz led however to a perpendicular alignment in the latter case, as for 2D cultures. The last condition that the authors tested is the one in which the collagen gel is pre-cultured without any constraint, and then a cyclic deformation is applied. Also in this case cells are found to align parallel to the strain direction. Unlike Foolen et al. [124], no difference was evident in orientations between the surface and the core of the gel.

Additional relevant results about the mechanical stimulation of 3D matrices are due to Lee et al. [217], who stretched a fibroblast-populated 3D collagen gel firstly in one direction for a time t^*, with $t^* \in \{5, 24, 48, 72\}$ hours, and then in the orthogonal direction. It was observed that, when the stretching direction is switched, the cells reorient themselves towards the direction of the newly applied load. The time required for reorientation was longer in specimen with larger values of pre-stretching time t^*, indicating that the remodelling of strongly aligned tissue constructs may be slower. However, even though the authors declare that their experimental conditions uncouple the effects of contact guidance and applied stretch, the surrounding collagen fibres are found to orient as well in the same direction as cells. Therefore, the impact of stretch compared with ECM guidance by such fibres is not fully clear.

Parallel alignment of cells to strain in 3D was also found by Gauvin et al. [130], Wakatsuki and Elson [373], and Asano et al. [20], both for step deformations and for cyclic stretching. Moreover, in [130, 373], it was highlighted that the application of a mechanical stimulus induced changes in the mechanical properties of the tissue engineered samples, with increased anisotropy and stiffness along the preferential direction. This is due do the compaction of the collagen gel by the cells, which can exert pulling forces up to

8 mN [373]. External mechanical fields can therefore be useful to modulate the mechanical properties in the design of engineered tissues.

In addition to gels, cellular alignment is also analysed in artificial tissue samples, like scaffolds and grafts. For instance, to reproduce the heart environment as realistically as possible, Tulloch et al. [366] assembled engineered 3D constructs of cardiomyocytes and collagen, both for rodent and human cells. The artificial grafts were then analysed from a mechanical viewpoint. In all cases, static and cyclic stretch promoted alignment parallel to the stress with no significant differences between the two loading conditions. However, the authors themselves warn that spontaneous contractions are observed in cells for both situations, and this may influence the results.

In contrast with almost all the experiments on three-dimensional matrices, Cha et al. [59] found that smooth muscle cells in a 3D porous scaffold oriented perpendicularly to the cyclic stretching direction; however, even if cells were firstly seeded onto the surface of the polymeric matrix, they observed a consistent number of stretched cells to penetrate deeper in the scaffold, which makes it difficult to discriminate the effects of contact guidance and cyclic strain.

2.2 Review of Mathematical Models

The consistent amount of experimental data reviewed in Section 2.1 shed some light into how a cell responds to mechanical stimulations. However, there are still a lot of unanswered questions, and the precise biological and physical mechanisms that underlie cellular reorientation are not fully clear. In this respect, starting from the early 2000s, mathematical models were proposed in order to provide a better understanding of experimental findings, as well as to develop meaningful theories to describe the cell alignment process. Since in Chapter 3 we will present our mechanical models for cytoskeletal reorientation, it is useful to provide here a review of the mathematical frameworks proposed in the literature, to couple them with the experimental review discussed above and at the same time establish a background for our work.

Several approaches have been adopted so far to target the modelling of cellular reorientation and alignment in response to mechanical cues. A sharp classification is difficult to perform, since several models deal with multiple tools and often with multiple scales. Here, we aim at providing a categorisation by highlighting the main mechanical structures and instruments upon which the models are grounded. Specifically, in Section 2.2.1 we present

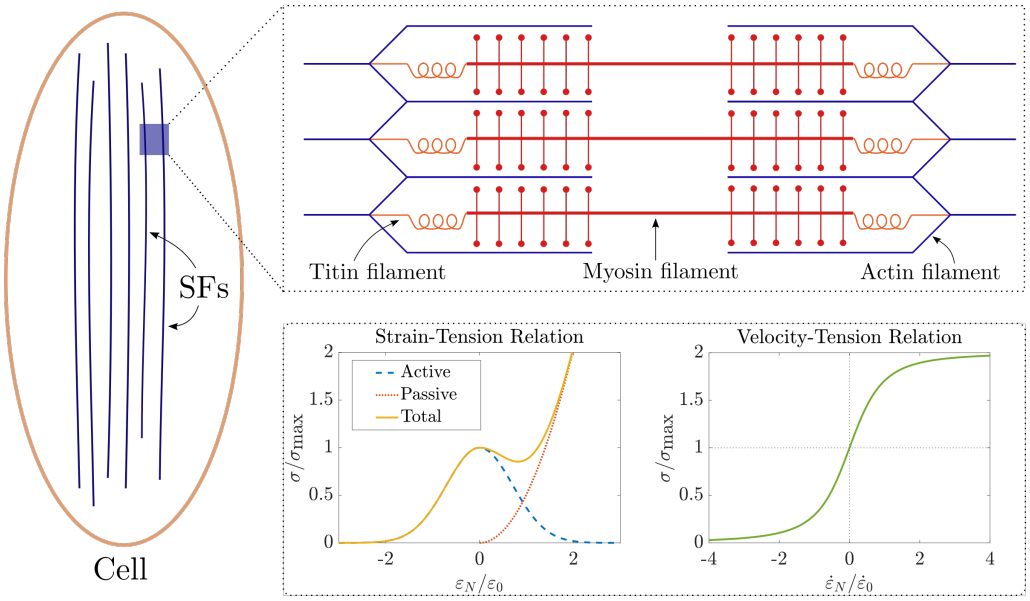

Fig. 2.13 Top panel: Sarcomeric-like structure of cellular stress fibres for modelling purposes, discussed in Section 2.2.1. The fibres are considered as composed by sequences of active contractile structures: the reciprocal sliding of actin and myosin filaments, as well as the elasticity of titin filaments, determine the development of internal tension. Bottom panel: strain-tension relation and velocity-tension relation used in some models [274, 369]. The velocity-tension curve is derived from the classical Hill dynamics for muscles. Instead, the strain-tension function is the sum of an active and a passive component.

the models that treat the stress fibres as active structures able to contract. Then, in Sections 2.2.2 and 2.2.3 we respectively discuss the strain and stress avoidance approaches. In the framework of Continuum Mechanics, Section 2.2.4 reviews some very relevant results about the use of elastic energies to find the cell preferred orientation, which will be widely employed in the remainder of the Thesis. Finally, we discuss some models that take into account viscoelasticity in Section 2.2.5, while Section 2.2.6 briefly provides an overview of articles in the Statistical Mechanics framework. Such a subdivision is not meant to be mutually exclusive, and some works will be discussed in more than one Section. However, we chose to put in evidence the features that are most strictly related to our subsequent work.

2.2.1 Modelling Stress Fibres as Active Contractile Structures

Most of the experimental works agree upon the highly mechanosensitive structure of actin stress fibres, which appear to have a fundamental role in cell reorientation. Moreover, they are able to develop contractile forces thanks to the bundling of actin filaments and myosin

heads: such a structure somehow reminds of the one of sarcomeres, i.e. the elementary contractile units composing muscles, as in Fig. 2.13. Even though there are several differences between SFs and sarcomeres [197], the similarities motivated some studies to tackle the problem of cell and cytoskeletal realignment by using an active contractility approach.

In this respect, a starting point for several modelling attempts of cell stress fibres orientation is the framework proposed by Deshpande and coworkers [103, 104]. In a series of papers, the authors developed a model for cell cytoskeletal contraction as an active phenomenon following an external chemical stimulus. The stress fibres are considered as active filaments capable of developing an internal tension, which resembles a Hill-like model for cross-bridge dynamics in muscles [162]. Moreover, the activation level of the fibres $\eta \in [0,1]$ is another key variable of their model that evolves according to

$$\frac{d\eta}{dt}(t;\theta) = \frac{k_+}{\tau_f}[1-\eta(t;\theta)]C - \frac{k_-}{\tau_f}\left(1-\frac{\sigma(\theta)}{\eta(t;\theta)\sigma_{\max}}\right)\eta(t;\theta)\,, \tag{2.5}$$

where k_+, k_- are dimensionless constants that govern the rate of stress fibres formation and dissociation, respectively; τ_f is a decay time constant; $C = \exp(-t_i/\tau_f)$ is the intensity of the chemical signal that triggers SF activation from time t_i; $\sigma(\theta)$ is an active stress related to the fibre tension along the orientation θ and $\sigma_{\max}$ is its value at full activation, i.e. with $\eta = 1$. In addition to the active stress, linear elasticity is employed to model the passive cell response. Although such a model does not deal with fibres preferential reorientation following mechanical stimuli, it predicts a number of interesting experimental features about the active contraction of the cytoskeleton. For instance, simulations show a decrease of the force exerted by the SFs with decreasing substrate stiffness, as well as a concentration of SFs activation near sites of localized tension, coherently with experimental observations for cells on an array of microposts. We remark that, in this model, stress within the SFs inhibits their disassembly. This is motivated by the will to have more SFs on stiffer substrates and is justified on the basis that tension is related to the amount of cross-bridging between actin and myosin, which stabilizes the fibres. Such an assumption is modified in other papers, as explained in the following.

Successive works by the same group [385] introduced the cyclic deformation and studied the subsequent remodelling of the cytoskeleton. Results in the periodic case capture the perpendicular preferential orientation if a pure uniaxial stretch ($r = 0$) is applied to the substrate, which is in line with several experimental settings described in Section 2.1.2. Furthermore, the degree of alignment is found to increase with the maximum amplitude of

the oscillation ε_0 and with the frequency ω. Instead, in the simple elongation or biaxial cases (see Fig. 2.3), the model suggests that two symmetric preferential orientations are found, which are given by the directions where the strain rate is null, namely,

$$\theta_a = \pm \arctan\left(\frac{1}{\sqrt{r}}\right). \tag{2.6}$$

However, as we will discuss in the following, such a prediction coincides with the one obtained with the strain avoidance approach, suggesting that the cell aligns along the direction of minimal stretch. An interesting prediction found in [385] is instead that changes in the stress fibre sensitivity to the strain rate are as effective as the stretch magnitude in enhancing the alignment. This might be coherent with experimental findings [198] which suggest that a reinforcement in the expression of a certain chemical pathway is equivalent to an additional 3% stretch.

A different framework, though still based on SFs activation and cross-bridge contraction dynamics, is developed by Vernerey and Farsad [369]. In detail, the authors propose a model grounded on constrained mixture theory, accounting for both passive elasticity and active contraction of the fibres that is driven by length-tension and velocity-tension relations, shown in Fig. 2.13. A relevant difference with previous approaches consists in how the contractile stress affects SF formation. While in [103] it is assumed that stress reduces fibre dissociation, in [369] such a stress increases fibre formation, thanks to a rate of actin monomer association k^f given by $k^f(\sigma_\theta) = k_0^f + k_1^f \sigma_\theta$, being σ_θ the tension along θ. The model furnishes interesting predictions and provides detailed insights into cell contractility mechanisms by using the well-established mixture theory. However, as pointed out in [274], it is not completely accurate in the description of cyclic strain reorientation, since at high amplitudes it would predict that a large amount of fibres is aligned to the strain direction. A similar constrained mixture approach had been used previously by Na et al. [263] who developed a theoretical model to describe the nonlinear elasticity of actin in equi-biaxial mechanical tests. Their model however does not account for SF realignment.

Later, in [274], the advantages of the models by Deshpande et al. [103] and Vernerey and Farasad [369] are combined, in an attempt to overcome the limitations of both. More in detail, the following equation for the stress fibre density $\Phi(t;\theta)$ in direction θ is proposed, which mimics and extends the one firstly introduced in [369]:

$$\frac{d\Phi}{dt}(t;\theta) = \left[k_0 + k_1 \sigma_{\max} f_\varepsilon^a(t;\theta) f_{\dot{\varepsilon}}(t;\theta)\right] \Phi_m - k_d \Phi(t;\theta), \tag{2.7}$$

where k_0, k_1, k_d are constants describing respectively basal SF formation, stress-induced SFs formation, and SFs dissociation. In addition, Φ_m is the fraction of monomeric actin, while

$$f_\varepsilon^a(t;\theta) = \exp\left(-\frac{\varepsilon_N^2(t;\theta)}{\varepsilon_0^2(t;\theta)}\right) \quad \text{and} \quad f_{\dot\varepsilon}(t;\theta) = \frac{1}{1+\frac{2}{\sqrt{5}}}\left(1+\frac{k_v\dot\varepsilon_N+2}{\sqrt{(k_v\dot\varepsilon_N+2)^2+1}}\right)$$

represent the active reduction in contraction due to strain (dashed blue curve in Fig. 2.13) and the tension-velocity Hill-like relation (akin to the green curve in Fig. 2.13), respectively. We remark that, differently from [103], increasing SF tension in this case leads to enhanced SF formation, rather than to reduced dissociation as per Eq. (2.5).

Then, this type of models was further developed by Vigliotti et al. [372] who proposed a very sophisticated thermodynamical framework, coupling the macroscopic evolution of the cytoskeleton with Statistical Mechanics considerations about stress fibre formation. In particular, they derived the evolution equation for the SF from the microscale and introduced micro-remodelling of the fibre functional structure, as well as diffusion of unbound actin in the cell. The model is capable of accurately predicting several experimental features, such as the discrepancy between perpendicular alignment on 2D substrates and parallel alignment to the deformation in 3D gels, as discussed in Section 2.1.4. Moreover, the model turns out to be sensitive to differences in the applied waveforms, allowing comparisons with specific experiments [362]. Nevertheless, the complex framework of [372] does not describe the dependence on the biaxiality ratio r.

Further investigations adapted the previous model to simulate also the reorientation of cells on grooved substrates, together with the competition between topographical and mechanical cues due to surface patterns and cyclic strain, respectively [304, 371]. In particular, computational studies showed that cells reorient if the pitch size is sufficiently small, whereas they align along the grooves if the pitch is large enough, coherently with experimental assays discussed in Section 2.1.3 [294]. Extensions and refinements were also developed to explain the transient force generation [249] experimentally noticed by Wille et al. [389], and to deal with the alignment in 3D collagen gel constructs [67, 299] described in Section 2.1.4.

Instead, the approach pursued by Hsu and coworkers [171, 172, 196] consists in a purely kinematical description of SF disassembly and preferential realignment, based on experimental reports that fibres are pre-stretched at a homeostatic level [230]. Mechanical perturbations then destabilise this state and provoke a reorganisation of the cytoskeleton.

In particular, after introducing the deformation gradient $\mathbb{F}_t(t') = \mathbb{F}(t')\mathbb{F}^{-1}(t)$ from the configuration at time t to the new configuration at time t', and the corresponding right Cauchy-Green tensor $\mathbb{C}_t(t') = \mathbb{F}_t(t')^{\mathrm{T}}\mathbb{F}_t(t')$, the authors define the stretch ratio of the i-th fibre directed along $\mathbf{N}^i$ as

$$\lambda_t^i(t') = \sqrt{\mathbf{N}^i(t) \cdot \mathbb{C}_t(t')\mathbf{N}^i(t)}\,.$$

Discretising time in intervals of amplitude Δt, the total stretch at time $t + \Delta t$ is therefore $\lambda^i(t)\lambda_t^i(t + \Delta t)$. A first version of their model was based on a deterministic evolution equation, with a time rate depending on the deviation from the homeostatic pre-stretch [196]. In subsequent works, the dynamic turnover of SFs was then described by a stochastic formulation [171, 172], with the probability of stress fibre disassembling during the time interval Δt which is taken to be

$$P = \left[k_0 + k_1 \left(\frac{\lambda^i - \lambda_0}{\lambda_0}\right)^2\right] \Delta t\,,$$

where λ_0 is the fibre homeostatic pre-stretch that is experimentally found to be $\lambda_0 \approx 1.1$ [230]. If a SF is disassembled, a new SF oriented randomly with a stretch λ_0 is immediately built. An additional assumption is that SFs can relax at a rate proportional to the perturbation in the set-point pre-stretch. The model turns out to be effective in predicting several behaviours of cell under stretch, including the reorientation away from the stretching direction and the absence of alignment for equi-biaxial deformation. However, the model seems to suggest that cells align along the direction of minimum deformation, which is not always accurate as we will discuss later. Moreover, another difference between [172] and [103] lies in the choice of initial conditions. While in the former the SFs are considered as randomly distributed at the beginning, the latter takes a cell devoid of fibres at the initial time instant and studies its rebuilding.

The same group [197, 362] successively proposed a sarcomeric model of a SF as a passive elastic element coupled with an active contractile myosin filament, borrowing again ideas from muscle contraction. The reference length of the sarcomere may change in time due to myosin sliding, which provides an equation that also embeds viscous-like effects. An Hill-type dynamics to relate force and contraction velocity is also chosen, as done by several other authors described in this Section. Thanks to these modelling choices, the results are able to capture the different evolution of SF orientation due to high and low frequency periodic strains. In particular, for high frequencies the changes in SF length are

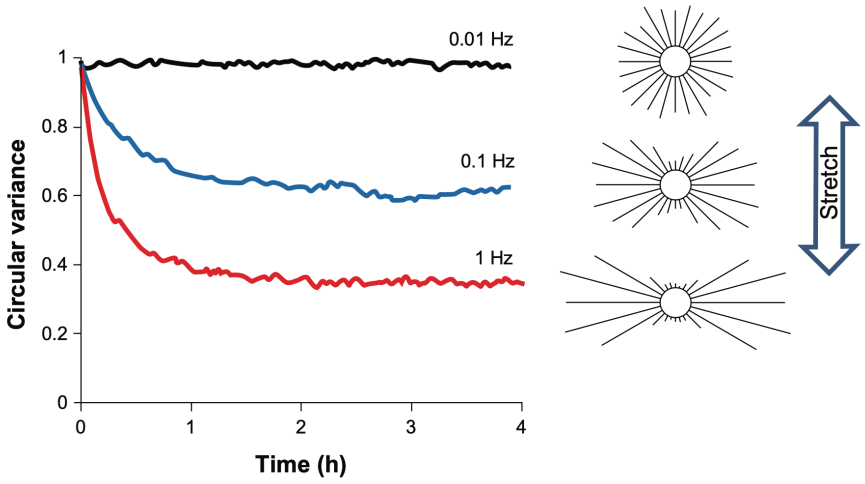

Fig. 2.14 Evolution of circular variance in time for different applied frequencies, taken from [197], where a model for active contractile stress fibres is proposed. An increase in the frequency leads to a decrease in the circular variance, that is, to a more pronounced orientation of SFs along the orthogonal direction, as shown by the circular histograms.

faster than the myosin can respond and the behaviour is elastic. Low frequencies instead allow the SF to maintain a constant force employing myosin sliding. An increase in the frequency also decreases the circular variance, as shown in Fig. 2.14. Analogous ideas are found in the work by Chen et al. [66], where the role of focal adhesions is taken explicitly into account in the elasto-sarcomere picture of SF. The existence of two activation modes for the SF, called *localized* and *homogeneous* activation, introduces two intrinsic time scales. These are related to a lower and an upper frequency, respectively, which represent the minimal and maximal threshold frequencies observed experimentally [190]. Again, the model predicts that SFs reorient towards the direction of least substrate deformation.

Another interesting contribution to the structural modelling of SFs is the one by the group of Qian [220, 295]. A mechano-chemical theory at the microscale is presented, which accounts for the formation of ligand-receptor bonds between cell and substrate through simple first-order kinetics. The activation of contractile fibres is based on a microscopic energy reduction that includes the force generated by the filaments and the stiffness of the substrate. In particular, the SF is modelled as a Maxwell element in parallel with an active component, and its reorientation happens as a stochastic Brownian process. By using this framework, the authors report several intriguing predictions, such as differences between reorientation on stiff and soft substrates, amplitude and frequency thresholds, and the role of the protein Rho [295]. However, a consistent limitation of this

model regards the fundamental hypothesis that cells align along the direction of maximum actin density, which is not strongly corroborated by experiments and also leads to a difficult interpretation of the results. Indeed, some simulations in [295] seem to show that the average actin density at 1 Hz frequency is almost the same for orientations between 75 and 90 degrees. Hence, it is unclear why the cell should prefer any of the directions inside this range. A refinement is then introduced by the same authors in [220] for neuron reorientation, accounting also for changes in neuronal length.

Finally, we mention the work by Zhong et al. [406], in which a multiscale link between the focal adhesion bond microscopic dynamics, the turnover of stress fibres and the cell-matrix coupling is drawn. Specifically, as done in a previous work by the same group [205] the FAs are described as a set of bonds connected to the substrate by linear elastic springs. These bonds might be open or closed, and the transition between the two states is regulated by the force acting on each spring. In addition, the SFs are modelled as viscoelastic Kelvin-Voigt elements, connected to the FAs, and undergoing turnover as a consequence of FA instability. The extracellular matrix is treated as a triangular lattice of elastic rods, to which a cyclic deformation is applied. Simulations show results compatible with experimental data, especially by Jungbauer et al. [190].

In most of the models presented so far, circular histograms are employed to represent the orientation of stress fibres, as shown in Fig. 2.14.

2.2.2 Strain Avoidance

Historically, the very first modelling approaches to describe cell reorientation under stretch were based on a strain minimization principle, which led to naming the phenomenon as *strain avoidance* [51, 375]. According to this hypothesis, the cell would preferentially align along the directions where it feels the minimum possible strain, so as to minimize the discomfort and the cyclic elongations of its cytoskeleton. Through standard calculations, we can therefore write the strain experienced along a direction $\mathbf{N} = (\cos\theta, \sin\theta, 0)$ as

$$\varepsilon_N = \varepsilon_{xx}\cos^2\theta + \varepsilon_{yy}\sin^2\theta = \varepsilon_{xx}[(1+r)\cos^2\theta - r], \tag{2.8}$$

where $\varepsilon_{xx}, \varepsilon_{yy}$ are the principal strains and $r := -\varepsilon_{yy}/\varepsilon_{xx}$. A direct application of the minimal strain principle to Eq. (2.8) readily allows to state that the preferred directions are given by

$$\theta_{eq} = \arccos\sqrt{\frac{r}{1+r}}, \tag{2.9}$$

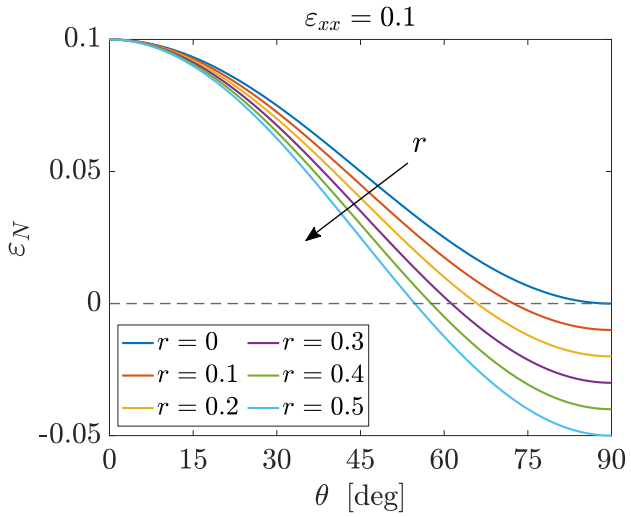

Fig. 2.15 Axial strain in direction θ, defined by Eq. (2.8), as a function of the angle for different values of r and a fixed value of $\varepsilon_{xx} = 0.1$. According to the strain avoidance approach, the cell preferential angle defined by Eq. (2.9) corresponds to the intersection between the coloured curves and the dashed line, which represents zero strain.

which is equivalent to (2.6). In particular, for $r = 0$, the only preferential orientation is $\theta_{eq} = \frac{\pi}{2}$. As shown in Fig. 2.15, θ_{eq} corresponds to the intersection of the strain curve, defined by Eq. (2.8), with the zero strain line.

With respect to this approach, Takemasa et al. [352] were among the first to suggest that the stress fibre orients to minimize changes in its length during cyclic stretch, i.e. along the direction of null stretch, based on geometrical considerations. Then, Wang et al. [375] proposed a more refined description based on strain avoidance, under the following assumptions:

(i) cell reorientation is initiated by the strain along the cell major axis;

(ii) each cell has an axial strain threshold it can sustain, and such threshold is normally distributed in the cell population, with 3% mean and 1.5% standard deviation estimated for melanocytes;

(iii) the cell avoids any direction where the axial strain exceeds its threshold;

(iv) the final orientation is selected randomly among the directions where the axial strain is less than the threshold.

Although some of the previous assumptions are quite strong, this is one of the first attempts to rationalise the strain avoidance mechanism, already observed in experiments by Buck [51] and Dartsch [88, 89] in the 80s. The model by Wang and collaborators was also

used by Barron et al. [32], who estimated a mean of 1.8% and a standard deviation of 0.75% for the normal distribution of tolerable strain in a population of endothelial cells. Neidlinger-Wilke and coworkers [267] estimated instead an axial strain limit of 6.4% for osteoblasts and of 4.2% for fibroblasts. More recently, a very similar approach was followed in [258], where a simple linear elastic model for SFs and MTs is proposed, though the role of the latter is not clear experimentally (see Section 2.1.2).

The reasoning put forward by Wang in 2000 [378] refined the previous description of actin filament dynamics. In particular, he evaluated the change in the strain energy of a fibre due to the action of the axial strain ε_f transmitted to it. It was also assumed that only a fraction of the substrate strain was effectively transferred to the filaments, that is, $\varepsilon_f = \alpha_t \varepsilon_N$ in tension and $\varepsilon_f = \alpha_c \varepsilon_N$ in compression, with $\alpha_t < \alpha_c$ and ε_N as in Eq. (2.8). The model is then developed under the following hypotheses:

(i) in absence of deformation, each filament of actin owns a basal strain energy given by $E_b = k\delta^2/2$, where δ is the pre-strain of the SF due to its inherent tension; then, the total energy of the fibre is $E_f = k(\delta + L\varepsilon_f)^2/2$, where L is the initial length of the filament;

(ii) only the normal strain ε_N is transmitted to the filaments;

(iii) the actin filaments cannot bear compression;

(iv) disassembly of SFs occurs if the strain energy E_f is decreased to zero or increased to twice the basal energy E_b.

The limits in hypothesis (iv) are crucial, since they allow to identify through Eq. (2.8) an interval of orientations:

$$\theta \in \left[\arccos \sqrt{\frac{r}{1+r} + \frac{(\sqrt{2}-1)\delta}{(1+r)\alpha_t \varepsilon_{xx} L}},\ \arccos \sqrt{\frac{r}{1+r} - \frac{\delta}{(1+r)\alpha_c \varepsilon_{xx} L}} \right]. \tag{2.10}$$

By taking $\alpha_t = (\sqrt{2}-1)\alpha_c$ and defining $B := \delta/(\alpha_c L)$, the interval (2.10) can be written as

$$\theta \in \left[\arccos \sqrt{\frac{r}{1+r} + \frac{B}{(1+r)\varepsilon_{xx}}},\ \arccos \sqrt{\frac{r}{1+r} - \frac{B}{(1+r)\varepsilon_{xx}}} \right]. \tag{2.11}$$

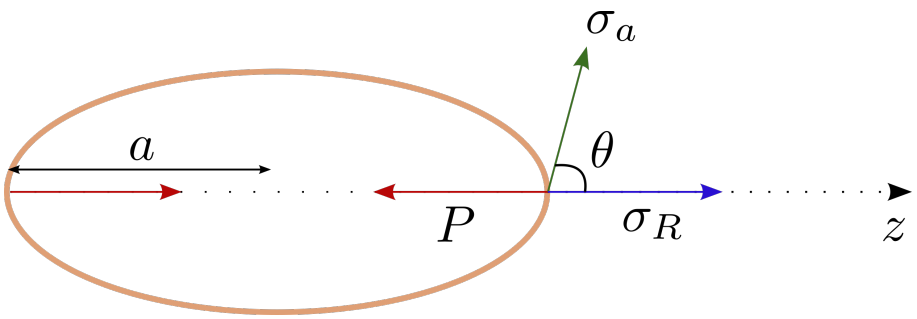

Fig. 2.16 Sketch of the force-dipole model for cell reorientation used in [93, 94]. The cell is assumed to have its major axis aligned with the z axis, whereas the externally applied stress σ_a is acting at an angle θ with respect to the cell axis. P is the cell dipole magnitude and σ_R is the subsequent reaction stress developed in the matrix due to active contractility.

It is immediate to observe that in the limit $B \to 0$, which corresponds to a vanishing pre-strain δ, the interval collapses to the point

$$\theta_{eq} = \arccos\sqrt{\frac{r}{1+r}} = \arctan\sqrt{\frac{1}{r}}, \tag{2.12}$$

that is again the direction of null strain. In addition, increasing the applied strain ε_{xx} (without conflicting with the small deformation assumption) leads as well to a narrowing of the range of preferential angles. This correlates with the fact that higher strain amplitudes are associated with a smaller range of observed orientation angles in experiments, and therefore to more peaked probability distributions as shown in Fig. 2.6.

A different but somehow related approach is pursued by De and co-workers [93, 94]. Using a coarse-grained picture, they model the cell as an anisotropic force dipole [39, 316] as sketched in Fig. 2.16, to mimic the action of a stress fibre along a given direction. In their work, the focus is on how the cell readjusts its contractile activity by developing a force along its major axis, which can be reoriented as a consequence of perceived mechanical cues. Additionally, the authors assume that such a reorganisation is driven by the maintenance of an optimal level of strain $\varepsilon_{\text{target}}$. As a consequence, a reaction strain in the surrounding matrix is identified:

$$\varepsilon_R = -\frac{(1+r)P}{\pi a^3 E},$$

where P is the (negative) cell contractile dipole magnitude, E is the Young modulus of the matrix and a is the cell size. Instead, the component of the applied strain along the cell

axis is

$$\varepsilon_a = \frac{\sigma_a}{E}\left[(1+r)\cos^2\theta - r\right],$$

with σ_a the external uniaxial applied stress. Starting from these considerations, a free energy is built:

$$\mathcal{U}_\varepsilon = \mathcal{U}_{\text{cell},\varepsilon} + \mathcal{U}_{\text{self}} + \mathcal{U}_{\text{int}},$$

where

$$\begin{aligned}
\mathcal{U}_{\text{cell},\varepsilon} &= \frac{1}{2}\chi\left[\frac{\sigma_a}{E}[(1+r)\cos^2\theta - r] - \frac{P(1+r)}{\pi a^3 E} - \varepsilon_{\text{target}}\right]^2, \\
\mathcal{U}_{\text{self}} &= (1+r)\frac{10r^2 - 14r + 9}{30(1-r)^2}\frac{P^2}{2\pi a^3 E}, \\
\mathcal{U}_{\text{int}} &= P\frac{\sigma_a}{E}\left[(1+r)\cos^2\theta - r\right].
\end{aligned} \tag{2.13}$$

In detail, the contribution $\mathcal{U}_{\text{cell},\varepsilon}$ is the free energy related to the contractile activity of the cell, which is minimized when $\varepsilon_a + \varepsilon_R = \varepsilon_{\text{target}}$, i.e. when the cell feels the optimal strain. On the other hand, $\mathcal{U}_{\text{self}}$ gives rise to a force that tends to reduce the magnitude of the dipole [93], whereas $\mathcal{U}_{\text{int}}$ represents the interaction between the dipole and the external strain. The variables of the model are therefore P and θ, with a dynamics assumed to be given by [94]:

$$\frac{dP}{dt} = -\frac{1}{\tau_P}\frac{\partial \mathcal{U}_\varepsilon}{\partial P}, \quad \frac{d\theta}{dt} = -\frac{1}{\tau_\theta}\frac{\partial \mathcal{U}_\varepsilon}{\partial \theta}. \tag{2.14}$$

Actually, in a subsequent work [93], the equation for θ is modified by multiplying for a factor $1/P^2$, even though the results are only altered slightly. When a cyclic deformation with a high frequency is applied, in the form $\sigma_a(t) = \sigma_a(1-\cos\omega t)$, the energy may be averaged over a period, since the cell is not able to follow the stress instantaneously. The resulting averaged energy has an additional contribution, namely,

$$\langle \mathcal{U}_\varepsilon \rangle = \mathcal{U}_{\text{cell},\varepsilon} + \mathcal{U}_{\text{self}} + \mathcal{U}_{\text{int}} + \mathcal{U}_{\text{av},\varepsilon}, \tag{2.15}$$

in which the first three terms have the same form as (2.13) and

$$\mathcal{U}_{\text{av},\varepsilon} = \frac{1}{4}\chi\left[\frac{\sigma_a}{E}[(1+r)\cos^2\theta - r]\right]^2.$$

The stationary solutions can be derived by imposing that the derivatives of such an energy with respect to both P and θ are null. These steady state solutions are found to be $\theta_{eq} = 0$,

$\theta_{eq} = \pi/2$ and an oblique one, which is defined in terms of its squared cosine. In the case where the interaction forces with the matrix are negligible, such an oblique orientation is given by

$$\cos^2\theta_{eq} = \frac{r}{1+r},$$

which again corresponds to the minimal strain direction. If all the terms in the energy are taken into account, the dependence is less trivial and the authors study it numerically, finding that the steady state preferential angle is a decreasing function of r. As we will discuss in the following Section, in [94] the possibility that cell remodelling aims at maintaining a target stress rather than a target strain is also investigated. We conclude this Section by mentioning that a similar approach may be generalized to the case of more than one cell [398]. A more recent work has been specifically focused on the role of focal adhesions [92] and on their catch-bond dynamics [206]. Finally, in Ref. [314] and [120] a random noise is added when studying the reorientation of cell dipoles.

2.2.3 Stress Avoidance

As just mentioned, in [93–95] the alternative hypothesis about the existence of a target stress is examined, within a framework akin to the one discussed in the previous Subsection. Specifically, if a single cell acting like a force dipole is considered, it is assumed that its contractile activity is devoted to maintaining an optimal local stress. In this case, the reaction stress writes

$$\sigma_R = -\frac{2-r}{1-r}\frac{P}{2\pi a^3},$$

with the same notation as above. The force component due to the applied stress on the surrounding matrix along the direction of the cell axis is given by $\sigma_a\cos^2\theta$ (see Fig. 2.16). The free energy of the system, which includes the active contribution from the cell cytoskeleton and the forces acting on the cellular dipole due to the elasticity of the matrix, becomes

$$\mathcal{U}_\sigma = \mathcal{U}_{\text{cell},\sigma} + \mathcal{U}_{\text{self}} + \mathcal{U}_{\text{int}},$$

where

$$\mathcal{U}_{\text{cell},\sigma} = \frac{1}{2}\chi\left[\sigma_a\cos^2\theta - \frac{2-r}{1-r}\frac{P}{2\pi a^3} - \sigma_{\text{target}}\right]^2,$$

is the active energy of the cell, whereas the contributions due to the interactions of the dipole with the surrounding matrix and the external stress are the same as in Eq. (2.13).

Instead, σ_{target} identifies the target stress of the cell, so that $\mathcal{U}_{\text{cell},\sigma}$ is minimized if the sum of the reactive stress σ_R and the applied stress σ_a is equal to the target. If an averaging over a cycle is performed, the energy becomes

$$\langle \mathcal{U}_\sigma \rangle = \mathcal{U}_{\text{cell},\sigma} + \mathcal{U}_{\text{self}} + \mathcal{U}_{\text{int}} + \mathcal{U}_{\text{av},\sigma} ,$$

with

$$\mathcal{U}_{\text{av},\sigma} = \frac{1}{4}\chi\sigma_a^2 \cos^4\theta .$$

The equilibrium orientations of the system, i.e. the solutions of (2.14), are then identified with $\theta_{eq} = 0$, $\theta_{eq} = \pi/2$ and an oblique orientation defined in general by the implicit relation

$$\cos^2\theta_{eq} = \frac{2}{3}\left[\frac{2-r}{1-r}\frac{P_{eq}(\theta_{eq})}{2\pi a^3\sigma_a} + \frac{\sigma_{\text{target}}}{\sigma_a} - \frac{P_{eq}(\theta_{eq})}{\chi E\sigma_a}(1+r)\right] . \tag{2.16}$$

It should be noticed that there are strong constraints, especially on r, for the existence of such an oblique equilibrium. For instance, it might not exist for values of r suitably close to 1, which correspond to a 2D incompressible situation. It is also worth to point out that, if solely the energy of the cell is considered, i.e. $\mathcal{U}_{\text{self}}$ and $\mathcal{U}_{\text{int}}$ are neglected, the only equilibrium orientations are $\theta_{eq} = 0$ and $\theta_{eq} = \pi/2$. The latter is the stable one and corresponds to the direction of minimal stress, if a uniaxial applied stress is considered. The authors then study the response of such a dipole model to external stresses, both in static and cyclic conditions [93, 94]. For the former, results predict an alignment parallel to the stress, while the latter induces a cellular orientation along one of the angles mentioned above. Moreover, for very low frequencies, their theory suggests that cells align nearly parallel to the applied load. The dependence of the reorientation time on the frequency is also considered, in accordance with experimental results [93].

2.2.4 Elastic Energy Approaches

In order to disentangle the dichotomy between optimal strain and optimal stress, Livne and coworkers [226] performed an extensive series of experiments carefully controlling the biaxiality ratio $r \in [0,1]$. In this way, the authors were able to show that neither the zero strain direction given by Eq. (2.6) nor the zero stress directions were accurate in fitting their experimental data. Specifically, for low values of r, a deviation from the zero strain prediction up to 10° emerged, which was 20 times greater than the error bars. In the zero stress case, such a discrepancy was even worse [226]. Therefore, they suggested

a novel approach, based on a different standpoint: instead of looking for the zero strain direction, the cell reorients to target the minimum of the passively stored 2D elastic energy. In other words, the cell attempts to minimize the energy expenditure and not the stress or strain, which is different from previous perspectives. Working in the framework of linear elasticity, they consider an energy in the form

$$\mathcal{U}_{\text{cell}} = \frac{1}{2}\varpi : \varepsilon\,, \tag{2.17}$$

where ϖ and ε are the stress and strain tensors in polar coordinates, respectively. By using anisotropic elasticity, the energy reads

$$\mathcal{U}_{\text{cell}} = \frac{1}{2}K\varepsilon_{xx}^2\left[\frac{(1+r)\cos^2\theta - 1}{b} + (1-r)\right]^2 + f(r)\,, \tag{2.18}$$

with $f(r)$ a function independent of θ, which is the cell orientation angle, while K and b are material parameters. Then, they consider a dissipative dynamics in the form

$$\frac{d\theta}{dt} = -\frac{1}{\eta}\frac{d\mathcal{U}_{\text{cell}}}{d\theta} \tag{2.19}$$

and calculate the steady states for a periodic strain $\varepsilon_{xx} = \frac{1}{2}\varepsilon_0(1-\cos\omega t)$. Upon averaging over a period, since the frequency is considered to be high, it is found that the steady states for the cell orientation satisfy

$$\cos^2\theta_{eq} = \frac{b(r-1)+1}{1+r} = b + \frac{1-2b}{1+r} \tag{2.20}$$

in addition to $\theta_{eq} = 0$ and $\theta_{eq} = \pi/2$. In particular, it is worth to stress that a linear relation between $\cos^2\theta_{eq}$ and $1/(1+r)$ for the oblique angle exists, and a fitting of data gives $b \approx 1.13$. Such a prediction appears to be in excellent agreement with their experimental data, as shown in Fig. 2.17, both for the equilibrium angles as functions of r and for the dynamical evolution of θ, even for amplitudes ε_0 up to 24%.

An energetic framework had been previously used by Lazopoulos and coworkers [214], working in a nonlinear elastic setting. The cell was modelled as a pre-stressed, isotropic, Mooney-Rivlin elastic material and analytical computations were performed, finding that the stable preferential orientation is almost perpendicular to the strain direction. However, their model predicts that the final orientation angle increases with the magnitude of applied strain, which does not seem to be the case in all experiments as discussed in Section 2.1.2.

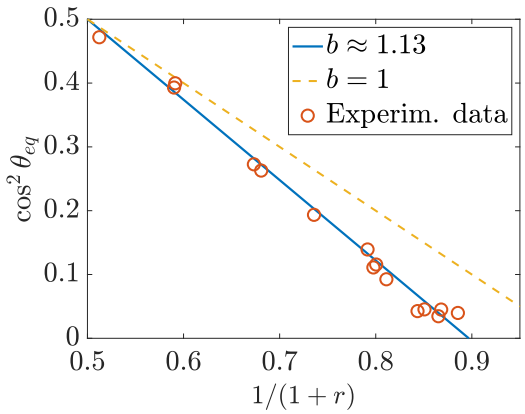

Fig. 2.17 Relation between the orientation angle θ_{eq} and the parameter r, according to the model in Eq. (2.20) proposed by Livne et al. [226]. The line with slope $b \approx 1.13$ accurately fits their experimental data, whereas the strain avoidance approach, corresponding to $b = 1$, does not.

Instead, experimental assays point towards a narrowing of the probability distribution for increasing strain. The model is then extended to account for the coexistence of symmetric orientations by considering a non-convex strain energy density function [213]. Such a choice allows to obtain two symmetric oblique orientations, albeit the energy is quite non-standard for stress fibres [98]. The same authors relax this assumption in a following work, by focusing on an individual SF-FA assembly with linear elastic behaviour at the microscopic scale [329]. In the latter, the emergence of stable oblique orientations requires the introduction of the chemical potential of the fibres, which has to be stress-dependent [329]. Moreover, the geometrical role of FAs in the reorientation process is underscored. Finally, in [290] the effect of cytoskeletal fluidisation and resolidification is also taken into account.

In a recent work, Gérémie et al. [152] derived an equation for the equilibrium orientations akin to Eq. (2.20) starting from a *vertex model*. They define the total mechanical energy as

$$\mathcal{U}_{\text{tot}} = \sum_{i=1}^{N} K_A (A_i - A_0)^2 + \gamma_P P_i + K_P P_i^2 \,, \tag{2.21}$$

where A_i is the area of the i-th cell and P_i denotes its perimeter. Hence, a penalization on area deformation from the optimal value A_0 is introduced, as well as an energy cost associated with cell perimeter changes and tension. Using a mean-field argument and an averaging procedure, the authors showed that the time-averaged energy for a single cell reads

$$\langle \mathcal{U}_{\text{cell}} \rangle = \kappa \left[(1+r)\cos^2\theta + b(1-r) - 1 \right]^2 ,$$

which leads exactly to Eq. (2.20). Interestingly, however, the authors in this case found a different fitting value for the parameter $b \approx 2.25$ compared with the one by Livne, probably due to the confluent conditions employed in their experiments.

Finally, in another recent publication, Chatterjee et al. [63] proposed a model based on the multiplicative decomposition of the deformation gradient for cell reorientation, where the cell is considered as a nonlinear elastic solid. In such a model, SFs can rotate and grow as a consequence of the deformation: their reorientation vector $\mathbf{m}$ follows an elementary evolution law given by

$$\frac{d\mathbf{m}}{dt} = \frac{1}{\tau}\left[\mathbf{m}_{\text{target}} - (\mathbf{m}_{\text{target}} \cdot \mathbf{m})\mathbf{m}\right] ,$$

which enforces the fibres to preferentially align along the direction $\mathbf{m}_{\text{target}}$. The latter is taken as orthogonal to the uniaxial applied stretch, so it is implicitly assumed that such an orientation is always preferential for the SFs, which might not be the case for all experimental conditions. Instead, the introduction of a growth tensor in the form

$$\mathbb{G} = \mathbb{I} - (\gamma_{\text{SF}} - 1)\mathbf{e}_r \otimes \mathbf{e}_r$$

accounts for stress fibre growth in the direction $\mathbf{e}_r$, with γ_{SF} being a phenomenological time-dependent parameter.

2.2.5 Viscoelasticity

Even though the equilibrium orientations obtained thanks to the purely elastic approaches of the previous Subsection compare well with experimental data, the process of cell realignment is intrinsically viscoelastic. Indeed, as discussed in Section 2.1.2, the frequency of the applied cyclic deformation appears to influence the reorientation time, and also involves threshold effects. Moreover, in some cases, experiments have shown that the strain rate of the cyclic stretch, or equivalently the choice of different waveforms, might affect the reorientation of cells. These mechanisms cannot be captured by elastic models, which by their nature imply an instantaneous response, and call for the introduction of characteristic times or viscous dynamical processes.

Almost all the models that, to our knowledge, account for viscoelastic properties are based on descriptions at the microscale. Indeed, some of the frameworks for stress fibre

modelling discussed in Section 2.2.1 embed viscosity in direct or indirect ways, taking into account that SFs have been shown experimentally to behave as viscoelastic cables [209].

Just to mention some examples, the simple sarcomeric model of SFs by Kaunas et al. [197] is certainly able to account for viscous-like effects. By considering the SF as a filament composed of actively contractile subunits in parallel, they derive an evolution equation for the force in each subunit:

$$\frac{dF}{dt} = \frac{k}{l_{\text{ref}}}\frac{dl}{dt} + \frac{2klv}{l_{\text{ref}}^2}, \tag{2.22}$$

in which F is the force, k is the stiffness of each actomyosin unit, l is the length of the SF whereas l_{ref} is the reference length, which can vary over time due to myosin sliding with velocity v. Specifically, the first term in Eq. (2.22) describes the purely elastic contribution, while the second one represents the rate of force relaxation due to myosin activity. For high applied frequencies, the SF is unable to respond quickly enough to mechanical changes and the second term vanishes, leading to an almost linear elastic behaviour. Conversely, for low frequencies the two terms compete and the SF manages to regulate the optimal force. Such a model therefore is able to qualitatively reproduce the differences due to frequency, by introducing viscous-like effects related to acto-myosin sliding. As already mentioned above, a similar approach is pursued by Chen and coworkers [66], with emphasis on the intrinsic clocks of the cell and on the role of focal adhesions; by Qian et al. [220, 295], who considered a Maxwell-like model with an active force contribution; and by Kong et al. [205, 406], where the cytoskeletal fibres were described by Kelvin-Voigt elements coupled with focal adhesions. The viscoelastic stress relaxation of SFs is instead modelled by Nagayama et al. [264] using a seven-parameter spring-dashpot scheme, which features three different characteristic times. Such a description turns out to be able to fit their experimental curves for different waveforms and suggests that SFs avoid directions where they undergo compressive forces for too long times.

The cell dipole model by De et al. [92, 93, 314] is also able to introduce a distinction in the outcomes between high and low frequency regimes. In their case, the relaxation dynamics is postulated, highlighting a relation between the frequency and the characteristic time which is coherent with experimental data.

Instead, to the best of our knowledge, macroscopic viscoelasticity frameworks to describe the reorientation of cells under stretch are very few. Here, we mention the work by McEvoy et al. [249], in which a nonlinear viscoelastic element composed of a spring in parallel with another spring and a dashpot is used to reproduce the passive mechanical

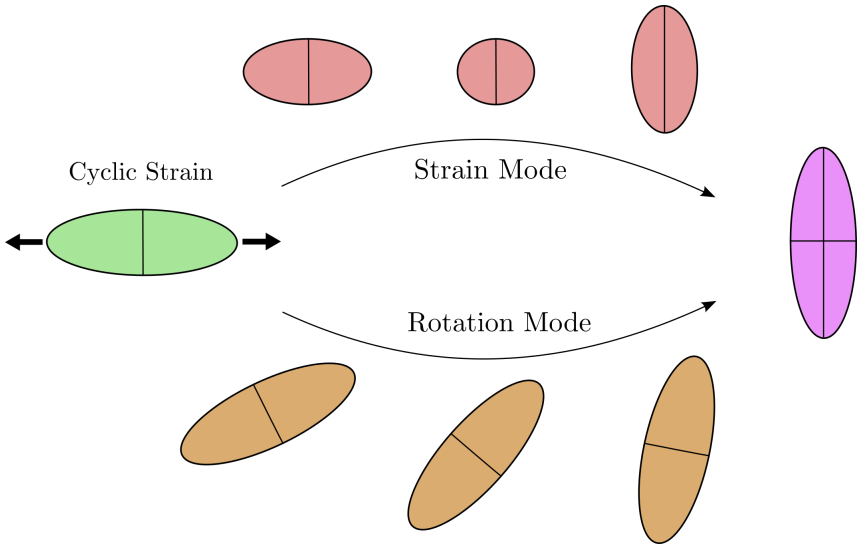

Fig. 2.18 Possible modes of cell reorientation under cyclic strain. In the strain mode, the cell disassembles the stress fibres aligned in the stretching direction, becomes rounded, and then rebuilds them in the newly preferential direction. Instead, in the rotation mode, the cell remains elongated and actually undergoes a rotation of its major axis. According to the Statistical Mechanics model in [90], the latter seems to be the preferable process. Redrawn from [90].

behaviour of the cell cytoskeleton, in addition to its active counterpart. Reynolds and collaborators [299] adopted an analogous framework, with an additional component to represent the mechanics of the hydrogel wherein the cells are embedded.

2.2.6 Statistical Mechanics

To conclude the review about mathematical models, we briefly mention some approaches based on Statistical Mechanics tools, even though they are not the focus of this Thesis. Indeed, almost all the approaches introduced so far worked in a deterministic framework, while biological processes like cell alignment are characterised by a certain degree of randomness. In this respect, De and collaborators [92, 314] and Qian et al. [295] implemented some non-deterministic effects in their models, mainly dealing with the association and dissociation processes of SFs under the action of stretch. In particular, in [314] the orientations of a single cell are described by a Boltzmann distribution, with a competition between the force determining the free energy of the dipole and an effective temperature. On the same basis, Faust et al. [120] extended the deterministic equilibrium determined by energy minimization by including a Boltzmann distribution over the angles. A Boltzmann-like probability density is also introduced in [239], where the energy is modelled as the sum of

three contributions given by the work done by focal adhesions, pulling force and elastic potential energy. In a similar spirit, the stochastic nature of SF formation and activation is included through proper probability functions in [171, 172, 197, 362], which were all discussed before.

Recently, a Fokker-Planck approach to describe the evolution in time of the probability density function of cell orientations has been proposed by Loy and Preziosi [229]. Both local and non-local Fokker-Planck equations are introduced, to model the stochastic sensing of the cell. Moreover, it is found that the distributions postulated by Faust et al. [120] and by Mao et al. [239] can be recovered as particular cases. The emergence of statistical distributions with a double peak is discussed also by Moriel et al. [257] and by Geremie et al. [152]. Both these groups extended the evolution equation (2.19) by adding a random noise term with zero mean and unit variance, and found results coherent with [229].

We also cite in this Section the work by Buskermolen et al. [55], who deal with a Statistical Mechanics framework for cell homeostasis. Such a description turns out to be appropriate for the modelling of cell alignment on micropatterned substrates as a function of stripe width, recalling the experiments presented in Section 2.1.3.

Finally, a very recent work by Das et al. [90] extended the Statistical Mechanics framework proposed in [321] to the cell cyclic straining experiment. The main outcomes of such a model involve the decoupling between the SFs and cell morphology dynamics. The authors in particular argue that cyclic strain mainly affects cell orientation away from stretch rather than SF alignment, and they explicitly consider the interplay of fibres and cell morphology, which was not taken into account before. Their results reproduce quite well the experimental data for strains of high frequency and for the case $r = 0$, in which the cell is expected to align perpendicularly. However, the model predicts that in general cells preferentially orient at the angle that minimizes the strain rate, following again Eq. (2.6). Although a certain qualitative agreement with experiments is also shown for the case $r \neq 0$, the direct comparison with data by Livne et al. [226] seems to confirm that the biaxial case requires a different approach to increase the accuracy of the predicted final orientation. An intriguing result proposed in [90] concerns instead the manner whereby cell reorientation towards the preferred direction happens. In fact, experimental results do not appear to fully clarify whether the cell follows a *strain mode*, firstly becoming rounded and then elongating towards the new direction, or a *rotation mode*, in which the cell elliptic body actually rotates (see Fig. 2.18). Remarkably, the simulations of the statistical framework in [90] strongly suggest that the rotation mode is the preferable process.

Chapter 3

Mechanical Modelling of Cytoskeletal Reorientation

In this Chapter, we present our results concerning the mechanical modelling of cell cytoskeletal realignment due to an applied stretch. Starting from the available experimental observations and from previous models describing such a behaviour of cells, we employ the framework of Continuum Mechanics to enrich the description of the phenomenon. First of all, in Section 3.1 we generalise the energetic approach proposed by Livne et al. [226] by using nonlinear anisotropic elasticity to predict the preferential orientations of stress fibres. We find that the impact of nonlinearities is slight and linear elastic models are therefore valid to characterise the equilibrium angles of cell alignment in a wide range of cases. Afterwards, in Section 3.2 we derive a thermodynamically consistent model of fibre reorientation in anisotropic materials and we show that it can be effectively applied to the dynamic realignment of cytoskeletal structures. Finally, to account for the effects of the deformation frequency on the reorientation time, in Section 3.3 we propose a simple linear anisotropic viscoelastic model which is able to capture some further experimental observations.

The results of this Chapter led to the following publications:

G. Lucci and L. Preziosi. A nonlinear elastic description of cell preferential orientations over a stretched substrate, *Biomechanics and Modeling in Mechanobiology* 20:631–649 (2021).

G. Lucci, C. Giverso, and L. Preziosi. Cell orientation under stretch: Stability of a linear viscoelastic model, *Mathematical Biosciences* 337:108630 (2021).

J. Ciambella, G. Lucci, P. Nardinocchi, and L. Preziosi. Passive and active fiber reorientation in anisotropic materials, *International Journal of Engineering Science* 176:103688 (2022).

3.1 Nonlinear Elastic Description of Preferential Orientations

As discussed in Chapter 2, several types of cells adhering to an elastic substrate tend to reorient themselves when the membrane is cyclically stretched, to achieve a stable configuration characterised by a well-defined angle between their main axis and the direction of stretching. The mechanisms behind this phenomenon and the relation between the preferred angle and the mechanical variables have been studied by several authors. In particular, Livne et al. [226] investigated the response of cells on a substrate subject to biaxial extensions using energetic arguments discussed in Section 2.2. They found that cells align the cytoskeletal stress fibres along directions that minimize the linear elastic energy. Moreover, the existence of a linear relation between $\cos^2\theta_{eq}$, where θ_{eq} is the angle formed by the main stretching direction and the most elongated axis of the cell, and $1/(1+r)$, with r being the biaxiality ratio, is highlighted, as in Eq. (2.20).

Nevertheless, as clearly evidenced by the data in Tables 2.1–2.3, it is worth to observe that several experimental assays are performed applying deformations for which the use of linear elasticity might be arguable, at least theoretically. For instance, maximum strains up to 24-25% [40, 226, 330] or even 32% [120] are applied to the specimen in some experiments. Therefore, an investigation of the possible presence of nonlinear effects at high strains is crucial, in order to quantify their relevance in cellular mechanosensing and orientation dynamics.

The aim of this Section is then to study the problem of cell cytoskeletal alignment in the framework of nonlinear elasticity, to understand why and to what extent the use of linear elasticity is justified. We find that, if we treat the substratum with seeded cells as a finite-elastic orthotropic material, a very large class of elastic energies is minimized by a relationship that can be considered as the nonlinear generalization of the one found in [226]. Specifically, introducing the parameter $\Lambda := \frac{\lambda_x - 1}{\lambda_x - \lambda_y}$ (where λ_x and λ_y are the principal stretches and $\lambda_x > \lambda_y$ without loss of generality) that quantifies the biaxiality of the finite deformation, we put in evidence a linear relation between Λ and $\cos^2\theta_{eq}$, where θ_{eq} is the equilibrium angle of the cell with respect to the x-axis. Instead, a nonlinear dependence

of the preferential angle on Λ comes out visibly if the elastic energy is allowed to depend on the anisotropic invariants related to the square of the Cauchy-Green strain tensor $\mathbb{C}^2$, defined in Section 1.2. For small values of the elastic coefficient related to the invariant I_5, the deviation from the linear behaviour is still compatible with experimental data and provides a slight improvement of the fitting. Conversely, a non-vanishing coefficient related to the invariant I_7 gives rise to results that look incompatible with experiments, suggesting this term is not present in the constitutive model [234].

Overall, our model turns out to be very general and provides a unified framework to study the preferential orientations of stress fibres on a planar substrate undergoing cyclic stretching. Moreover, we are able to study the appearance of bifurcations depending on Λ, i.e. the nonlinear generalisation of the biaxiality ratio r, and on the values of the energy coefficients. The results suggest that nonlinearities do not play a dominant role in finding the preferred angles of cell alignment: this might be the reason why experimental results obtained with high stretches are still well described by linear models.

3.1.1 Problem Set-Up

We consider a substratum provided with an ensemble of cells adherent to its surface in a sub-confluent configuration, to rule out the possible influence of cell-cell interaction, as discussed in the previous Chapter. The whole system is then subject to a biaxial deformation, due to pulling and compression of its lateral sides performed by an external device. Following this mechanical stimulus, cells on the substrate orient preferentially along a certain direction, which can be identified through a unit vector $\mathbf{N}$ in the first quadrant of a reference frame with axes aligned with the principal directions of the biaxial deformation. A sketch of the experimental set-up that we consider here is depicted in Fig. 3.1.

If we assume that the system composed by the substrate and the overlying cells behaves as an elastic continuum, the deformation will induce a storage of energy into the body that depends on the cell orientation $\mathbf{N}$. We want here to study how the elastic strain energy of such a system subject to a biaxial stretch depends on the preferential direction of the stress fibres.

For this purpose, we consider a general elastic energy density $\mathcal{W}$ for an orthotropic material

$$\mathcal{W} = \mathcal{W}(I_1, I_2, I_3, I_4, I_5, I_6, I_7, I_8), \tag{3.1}$$

which depends on the deformation gradient $\mathbb{F}$ through the invariants of the right Cauchy-Green deformation tensor $\mathbb{C} = \mathbb{F}^{\mathrm{T}}\mathbb{F}$, namely,

$$\begin{aligned}
&\mathrm{I}_1 := \mathrm{tr}\,\mathbb{C}, && \mathrm{I}_2 := \frac{1}{2}\left[(\mathrm{tr}\,\mathbb{C})^2 - \mathrm{tr}\,\mathbb{C}^2\right], && \mathrm{I}_3 := \det\mathbb{C},\\
&\mathrm{I}_4 := \mathbf{N}\cdot\mathbb{C}\mathbf{N} = |\mathbb{F}\mathbf{N}|^2, && \mathrm{I}_5 := \mathbf{N}\cdot\mathbb{C}^2\mathbf{N} = |\mathbb{C}\mathbf{N}|^2, &&\\
&\mathrm{I}_6 := \mathbf{N}_\perp\cdot\mathbb{C}\mathbf{N}_\perp = |\mathbb{F}\mathbf{N}_\perp|^2, && \mathrm{I}_7 := \mathbf{N}_\perp\cdot\mathbb{C}^2\mathbf{N}_\perp = |\mathbb{C}\mathbf{N}_\perp|^2, &&\\
&\mathrm{I}_8 := \mathbf{N}_\perp\cdot\mathbb{C}\mathbf{N} = (\mathbb{F}\mathbf{N}_\perp)\cdot\mathbb{F}\mathbf{N}, &&&&
\end{aligned} \tag{3.2}$$

where $\mathbf{N}_\perp$ is the direction perpendicular to $\mathbf{N}$ in the plane of the substratum.

This kind of strain energy is commonly used to describe the mechanical behaviour of hyperelastic anisotropic materials which exhibit two preferential directions [166, 168, 276, 289]. For instance, it is employed for fibre-reinforced materials with two orthogonal bundles of fibres that influence the mechanical response of the body: a relevant example in the context of biology is represented by blood vessel walls, showing fibre bundles in different directions [166–168]. In our case, the system displays a natural anisotropy of this kind due to the presence in the cells of aligned stress fibres and actin filament structures that are cross-linked by several types of proteins, like fascin, fimbrin, α-actinin, filamin, ARP2-3 [75, 231, 392] (see Figure 3.1). Since SF are two to even ten times stiffer than the lateral actin network [174, 231, 245, 325] and the cytoplasm, they induce bidirectional anisotropy in the mechanical response, justifying the general assumption (3.1) to consider the system as orthotropic. Indeed, experimental measurements on cell stiffness demonstrated that a mechanical anisotropy exists and is due to the presence of SF bundles, since their disruption restores a more isotropic response [174]. Analogous results were reported in [325], where cells subjected to cyclic strain were found to be consistently stiffer along their main axis due to the alignment of SFs.

We also observe that, in the context of reorientation following a mechanical cue, cells do not own a polarization, namely, it is not possible to identify a head and a tail [75, 375]. Therefore, configurations with cells aligned along $\mathbf{N}$ and $-\mathbf{N}$ are geometrically indistinguishable and must be energetically equivalent. A similar fact holds true if we replace $\mathbf{N}_\perp$ with $-\mathbf{N}_\perp$. To guarantee that there is not a preference for either of these orientations with respect to the other, it is necessary that the energy be the same under the related symmetry transformations. In this respect, all the invariants mentioned in Eq. (3.2) achieve the same values under the symmetry transformations above, except for

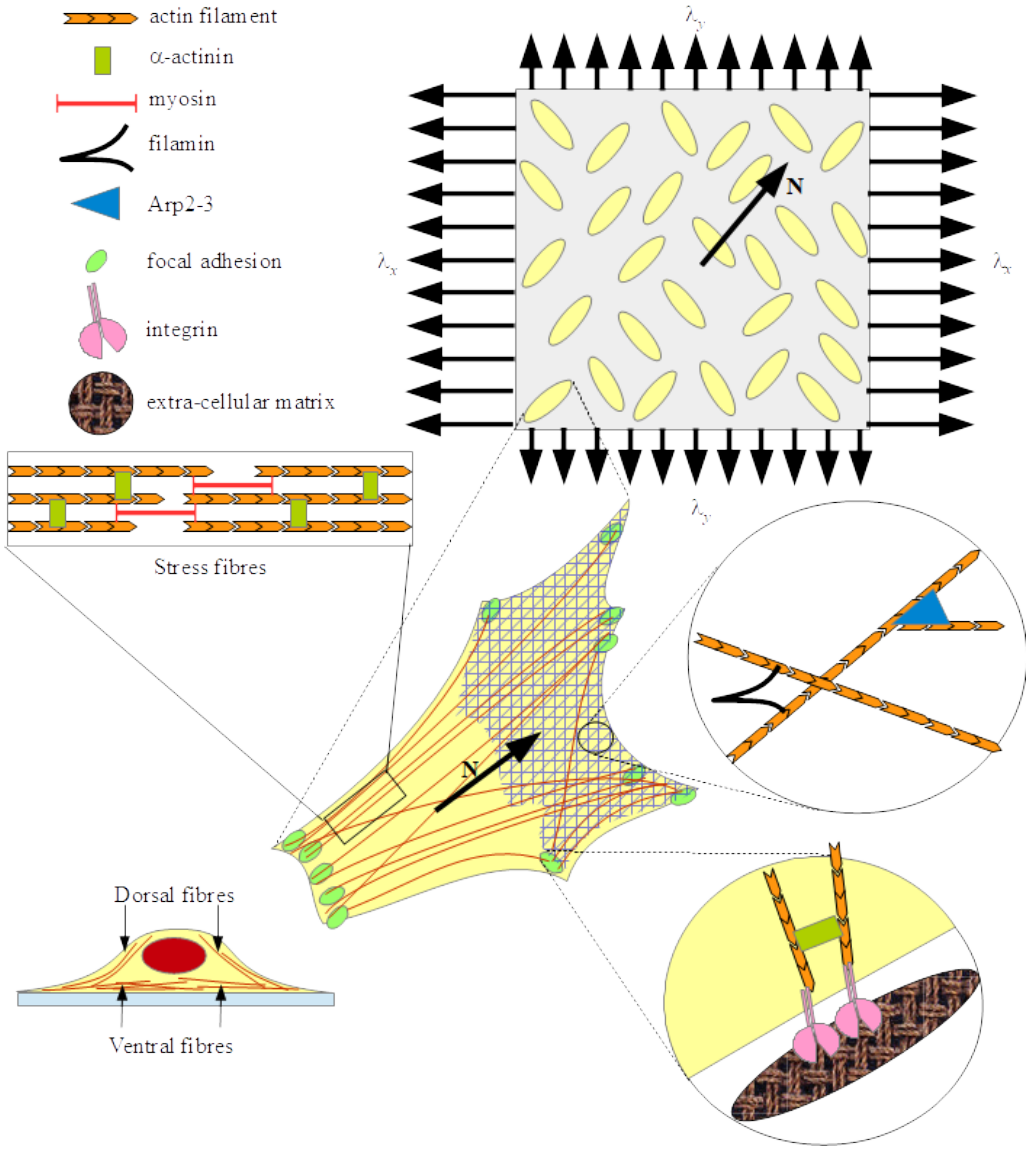

Fig. 3.1 Sketch of typical experimental set-up and consequent inner structure of a cell, highlighting the principal cytoskeletal structures and proteins involved in the process of reorientation.

I_8 that changes sign, i.e., for a given deformation, $\mathrm{I}_8(-\mathbf{N},\mathbf{N}_\perp,\mathbb{C}) = -\mathrm{I}_8(\mathbf{N},\mathbf{N}_\perp,\mathbb{C})$ and $\mathrm{I}_8(\mathbf{N},-\mathbf{N}_\perp,\mathbb{C}) = -\mathrm{I}_8(\mathbf{N},\mathbf{N}_\perp,\mathbb{C})$. Therefore, to satisfy the symmetry requirements, $\mathcal{U}$ must be an even function of I_8.

Remark 3.1. As pointed out in Chapter 1, the definition of the invariant I_8 used in this Section is not the only one found in the literature. Indeed, several works dealing with orthotropic materials use instead $\mathrm{I}_8 := (\mathbf{a}\cdot\mathbf{b})(\mathbf{a}\cdot\mathbb{C}\mathbf{b})$, where $\mathbf{a}$ and $\mathbf{b}$ are the vectors of the preferential directions. If such a definition is adopted, then the energy is automatically invariant under change of sign of either fibre vector. A shortcoming of this formulation, instead, is that for orthogonal fibres we have $\mathrm{I}_8 = 0$ identically. In Section 3.2 we will consider the new definition and show that the conclusions derived in the following do not change.

If we orient the x- and y-axes of the reference frame along the principal stretching directions, the right Cauchy-Green tensor is diagonal and its eigenvalues are the principal stretches, i.e.

$$\mathbb{C} = \begin{pmatrix} \lambda_x & 0 & 0 \\ 0 & \lambda_y & 0 \\ 0 & 0 & \lambda_z \end{pmatrix},$$

with $\lambda_x > \lambda_y$ and $\lambda_x > 1$. The reason why we exclude the case $\lambda_x = \lambda_y$ is that, for equi-biaxial deformations of the substrate, cells do not show a preferential orientation, but rather protrude outside the plane of the membrane [377]. Once the deformation is fixed, our goal is to study which orientations for the stress fibres and cells correspond to minima of the elastic energy. Following the line of thought put forward by Livne and coworkers [226], these directions will correspond to the preferential orientations of the cells.

3.1.2 Stationary Points by the Coaxiality Approach

The general problem of finding the critical points of an hyperelastic anisotropic strain energy for a body subject to a rotation and a deformation has been studied by Vianello and coworkers [313, 319, 370]. In particular, it has been shown that the critical points of the energy are achieved for those rotations that make the stress and strain tensors coaxial. Since, two symmetric tensors are coaxial if and only if they commute, according to the definition considered by Vianello [370], we have to find the rotations $\mathbb{Q}$ about the z-axis such that

$$\mathbb{S}^*\mathbb{C}^* = \mathbb{C}^*\mathbb{S}^*, \tag{3.3}$$

where $\mathbb{C}^* = \mathbb{Q}^{\mathrm{T}}\mathbb{C}\mathbb{Q}$ is the Cauchy-Green tensor obtained rotating by $\mathbb{Q}$ before applying the deformation $\mathbb{F}$ and $\mathbb{S}^* = \mathbb{S}(\mathbb{C}^*)$ is the second Piola-Kirchhoff stress tensor associated with $\mathbb{C}^*$ [319]. To explicitly write $\mathbb{S}^*$ in our case, we define the structural tensors

$$\mathbb{A}^0 := \mathbf{N}^0 \otimes \mathbf{N}^0, \quad \mathbb{A}^0_\perp := \mathbf{N}^0_\perp \otimes \mathbf{N}^0_\perp, \quad \mathbb{V}^0 := \frac{1}{2}\left[\mathbf{N}^0 \otimes \mathbf{N}^0_\perp + \mathbf{N}^0_\perp \otimes \mathbf{N}^0\right], \tag{3.4}$$

where $\mathbf{N}^0$, $\mathbf{N}^0_\perp$ are the preferential orientation and its orthogonal, respectively, before rotation happens. By recalling that

$$\begin{aligned}
&\frac{\partial \mathrm{I}_1}{\partial \mathbb{C}}(\mathbb{C}) = \mathbb{I}, && \frac{\partial \mathrm{I}_2}{\partial \mathbb{C}}(\mathbb{C}) = \mathrm{I}_1(\mathbb{C})\mathbb{I} - \mathbb{C}, && \frac{\partial \mathrm{I}_3}{\partial \mathbb{C}}(\mathbb{C}) = \mathrm{I}_3(\mathbb{C})\mathbb{C}^{-1},\\
&\frac{\partial \mathrm{I}_4}{\partial \mathbb{C}}(\mathbf{N}^0, \mathbb{C}) = \mathbb{A}^0, && \frac{\partial \mathrm{I}_5}{\partial \mathbb{C}}(\mathbf{N}^0, \mathbb{C}) = \mathbb{A}^0\mathbb{C} + \mathbb{C}\mathbb{A}^0,\\
&\frac{\partial \mathrm{I}_6}{\partial \mathbb{C}}(\mathbf{N}^0_\perp, \mathbb{C}) = \mathbb{A}^0_\perp, && \frac{\partial \mathrm{I}_7}{\partial \mathbb{C}}(\mathbf{N}^0_\perp, \mathbb{C}) = \mathbb{A}^0_\perp\mathbb{C} + \mathbb{C}\mathbb{A}^0_\perp,\\
&\frac{\partial \mathrm{I}_8}{\partial \mathbb{C}}(\mathbf{N}^0, \mathbf{N}^0_\perp, \mathbb{C}) = \mathbb{V}^0,
\end{aligned} \tag{3.5}$$

the second Piola-Kirchhoff stress tensor reads

$$\begin{aligned}
\mathbb{S}^* &= 2\frac{\partial \mathcal{W}}{\partial \mathbb{C}}(\mathbb{C}^*) = 2\sum_{p=1}^{8} \frac{\partial \mathcal{W}}{\partial \mathrm{I}_p}\frac{\partial \mathrm{I}_p}{\partial \mathbb{C}}(\mathbb{C}^*)\\
&= 2\left[w_1\mathbb{I} + w_2(\mathrm{I}_1(\mathbb{C}^*)\mathbb{I} - \mathbb{C}^*) + w_3\mathrm{I}_3(\mathbb{C}^*)(\mathbb{C}^*)^{-1} + w_4\mathbb{A}^0 + w_5(\mathbb{A}^0\mathbb{C}^* + \mathbb{C}^*\mathbb{A}^0) + \right.\\
&\left. + w_6\mathbb{A}^0_\perp + w_7(\mathbb{A}^0_\perp\mathbb{C}^* + \mathbb{C}^*\mathbb{A}^0_\perp) + w_8\mathbb{V}^0\right],
\end{aligned} \tag{3.6}$$

where we have defined

$$w_p := \frac{\partial \mathcal{W}}{\partial \mathrm{I}_p}\left(\mathrm{I}_1(\mathbb{C}^*), \ldots, \mathrm{I}_8(\mathbf{N}^0, \mathbf{N}^0_\perp, \mathbb{C}^*)\right), \quad p = 1, \ldots, 8.$$

Then, using (3.6), Eq. (3.3) leads to the condition

$$\begin{aligned}
w_4\left[\mathbb{A}^0\mathbb{C}^* - \mathbb{C}^*\mathbb{A}^0\right] + w_5\left[\mathbb{A}^0(\mathbb{C}^*)^2 - (\mathbb{C}^*)^2\mathbb{A}^0\right] + w_6\left[\mathbb{A}^0_\perp\mathbb{C}^* - \mathbb{C}^*\mathbb{A}^0_\perp\right] +\\
+ w_7\left[\mathbb{A}^0_\perp(\mathbb{C}^*)^2 - (\mathbb{C}^*)^2\mathbb{A}^0_\perp\right] + w_8\left[\mathbb{V}^0\mathbb{C}^* - \mathbb{C}^*\mathbb{V}^0\right] = \mathbb{O}.
\end{aligned} \tag{3.7}$$

Multiplying both sides by $\mathbb{Q}^{\mathrm{T}}$ on the right and by $\mathbb{Q}$ on the left, one obtains

$$w_4\left[\mathbb{A}\mathbb{C}-\mathbb{C}\mathbb{A}\right]+w_5\left[\mathbb{A}\mathbb{C}^2-\mathbb{C}^2\mathbb{A}\right]+w_6\left[\mathbb{A}_\perp\mathbb{C}-\mathbb{C}\mathbb{A}_\perp\right]+ \\ +w_7\left[\mathbb{A}_\perp\mathbb{C}^2-\mathbb{C}^2\mathbb{A}_\perp\right]+w_8\left[\mathbb{V}\mathbb{C}-\mathbb{C}\mathbb{V}\right]=\mathbb{O}, \tag{3.8}$$

in which we have set $\mathbb{A}:=\mathbb{Q}\mathbb{A}^0\mathbb{Q}^{\mathrm{T}}$, $\mathbb{A}_\perp=\mathbb{Q}\mathbb{A}^0_\perp\mathbb{Q}^{\mathrm{T}}$ and $\mathbb{V}:=\mathbb{Q}\mathbb{V}^0\mathbb{Q}^{\mathrm{T}}$. Now, we use the fact that $\mathbb{A}^0_\perp=\mathbb{I}-\mathbb{A}^0-\mathbf{k}\otimes\mathbf{k}$, where $\mathbf{k}:=\mathbf{N}^0\times\mathbf{N}^0_\perp$ is the axis of rotation of $\mathbb{Q}$, perpendicular to the plane of the substrate. As a consequence, we immediately have $\mathbb{A}_\perp=\mathbb{I}-\mathbb{A}-\mathbf{k}\otimes\mathbf{k}$, since $\mathbb{Q}\mathbf{k}=\mathbf{k}$. It is therefore immediate to find that

$$(w_4-w_6)\left[\mathbb{A}\mathbb{C}-\mathbb{C}\mathbb{A}\right]+(w_5-w_7)\left[\mathbb{A}\mathbb{C}^2-\mathbb{C}^2\mathbb{A}\right]+w_8\left[\mathbb{V}\mathbb{C}-\mathbb{C}\mathbb{V}\right]=\mathbb{O}\,, \tag{3.9}$$

where we have used the fact that $\mathbf{k}$ is an eigenvector of $\mathbb{C}$, and then $\mathbf{k}\otimes\mathbb{C}\mathbf{k}=\mathbb{C}\mathbf{k}\otimes\mathbf{k}$ and $\mathbf{k}\otimes\mathbb{C}^2\mathbf{k}=\mathbb{C}^2\mathbf{k}\otimes\mathbf{k}$.

Focusing on the last term on the left-hand side of (3.9), elementary tensor algebra allows to rewrite it as

$$\mathbb{V}\mathbb{C}-\mathbb{C}\mathbb{V}=\mathrm{Sym}(\mathbb{Q}\mathbf{N}^0\otimes\mathbb{Q}\mathbf{N}^0_\perp)\mathbb{C}-\mathbb{C}\,\mathrm{Sym}(\mathbb{Q}\mathbf{N}^0\otimes\mathbb{Q}\mathbf{N}^0_\perp)=\mathrm{Sym}(\mathbb{R})\mathbb{C}-\mathbb{C}\,\mathrm{Sym}(\mathbb{R}),$$

with

$$\mathbb{R}:=\mathbb{Q}\mathbf{N}^0\otimes\mathbb{Q}\mathbf{N}^0_\perp\,, \tag{3.10}$$

whereas the operator Sym takes the symmetric part of its tensorial argument. A direct substitution into (3.9) leads to

$$\left[(w_4-w_6)\mathbb{A}+w_8\,\mathrm{Sym}(\mathbb{R})\;+(w_5-w_7)\mathbb{A}\mathbb{C}\right]\mathbb{C} \\ -\mathbb{C}\left[(w_4-w_6)\mathbb{A}+w_8\,\mathrm{Sym}(\mathbb{R})+(w_5-w_7)\mathbb{C}\mathbb{A}\right]=\mathbb{O},$$

or equivalently

$$\widehat{\mathbb{A}}\mathbb{C}-\mathbb{C}\widehat{\mathbb{A}}=\mathbb{O}, \tag{3.11}$$

where

$$\widehat{\mathbb{A}}:=(w_4-w_6)\mathbb{A}+2(w_5-w_7)\,\mathrm{Sym}(\mathbb{A}\mathbb{C})+w_8\,\mathrm{Sym}(\mathbb{R}). \tag{3.12}$$

Eq. (3.11) states that stationary configurations are identified by the rotations $\mathbb{Q}$ about the z-axis which make the tensors $\mathbb{C}$ and $\widehat{\mathbb{A}}$, defined in (3.12), commute. As pointed out in [70, 72, 319, 370], there are always at least two solutions, which can be easily identified in

this case. In fact, if $\mathbb{Q}$ is such that $\mathbb{Q}\mathbf{N}^0$ is along one of the principal strain directions, then trivially $\mathbb{A} = \mathbb{Q}\mathbf{N}^0 \otimes \mathbb{Q}\mathbf{N}^0$ commutes with $\mathbb{C}$ and with $\mathbb{C}^2$. On the other hand, we have that $\mathrm{I}_8(\mathbf{N}^0, \mathbf{N}^0_\perp, \mathbb{C}^*) = \mathrm{I}_8(\mathbb{Q}\mathbf{N}^0, \mathbb{Q}\mathbf{N}^0_\perp, \mathbb{C})$ which vanishes because in this case $\mathbb{Q}\mathbf{N}^0$ and $\mathbb{Q}\mathbf{N}^0_\perp$ are both eigenvectors of $\mathbb{C}$. Consequently, $w_8(\mathrm{I}_8)$ must be null as well, since it is assumed to be an odd function of I_8 due to the symmetry requirements on $\mathcal{W}$ which prescribe the energy to be even in I_8.

We conclude that configurations with cells oriented along the principal stretching direction or perpendicularly to it always correspond to stationary points of the elastic energy. However, one might have further stationary solutions for other possible rotations satisfying (3.11), which will depend in general on the specific energy functional considered. In the following we will show that, for a large class of elastic energies, there might be two symmetric equilibria and we will study the stability of all configurations.

3.1.3 Stability Conditions for a Quadratic-Like Energy

Since we are using the reference frame with axes aligned with the principal stretching directions, so that $\mathbb{C}$ is diagonal, it is convenient to identify the cell major axis through the angle θ it forms with the x-axis (see Fig. 2.3), so that $\mathbf{N} = \mathbb{Q}\mathbf{N}^0 = (\cos\theta, \sin\theta, 0)$ and $\mathbf{N}_\perp = \mathbb{Q}\mathbf{N}^0_\perp = (-\sin\theta, \cos\theta, 0)$. This angle is univocally associated with a rotation $\mathbb{Q}$ in the framework of the previous Subsection and in the following will be used as our main variable. With this choice, the invariants in (3.2) read

$$\begin{aligned}
\mathrm{I}_4 &= \lambda_x \cos^2\theta + \lambda_y \sin^2\theta = (\lambda_x - \lambda_y)\cos^2\theta + \lambda_y\,,\\
\mathrm{I}_5 &= \lambda_x^2 \cos^2\theta + \lambda_y^2 \sin^2\theta = (\lambda_x^2 - \lambda_y^2)\cos^2\theta + \lambda_y^2\,,\\
\mathrm{I}_6 &= \lambda_x \sin^2\theta + \lambda_y \cos^2\theta = \lambda_x - (\lambda_x - \lambda_y)\cos^2\theta\,,\\
\mathrm{I}_7 &= \lambda_x^2 \sin^2\theta + \lambda_y^2 \cos^2\theta = \lambda_x^2 - (\lambda_x^2 - \lambda_y^2)\cos^2\theta\,,\\
\mathrm{I}_8 &= -(\lambda_x - \lambda_y)\sin\theta\cos\theta\,,
\end{aligned} \tag{3.13}$$

and can be compactly rewritten as

$$\hat{\mathrm{I}}_i := \mathrm{I}_i - 1 = a_i \cos^2\theta + b_i\,, \qquad \text{for} \quad i = 4,5,6,7$$

where

$$\begin{aligned}
a_4 &:= \lambda_x - \lambda_y\,, & b_4 &:= \lambda_y - 1\,,\\
a_5 &:= \lambda_x^2 - \lambda_y^2 = a_4(\lambda_x + \lambda_y)\,, & b_5 &:= \lambda_y^2 - 1 = b_4(\lambda_y + 1)\,,\\
a_6 &:= -(\lambda_x - \lambda_y) = -a_4\,, & b_6 &:= \lambda_x - 1\,,\\
a_7 &:= -(\lambda_x^2 - \lambda_y^2) = -a_5 = -a_4(\lambda_x + \lambda_y)\,, & b_7 &:= \lambda_x^2 - 1 = b_6(\lambda_x + 1)\,.
\end{aligned} \tag{3.14}$$

The Elastic Energy

In order to investigate the existence of other stationary configurations in addition to the trivial ones, and to study their stability, we need now to specialize the elastic energy, trying to keep it as general as possible. We consider then a class of elastic energies that can be written as a homogeneous second order polynomial in the variables $\hat{\mathrm{I}}_i$, for $i = 4,5,6,7$, and I_8, plus a term related to the isotropic response:

$$\mathcal{W}(\mathbf{I}) = \frac{1}{2}\mathbf{I}\cdot\mathbb{K}_{\mathrm{e}}\mathbf{I} + \mathcal{U}\,, \tag{3.15}$$

where $\mathbf{I} := \left(\hat{\mathrm{I}}_4, \hat{\mathrm{I}}_5, \hat{\mathrm{I}}_6, \hat{\mathrm{I}}_7, \mathrm{I}_8\right)$ and $\mathbb{K}_{\mathrm{e}}$ is the symmetric matrix of elastic coefficients, while $\mathcal{U}$ is the purely isotropic contribution that depends on $(\mathrm{I}_1, \mathrm{I}_2, \mathrm{I}_3)$. We remark that, in order to slightly reduce the terms influencing the stability analysis, we do not consider here possible isotropic-anisotropic couplings in the energy (3.15), that is, we exclude for the moment terms like $\mathrm{I}_h\hat{\mathrm{I}}_l$, where $h \in \{1,2,3\}$ and $l \in \{4,5,6,7,8\}$. However, in Section 3.3 we will show that their introduction does not change the conclusions about the preferential orientations, but only the definition of some parameters.

We also observe that the following analysis can be straightforwardly repeated for a Fung-type energy

$$\mathcal{W}_F = C\left[\exp\left(\frac{\mathcal{W}}{\mathcal{W}_0} - 1\right) - 1\right], \tag{3.16}$$

that is often used in biomechanical applications [127, 166–168, 273, 289], giving rise to the same results. In fact, the stationary points of $\mathcal{W}_F$ coincide with the ones of $\mathcal{W}$. Moreover, their stability character may be identified by the second derivative of $\mathcal{W}$ and then it is the same as well. Therefore, the results obtained for a quadratic energy also hold for an exponential-like energy, amplifying the validity of our conclusions.

For future notational convenience, it is useful to denote by k_{ij}, for $i,j = 4,\dots,8$ the coefficients of the matrix $\mathbb{K}_e$. For example, k_{44} stands for the coefficient in the top left corner of the matrix. For what concerns the physical meaning, the coefficient k_{44} is related to the stiffness along the major axis of the cell, whereas k_{66} refers to the stiffness along the direction orthogonal to the one of cell orientation. By considering that stress fibres are mainly aligned to the cell axis, coherently with [57] we will assume that

$$k_{44} > k_{66}\,.$$

We also point out that the coefficient k_{88} is related to the response to shear and to the coupling of the fibres. At the microscopic level, therefore, it may correspond to the resistance of changing angle among actin fibres, also involving the action of actin cross-linking proteins, such as filamin, Rho/Rac GTPases [75, 377] and Arp2/3 as well [138, 310] (see Figure 3.1).

As a final remark we note that, because of the symmetry conditions related to a switching of the orientation axis, the coefficients k_{i8} (and k_{8i}), $i = 4,5,6,7$ must vanish. Indeed, they appear in front of cross-terms involving the invariant I_8 linearly, which would change sign if the preferential direction is reversed from $\mathbf{N}$ to $-\mathbf{N}$. Thus, their inclusion would break the symmetries of the energy and introduce an imbalance between some directions that should be equivalent to each other, as discussed before. To avoid such a biologically unfeasible situation, we consider $k_{i8} = 0$ for $i = 4,5,6,7$.

Critical Points of the Energy and their Stability

Taking into account the consequences of symmetry on the coefficients of matrix $\mathbb{K}_e$ in (3.15), the critical points of the energy as a function of the angle are identified by the solutions of

$$\mathbf{I}(\theta)\cdot\mathbb{K}_e\frac{\partial\mathbf{I}}{\partial\theta}(\theta) = 0\,,$$

that can be explicitly written as

$$\sum_{i,j=4}^{7} k_{ij}\hat{\mathrm{I}}_i\frac{\partial\hat{\mathrm{I}}_j}{\partial\theta} + k_{88}\mathrm{I}_8\frac{\partial\mathrm{I}_8}{\partial\theta} = 0\,.$$

By recalling the form of the coefficients defined in Eq. (3.14), the previous equation reads

$$\left[-2\sum_{i,j=4}^{7} k_{ij}a_i a_j \cos^2\theta - 2\sum_{i,j=4}^{7} k_{ij}b_i a_j + k_{88}a_4^2(\cos^2\theta - \sin^2\theta)\right]\sin\theta\cos\theta = 0\,.$$

As already underscored, the configurations with $\theta = 0$ and $\theta = \pi/2$ (which in the following will sometimes be referred to as *parallel* and *perpendicular* orientation, respectively) always correspond to critical points of the energy. However, for the choice we made, there might be additional non-trivial critical angles that satisfy

$$\cos^2\theta_{eq} = \frac{1}{2a_4}\frac{2\Sigma_2 - k_{88}a_4}{\Sigma_1 - k_{88}}\,,$$

or equivalently

$$\cos^2\theta_{eq} = \frac{1}{2} - \frac{1}{2}\frac{\Sigma_1}{\Sigma_1 - k_{88}} + \frac{1}{a_4}\frac{\Sigma_2}{\Sigma_1 - k_{88}}\,, \tag{3.17}$$

where we have set

$$\Sigma_1 := \frac{1}{a_4^2}\sum_{i,j=4}^{7} k_{ij}a_i a_j\,, \qquad \text{and} \qquad \Sigma_2 := -\frac{1}{a_4}\sum_{i,j=4}^{7} k_{ij}b_i a_j\,.$$

In particular, the coefficients Σ_1 and Σ_2 can be made explicit as

$$\Sigma_1 = k_{44} - 2k_{46} + k_{66} + 2(k_{45} - k_{47} - k_{56} + k_{67})(\lambda_x + \lambda_y) + (k_{55} - 2k_{57} + k_{77})(\lambda_x + \lambda_y)^2\,,$$

and

$$\begin{aligned}\Sigma_2 \quad &= k_{44}(1-\lambda_y) + k_{55}(\lambda_x+\lambda_y)(1-\lambda_y^2) + k_{66}(\lambda_x - 1) + k_{77}(\lambda_x+\lambda_y)(\lambda_x^2 - 1)\\ &+k_{45}(1-\lambda_y)(\lambda_x + 2\lambda_y + 1) - k_{46}(\lambda_x - \lambda_y) - k_{47}(\lambda_x^2 - \lambda_y^2 - \lambda_x\lambda_y + \lambda_x + \lambda_y - 1)\\ &-k_{56}(\lambda_x^2 - \lambda_y^2 + \lambda_x\lambda_y - \lambda_x - \lambda_y + 1) - k_{57}(\lambda_x+\lambda_y)^2(\lambda_x - \lambda_y)\\ &+k_{67}(\lambda_x - 1)(2\lambda_x + \lambda_y + 1).\end{aligned}$$

The nontrivial solution θ_{eq}, also called *oblique* orientation, exists if and only if

$$0 \le \frac{2\Sigma_2 - k_{88}a_4}{\Sigma_1 - k_{88}} \le 2a_4\,, \tag{3.18}$$

or analogously if

$$\frac{2\Sigma_2 - k_{88}a_4}{\Sigma_1 - k_{88}} \geq 0 \qquad \text{and} \qquad \frac{2\Sigma_2 - 2a_4\Sigma_1 + k_{88}a_4}{\Sigma_1 - k_{88}} \leq 0\,. \tag{3.19}$$

It is immediate to observe that, if θ_{eq} is an angle satisfying (3.17), then $-\theta_{eq}$ and $\pi + \theta_{eq}$ are critical points of the energy as well. This is in line with the symmetries discussed before, leading to configurations which are equivalent for the cell from an energetic viewpoint.

As far as stability is concerned, we need to evaluate the second derivative of the energy, that is,

$$\mathcal{W}''(\theta) = \Bigg[4 \sum_{i,j=4}^{7} k_{ij} a_i a_j \cos^2\theta \sin^2\theta - 2 \sum_{i,j=4}^{7} k_{ij} a_j (a_i \cos^2\theta + b_i)(\cos^2\theta - \sin^2\theta) \\ + k_{88} a_4^2 \left((\cos^2\theta - \sin^2\theta)^2 - 4\cos^2\theta \sin^2\theta \right) \Bigg].$$

If we impose the positivity of $\mathcal{W}''$, we are led to the following stability conditions:

$$\begin{aligned}
&\theta = 0: \quad \text{stable} \iff 2\Sigma_2 - 2a_4\Sigma_1 + k_{88}a_4 > 0\,, \\
&\theta = \frac{\pi}{2}: \quad \text{stable} \iff 2\Sigma_2 - k_{88}a_4 < 0\,, \\
&\theta = \theta_{eq}: \quad \text{stable} \iff 2\Sigma_2 - k_{88}a_4 \geq 0 \quad \text{and} \quad 2\Sigma_2 - 2a_4\Sigma_1 + k_{88}a_4 \leq 0\,,
\end{aligned} \tag{3.20}$$

where in the last condition we have used the fact that the positivity of the second derivative $\mathcal{W}''(\theta_{eq}) > 0$ requires $\Sigma_1 - k_{88} > 0$ to simplify the existence condition (3.19).

In the following, we will sometimes refer to the orientations of Eq. (3.20) as *equilibrium angles*. However, we remark that they are not in general solutions of the elastic problem, but only critical points of the elastic energy.

3.1.4 Bifurcation Results and Nonlinear Effects

In this Section, by means of a bifurcation analysis, we discuss the preferential orientations of cells on a stretched substrate, for an elastic energy given by (3.15) or (3.16). We firstly consider the case in which the strain energy does not depend on the invariants related to $\mathbb{C}^2$, i.e. I_5 and I_7. This is a simplified but very relevant situation, since it allows to extend the range of validity of previous linear models. Then, we thoroughly analyse the effects of

the corrections brought along by those invariants, since they introduce a significant change in the predicted behaviour.

Hereafter, we consider three types of finite deformation: in the first one, we fix the stretch in the y-direction λ_y to a certain value and $\lambda_z = 1$, while letting λ_x vary. In the second one, we keep $\lambda_x\lambda_y = 1$, corresponding to an isochoric planar deformation if $\lambda_z = 1$. Finally, we set $\lambda_y = 1/\sqrt{\lambda_x}$, equivalent to a pure isochoric deformation that involves also the z-direction. Although we do not have any experimental information on λ_z, it does not affect the discussion on equilibrium angles or on their stability character.

Energy Independent of $\mathbb{C}^2$

Let us firstly consider the case in which the elastic energy is independent of terms containing $\mathbb{C}^2$, that is, of the anisotropic invariants I_5 and I_7. More explicitly, recalling Eq. (3.15), we deal with an energy in the form

$$\mathcal{W}(\hat{\mathrm{I}}_4, \hat{\mathrm{I}}_6, \mathrm{I}_8) = \frac{1}{2}k_{44}\hat{\mathrm{I}}_4^2 + \frac{1}{2}k_{66}\hat{\mathrm{I}}_6^2 + k_{46}\hat{\mathrm{I}}_4\hat{\mathrm{I}}_6 + \frac{1}{2}k_{88}\mathrm{I}_8^2 + \mathcal{U}\,, \tag{3.21}$$

where $k_{44}, k_{46}, k_{66}, k_{88} > 0$ and with the following constraint in order to ensure the positive definiteness of the elastic coefficients matrix: $k_{44}k_{66} - k_{46}^2 > 0$. The results for such a particular situation can be easily obtained from the previous computations by setting $k_{45} = k_{47} = k_{55} = k_{56} = k_{57} = k_{67} = k_{77} = 0$. Doing so, we can get simplified forms for the terms

$$\Sigma_1 = k_{44} - 2k_{46} + k_{66} \qquad \text{and} \qquad \Sigma_2 = k_{44}(1-\lambda_y) - k_{46}(\lambda_x - \lambda_y) + k_{66}(\lambda_x - 1)\,.$$

Thus, in addition to the trivial equilibria, Eq. (3.17) simplifies to

$$\cos^2\theta_{eq} = \frac{1}{2} + \frac{k_{44} - k_{66}}{k_{44} + k_{66} - 2k_{46} - k_{88}}\left(\frac{1}{2} - \frac{\lambda_x - 1}{\lambda_x - \lambda_y}\right), \tag{3.22}$$

putting in clear evidence a linear relationship between $\cos^2\theta_{eq}$ and the parameter

$$\Lambda := \frac{\lambda_x - 1}{\lambda_x - \lambda_y}\,, \tag{3.23}$$

which compares the elongation along x with respect to the sum of elongation and contraction along y. It is interesting to notice that Eq. (3.22) is a generalisation to the nonlinear

case of the relation derived by Livne et al. [226] in Eq. (2.20). Indeed, Λ represents the corresponding biaxiality parameter and reduces to $\frac{1}{1+r}$ in the linear elastic case.

The slope of the straight line in Eq. (3.22) is determined by the combination of coefficients

$$\mathcal{K} := \frac{k_{44} - k_{66}}{k_{44} + k_{66} - 2k_{46} - k_{88}},$$

or equivalently by its inverse

$$\alpha := \frac{1}{\mathcal{K}} = \frac{k_{44} + k_{66} - 2k_{46} - k_{88}}{k_{44} - k_{66}}, \tag{3.24}$$

as shown in Fig. 3.2. Actually, data from [120, 226] suggest a slope for such a straight line of $\mathcal{K} = 1.26 \pm 0.08$, corresponding to $\alpha = 0.794 \pm 0.08$. It is also worth to observe that such line always passes through the point corresponding to $\cos^2 \theta_{eq} = 1/2$ (i.e., $\theta_{eq} = \pi/4$) when $\Lambda = 1/2$, for any values of the elastic parameters. This is explained by the fact that, for a deformation satisfying $\Lambda = 1/2$ (or equivalently $\lambda_x - 1 = 1 - \lambda_y$), the minimum of the energy coincides with the direction of minimal strain. Indeed, the latter is given by the angle $\widetilde{\theta}$ such that $\mathrm{I}_4 = 1$, that is,

$$\widetilde{\theta} = \arctan\left(\sqrt{\frac{\lambda_x - 1}{1 - \lambda_y}}\right) = \arctan\left(\sqrt{\frac{\Lambda}{1 - \Lambda}}\right).$$

Therefore, when $\Lambda = 1/2$, we have $\widetilde{\theta} = \pi/4$ which coincides with θ_{eq} obtained using Eq. (3.22). This is not true in general, since the minimal strain angle $\widetilde{\theta}$ satisfies

$$\cos^2 \widetilde{\theta} = 1 - \Lambda,$$

differently from what is found through energy minimization in Eq. (3.22) except for the case $\alpha = 1$, which does not fit the experimental data [120, 226]. In fact, as pointed out in [226], choosing the minimal strain direction as the preferential one for cell orientation does not allow to describe the experimental observations, while an energetic approach does. The only case in which the minimal strain direction and the minimal energy direction coincide is precisely when $\Lambda = 1/2$. These observations also allow us to justify the need of choosing an orthotropic constitutive model instead of a purely transversely isotropic one. In fact, the elastic strain energy for a transversely isotropic medium only depends on I_4 and I_5 in addition to the three isotropic invariants, and then only on I_4 when the dependence on $\mathbb{C}^2$ is not considered as done in this Section. However, in such a case

one obtains $\alpha = 1$ and so minimizing a transversely isotropic energy would be equivalent to choosing the minimal strain direction again, which as just discussed does not seem accurate. We also remark that $\Lambda = 1$ corresponds to clamping the specimen, so that $\lambda_y = 1$, while $\Lambda > 1$ corresponds to stretching also along y, still keeping $\lambda_y < \lambda_x$. On the other hand, values of $\Lambda < \frac{1}{2}$ correspond to $\lambda_x - 1 < 1 - \lambda_y$, i.e. compressions along y are stronger than elongations along x, which is not done in experiments reported in the literature.

Finally, we observe the following cases related to isochoric deformations, which will be examined in detail later:

$$\begin{aligned} &\text{If} \quad \lambda_y = \frac{1}{\lambda_x}, \quad \text{then} \quad \Lambda = \frac{\lambda_x}{1+\lambda_x} \in \left[\frac{1}{2}, 1\right); \\ &\text{If} \quad \lambda_y = \frac{1}{\sqrt{\lambda_x}}, \quad \text{then} \quad \Lambda = \frac{\lambda_x + \sqrt{\lambda_x}}{\lambda_x + \sqrt{\lambda_x} + 1} \in \left[\frac{2}{3}, 1\right), \end{aligned} \tag{3.25}$$

with $\Lambda \to 1$ for very large λ_x and the lower extremum of the interval achieved in the limit of no stretching. Of course, for these types of finite deformation, the case $\Lambda > 1$ is unfeasible. In terms of α and Λ, the existence condition for the non-trivial equilibrium (3.18) writes as

$$\frac{1-|\alpha|}{2} \leq \Lambda \leq \frac{1+|\alpha|}{2}.$$

When $\alpha > 0$, the stability conditions (3.20) become

$$\begin{aligned} \theta = 0: &\quad \text{stable} \iff \Lambda < \frac{1-\alpha}{2}, \\ \theta = \frac{\pi}{2}: &\quad \text{stable} \iff \Lambda > \frac{1+\alpha}{2}, \\ \theta = \theta_{eq}: &\quad \text{stable} \iff \Lambda \in \left[\frac{1-\alpha}{2}, \frac{1+\alpha}{2}\right], \end{aligned} \tag{3.26}$$

that is, the non-trivial equilibrium position is stable whenever it exists.

Recalling that $k_{44} > k_{66}$ and focusing for the moment only on the case $\alpha > 0$, there are two relevant sub-cases to discuss, depending on the following relationships between parameters:

i) $k_{46} + \dfrac{k_{88}}{2} < k_{66} \qquad \Longleftrightarrow \qquad \alpha > 1\,, \quad \text{or}$

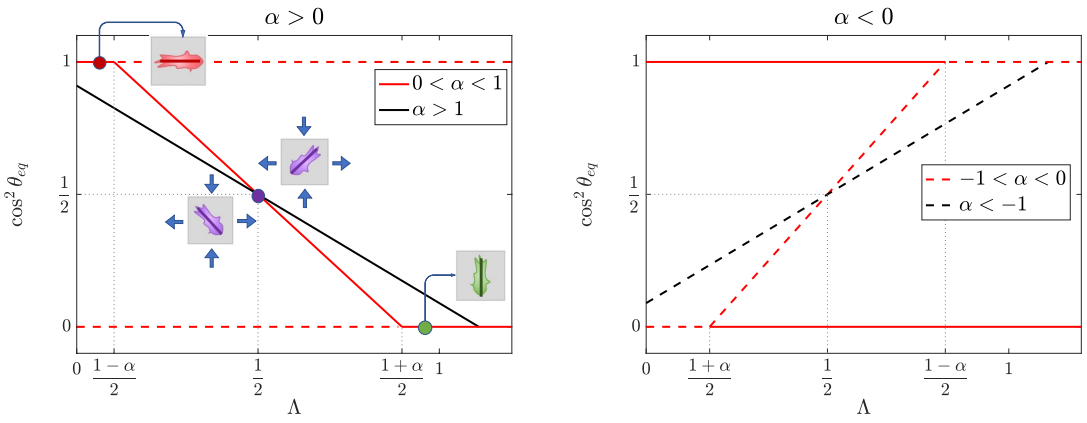

(a) (b)

Fig. 3.2 Bifurcation diagram of equilibrium angles in terms of Λ, defined in Eq. (3.23), with α from Eq. (3.24) positive in (a) and negative in (b). The black lines refer to the case $|\alpha| > 1$ and the red lines to $|\alpha| < 1$, while dashed lines represent unstable configurations and full lines stable ones. In (b) full lines indicating the stability of $\theta = 0$ till the bifurcation point and of $\theta = \pi/2$ for $\alpha < -1$ are not drawn. The area with $\Lambda < 0$ is not shown because of the pulling characteristics of the experiments.

$$\text{ii) } k_{66} < k_{46} + \frac{k_{88}}{2} < \frac{k_{44} + k_{66}}{2} \qquad \Longleftrightarrow \qquad 0 < \alpha < 1.$$

Referring to Fig. 3.2a, in case ii) – represented by red lines – we have two supercritical bifurcation points at

$$\Lambda = \frac{1 \pm \alpha}{2}.$$

The configuration with orientation perpendicular to the stretching direction (i.e., $\theta_{eq} = \pi/2$, $\cos^2 \theta_{eq} = 0$) is stable if $\Lambda > \frac{1+\alpha}{2}$. When Λ is decreased below this value, the preferential axis of the cell tends instead to be oriented obliquely, until it becomes completely aligned to the stretching direction if $\Lambda < \frac{1-\alpha}{2}$. However, in case i), represented by the black line in Fig. 3.2a, this value is negative and so it cannot be physically achieved in the usual experimental set-up. In this situation, cells will never orient themselves parallel to the stretching direction.

In order to compare this behaviour with previous linear elasticity results, since in [226] $\alpha = 0.794 \pm 0.08 < 1$ was found, the situation observed in the experiments by Livne and collaborators seems to correspond to case ii). In addition, the results are coherent with a previous analysis for optimal orientation of orthotropic materials by Pedersen [285, 286], carried out in a linear elastic regime.

The computation done here shows, in particular, that any model of quadratic type (3.15) or of Fung type (3.16) independent of I_5 and I_7 with the following relation among the elastic coefficients:

$$\frac{k_{44}+k_{66}-2k_{46}-k_{88}}{k_{44}-k_{66}} \approx 0.794 \tag{3.27}$$

is able to fit the data on cell orientation in a way that is independent of the magnitude of the applied strain, even outside the range of validity of linear elasticity. This explains why the experimental behaviour shown in [120, 226] seems to be independent or nearly independent of the magnitude of the applied strain.

For the sake of completeness, we also analyse the case in which $\alpha < 0$, which can occur, for instance, if k_{88} is much larger than the other parameters. If this is the case, noticing that $\frac{1+\alpha}{2} < \frac{1-\alpha}{2}$, the stability conditions are the following:

$$\begin{aligned} \theta = 0: &\quad \text{stable} \quad \Longleftrightarrow \quad \Lambda < \frac{1-\alpha}{2}, \\ \theta = \frac{\pi}{2}: &\quad \text{stable} \quad \Longleftrightarrow \quad \Lambda > \frac{1+\alpha}{2}, \\ \theta = \theta_{eq}: &\quad \text{unstable} \qquad \forall \Lambda > 0. \end{aligned} \tag{3.28}$$

More precisely, in this case there are as well two distinct situations to be considered:

$$\text{iii)}\ \frac{k_{44}+k_{66}}{2} < k_{46}+\frac{k_{88}}{2} < k_{44} \quad \Longleftrightarrow \quad -1 < \alpha < 0, \quad \text{or}$$

$$\text{iv)}\ k_{44} < k_{46}+\frac{k_{88}}{2} \quad \Longleftrightarrow \quad \alpha < -1.$$

Referring to Fig. 3.2b, in case iii) – corresponding to red lines – one has two admissible subcritical bifurcation points with coexistence of two critical equilibria if $\Lambda \in \left[\frac{1+\alpha}{2}, \frac{1-\alpha}{2}\right]$, corresponding to the parallel and perpendicular orientation, and only one of them is stable outside this range. In case iv) the equilibrium $\theta = \pi/2$ is always stable while $\theta = 0$ is stable only if $\Lambda < \frac{1-\alpha}{2}$. In all cases, if $\alpha < 0$ the oblique orientation is unstable.

A detailed analytical characterisation of the bifurcations presented so far will be carried out in Section 3.3. We conclude this Section by making a remark concerning the global or local character of the energy extrema that we found through the stability analysis. Clearly, the oblique equilibrium angle corresponds to a global extremum, whenever it exists. In particular, it is a global minimum for $\alpha > 0$ and a global maximum for $\alpha < 0$. It is however more interesting to evaluate the behaviour of the trivial extrema, i.e. $\theta = 0$ and $\theta = \pi/2$.

In particular, for an energy in the form (3.21), we have

$$\mathcal{W}(\theta=0)-\mathcal{W}(\theta=\pi/2)=\frac{1}{2}(k_{44}-k_{66})\left[\lambda_x^2-\lambda_y^2-2(\lambda_x-\lambda_y)\right], \tag{3.29}$$

which is positive if and only if $\Lambda>1/2$. Therefore, for $\alpha>0$, we have the following cases:

- $\dfrac{1-\alpha}{2}<\Lambda<\dfrac{1}{2} \quad\Longrightarrow\quad \theta=0$ local max , $\quad \theta=\dfrac{\pi}{2}$ global max,
- $\dfrac{1}{2}<\Lambda<\dfrac{1+\alpha}{2} \quad\Longrightarrow\quad \theta=0$ global max , $\quad \theta=\dfrac{\pi}{2}$ local max.

The situation is reversed if $\alpha<0$, namely,

- $\dfrac{1+\alpha}{2}<\Lambda<\dfrac{1}{2} \quad\Longrightarrow\quad \theta=0$ global min , $\quad \theta=\dfrac{\pi}{2}$ local min,
- $\dfrac{1}{2}<\Lambda<\dfrac{1-\alpha}{2} \quad\Longrightarrow\quad \theta=0$ local min , $\quad \theta=\dfrac{\pi}{2}$ global min.

Influence of I_5 and I_7

We now analyse the modification that is introduced if a dependence of the energy on the invariants involving $\mathbb{C}^2$, that is, I_5 and I_7, is allowed. The presence of these invariants was neglected so far, but it is interesting to study how they affect the oblique angle given by Eq. (3.22). For this purpose, it is convenient to rewrite

$$\Sigma_1=k_{44}-2k_{46}+k_{66}+A_1\,,$$

with

$$A_1:=2(k_{45}-k_{47}-k_{56}+k_{67})(\lambda_x+\lambda_y)+(k_{55}-2k_{57}+k_{77})(\lambda_x+\lambda_y)^2\,,$$

and

$$\Sigma_2=(k_{44}-k_{46}+A_2)(\lambda_x-\lambda_y)-(k_{44}-k_{66}+B_2)(\lambda_x-1)\,,$$

where

$$A_2 := [k_{55}(\lambda_y+1) - k_{47} - k_{56} - k_{57}(\lambda_x+\lambda_y)](\lambda_x+\lambda_y) + k_{45}(\lambda_x+2\lambda_y+1) - \frac{k_{47}-k_{56}}{2}(\lambda_x-1),$$

$$B_2 := [k_{55}(\lambda_y+1) - k_{77}(\lambda_x+1)](\lambda_x+\lambda_y) + k_{45}(\lambda_x+2\lambda_y+1) - k_{67}(2\lambda_x+\lambda_y+1) - (k_{47}-k_{56})\left(\lambda_x - 1 - \frac{\lambda_x-\lambda_y}{2}\right).$$

After some computation, we can explicit the nontrivial equilibrium (3.17) as

$$\begin{aligned}\cos^2\theta_{eq} &= \frac{k_{44}-k_{46}-\frac{k_{88}}{2}+A_2-(k_{44}-k_{66}+B_2)\Lambda}{k_{44}+k_{66}-2k_{46}-k_{88}+A_1} \\ &= \frac{1}{2} + \frac{k_{44}-k_{66}}{k_{44}+k_{66}-2k_{46}-k_{88}+A_1}\left(\frac{1}{2}-\Lambda\right) - \frac{\frac{A_1}{2}-A_2+B_2\Lambda}{k_{44}+k_{66}-2k_{46}-k_{88}+A_1} \\ &= \frac{1}{2} + \alpha_1(\Lambda)\left(\frac{1}{2}-\Lambda\right) + \alpha_2(\Lambda), \end{aligned} \tag{3.30}$$

where we defined for the sake of conciseness

$$\alpha_1(\Lambda) := \frac{k_{44}-k_{66}}{k_{44}+k_{66}-2k_{46}-k_{88}+A_1}, \tag{3.31}$$

$$\alpha_2(\Lambda) := -\frac{\frac{A_1}{2}-A_2+B_2\Lambda}{k_{44}+k_{66}-2k_{46}-k_{88}+A_1}. \tag{3.32}$$

We notice that Eq. (3.30) represents a generalisation of the oblique angle expression (3.22), with the terms A_1, A_2 and B_2 representing the corrections related to the presence of $\mathbb{C}^2$-dependent terms through the invariants I_5 and I_7. Indeed, when the elastic energy does not include their contribution, we recover Eq. (3.22), i.e. the linear relationship between $\cos^2\theta$ and Λ discussed previously. However, since the correction coefficients depend on λ_x and λ_y and therefore on Λ, Eq. (3.30) does not represent a straight line any longer in the parameter space $(\Lambda, \cos^2\theta_{eq})$.

An additional remark concerns the behaviour of Eq. (3.30) in the limit of small deformations. In this case, the zero-th order approximations of the correction coefficients

become

$$A_1(\Lambda) \approx \widetilde{A}_1 := 4(k_{45} + k_{55} - k_{47} - k_{56} + k_{67} - 2k_{57} + k_{77}),$$

$$A_2(\Lambda) \approx \widetilde{A}_2 := 2(2k_{45} + 2k_{55} - k_{47} - k_{56} - 2k_{57}),$$

$$B_2(\Lambda) \approx \widetilde{B}_2 := 4(k_{45} + k_{55} - k_{67} - k_{77}),$$

with $\widetilde{A}_1, \widetilde{A}_2, \widetilde{B}_2$ constants. As a consequence, if we substitute in Eq. (3.30) and rearrange the terms, we find that the approximating curve is again a straight line:

$$\cos^2\theta_{eq} \approx \frac{1}{2} + \frac{k_{44} - k_{66} + \widetilde{B}_2}{k_{44} + k_{66} - 2k_{46} - k_{88} + \widetilde{A}_1}\left(\frac{1}{2} - \Lambda\right), \tag{3.33}$$

which still has the property that $\theta_{eq} = \pi/4$ when $\Lambda = 1/2$. Hence, in the small deformation limit, we are able to find a relation that is akin to the one derived in the previous Subsection. In fact, Eq. (3.33) can be rewritten in the same form as (3.22) by making the following formal substitutions:

$$\begin{cases} k_{44} & \longrightarrow & K_{\parallel} := k_{44} + 4k_{45} + 4k_{55}, & (3.34) \\ k_{66} & \longrightarrow & K_{\perp} := k_{66} + 4k_{67} + 4k_{77}, & (3.35) \\ k_{46} & \longrightarrow & K_{\parallel\perp} := k_{46} + 2k_{47} + 2k_{56} + 4k_{57}, & (3.36) \\ k_{88} & \longrightarrow & K_s := k_{88}, & (3.37) \end{cases}$$

which lead us to

$$\cos^2\theta_{eq} = \frac{1}{2} + \frac{K_{\parallel} - K_{\perp}}{K_{\parallel} + K_{\perp} - 2K_{\parallel\perp} - K_s}\left(\frac{1}{2} - \Lambda\right). \tag{3.38}$$

The formal analogy of Eq. (3.38) and Eq. (3.22) is evident: the only difference from the case discussed previously lies in the fact that more coefficients contribute to the identification of the line slope. In other words, given the experimental data about the angle and the deformation, it is impossible to distinguish which coefficients of the energy defined by (3.15) contribute to the slope of the line. This is coherent with the inherent nonlinearity of the corrections introduced by the invariants related to $\mathbb{C}^2$. Indeed, for small deformations, the contribution to the energy of I_4 is indistinguishable from that of I_5. Likewise, the dependence on I_6 merges with the one on I_7, as it is evident from the re-definition of the coefficients provided by Eqs. (3.34)–(3.37).

We now turn the attention to the fitting of experimental data, to investigate whether the introduction of the nonlinear contributions may give an improvement in the prediction of preferential orientations. To evaluate the influence of $\mathbb{C}^2$-corrections, we change one parameter at a time while keeping the slope of the straight line in Eq. (3.33) constant, in order to start from the same linear dependence. For instance, when $k_{55} > 0$, then, recalling Eq. (3.34), k_{44} is decreased accordingly, so that the value of $K_{\|}$ is maintained constant. In particular, with this idea in mind, we fix the coefficients to representative values of $K_{\|} = 0.4\,, K_{\|\perp} = 0.1\,, K_{\perp} = 0.1$ and $K_s = 0.0618$ in order to match the experimental fitting value for the slope reported in Eq. (3.27).

First of all, we focus on the effect of a non-vanishing k_{55}, keeping all the other coefficients with indices 5 and 7 equal to zero. The results are reported in Fig. 3.3. As already stated above, to keep the same value of $K_{\|}$ and therefore the same linear limit given by (3.33), as we vary k_{55} we accordingly change $k_{44} = K_{\|} - 4k_{55}$. To observe how the non-trivial equilibrium is changed, we focus on the three types of deformation defined at the beginning of the Section. One can observe that, in all cases, increasing k_{55} leads to a deviation of the curve defining the equilibrium angles from the straight line limit. In addition, keeping λ_y fixed and changing Λ as in Fig. 3.3a, one can appreciate a decrease in the value of $\cos^2\theta_{eq}$, which means an increase in the equilibrium angle, for $\Lambda = 1/2$.

If we consider a deformation such that $\lambda_x\lambda_y = 1$, as in Fig. 3.3b, recalling Eq. (3.25) the admissible values of Λ range between $1/2$ and 1. Specifically, we have that θ_{eq} stays fixed at $\pi/4$ if $\Lambda = 1/2$. In fact, in the latter case $A_1 = A_2 = B_2 = 4k_{55}$ and the numerator of the last term in Eq. (3.30) vanishes for $\Lambda = 1/2$. Instead, when $\Lambda \to 1$, then $\alpha_1(\Lambda) \to 0$, whereas $\alpha_2(\Lambda) \to 1/2$, since all the coefficients except k_{55} are null. Thus, the curve given by Eq. (3.30) tends to 0 when $\Lambda \to 1$, even though such effect is not evident from the Figures since the curve becomes negative and a bifurcation between the perpendicular and oblique orientation happens.

Finally, in the third deformation case $\lambda_y = 1/\sqrt{\lambda_x}$ shown in Fig. 3.3c, we have a minimal possible value of $\Lambda = 2/3$, corresponding to an equilibrium angle such that $\cos^2\theta_{eq} = 0.29$, i.e., $\theta_{eq} \approx 57°$, that is reported in some discussions of experiments (see, for instance, [375, 376]).

As regards the bifurcation point between the perpendicular equilibrium branch $\theta = \pi/2$ and the oblique one given by Eq. (3.30), it is implicitly defined by the value Λ_b such that

$$\Lambda_b = \frac{k_{44} - k_{46} - \frac{k_{88}}{2} + A_2}{k_{44} - k_{66} + B_2}, \tag{3.39}$$

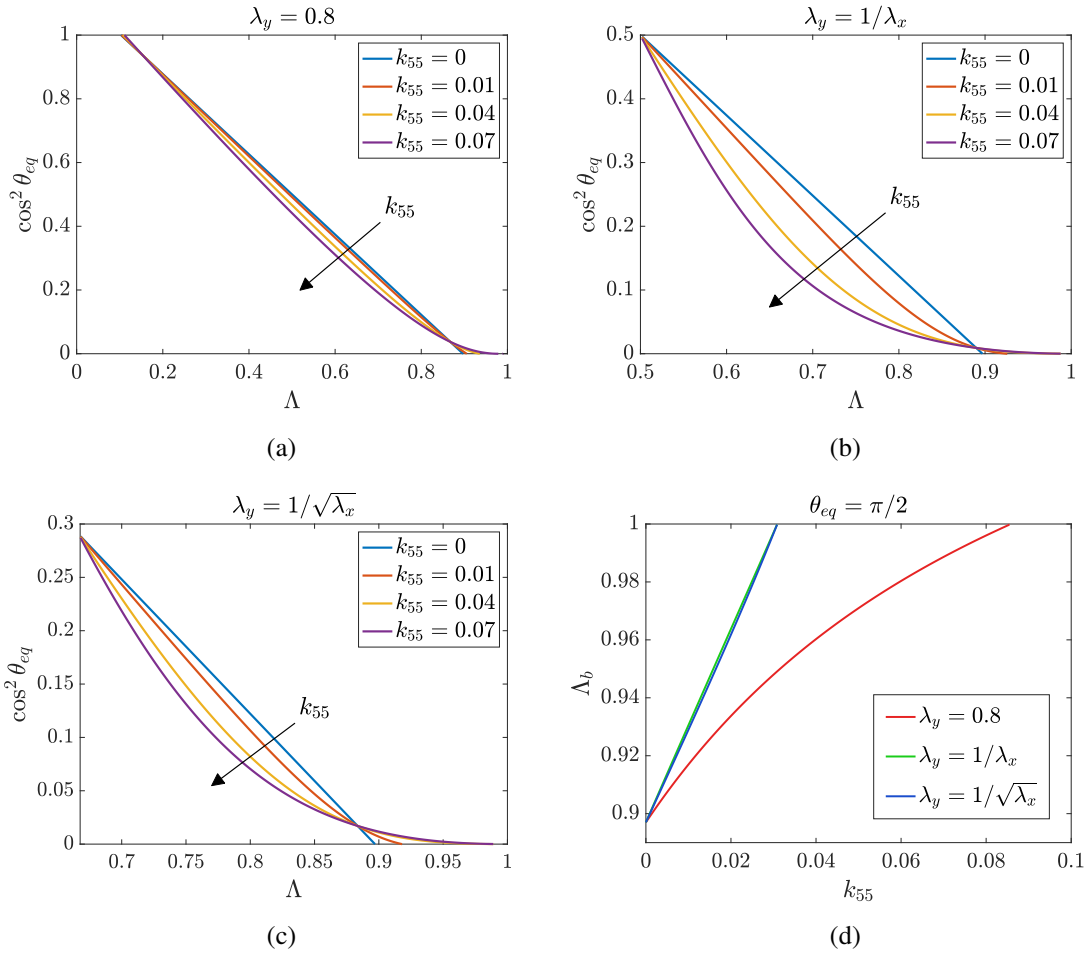

Fig. 3.3 Analysis of non-trivial equilibrium position for $k_{55} \neq 0$ and $k_{44} = 0.4 - 4k_{55}$ to keep the same linear limit. The other non-vanishing parameters are $k_{66} = k_{46} = 0.1$, and $k_{88} = 0.0618$. In (a) $\lambda_y = 0.8$ while in (b) $\lambda_y = 1/\lambda_x$ and in (c) $\lambda_y = 1/\sqrt{\lambda_x}$. For all the three types of deformation, we see that the presence of k_{55} leads to a departure from the linear relation between $\cos^2\theta_{eq}$ and Λ. In (d) the bifurcation point Λ_b for which $\theta_{eq} = \pi/2$ is shown as a function of k_{55}: the plot highlights that, for sufficiently high values of k_{55} (for instance $k_{55} > 0.086$ for $\lambda_y = 0.8$, and $k_{55} > k_{88}/2 \approx 0.03$ for the other two deformations), the bifurcation point disappears, since values of $\Lambda_b > 1$ are not admissible for the deformations we consider.

since the coefficients A_2 and B_2 also depend on Λ_b itself. Therefore, while we have seen that the energy dependence on I_4, I_6 and I_8 does not modify the bifurcation obtained in the linearised theory, introducing the invariants related to $\mathbb{C}^2$ entails an identifiable shift of the bifurcation point between the perpendicular orientation and the oblique one that may also disappear for large values of k_{55}, as shown in Fig. 3.3d. Since we are considering $k_{55} \neq 0$, the shift of the bifurcation point for $\theta = \pi/2$ can be evaluated through Eq. (3.39), which

becomes

$$\Lambda_b = \frac{k_{44} - k_{46} - \frac{k_{88}}{2} + k_{55}(1+\lambda_y)(\lambda_x+\lambda_y)}{k_{44} - k_{66} + k_{55}(1+\lambda_y)(\lambda_x+\lambda_y)}\,. \tag{3.40}$$

Thus, if all the coefficients but k_{55} are prescribed, Eq. (3.40) implicitly defines Λ_b in terms of k_{55} that, actually, can be made explicit by writing

$$k_{55} = \frac{(k_{44} - k_{66})\Lambda_b - k_{44} + k_{46} + \frac{k_{88}}{2}}{(1-\Lambda_b)(1+\lambda_y)(\lambda_x+\lambda_y)}\,. \tag{3.41}$$

In Eq. (3.40), the term $(1+\lambda_y)(\lambda_x+\lambda_y)$ is a function of Λ_b, given, for instance, by

$$(1+\lambda_y)(\lambda_x+\lambda_y) = \frac{1 - 2\Lambda_b + 2\Lambda_b^2}{\Lambda_b^2(1-\Lambda_b)} \qquad \text{if } \lambda_x\lambda_y = 1\,, \tag{3.42}$$

and by

$$(1+\lambda_y)(\lambda_x+\lambda_y) = (1+\bar{\lambda}_y)\frac{1+\bar{\lambda}_y - 2\bar{\lambda}_y\Lambda_b}{1-\Lambda_b} \qquad \text{for fixed } \lambda_y = \bar{\lambda}_y. \tag{3.43}$$

If $\lambda_y = 1/\sqrt{\lambda_x}$ we have that

$$1 - \Lambda_b = \frac{1}{\lambda_x + \sqrt{\lambda_x} + 1}$$

which corresponds to

$$\lambda_x = \left(-\frac{1}{2} + \frac{1}{2}\sqrt{\frac{4}{1-\Lambda_b} - 3}\right)^2.$$

These relations can be employed to plot the variation of the bifurcation point Λ_b as a function of the parameter k_{55}, as done in Fig. 3.3d. Such a point clearly approaches 1 for increasing values of k_{55} for all the types of deformation considered, eventually leading to a disappearance of the bifurcation, since $\Lambda_b > 1$ lies outside the admissible values of Λ. More specifically, if $\lambda = \bar{\lambda}_y$, for

$$k_{55} > \frac{k_{46} - k_{66} + \frac{k_{88}}{2}}{1 - \bar{\lambda}_y^2}$$

the branches relative to the oblique equilibrium and $\theta = \pi/2$ do not cross for physically admissible values of Λ and therefore the perpendicular orientation is always unstable. For the value of $\bar{\lambda}_y = 0.8$ that we consider as reference, the critical value amounts at $k_{55} \approx 0.086$. Differently, for the other two deformation modes, the threshold value of k_{55}

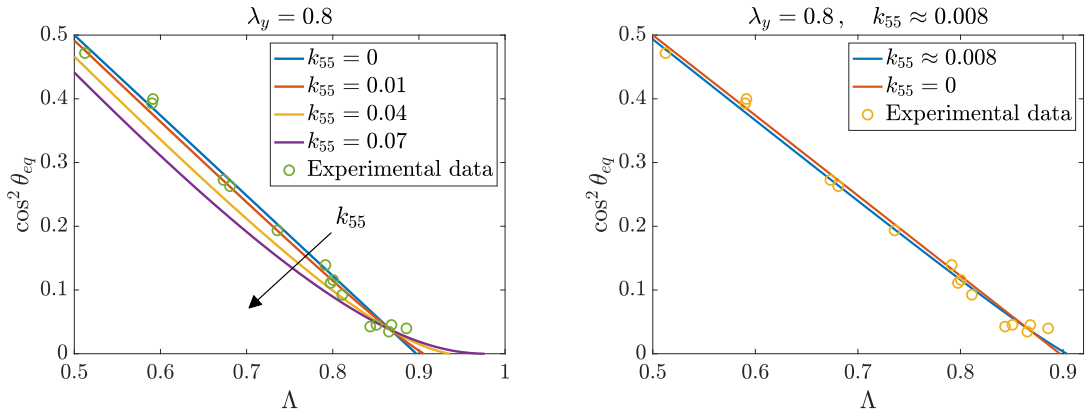

Fig. 3.4 Nonlinear fitting of experimental data with $k_{55} \neq 0$. Data from [226] are compared with the family of curves obtained for $\lambda_y = 0.8$ and different values of k_{55} in (a) and with the best fitting value $k_{55} = 0.008$ in (b).

above which the bifurcation disappears is the same and amounts to

$$k_{55} = k_{46} - k_{66} + \frac{k_{88}}{2}\,.$$

This can be derived immediately from Eqs. (3.41) and (3.42) for $\lambda_y = 1/\lambda_x$, while in the case $\lambda_y = 1/\sqrt{\lambda_x}$ it is enough to observe that

$$\begin{aligned}(1-\Lambda_b)(1+\lambda_y)(\lambda_x+\lambda_y) &= (1-\Lambda_b)\left(1+\frac{1}{\sqrt{\lambda_x}}\right)\left(\lambda_x+\frac{1}{\sqrt{\lambda_x}}\right)\\ &= 1+\frac{1}{\lambda_x}-2\,(1-\Lambda_b)\,. \end{aligned} \tag{3.44}$$

Substituting into (3.41) and recalling that $\Lambda_b \to 1$ means $\lambda_x \to +\infty$ immediately leads to $k_{55} = k_{46} - k_{66} + k_{88}/2$, coherently with Fig. 3.3d.

In order to evaluate the relevance of the nonlinear correction due to k_{55}, we performed a fitting of experimental data extracted from [226] where, using a biaxial experiment, the stretches in the two directions are controlled. Although the precise value of λ_y is not given, we fix it to be $\lambda_y = 0.8$, taking into account that $\lambda_y = 1$ would correspond to $\Lambda = 1$ identically. Thus, in Fig. 3.4, we explored the possibility of an improvement in the fitting using nonlinear elasticity and $\mathbb{C}^2$-related terms. Actually, as already observed, the straight line passing through $(1/2, 1/2)$ with slope determined by the inverse of (3.27) already provides a very good and robust fitting. However, by using a nonlinear regression

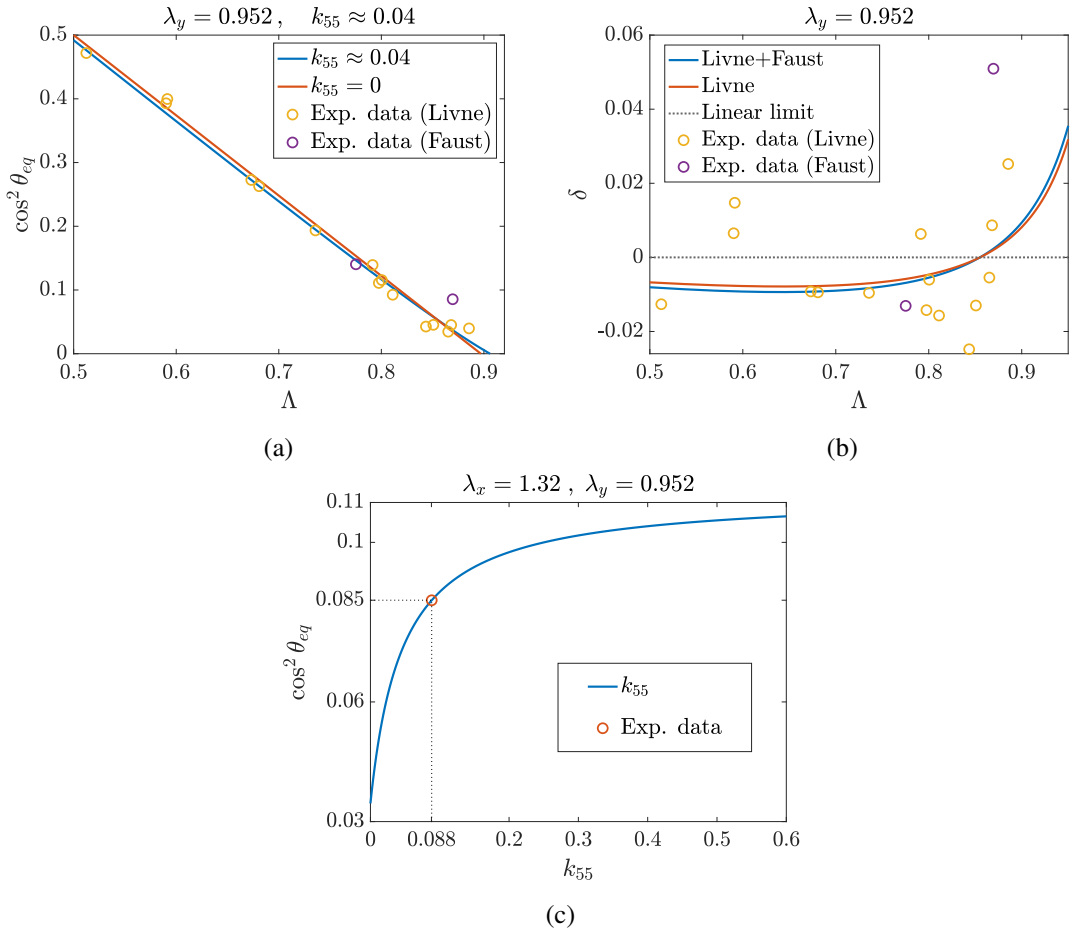

Fig. 3.5 Nonlinear fitting of experimental data taken from [120] and [226]. (a): Best fitting for $\lambda_y = 0.952$ obtained for $k_{55} \approx 0.04$. (b): Deviation δ from the straight line approximation when fitting all data (blue curve) and only data from [226] for a fixed $\lambda_y = 0.952$ (red curve; in this case, the best $k_{55} \approx 0.03$). (c): Equilibrium orientation as a function of k_{55} for $\lambda_x = 1.32$ and $\lambda_y = 0.952$, related to experimental actin orientations obtained by Faust et al. [120] (represented by the circle). As shown, a value of $k_{55} = 0.088$ is able to capture the experimental orientation precisely.

estimation, we are able to find that a small value of $k_{55} = 0.008$ slightly improves the fitting for data extracted by [226]. We also find that, if we increase the fixed value of λ_y, a higher value of the coefficient k_{55} is needed to fit the data. For instance, when we take $\lambda_y = 0.98$, the best fitting value amounts at $k_{55} = 0.08$, which is an order of magnitude greater than the one obtained when $\lambda_y = 0.8$. To explain this fact we notice that, when $\lambda_y \approx 1$, a small stretch λ_x in the x-direction is sufficient to span all the admissible values of Λ. Consequently, nonlinear effects become less relevant and to fit the nonlinear model we need to take very high values of the related coefficients.

In Fig. 3.5 we present the fitting using also the data by Faust et al. [120]. Specifically, considering the experimental settings with $\lambda_x = 1.32$, one finds a value of $\lambda_y = 0.952$, since $\Lambda \approx 0.87$. As a first attempt, we tried to fit the data from [120, 226] simultaneously, to assess whether a nonlinear correction could better explain the experimental observations in different settings. The results are shown in Fig. 3.5a and suggest that a value of $k_{55} = 0.04$ provides a slightly better fitting than the straight line approximation. Instead, a nonlinear regression performed only on the dataset by Livne [226] returns a value of $k_{55} = 0.03$ for the same λ_y. To highlight this difference, in Fig. 3.5b we plot the deviation δ from the linear approximation, that is,

$$\delta(\Lambda) := \cos^2\theta_{eq}(\Lambda) - \left[\frac{1}{2} + \frac{k_{44} - k_{66}}{k_{44} + k_{66} - 2k_{46} - k_{88}}\left(\frac{1}{2} - \Lambda\right)\right], \tag{3.45}$$

as a function of Λ. Clearly, if $\delta = 0$, then the squared cosine of the experimental angle is exactly given by the linear relation and no correction is needed. However, since the majority of experimental data falls below the horizontal line $\delta = 0$, the introduction of k_{55} makes the curve convex and is able to provide an overall better approximation of the observed behaviour, even if the difference is of the order of 10^{-2}. As a final comparison, we chose one of the experimental actin angle values obtained in [120] while fixing λ_x and λ_y to have the same value of Λ used in the experiment. After that, we looked for a value of k_{55} able to capture the experimental point using the nonlinear Eq. (3.30): as shown in Fig. 3.5c, choosing $k_{55} = 0.088$ precisely fits the orientation angle for such a fixed deformation.

We conclude our analysis about the role of k_{55} by making a comparison with the transversely isotropic case, which we already discussed as inadequate to fit the experimental data for an energy in the form given by Eq. (3.15). This is confirmed by the curves reported in Fig. 3.6. Indeed, if we consider a transversely isotropic energy that depends only on five invariants, recalling (3.30) we get:

$$\cos^2\theta_{eq} = \frac{k_{44} + k_{55}(\lambda_y + 1)(\lambda_x + \lambda_y) + k_{45}(\lambda_x + 2\lambda_y + 1)}{k_{44} + 2k_{45}(\lambda_x + \lambda_y) + k_{55}(\lambda_x + \lambda_y)^2}(1 - \Lambda). \tag{3.46}$$

In Fig. 3.6a we plot the relationship (3.46) for different values of k_{55} and $k_{45} = 0$, while in Fig. 3.6b the case $k_{45} \neq 0$ is shown. It is clearly observed that, in both cases, the transversely isotropic model provides a fitting which is not satisfactory compared to the orthotropic one reported in Fig. 3.4. To have a better insight, in Fig. 3.6c we show a direct

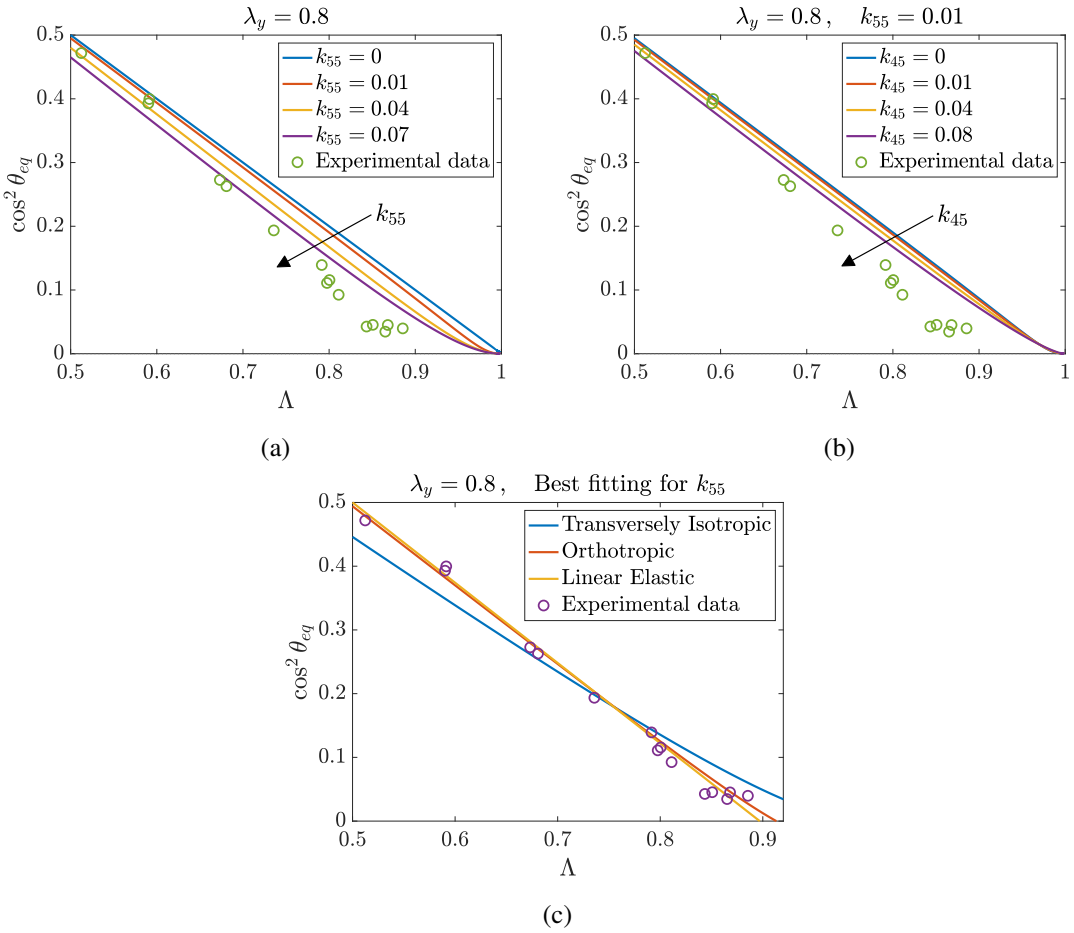

Fig. 3.6 Nonlinear fitting of experimental data from [226] with a transversely isotropic model, in the case $\lambda_y = 0.8$. In (a) the family of curves obtained from Eq. (3.46) for different values of k_{55} is shown, while in (b) the effect of k_{45} is investigated. In (c) a direct comparison between the best fitting curves for the transversely isotropic and orthotropic case is provided, showing that the latter is more accurate.

comparison between the best fitting curves in the transversely isotropic and orthotropic case: in the latter, there is a significant improvement in the fitting of experimental data.

We turn now the attention to the effect of a non-vanishing k_{77}, keeping $K_\perp$ fixed, and perform a similar reasoning as we did for k_{55}. Again, as shown in Fig. 3.7b, if $\lambda_x\lambda_y = 1$ then $\theta = \pi/4$ when $\Lambda = 1/2$ for any value of k_{77}. In fact, in this case, $A_1 = 4k_{77}$ and $B_2 = -4k_{77}$, while $A_2 = 0$ and therefore $\alpha_2(\Lambda) = 0$. This is not the case if λ_y is kept fixed, as shown in Fig. 3.7a where it is clear that the value of $\cos^2\theta_{eq}$ corresponding to $\Lambda = 1/2$ slightly increases for increasing values of k_{77}. A more noticeable effect occurs if $k_{77} \neq 0$ when $\Lambda \to 1$: the results are reported in Figs. 3.7b–3.7c. Indeed, in this situation we have that $\alpha_1(\Lambda) \to 0$ but $\alpha_2(\Lambda) \to -1/2$. As a consequence, the curve in Eq. (3.30) tends

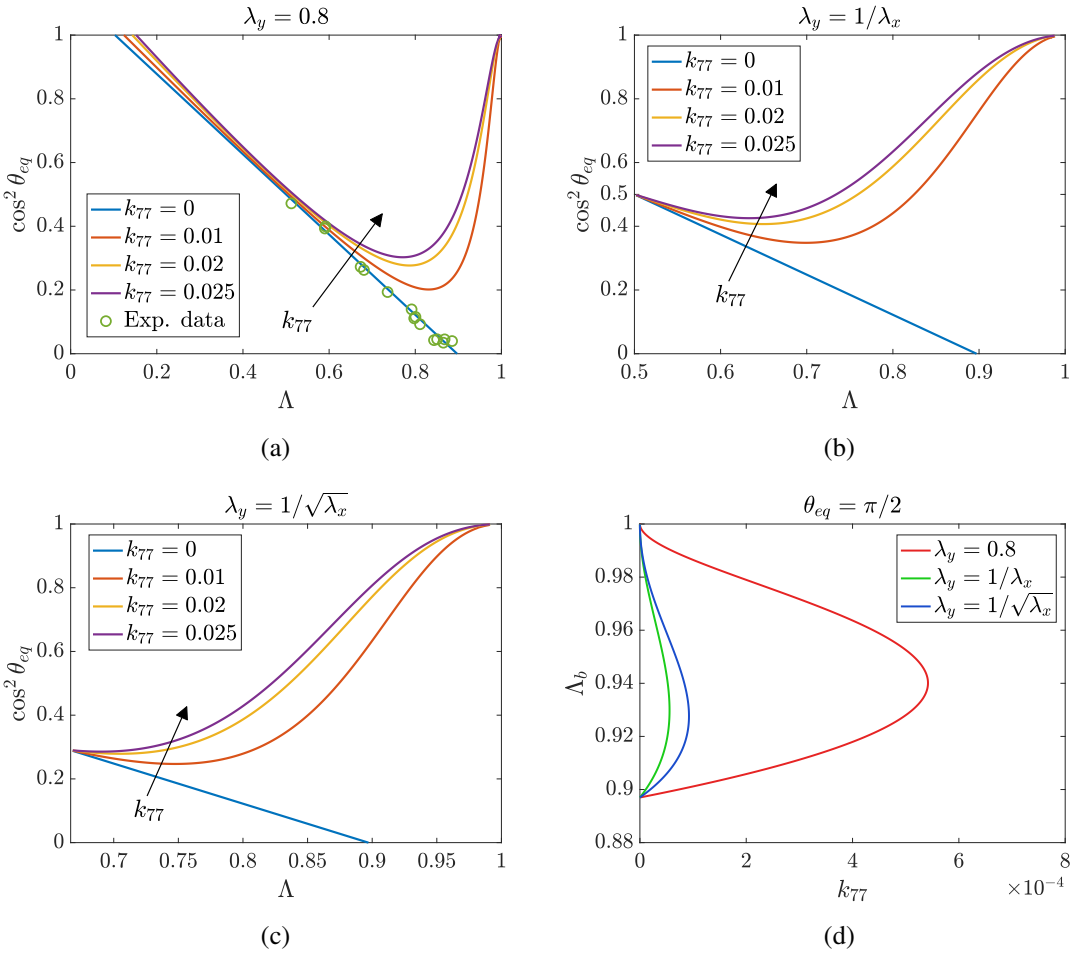

Fig. 3.7 Analysis of non-trivial equilibrium position for $k_{77} \neq 0$ and $k_{66} = 0.1 - 4k_{77}$ to keep the same linear limit. The other non-vanishing parameters are $k_{44} = 0.4$, $k_{46} = 0.1$, and $k_{88} = 0.0618$. In (a) $\lambda_y = 0.8$, while in (b) $\lambda_y = 1/\lambda_x$ and in (c) $\lambda_y = 1/\sqrt{\lambda_x}$. For all the three types of deformation, one can see that introducing k_{77} provokes a significant difference from the linear behaviour which is not observed in experiments, suggesting that such a parameter is not present in the constitutive model. In (d) the bifurcation points Λ_b for which $\theta_{eq} = \pi/2$ are shown as a function of k_{77}. The region enclosed by the curve identifies the values of Λ for which $\theta_{eq} = \pi/2$ is stable. For sufficiently high values of k_{77} the bifurcation points disappears and the configuration $\theta_{eq} = \pi/2$ is always unstable.

to 1 when $\Lambda \to 1$. Moreover, there are two bifurcation values between the equilibrium configuration $\theta_{eq} = \pi/2$ and the oblique one, given by the implicit relationship

$$\Lambda_b = \frac{k_{44} - k_{46} - \frac{k_{88}}{2}}{k_{44} - k_{66} - k_{77}(\lambda_x + 1)(\lambda_x + \lambda_y)}, \tag{3.47}$$

which for instance in the case $\lambda_x\lambda_y = 1$ can be specialised as

$$k_{77} = \frac{\left[(k_{44} - k_{66})\Lambda_b - k_{44} + k_{46} + \frac{k_{88}}{2}\right](1-\Lambda_b)^2}{2\Lambda_b^2 - 2\Lambda_b + 1}. \tag{3.48}$$

As reported in Fig. 3.7d, the two bifurcation points disappear for very small values of k_{77} and the branch represented in Fig. 3.7 is always stable. This does not seem to correspond to what is observed in experiments, suggesting that $k_{77} = 0$ or that it must have a very small value in the constitutive model.

Finally, we discuss the effect of coupling terms other than k_{46}, which was already present in the analysis carried out above since it is related to $\mathbb{C}$. Having ruled out the importance of k_{77}, we do not evaluate the impact of other coefficients related to I_7, namely k_{47}, k_{57} and k_{67}, and we focus instead on the mixing parameter k_{45}. The results of its introduction in the model are shown in Fig. 3.8. In particular, we fixed a value of $k_{55} = 0.01$ and plotted the equilibrium angle as a function of Λ for the three different deformations considered. We observe an effect on the equilibrium curve similar to the one encountered increasing k_{55}. The deviation from the straight line is slighter if $\lambda_y = 0.8$, and greater in the other two cases. Referring to Fig. 3.8d, the bifurcation point Λ_b moves towards 1 as k_{45} is increased, finally disappearing for high values of this parameter. As a last observation, comparing the theoretical results with experimental data shown in Fig. 3.8a, it does not seem that the introduction of the mixing term k_{45} is relevant for a better fit, as confirmed by nonlinear regression.

3.1.5 Discussion

In this Section, we have used theoretical tools of anisotropic hyperelasticity to investigate the problem of cell orientation on a planar substrate undergoing a deformation. We employed therefore an energetic approach, which in previous studies was shown to be effective [226], to characterise the preferential angles for stress fibre alignment. Assuming that the system behaves as an orthotropic elastic continuum, our goal was to determine the minima of the elastic energy stored in the system, corresponding to stable orientation angles for the cell. Moreover, we focused on constitutive models pertaining to nonlinear elasticity, in order to analyse the effects of large deformations on the reorientation process.

As a starting point, we have formulated the problem using the very general theory of coaxiality proposed by Vianello and coworkers [313, 319, 370]. In this way, in Eq. (3.11)

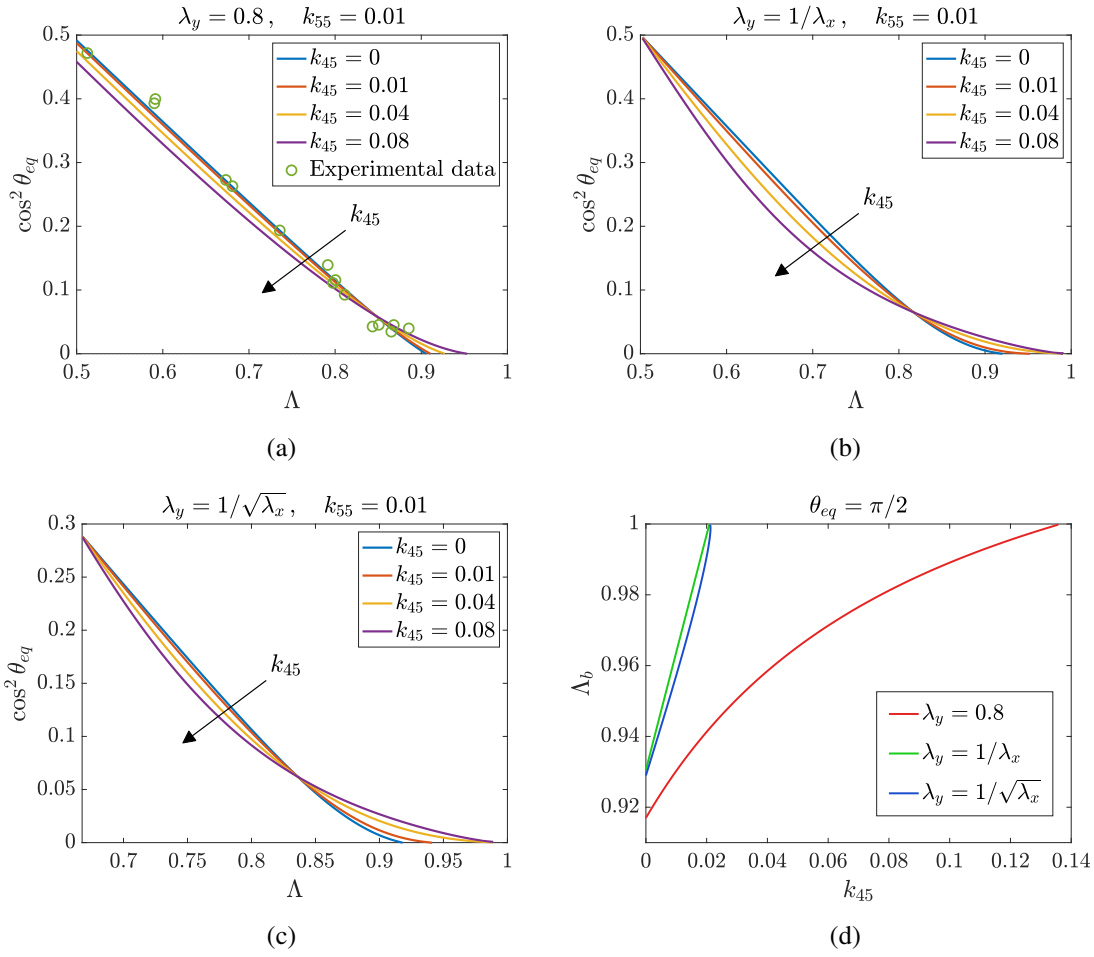

Fig. 3.8 Analysis of non-trivial equilibrium position for $k_{45} \neq 0$, considering $k_{55} = 0.1$ and $k_{44} = 0.4 - 4k_{55} - 4k_{45}$ to keep the same linear limit. The other non-vanishing parameters are $k_{46} = 0.1$ and $k_{88} = 0.0618$. In (a) we set $\lambda_y = 0.8$, while in (b) $\lambda_y = 1/\lambda_x$ and in (c) $\lambda_y = 1/\sqrt{\lambda_x}$. Moreover, in (a) we reported the experimental data obtained in [226]: the introduction of the mixing parameter k_{45} does not improve significantly the fitting of such data. In (d) the bifurcation point Λ_b for which $\theta_{eq} = \pi/2$ is shown as a function of k_{45}, when $k_{55} = 0.01$ is kept fixed. For all the types of deformation considered, the bifurcation disappears when k_{45} crosses a critical value, which is the same for $\lambda_y = 1/\lambda_x$ and $\lambda_y = 1/\sqrt{\lambda_x}$.

we are able to provide a condition which identifies the rotations that make the energy critical. Such a condition will be derived again in Section 3.2 using a slightly different framework and is also coherent with a one derived for transversely isotropic materials in [72].

Then, to allow a more direct comparison with experimental data and simplify the stability analysis, we chose to work with a class of energies that is widely used in biomechanical applications. Firstly, we considered an elastic energy independent of the invariants I_5 and

I_7, related to the square of the right Cauchy-Green strain tensor. In this setting, we found that a linear relation exists between $\cos^2\theta_{eq}$, where θ_{eq} is the preferential angle, and a deformation parameter Λ, defined in Eq. (3.23). A relation of this form was already found by Livne et al. [226] in a linear elastic framework, showing a very good agreement with experimental data, recalling Fig. 2.17. Therefore, our model suggests that the results obtained with linear elasticity extend their validity also in the nonlinear regime, for a wide class of orthotropic energies. This might be an explanation of why experimental results obtained with large stretch amplitudes are still well described by a linearised theory. In summary, we demonstrated that any quadratic-like or Fung-type constitutive model independent of the invariants involving $\mathbb{C}^2$ can fit the experimental data, provided that the energy coefficients satisfy the condition (3.27). The only difference from the theoretical point of view is that, using finite elasticity, one has more coefficients contributing to the slope of the straight line. For what concerns the bifurcations, we also showed that variations of Λ may be associated with changes of preferential orientations from oblique to perpendicular or parallel. In particular, for $\Lambda > (1+\alpha)/2 \approx 0.897$ the only stable orientation is the perpendicular one, which is very often seen in experimental assays.

Next, we introduced the corrections due to $\mathbb{C}^2$ and analysed their influence. It is found that the presence of the invariant I_5 has an effect which is still compatible with experimental data, for small values of the pertaining coefficient k_{55} and for all the three types of deformation considered. In this case, however, the dependence discussed above is no longer linear and the effect due to finite elasticity comes out clearly. This allows us to speculate that there might be a weak nonlinear impact in the phenomenon, since the introduction of k_{55} provided a slightly better fit to experimental data. On the contrary, we showed that a dependence of the strain energy on the invariant I_7 yields results that look incompatible with experiments. Finally, we showed that the influence of a mixing parameter related to $\mathbb{C}^2$ like k_{45}, which couples the effect of the invariants I_4 and I_5, is negligible and does not provide a consistent improvement of the fitting.

In summary, we have provided a characterisation of the preferential orientations of cells on a substrate by looking for the critical points of the system's elastic energy as a function of the alignment angle. Our results suggest that intrinsically nonlinear effects do not play a fundamental role in identifying the alignment of the cytoskeleton, even though further experimental confirmation is needed. The identification of cell orientation angles as a function of the deformation may be important to understand how cells respond to mechanical stimuli and to take advantage of such orientation in applications like tissue engineering. However, the theoretical foundations of the model and the procedure for

energy minimization are very general and might also be of interest in other circumstances, like the optimization of fibre orientation in elastic composites.

In what follows, we will extend this framework to account for two additional relevant points: the dynamic remodelling of the cytoskeleton, discussed in Section 3.2, and the introduction of viscous effects, for which a model is proposed in Section 3.3.

3.2 Cytoskeletal Alignment as a Fibre Reorientation Problem

The energetic approach presented in the previous Section can be effectively applied to the deduction of cell preferential orientations, given a certain deformation of the elastic substrate. However, as pointed out in Chapter 2, the reorientation of a cell subsequent to the mechanical prompt involves a reorganisation of the cytoskeletal architecture and microstructure in a dynamic way. Therefore, the change in the cell internal structure and in the alignment of the cytoskeletal fibres can be regarded as a *remodelling* problem. In fact, the reorientation of fibres, which can be defined as a change in their local orientation due to some external actions, represents a particular type of remodelling that can be studied using Continuum Mechanics tools.

For transversely isotropic materials, with a single preferential direction, the problem of fibre reorientation has been recently studied by Ciambella and Nardinocchi [71, 72], taking into account both passive and active changes in the fibre directions. The introduction of a remodelling equation, that complements the usual mechanical balances, allows to describe the evolution of fibre orientation under mechanical [72] and magnetic [71] stimuli. Moreover, in [72], it was shown that the stationary solutions of the remodelling equation are the ones that make the remodelled stress and strain tensors coaxial [370]. However, the framework proposed in [72] is limited to transversely isotropic materials, for which only one preferential direction exists.

Instead, in the nonlinear elastic description of cell orientations proposed in Section 3.1, the material composed by substrate and cells is treated as orthotropic [234], even though it does not include an explicit remodelling in time of the cytoskeletal structure. It seems then quite natural to provide an extension of the results presented in [72] to a more general case, where an hyperelastic material is endowed with a double fibre microstructure, as in the cellular orientation example. Furthermore, while in Section 3.1 the two fibres were fixed to be perpendicular [234], it is of interest to characterize the remodelling of the different

fibre families independently, in a way that each fibre can change the orientation according to its own rotation.

Motivated by these observations, in this Section we propose a mechanical model that describes the reorganization of an anisotropic material structure, characterized by two fibre families that can modify their orientation following different evolution equations. Both active contributions affecting the reorientation process and purely passive material remodelling can be incorporated in the proposed framework. In doing so, we are able to extend the energetic modelling of cell alignment put forward in the previous Section [226, 234] using the fibre reorientation framework from [72], in which the rotation of the cells due to the mechanical prompt is treated as an additional variable for the model. This allows us to derive the reorientation equations on a rigorous and thermodynamically consistent basis, recovering the results presented in Section 3.1 as a particular case. At the same time, we provide an extension of the fibre reorientation model proposed in [72], adapting it to anisotropic materials with two preferential directions that can change their orientation in different manners, even though they can be properly coupled. The limit of two families of fibres which cannot change their relative orientation, as done for instance by Menzel [250] in the orthotropic case, is recovered within the terms of a constrained model.

The advantages of the proposed framework consist in its generality as well as in its consistency from a thermodynamical viewpoint. Moreover, it is possible to show that the inclusion of an additional family of fibres, which is able to reorient without remaining orthogonal to the first one, completely changes the behaviour of the system, leading to an extension of the coaxiality results by Vianello [319, 370]. At the same time, the model provides a good fitting of experimental data for peripheral and nuclear stress fibres, highlighting the key role played by the coupling between the two fibre families. Finally, we are able to recover the results for the stationary solutions discussed in Section 3.1, by introducing a constraint between the fibres that enforces the orthogonality.

3.2.1 Remodelling Framework

Before moving to the biological application of interest, in this Subsection we present the general remodelling framework, following the theory of finite elasticity with remodelling [72, 107]. We consider a material equipped with an anisotropic two families of fibres (TFF) internal structure whose change of orientation is not simply dragged by the deformation but described by additional state variables, therefore including a remodelling of the fibre

structure. The relationship between fibre orientations and mechanical forces, as well as the constitutive coupling between the two fibre families which characterize the anisotropic structure, are derived in the following on a thermodynamically consistent basis.

Kinematics

Recalling the notation introduced in Section 1.2, we consider a body, identified with a region Ω_0 of the Euclidean three-dimensional space $\mathcal{E}$, and a time interval $\mathcal{T}$, to define the motion $\boldsymbol{\chi}$ and the current configuration Ω. The first kinematic variable of our model is the displacement field $\mathbf{u}$, which is related to the deformation gradient by $\mathbb{F} = \mathbb{I} + \operatorname{Grad}\mathbf{u}$.

Then, in addition to the displacement field describing the current position of the body, we are interested in the evolution of the orientation of the anisotropic TFF internal structure, which in Ω_0 is identified by a pair of material unit vector fields $\mathbf{a}_0 : \Omega_0 \to \mathcal{V}$ and $\mathbf{b}_0 : \Omega_0 \to \mathcal{V}$ (with $|\mathbf{a}_0| = |\mathbf{b}_0| = 1$); they represent the preferred directions that the internal structure endows to the material, i.e., the direction of each fibre at $\mathbf{X} \in \Omega_0$. For practical usage, it is convenient to introduce the corresponding *structural or orientation tensors* at Ω_0, defined as $\mathbb{A}_0 := \mathbf{a}_0 \otimes \mathbf{a}_0$ and $\mathbb{B}_0 := \mathbf{b}_0 \otimes \mathbf{b}_0$. In the following, we will sometimes refer to the field $\mathbf{a}_0$ as the *primary structure* of the material, while $\mathbf{b}_0$ will be consequently called *secondary structure*. Both $\mathbb{A}_0$ and $\mathbb{B}_0$ contribute to the material anisotropy and can reorient as prescribed by two different rotation fields, each one interpreted as the rotation of a single fibre family. In this respect, we will consider a time-dependent tensor field $\mathbb{R}_p : \Omega_0 \times \mathcal{T} \to \mathbb{R}\mathtt{ot}$, with $\mathbb{R}\mathtt{ot}$ denoting the space of rotations, which represents the reorientation of the primary structure and changes the reference orientation from $\mathbf{a}_0(\mathbf{X})$ to

$$\mathbf{a}(\mathbf{X},t) = \mathbb{R}_p(\mathbf{X},t)\mathbf{a}_0(\mathbf{X})\,, \tag{3.49}$$

or equivalently $\mathbb{A}_0(\mathbf{X})$ to

$$\mathbb{A}(\mathbf{X},t) = \mathbb{R}_p(\mathbf{X},t)\mathbb{A}_0(\mathbf{X})\mathbb{R}_p^{\mathrm{T}}(\mathbf{X},t), \tag{3.50}$$

where $\mathbb{A} := \mathbf{a} \otimes \mathbf{a}$. Likewise, the second rotation field $\mathbb{R}_s : \Omega_0 \times \mathcal{T} \to \mathbb{R}\mathtt{ot}$ describes the reorientation of the secondary structure and changes $\mathbf{b}_0(\mathbf{X})$ to

$$\mathbf{b}(\mathbf{X},t) = \mathbb{R}_s(\mathbf{X},t)\mathbf{b}_0(\mathbf{X}) \tag{3.51}$$

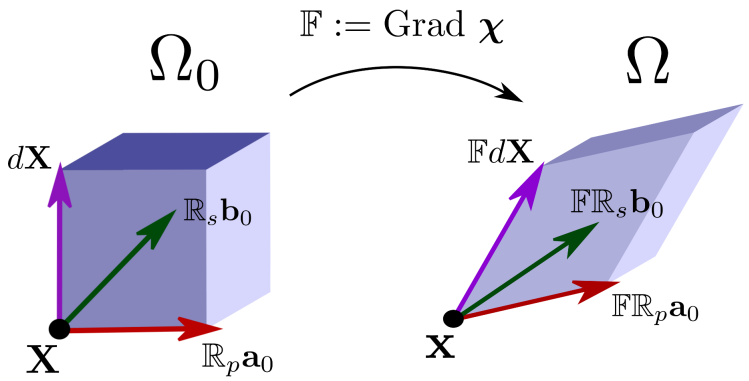

Fig. 3.9 Schematic representation of the reorientation process at a material point. A material line element $d\mathbf{X}$ in the reference configuration Ω_0 is deformed to the corresponding line element $\mathbb{F}d\mathbf{X}$ in the current configuration Ω. Instead, the primary structure $\mathbf{a}_0$ firstly undergoes remodelling due to the rotation $\mathbb{R}_p$ while the secondary structure $\mathbf{b}_0$ is reoriented according to another rotation $\mathbb{R}_s$.

and $\mathbb{B}_0(\mathbf{X})$ to

$$\mathbb{B}(\mathbf{X},t) = \mathbb{R}_s(\mathbf{X},t)\mathbb{B}_0(\mathbf{X})\mathbb{R}_s(\mathbf{X},t)^{\mathrm{T}}, \tag{3.52}$$

having denoted $\mathbb{B} := \mathbf{b}\otimes\mathbf{b}$. Each fibre family of such an anisotropic material may change its orientation as time evolves; then, the deformation gradient tensor $\mathbb{F}$ maps each remodelled fibre to the current configuration, as sketched in Fig. 3.9. With these definitions at hand, the state variables of the problem are the displacement and rotation fields, that is, the triple $(\mathbf{u},\mathbb{R}_p,\mathbb{R}_s) \in \mathcal{V}\times\mathbb{R}\mathtt{ot}\times\mathbb{R}\mathtt{ot}$, and the corresponding velocity fields are identified by the time derivatives $(\dot{\mathbf{u}},\dot{\mathbb{R}}_p\mathbb{R}_p^{\mathrm{T}},\dot{\mathbb{R}}_s\mathbb{R}_s^{\mathrm{T}}) \in \mathcal{V}\times\mathbb{S}\mathrm{kw}\times\ \mathbb{S}\mathrm{kw}$, where $\mathbb{S}\mathrm{kw}$ denotes the space of skew-symmetric tensors. Finally, we denote as $(\mathbf{w},\mathbb{W}_p,\mathbb{W}_s) \in \mathcal{V}\times\mathbb{S}\mathrm{kw}\times\ \mathbb{S}\mathrm{kw}$ the associated virtual velocity fields.

Remark 3.2. Let us note that our kinematic framework does not filter out the rotation fields $\mathbb{R}_p$ and $\mathbb{R}_s$ such that $\mathbb{R}_p\mathbf{a}_0 = \mathbf{a}_0$ and $\mathbb{R}_s\mathbf{b}_0 = \mathbf{b}_0$, which are included in the admissible rotation fields even if they maintain the energy unchanged and so are of no interest in the remodelling problem.

Balance Equations

The balance equations of the model are delivered by the principle of virtual working, based on the choice of the external and internal virtual workings defined as continuous, linear, real-valued functionals defined on the space of virtual velocities [107]. By introducing forces and torques of the model which are working-conjugate to each kinematic variable

[9, 72, 107, 146, 278], we write

$$\mathcal{L}_e(\mathbf{w},\mathbb{W}_p,\mathbb{W}_s)=\int_{\Omega_0}(\mathbf{z}\cdot\mathbf{w}+\mathbb{Z}_p:\mathbb{W}_p+\mathbb{Z}_s:\mathbb{W}_s)\,\mathrm{d}V+\int_{\partial_t\Omega_0}\mathbf{s}\cdot\mathbf{w}\,\mathrm{d}A \tag{3.53}$$

for the external virtual working and

$$\mathcal{L}_i(\mathbf{w},\mathbb{W}_p,\mathbb{W}_s)=\int_{\Omega_0}(\mathbb{P}:\mathrm{Grad}\,\mathbf{w}+\Sigma_p:\mathbb{W}_p+\Sigma_s:\mathbb{W}_s)\,\mathrm{d}V \tag{3.54}$$

for the internal virtual working. The pair $(\mathbf{z},\mathbf{s})$ are forces per unit of referential volume and area, respectively, while $\mathbb{P}$ is the first Piola–Kirchhoff stress tensor. The pair of skew tensors $(\mathbb{Z}_i,\Sigma_i)$, with $i=p,s$, are torques per unit of referential volume, and represent the outer and inner remodelling torques, as $\mathbb{W}_p$, $\mathbb{W}_s$ are skew-symmetric tensors. More specifically, the outer torques $\mathbb{Z}_p$ and $\mathbb{Z}_s$ represent external source terms which may affect fibre reorientation, for instance magnetic effects [71] or chemo-mechanical processes. On the other side, the inner remodelling torques Σ_p and Σ_s take into account the internal actions driving the reorientation of the primary and secondary material structures, respectively. It is worth remarking that, for what concerns the remodelling torques, our theory is of order zero-th, i.e., we do not take into account the gradients of the rotation fields, which instead may become relevant when the fibres are closely packed.

By enforcing the condition that the external and internal virtual working be equal for any virtual velocities $(\mathbf{w},\mathbb{W}_p,\mathbb{W}_s)\in\mathcal{V}\times\mathbb{S}\mathrm{kw}\times\mathbb{S}\mathrm{kw}$ and for any subregion $\mathcal{R}\subset\Omega_0$, we obtain the following balance equations and associated boundary conditions:

$$\mathrm{Div}\,\mathbb{P}+\mathbf{z}=\mathbf{0}\quad\text{and}\quad\Sigma_p=\mathbb{Z}_p\quad\text{and}\quad\Sigma_s=\mathbb{Z}_s\ \text{ in }\ \Omega_0\,, \tag{3.55}$$

$$\mathbf{u}=\widehat{\mathbf{u}}\ \text{ on }\ \partial_u\Omega_0\quad\text{and}\quad\mathbb{P}\mathbf{n}_*=\mathbf{s}\ \text{ on }\ \partial_t\Omega_0\,, \tag{3.56}$$

with $\partial_u\Omega_0$ and $\partial_t\Omega_0$ denoting parts of the boundary $\partial\Omega_0$ where displacements and tractions are respectively prescribed, and $\mathbf{n}_*$ denoting the unit normal to $\partial_t\Omega_0$ pointing outwards. Equations (3.55) are the three balance equations of our theory. The first is the usual balance of mechanical forces, where inertial effects can be included in the bulk force $\mathbf{z}$, even if in the present model they are neglected since the remodelling time scale is typically much longer than the inertial one. The second and third equations are the balances of the remodelling torques, which drive the reorientation of the primary and secondary structures, respectively, once the appropriate constitutive equations will be considered. In particular, they prescribe that the outer and inner remodelling torques be equal. These equations generalise the theory

presented in [72], where only a transversely isotropic internal structure was considered. The external working, that corresponds to balanced forces and torques and is evaluated on the actual velocity fields $(\dot{\mathbf{u}}, \dot{\mathbb{R}}_p\mathbb{R}_p^{\mathrm{T}}, \dot{\mathbb{R}}_s\mathbb{R}_s^{\mathrm{T}})$, identifies the external actual power $\mathcal{P}_e$ expended during the evolution of the continuum:

$$\begin{aligned}\mathcal{L}_e(\dot{\mathbf{u}}, \dot{\mathbb{R}}_p\mathbb{R}_p^{\mathrm{T}}, \dot{\mathbb{R}}_s\mathbb{R}_s^{\mathrm{T}}) &= \int_{\Omega_0} \left(\mathbf{z}\cdot\dot{\mathbf{u}} + \mathbb{Z}_p : \dot{\mathbb{R}}_p\mathbb{R}_p^{\mathrm{T}} + \mathbb{Z}_s : \dot{\mathbb{R}}_s\mathbb{R}_s^{\mathrm{T}}\right) \mathrm{d}V + \int_{\partial_t\Omega_0} \mathbf{s}\cdot\dot{\mathbf{u}}\,\mathrm{d}A \\ &= \int_{\Omega_0} \left(\mathbb{P} : \dot{\mathbb{F}} + \Sigma_p : \dot{\mathbb{R}}_p\mathbb{R}_p^{\mathrm{T}} + \Sigma_s : \dot{\mathbb{R}}_s\mathbb{R}_s^{\mathrm{T}}\right) \mathrm{d}V = \mathcal{P}_e\,. \end{aligned} \tag{3.57}$$

Constitutive Equations and Energy Imbalance

The constitutive prescriptions to describe the behaviour of the material with the reorientable anisotropic TFF internal structure are imposed in a thermodynamically consistent way, through the following steps. Firstly, we take into account a class of materials that admits an elastic strain energy density in the form

$$\mathcal{W} = \mathcal{W}(\mathbb{E}, \mathbb{A}, \mathbb{B})\,, \tag{3.58}$$

dependent upon the deformation $\mathbb{F}$ through the Green–Lagrange strain tensor $\mathbb{E}$, defined in Eq. (1.5), and on the remodelled orientation tensors $\mathbb{A}$ and $\mathbb{B}$ or, equivalently, on the rotations $\mathbb{R}_p$ and $\mathbb{R}_s$ that transform the primary and secondary structures. More specifically, following the theory of double-fibred finite elasticity, we assume that $\mathcal{W}$ is an isotropic function of its arguments [151, 224].

We also assume that dissipation is only associated with the remodelling processes, and the dissipation density δ can be written as

$$\delta = \delta\left(\dot{\mathbb{R}}_p\mathbb{R}_p^{\mathrm{T}}, \dot{\mathbb{R}}_s\mathbb{R}_s^{\mathrm{T}}\right)\,. \tag{3.59}$$

To derive constitutive equations that are consistent with the first and second laws of thermodynamics, we enforce the energy imbalance, stating that for any admissible process, characterised by the state variables $(\mathbf{u}, \mathbb{R}_p, \mathbb{R}_s)$, the time derivative of the energy must not exceed the external actual power expended on the body along the same process, i.e., the dissipation must be positive:

$$\int_{\Omega_0} \delta\,\mathrm{d}V = \mathcal{P}_e - \int_{\Omega_0} \dot{\mathcal{W}}\,\mathrm{d}V \geq 0. \tag{3.60}$$

Within the framework discussed so far and using Eq. (3.58), we can write the time derivative of the elastic energy as

$$\dot{\mathcal{W}} = \frac{\partial \mathcal{W}}{\partial \mathbb{E}} : \dot{\mathbb{E}} + \frac{\partial \mathcal{W}}{\partial \mathbb{A}} : \dot{\mathbb{A}} + \frac{\partial \mathcal{W}}{\partial \mathbb{B}} : \dot{\mathbb{B}} . \tag{3.61}$$

At this point, it is useful to introduce the commutator operator between two tensors $[\cdot,\cdot] : \mathbb{L}\mathtt{in} \times \mathbb{L}\mathtt{in} \to \mathbb{L}\mathtt{in}$, where $\mathbb{L}\mathtt{in}$ stands for the space of second-order tensors, defined as:

$$[\mathbb{X},\mathbb{Y}] = \mathbb{X}\mathbb{Y} - \mathbb{Y}\mathbb{X}, \quad \forall \mathbb{X},\mathbb{Y} \in \mathbb{L}\mathtt{in}.$$

With this definition on hand, recalling Eqs. (3.50)–(3.52) we have

$$\dot{\mathbb{A}} = [\dot{\mathbb{R}}_p \mathbb{R}_p^{\mathrm{T}}, \mathbb{A}] \quad \text{and} \quad \dot{\mathbb{B}} = [\dot{\mathbb{R}}_s \mathbb{R}_s^{\mathrm{T}}, \mathbb{B}] , \tag{3.62}$$

and, in general, for any $\mathbb{X},\mathbb{Y} \in \mathbb{L}\mathtt{in}$,

$$\mathbb{X} : [\dot{\mathbb{R}}_p \mathbb{R}_p^{\mathrm{T}}, \mathbb{A}] = \dot{\mathbb{R}}_p \mathbb{R}_p^{\mathrm{T}} : [\mathbb{X}, \mathbb{A}] \quad \text{and} \quad \mathbb{Y} : [\dot{\mathbb{R}}_s \mathbb{R}_s^{\mathrm{T}}, \mathbb{B}] = \dot{\mathbb{R}}_s \mathbb{R}_s^{\mathrm{T}} : [\mathbb{Y}, \mathbb{B}] ,$$

which allow Eq. (3.61) to be rewritten as

$$\dot{\mathcal{W}} = \frac{\partial \mathcal{W}}{\partial \mathbb{E}} : \dot{\mathbb{E}} + [\frac{\partial \mathcal{W}}{\partial \mathbb{A}}, \mathbb{A}] : \dot{\mathbb{R}}_p \mathbb{R}_p^{\mathrm{T}} + [\frac{\partial \mathcal{W}}{\partial \mathbb{B}}, \mathbb{B}] : \dot{\mathbb{R}}_s \mathbb{R}_s^{\mathrm{T}} . \tag{3.63}$$

The constitutive prescriptions for the stress $\mathbb{P}$ and for the inner remodelling actions Σ_p and Σ_s have to satisfy the imbalance principle stated above, which can be rephrased in local form by requiring that

$$\delta = \mathbb{P} : \dot{\mathbb{F}} + \Sigma_p : \dot{\mathbb{R}}_p \mathbb{R}_p^{\mathrm{T}} + \Sigma_s : \dot{\mathbb{R}}_s \mathbb{R}_s^{\mathrm{T}} - \dot{\mathcal{W}} \geq 0 \tag{3.64}$$

has to be positive for every realizable process [80]. By using Eqs. (3.61)–(3.63), we reduce the inequality (3.64) to:

$$\left(\mathbb{P} - \mathbb{F}\frac{\partial \mathcal{W}}{\partial \mathbb{E}}\right) : \dot{\mathbb{F}} + \left(\Sigma_p - [\frac{\partial \mathcal{W}}{\partial \mathbb{A}}, \mathbb{A}]\right) : \dot{\mathbb{R}}_p \mathbb{R}_p^{\mathrm{T}} + \left(\Sigma_s - [\frac{\partial \mathcal{W}}{\partial \mathbb{B}}, \mathbb{B}]\right) : \dot{\mathbb{R}}_s \mathbb{R}_s^{\mathrm{T}} \geq 0 . \tag{3.65}$$

Since we assume that dissipation is only due to remodelling, the constitutive equation for the stress can be chosen as a standard hyperelastic law:

$$\mathbb{P} = \mathbb{F}\frac{\partial \mathcal{W}}{\partial \mathbb{E}}, \qquad \mathbb{S} = \mathbb{F}^{-1}\mathbb{P} = \frac{\partial \mathcal{W}}{\partial \mathbb{E}}, \tag{3.66}$$

where $\mathbb{S}$ is the second Piola-Kirchhoff stress tensor. The remainder of the dissipation inequality (3.65) can be satisfied on assuming that each inner remodelling torque can be additively decomposed into an elastic and a dissipative part:

$$\Sigma_p = \Sigma_p^{(e)} + \Sigma_p^{(d)} = [\frac{\partial \mathcal{W}}{\partial \mathbb{A}}, \mathbb{A}] + \mathsf{D}_p \dot{\mathbb{R}}_p \mathbb{R}_p^{\mathrm{T}}, \tag{3.67}$$

$$\Sigma_s = \Sigma_s^{(e)} + \Sigma_s^{(d)} = [\frac{\partial \mathcal{W}}{\partial \mathbb{B}}, \mathbb{B}] + \mathsf{D}_s \dot{\mathbb{R}}_s \mathbb{R}_s^{\mathrm{T}}, \tag{3.68}$$

where D_p and D_s are positive-definite fourth order tensors that represent the resistance to remodelling of the primary and secondary material structure, respectively.
By substituting the constitutive equations (3.66)–(3.68) in the balance equations (3.55), we are able to obtain two differential equations that describe the evolution of the rotation fields, and therefore of the associated fibre families. The general remodelling problem for the anisotropic TFF microstructure can then be expressed as the following system of nonlinear ordinary differential equations in $\Omega_0 \times \mathcal{T}$:

$$\begin{cases} \mathsf{D}_p \dot{\mathbb{R}}_p \mathbb{R}_p^{\mathrm{T}} = \mathbb{Z}_p - [\dfrac{\partial \mathcal{W}}{\partial \mathbb{A}}, \mathbb{A}], \\ \mathsf{D}_s \dot{\mathbb{R}}_s \mathbb{R}_s^{\mathrm{T}} = \mathbb{Z}_s - [\dfrac{\partial \mathcal{W}}{\partial \mathbb{B}}, \mathbb{B}], \end{cases} \tag{3.69}$$

with initial conditions

$$\mathbb{R}_p = \mathbb{I} \quad \text{and} \quad \mathbb{R}_s = \mathbb{I} \quad \text{in} \quad \Omega_0 \times \{t_0\}. \tag{3.70}$$

The problem (3.69) has to be solved together with the balance of forces $(3.55)_1$ and the constitutive prescription (3.66). We observe that the elastic terms on the right-hand side of Eqs. (3.69), represented by the commutators, include the mutual interaction between the two fibre families, as it will be explicitly shown in the case of plane remodelling. Moreover, when $\mathbb{Z}_p = \mathbb{Z}_s = \mathbb{O}$, as we will assume hereafter, we notice that the stationary solutions of the system (3.69) are determined by solving the equations

$$[\frac{\partial \mathcal{W}}{\partial \mathbb{A}}, \mathbb{A}] = \mathbb{O} \quad \text{and} \quad [\frac{\partial \mathcal{W}}{\partial \mathbb{B}}, \mathbb{B}] = \mathbb{O}. \tag{3.71}$$

Further Constitutive Prescriptions

For the calculations carried out in the following, it is convenient to express the strain energy density in terms of the invariants of the tensors $\mathbb{E}$, $\mathbb{A}$ and $\mathbb{B}$. In doing so, we introduce the following classical set of isotropic invariants of $\mathbb{E}$:

$$\mathrm{J}_1 = \mathbb{E} : \mathbb{I}, \qquad \mathrm{J}_2 = \mathbb{E}^\dagger : \mathbb{I}, \qquad \mathrm{J}_3 = \det(\mathbb{I} + 2\mathbb{E}), \tag{3.72}$$

where $\mathbb{E}^\dagger := (\det\mathbb{E})\mathbb{E}^{-\mathrm{T}}$, together with the anisotropic ones [327]

$$\begin{aligned} &\mathrm{J}_4 = \mathbb{E} : \mathbb{A}, && \mathrm{J}_5 = \mathbb{E}^2 : \mathbb{A}, \\ &\mathrm{J}_6 = \mathbb{E} : \mathbb{B}, && \mathrm{J}_7 = \mathbb{E}^2 : \mathbb{B}, \\ &\mathrm{J}_8 = \mathbb{E} : \mathrm{Sym}(\mathbb{A}\mathbb{B}) = (\mathbf{a}\cdot\mathbf{b})\big(\mathbb{E}\mathbf{a}\cdot\mathbf{b}\big). \end{aligned} \tag{3.73}$$

The anisotropic invariants J_4 and J_6 take into account the deformations along the directions of the primary and secondary internal structures, while J_5 and J_7 are also measures of fibre stretch but include the influence of shear on the fibres [251]; J_8 is instead used to account for the interactions between the two fibre families.

Remark 3.3. As mentioned previously, the definition of J_8 is slightly different from the one used in Section 3.1 for I_8. However, at the end of the present Section we will show that the results do not change.

If we use the representation theorem for isotropic scalar functions of three symmetric tensors (see [225, 399, 405]), we can write

$$\mathcal{W}(\mathbb{E},\mathbb{A},\mathbb{B}) = \widehat{\mathcal{W}}(\mathrm{J}_1,\mathrm{J}_2,\mathrm{J}_3,\mathrm{J}_4,\mathrm{J}_5,\mathrm{J}_6,\mathrm{J}_7,\mathrm{J}_8). \tag{3.74}$$

On adopting the representation (3.74) and denoting with $w_i := \partial\widehat{\mathcal{W}}/\partial\mathrm{J}_i$, $i = 1,\dots,8$, one has:

$$\begin{aligned} \frac{\partial\mathcal{W}}{\partial\mathbb{E}} &= w_1\mathbb{I} + w_2(\mathrm{J}_1\mathbb{I} - \mathbb{E}) + 2w_3\mathrm{J}_3\big(2\mathbb{E}+\mathbb{I}\big)^{-1} + w_4\mathbb{A} + w_5(\mathbb{A}\mathbb{E}+\mathbb{E}\mathbb{A}), \\ &+ w_6\mathbb{B} + w_7(\mathbb{B}\mathbb{E}+\mathbb{E}\mathbb{B}) + \frac{1}{2}w_8\,(\mathbb{A}\mathbb{B}+\mathbb{B}\mathbb{A}), \end{aligned} \tag{3.75}$$

$$\frac{\partial\mathcal{W}}{\partial\mathbb{A}} = w_4\mathbb{E} + w_5\mathbb{E}^2 + \frac{1}{2}w_8(\mathbb{E}\mathbb{B}+\mathbb{B}\mathbb{E}), \tag{3.76}$$

$$\frac{\partial\mathcal{W}}{\partial\mathbb{B}} = w_6\mathbb{E} + w_7\mathbb{E}^2 + \frac{1}{2}w_8(\mathbb{E}\mathbb{A}+\mathbb{A}\mathbb{E}). \tag{3.77}$$

Remark 3.4. It is often customary to express $\widehat{\mathcal{W}}$ in terms of the invariants of the right Cauchy–Green strain tensor $\mathbb{C}$ rather than $\mathbb{E}$, which can be rewritten similarly to Eq. (3.73) as:

$$\begin{aligned} &\mathrm{I}_1 = \mathbb{C} : \mathbb{I}, && \mathrm{I}_2 = \mathbb{C}^\dagger : \mathbb{I}, && \mathrm{I}_3 = \det \mathbb{C}, \\ &\mathrm{I}_4 = \mathbb{C} : \mathbb{A}, && \mathrm{I}_5 = \mathbb{C}^2 : \mathbb{A}, && \\ &\mathrm{I}_6 = \mathbb{C} : \mathbb{B}, && \mathrm{I}_7 = \mathbb{C}^2 : \mathbb{B}, && \\ &\mathrm{I}_8 = \mathbb{C} : \mathrm{Sym}(\mathbb{A}\mathbb{B}). && && \end{aligned} \tag{3.78}$$

However, recalling Eq. (1.5), the relationship $\mathbb{C} = 2\mathbb{E} + \mathbb{I}$ holds true, so the two sets of invariants are connected by the following linear transformations:

$$\begin{aligned} &\mathrm{J}_1 = \frac{1}{2}\big(\mathrm{I}_1 - 3\big), && \mathrm{J}_2 = \frac{1}{4}\big(\mathrm{I}_2 - 3\big) - \frac{1}{2}\big(\mathrm{I}_1 - 3\big), && \mathrm{J}_3 = \mathrm{I}_3, \\ &\mathrm{J}_4 = \frac{1}{2}\big(\mathrm{I}_4 - 1\big), && \mathrm{J}_5 = \frac{1}{4}\big(\mathrm{I}_5 - 1\big) - \frac{1}{2}\big(\mathrm{I}_4 - 1\big), && \\ &\mathrm{J}_6 = \frac{1}{2}\big(\mathrm{I}_6 - 1\big), && \mathrm{J}_7 = \frac{1}{4}\big(\mathrm{I}_7 - 1\big) - \frac{1}{2}\big(\mathrm{I}_6 - 1\big), && \\ &\mathrm{J}_8 = \frac{1}{2}\big(\mathrm{I}_8 - \mathbb{A}\cdot\mathbb{B}\big). && && \end{aligned} \tag{3.79}$$

3.2.2 Characterisation of the Remodelling Stationary Solutions

In [72], it was proved that, for materials equipped with a reorientable transversely isotropic internal structure described by a rotation field $\mathbb{Q}$ and in absence of external stimuli, the stationary solutions of the remodelling equations are those rotations which make stress $\mathbb{S}$ and strain $\mathbb{E}$, or equivalently $\mathbb{C}$, coaxial. In addition, those rotations render the map

$$\boldsymbol{\sigma} : \mathbb{R}\mathtt{ot} \ni \mathbb{Q} \mapsto \boldsymbol{\sigma}(\mathbb{Q}) = \psi(\mathbb{C}, \mathbb{Q})$$

stationary, where $\psi(\mathbb{C}, \mathbb{Q})$ is the elastic strain energy (see Proposition 1 of [72] and also [370]).

In this Section, it is shown that these results can be partially extended to include the anisotropic double-fibred internal structure considered here. To do so, we first note that the results in [370] about coaxiality, which were already employed in Section 3.1.2, hold true whatever class of material symmetry is considered, either transversely isotropic or orthotropic, granted that all fibre families are transformed under the same rotation acting on the body. It is then reasonable to expect that, under our more general framework in

which two rotations appear, there could be a loss of equivalence between coaxiality and stationarity of the energy, as we shall prove in the following.

Stationarity and Coaxiality

Before passing to the main result of this Section, we recall that two symmetric tensors $\mathbb{U},\mathbb{V}$ are said to be coaxial if they commute, or equivalently if their commutator vanishes, i.e. $[\mathbb{U},\mathbb{V}]=\mathbb{O}$. Moreover, we prove the following relation:

$$[\frac{\partial \mathcal{W}}{\partial \mathbb{A}},\mathbb{A}]+[\frac{\partial \mathcal{W}}{\partial \mathbb{B}},\mathbb{B}]=[\mathbb{E},\mathbb{S}]\,. \tag{3.80}$$

By recalling Eq. (3.76) and Eq. (3.77), the left-hand side of Eq. (3.80) can be written as

$$\begin{aligned}
[\frac{\partial \mathcal{W}}{\partial \mathbb{A}},\mathbb{A}]+[\frac{\partial \mathcal{W}}{\partial \mathbb{B}},\mathbb{B}] &= w_4[\mathbb{E},\mathbb{A}]+w_5[\mathbb{E}^2,\mathbb{A}]+w_6[\mathbb{E},\mathbb{B}]+w_7[\mathbb{E}^2,\mathbb{B}]\\
&\quad+\frac{w_8}{2}(\mathbb{E}\mathbb{B}\mathbb{A}+\mathbb{B}\mathbb{E}\mathbb{A}-\mathbb{A}\mathbb{E}\mathbb{B}-\mathbb{A}\mathbb{B}\mathbb{E})\\
&\quad+\frac{w_8}{2}(\mathbb{E}\mathbb{A}\mathbb{B}+\mathbb{A}\mathbb{E}\mathbb{B}-\mathbb{B}\mathbb{E}\mathbb{A}-\mathbb{B}\mathbb{A}\mathbb{E})\\
&= w_4[\mathbb{E},\mathbb{A}]+w_5[\mathbb{E}^2,\mathbb{A}]+w_6[\mathbb{E},\mathbb{B}]+w_7[\mathbb{E}^2,\mathbb{B}]\\
&\quad+\frac{w_8}{2}\mathbb{E}(\mathbb{B}\mathbb{A}+\mathbb{A}\mathbb{B})-\frac{w_8}{2}(\mathbb{A}\mathbb{B}+\mathbb{B}\mathbb{A})\mathbb{E}\\
&= w_4[\mathbb{E},\mathbb{A}]+w_5[\mathbb{E}^2,\mathbb{A}]+w_6[\mathbb{E},\mathbb{B}]+w_7[\mathbb{E}^2,\mathbb{B}]+w_8[\mathbb{E},\mathrm{Sym}(\mathbb{A}\mathbb{B})]
\end{aligned}$$

which, in view of Eq. (3.75) and Eq. (3.66), is indeed equivalent to

$$\left[\mathbb{E},w_4\mathbb{A}+w_5(\mathbb{A}\mathbb{E}+\mathbb{E}\mathbb{A})+w_6\mathbb{B}+w_7(\mathbb{B}\mathbb{E}+\mathbb{E}\mathbb{B})+w_8\,\mathrm{Sym}(\mathbb{A}\mathbb{B})\right]=[\mathbb{E},\mathbb{S}]\,,$$

which proves Eq. (3.80). Then, at stationarity, since both commutators on the left-hand side of Eq. (3.80) vanish, $\left[\mathbb{E},\mathbb{S}\right]=\mathbb{O}$ holds, that is, the stationary solutions of Eq. (3.69) in the passive case are rotations $\left(\mathbb{R}_p^*,\mathbb{R}_s^*\right)$ which make stress and strain coaxial. This result generalizes the one derived in [72] for transversely isotropic materials. We note however that the inverse statement is not necessarily true: in fact, coaxiality of stress and strain does not imply that both commutators have to vanish, and therefore need not be equivalent to a stationary solution of the remodelling system.

Taking into account these observations, we are now in the position of proving the following result.

Proposition 3.1. *Let* $\mathbb{E}$ *be a given deformation.*

(a) $(\mathbb{R}_p^*, \mathbb{R}_s^*)$ *is a stationary solution of the passive remodelling system of equations if and only if* $(\mathbb{R}_p^*, \mathbb{R}_s^*)$ *is a critical point of the map*

$$\begin{aligned} &\sigma : \mathbb{R}\mathtt{ot} \times \mathbb{R}\mathtt{ot} \to \mathbb{R} \\ &(\mathbb{R}_p, \mathbb{R}_s) \mapsto \sigma(\mathbb{R}_p, \mathbb{R}_s) = \mathcal{W}(\mathbb{E}, \mathbb{A}, \mathbb{B}) = \mathcal{W}(\mathbb{E}, \mathbb{R}_p \mathbb{A}_0 \mathbb{R}_p^{\mathrm{T}}, \mathbb{R}_s \mathbb{B}_0 \mathbb{R}_s^{\mathrm{T}}), \end{aligned} \tag{3.81}$$

where $\mathcal{W}$ *is the strain energy density.*

(b) If $(\mathbb{R}_p^*, \mathbb{R}_s^*)$ *is a stationary solution of the remodelling system of equations, then the stress* $\mathbb{S}^* = \mathcal{S}(\mathbb{E}, \mathbb{R}_p^*, \mathbb{R}_s^*)$ *and strain* $\mathbb{E}$ *tensors are* coaxial.

Proof. Statement (b) follows from the discussion carried out at the beginning of this Subsection. As a matter of fact, if $(\mathbb{R}_p^*, \mathbb{R}_s^*)$ is a stationary solution of the passive remodelling system (3.69), then

$$[\frac{\partial \mathcal{W}}{\partial \mathbb{A}}, \mathbb{A}]^* = \mathbb{O} \quad \text{and} \quad [\frac{\partial \mathcal{W}}{\partial \mathbb{B}}, \mathbb{B}]^* = \mathbb{O},$$

where we have used a superscript $*$ to denote quantities at stationarity. Consequently, by (3.80),

$$\mathbb{O} = [\frac{\partial \mathcal{W}}{\partial \mathbb{A}}, \mathbb{A}]^* + [\frac{\partial \mathcal{W}}{\partial \mathbb{B}}, \mathbb{B}]^* = [\mathbb{E}, \mathbb{S}^*]$$

and therefore the stress and strain tensors are coaxial. To prove statement (a), we follow the procedure put forward by Vianello [370]. In this case, however, we need to exploit the canonical isomorphism between the tangent space $\mathrm{Rot}(\mathbb{R}_p, \mathbb{R}_s)$ to the product manifold $\mathbb{R}\mathtt{ot} \times \mathbb{R}\mathtt{ot}$ at $(\mathbb{R}_p, \mathbb{R}_s)$ and the product space $\mathbb{S}\mathrm{kw} \times \mathbb{S}\mathrm{kw}$, for which

$$\mathrm{Rot}(\mathbb{R}_p, \mathbb{R}_s) = \{(\mathbb{W}_p \mathbb{R}_p, \mathbb{W}_s \mathbb{R}_s) \,|\, (\mathbb{W}_p, \mathbb{W}_s) \in \mathbb{S}\mathrm{kw} \times \mathbb{S}\mathrm{kw}\}.$$

In such a case, the derivative of the energy at $(\mathbb{R}_p, \mathbb{R}_s)$ in the direction $(\mathbb{W}_p \mathbb{R}_p, \mathbb{W}_s \mathbb{R}_s)$ becomes

$$\begin{aligned} \dot{\sigma}(\mathbb{R}_p, \mathbb{R}_s) = D\sigma(\mathbb{R}_p, \mathbb{R}_s)[\mathbb{W}_p \mathbb{R}_p, \mathbb{W}_s \mathbb{R}_s] &= \frac{\partial \mathcal{W}}{\partial \mathbb{R}_p} : \mathbb{W}_p \mathbb{R}_p + \frac{\partial \mathcal{W}}{\partial \mathbb{R}_s} : \mathbb{W}_s \mathbb{R}_s \\ &= [\frac{\partial \mathcal{W}}{\partial \mathbb{A}}, \mathbb{A}] : \mathbb{W}_p + [\frac{\partial \mathcal{W}}{\partial \mathbb{B}}, \mathbb{B}] : \mathbb{W}_s, \end{aligned}$$

which is null for every pair $(\mathbb{W}_p, \mathbb{W}_s) \in \mathbb{S}\mathrm{kw} \times \mathbb{S}\mathrm{kw}$ if and only if

$$[\frac{\partial \mathcal{W}}{\partial \mathbb{A}}, \mathbb{A}]^* = \mathbb{O} \qquad \text{and} \qquad [\frac{\partial \mathcal{W}}{\partial \mathbb{B}}, \mathbb{B}]^* = \mathbb{O}, \tag{3.82}$$

i.e., if and only if $(\mathbb{R}_p^*, \mathbb{R}_s^*)$ is a stationary solution of the remodelling equations. □

Previous derivations confirm the loss of equivalence between critical points of the energy and coaxiality of stress and strain; indeed, in this anisotropic TFF context, stationarity is a stronger requirement than coaxiality, since it requires that both commutators have to vanish. In other words, the set of stationary solutions is a proper subset of the set of rotations that make the stress and strain coaxial.

3.2.3 In-Plane Remodelling

There are many situations of interest in which both fibre families lie and rotate in the same plane; we refer to this situation as *in–plane remodelling* and study it in more detail, since it is closely related to the cell reorientation problem that we ultimately have in mind as an application.

By introducing an orthonormal basis $\{\mathbf{e}_1, \mathbf{e}_2, \mathbf{e}_3\}$ in the vector space $\mathcal{V}$, we assume that the fibres lie in the plane spanned by $\{\mathbf{e}_1, \mathbf{e}_2\}$, whereas the rotations have an axis parallel to $\mathbf{e}_3$, so that $\mathbb{R}_p\mathbf{e}_3 = \mathbb{R}_s\mathbf{e}_3 = \mathbf{e}_3$. For simplicity, we also assume that the mobility tensors introduced in Eq. (3.69) are both spherical. Therefore, they are fully determined by two positive scalar constants $m_p = \mu\tau_p$ and $m_s = \mu\tau_s$, with $m_p \neq m_s$ in general, μ is a shear modulus and τ_p, τ_s are two characteristic times of the remodelling processes:

$$\mathsf{D}_p = m_p \mathsf{I} \qquad \text{and} \qquad \mathsf{D}_s = m_s \mathsf{I}, \tag{3.83}$$

with I the fourth-order identity tensor with components $\mathsf{I}_{ijkl} = \delta_{ik}\delta_{jl}$. Taking into account that $\dot{\mathbf{a}} = \dot{\mathbb{R}}_p\mathbb{R}_p^{\mathrm{T}}\mathbf{a}$ and $\dot{\mathbf{b}} = \dot{\mathbb{R}}_s\mathbb{R}_s^{\mathrm{T}}\mathbf{b}$, the remodelling system of equations becomes

$$\begin{cases} m_p\,\dot{\mathbf{a}} = -[\dfrac{\partial \mathcal{W}}{\partial \mathbb{A}}, \mathbb{A}]\mathbf{a}\,, \\ m_s\,\dot{\mathbf{b}} = -[\dfrac{\partial \mathcal{W}}{\partial \mathbb{B}}, \mathbb{B}]\mathbf{b}\,. \end{cases} \tag{3.84}$$

On recalling Eqs. (3.76)–(3.77), the previous system can be recast in the following form:

$$\begin{cases} m_p\,\dot{\mathbf{a}} = \left(\mathbb{A}-\mathbb{I}\right)\left(w_4\,\mathbb{E}\mathbf{a} + w_5\,\mathbb{E}^2\mathbf{a} + \frac{w_8}{2}\,\mathbb{B}\mathbb{E}\mathbf{a} + \frac{w_8}{2}\,\mathbb{E}\mathbb{B}\mathbf{a}\right), \\ m_s\,\dot{\mathbf{b}} = \left(\mathbb{B}-\mathbb{I}\right)\left(w_6\,\mathbb{E}\mathbf{b} + w_7\,\mathbb{E}^2\mathbf{b} + \frac{w_8}{2}\,\mathbb{A}\mathbb{E}\mathbf{b} + \frac{w_8}{2}\,\mathbb{E}\mathbb{A}\mathbf{b}\right). \end{cases} \tag{3.85}$$

Since the problem is in-plane, it is convenient to introduce a parametrization in terms of the remodelling angles θ_p and θ_s, that is, we set $\mathbf{a} = \cos\theta_p\,\mathbf{e}_1 + \sin\theta_p\,\mathbf{e}_2$ for the primary structure and $\mathbf{b} = \cos\theta_s\,\mathbf{e}_1 + \sin\theta_s\,\mathbf{e}_2$ for the secondary one. In addition, without loss of generality, we can assume that $\mathbf{e}_1$, $\mathbf{e}_2$ and $\mathbf{e}_3$ are the principal strain directions of $\mathbb{E}$ associated with the principal strains ε_1, ε_2 and ε_3.
Equations (3.85) correspond therefore to the following system of scalar evolution equations for the angles:

$$\begin{cases} 2\,m_p\,\dot{\theta}_p = \left[w_4 + \frac{w_8}{2} + w_5(\varepsilon_1+\varepsilon_2)\right](\varepsilon_1-\varepsilon_2)\sin 2\theta_p + \frac{w_8}{2}(\varepsilon_1+\varepsilon_2)\sin\left[2(\theta_p-\theta_s)\right], \\ 2\,m_s\,\dot{\theta}_s \;= \left[w_6 + \frac{w_8}{2} + w_7(\varepsilon_1+\varepsilon_2)\right](\varepsilon_1-\varepsilon_2)\sin 2\theta_s + \frac{w_8}{2}(\varepsilon_1+\varepsilon_2)\sin\left[2(\theta_s-\theta_p)\right], \end{cases} \tag{3.86}$$

to be solved with the initial conditions $\theta_p(0) = \theta_{p0}$ and $\theta_s(0) = \theta_{s0}$, in which θ_{p0}, θ_{s0} are the referential primary and secondary orientation angles, respectively.

The following observations are duly noted:

1. depending on the representation form of the elastic strain energy, the strain component ε_3 of $\mathbb{E}$ may or may not enter the system (3.86); indeed, ε_3 does not appear explicitly, but it may be included in one of the energy derivatives w_i, $i = 4,\dots,8$. For the sake of simplicity, in the following we will assume that the deformation in the direction of $\mathbf{e}_3$ is negligible, and therefore $\varepsilon_3 = 0$;

2. the directions of principal strain $\mathbf{e}_1$, $\mathbf{e}_2$, that correspond to $\theta_p = k\frac{\pi}{2}$ and $\theta_s = j\frac{\pi}{2}$ ($k, j = 0, 1, 2\ldots$) are stationary solutions of the remodelling equations (3.86);

3. if $\varepsilon_1 = \varepsilon_2 = \varepsilon$, i.e., the deformation is equibiaxial, the system of equations (3.86) simplifies into

$$\begin{cases} m_p\,\dot{\theta}_p = \frac{1}{2}w_8\,\varepsilon\,\sin\left[2(\theta_p-\theta_s)\right], \\ m_s\,\dot{\theta}_s = \frac{1}{2}w_8\,\varepsilon\,\sin\left[2(\theta_s-\theta_p)\right], \end{cases} \tag{3.87}$$

and the stationary solutions are achieved either if $w_8(\varepsilon,\theta_p,\theta_s) = 0$ for some θ_p, θ_s or if $\sin 2(\theta_p-\theta_s) = 0$. The latter means that $\Delta\theta = \theta_s - \theta_p = k\frac{\pi}{2}$ ($k = 0, 1, \ldots$), i.e., the

fibres become either parallel or orthogonal, yet their "absolute" angle with respect to $\mathbf{e}_1$ remains undetermined. On the other hand, if $w_8 = 0$ identically, meaning that the energy does not depend on J_8, then no remodelling occurs, as found also for transversely isotropic materials [72].

To solve the remodelling problem (3.86) and make comparisons with experiments, as we shall do in the following Subsection, we need an *ansätz* on the strain energy function. In this respect, one could consider the most general form of the strain energy function which is quadratic in the deformation measure $\mathbb{E}$. To do so, we generalize the well-known Saint Venant–Kirchhoff model, that in its original formulation only depends on the isotropic invariants, to a double-fibred material [28, 181]. The minimal representation of that energy which provides the simplest coupling between the fibres and allows to fit data from experiments on biaxial tests is:

$$\begin{aligned}\widehat{\mathcal{W}}(\mathrm{J}_1,\dots,\mathrm{J}_8) = \frac{1}{2}k_1\,\mathrm{J}_1^2 + k_2\,\mathrm{J}_2 + \frac{1}{2}k_4\,\mathrm{J}_4^2 + \frac{1}{2}k_6\,\mathrm{J}_6^2 + \\ + k_{14}\,\mathrm{J}_1\mathrm{J}_4 + k_{16}\,\mathrm{J}_1\mathrm{J}_6 + \frac{1}{2}k_8\mathrm{J}_8^2.\end{aligned} \tag{3.88}$$

With these assumptions, the remodelling problem takes the following form:

$$2\,m_p\,\dot{\theta}_p = (1+r)\varepsilon_1^2\,F(\theta_p, r; k_4, k_{14}) + \frac{1}{2}\varepsilon_1^2\,k_8\,[G(\theta_p,\theta_s,r) + H(\theta_p,\theta_s,r)]\,, \tag{3.89}$$

$$2\,m_s\,\dot{\theta}_s = (1+r)\varepsilon_1^2\,F(\theta_s, r; k_6, k_{16}) + \frac{1}{2}\varepsilon_1^2\,k_8\,[G(\theta_s,\theta_p,r) + H(\theta_s,\theta_p,r)]\,, \tag{3.90}$$

where we have introduced the biaxiality ratio $r := -\varepsilon_2/\varepsilon_1$ between the transverse and longitudinal deformation, while the functions F, G and H are defined as

$$F(\theta_p, r; k_4, k_{14}) := \left[k_4(\cos^2\theta_p - r\sin^2\theta_p) + k_{14}(1-r)\right]\sin 2\theta_p\,, \tag{3.91}$$

$$G(\theta_p,\theta_s,r) := 2(1-r)\cos^2(\theta_p-\theta_s)\left(\cos\theta_p\cos\theta_s - r\sin\theta_p\sin\theta_s\right)\sin(\theta_p-\theta_s)\,, \tag{3.92}$$

$$H(\theta_p,\theta_s,r) := (1+r)\cos(\theta_p-\theta_s)\left(\cos\theta_p\cos\theta_s - r\sin\theta_p\sin\theta_s\right)\sin 2\theta_p\,. \tag{3.93}$$

A discussion of the reorientation dynamics prescribed by the equations above is postponed to the next Subsection.

Remark 3.5. The representation form of Eqs. (3.89)–(3.90) suggests to identify a system of elastic actions which contribute to the time rate of the fibre orientation angles θ_p and θ_s.

Firstly, we introduce the pair

$$\mathcal{T}_p := (1+r)\varepsilon_1^2 F(\theta_p, r; k_4, k_{14}) \quad \text{and} \quad \mathcal{T}_s := (1+r)\varepsilon_1^2 F(\theta_s, r; k_6, k_{16}) . \tag{3.94}$$

Then, we note that

$$G(\theta_s, \theta_p, r) = -G(\theta_p, \theta_s, r) . \tag{3.95}$$

As a consequence, we can identify the following mutual elastic interaction between the fibres:

$$\mathcal{T}_{ps} := \frac{1}{2}\varepsilon_1^2 k_8 G(\theta_p, \theta_s, r) , \tag{3.96}$$

dependent upon the constitutive coefficient k_8. In addition, we can define

$$\mathcal{T}_{Hp} := \frac{1}{2}\varepsilon_1^2 k_8 H(\theta_p, \theta_s, r) \quad \text{and} \quad \mathcal{T}_{Hs} := \frac{1}{2}\varepsilon_1^2 k_8 H(\theta_s, \theta_p, r) . \tag{3.97}$$

With these definitions on hand, the remodelling equations are compactly restated as

$$2m_p \dot{\theta}_p = \mathcal{T}_p + \mathcal{T}_{ps} + \mathcal{T}_{Hp} \quad \text{and} \quad 2m_s \dot{\theta}_s = \mathcal{T}_s - \mathcal{T}_{ps} + \mathcal{T}_{Hs} , \tag{3.98}$$

which have a more clear physical interpretation. Specifically, the time evolution of the orientation of the primary (resp. secondary) angle depends on the elastic actions $\mathcal{T}_p$ (resp. $\mathcal{T}_s$), $\mathcal{T}_{Hp}$ (resp. $\mathcal{T}_{Hs}$) and $\mathcal{T}_{ps}$ (resp. $-\mathcal{T}_{ps}$). $\mathcal{T}_p$ is defined in Eq. (3.94) and depends on the orientation θ_p (resp. θ_s) of the fibre itself and on the stretches ε_1, ε_2. On the other hand, the interactions $\mathcal{T}_{ps}$ and $\mathcal{T}_{Hp}$ (resp. $\mathcal{T}_{Hs}$) depend on both the orientations θ_p and θ_s and in particular they vanish when the two fibre families are constitutively uncoupled, that is, when k_8 is equal to zero.

It is of particular interest the evaluation of $\mathcal{T}_p$, $\mathcal{T}_s$, $\mathcal{T}_{Hp}$, $\mathcal{T}_{Hs}$ and $\mathcal{T}_{ps}$ when the stretch is equibiaxial, i.e., for $r = -1$, and then $\varepsilon_1 = \varepsilon_2 = \varepsilon$. In such a case, Eqs. (3.92), (3.96) and (3.97) imply $\mathcal{T}_p = \mathcal{T}_s = \mathcal{T}_{Hp} = \mathcal{T}_{Hs} = 0$ and

$$\mathcal{T}_{ps} = 2k_8 \varepsilon^2 \cos^3(\theta_p - \theta_s) \sin(\theta_p - \theta_s) = k_8 \varepsilon^2 \cos^2(\theta_p - \theta_s) \sin 2(\theta_p - \theta_s) , \tag{3.99}$$

meaning that the only non-zero term in the right-hand side of (3.98) is $\mathcal{T}_{ps}$. We recall that, as per Eq. (3.87), stationarity under equibiaxal stretch is attained if either $\sin 2(\theta_p - \theta_s) = 0$ or $w_8(\theta_p, \theta_s) = k_8 \mathrm{J}_8 = k_8 \varepsilon \cos^2(\theta_p - \theta_s) = 0$, for the specific energy that we are considering. Therefore, Eq. (3.99) states that the stationary value of the elastic interaction is zero in the equibiaxial case.

3.2.4 Constrained Reorientation

There may be practical cases in which the rotation of a fibre family induces the same rotation in the other family, in the sense that, during the remodelling process, the difference between the reoriented fibre angles remains the same. This behaviour is introduced in the modelling framework detailed above by properly constraining the elastic energy with a Lagrange multiplier. Among the many possible choices (see for instance [177]), guided by the experiments in [226] we require that the primary $\mathbb{R}_p$ and secondary $\mathbb{R}_s$ rotation tensors be equal at any time instant. As such, we introduce the representation of rotation tensors through the exponential maps [177] given by

$$\mathbb{R}_p = \exp \mathbb{\Omega}_p \quad \text{and} \quad \mathbb{R}_s = \exp \mathbb{\Omega}_s \,. \tag{3.100}$$

Then, $\mathbb{\Omega}_p = \mathbb{\Omega}_s$ implies $\mathbb{R}_p = \mathbb{R}_s$, and the constraint expression takes the form

$$\mathbb{\lambda}_{\mathrm{c}}(\mathbb{\Omega}_p, \mathbb{\Omega}_s) = \mathbb{\Omega}_p - \mathbb{\Omega}_s \,, \tag{3.101}$$

with the corresponding constrained energy given by

$$\widetilde{\mathcal{W}}(\mathbb{E}, \mathbb{A}, \mathbb{B}) = \mathcal{W}(\mathbb{E}, \mathbb{A}, \mathbb{B}) + \mathbb{\Lambda} : \mathbb{\lambda}_{\mathrm{c}}(\mathbb{\Omega}_p, \mathbb{\Omega}_s) \,. \tag{3.102}$$

Hence, the skew tensor field $\mathbb{\Lambda}$ is the Lagrange multiplier, which physically represents the reaction needed to maintain the relative rotation between the two fibre families the same. Equation (3.101) implies

$$\dot{\mathbb{\lambda}}_{\mathrm{c}}(\mathbb{R}_p, \mathbb{R}_s) = \dot{\mathbb{R}}_p \mathbb{R}_p^{\mathrm{T}} - \dot{\mathbb{R}}_s \mathbb{R}_s^{\mathrm{T}} \,. \tag{3.103}$$

On substituting (3.101) and (3.102) into the dissipation inequality, we arrive at

$$\begin{aligned} &\big(-\mathbb{P} + \mathbb{F} \frac{\partial \mathcal{W}}{\partial \mathbb{E}} \big) : \dot{\mathbb{F}} + \dot{\mathbb{\Lambda}} : \mathbb{\lambda}_{\mathrm{c}}(\mathbb{\Omega}_p, \mathbb{\Omega}_s) \\ &+ \big(-\mathbb{\Sigma}_p + [\frac{\partial \mathcal{W}}{\partial \mathbb{A}}, \mathbb{A}] + \mathbb{\Lambda} \big) : \dot{\mathbb{R}}_p \mathbb{R}_p^{\mathrm{T}} \\ &+ \big(-\mathbb{\Sigma}_s + [\frac{\partial \mathcal{W}}{\partial \mathbb{B}}, \mathbb{B}] - \mathbb{\Lambda} \big) : \dot{\mathbb{R}}_s \mathbb{R}_s^{\mathrm{T}} \leq 0 \,, \end{aligned}$$

which leads to the following system of *constrained* remodelling equations:

$$\begin{cases} \mathsf{D}_p\dot{\mathbb{R}}_p\mathbb{R}_p^{\mathrm{T}} = -[\dfrac{\partial\mathcal{W}}{\partial\mathbb{A}},\mathbb{A}] - \mathbb{\Lambda}, \\ \mathsf{D}_s\dot{\mathbb{R}}_s\mathbb{R}_s^{\mathrm{T}} = -[\dfrac{\partial\mathcal{W}}{\partial\mathbb{B}},\mathbb{B}] + \mathbb{\Lambda}, \\ \lambda(\mathbb{\Omega}_p,\mathbb{\Omega}_s) = \mathbb{O}. \end{cases} \tag{3.104}$$

Summing up the first two equations in (3.104), we obtain an evolution equation independent of the Lagrange multiplier $\mathbb{\Lambda}$:

$$\mathsf{D}_p\dot{\mathbb{R}}_p\mathbb{R}_p^{\mathrm{T}} + \mathsf{D}_s\dot{\mathbb{R}}_s\mathbb{R}_s^{\mathrm{T}} = -[\frac{\partial\mathcal{W}}{\partial\mathbb{A}},\mathbb{A}] - [\frac{\partial\mathcal{W}}{\partial\mathbb{B}},\mathbb{B}]$$

which, at stationarity, gives

$$[\frac{\partial\mathcal{W}}{\partial\mathbb{A}},\mathbb{A}]^* + [\frac{\partial\mathcal{W}}{\partial\mathbb{B}},\mathbb{B}]^* = \mathbb{O} = [\mathbb{E},\mathbb{S}]^*, \tag{3.105}$$

recovering the result in Eq. (3.80). On the other hand, by subtracting $(3.104)_1$ from $(3.104)_2$ and using (3.105), at stationarity we obtain

$$\mathbb{\Lambda}^* = [\frac{\partial\mathcal{W}}{\partial\mathbb{B}},\mathbb{B}]^*. \tag{3.106}$$

which furnishes the stationary values of the Lagrange multiplier $\mathbb{\Lambda}^*$. Equations (3.105), (3.106) together with the constraint equation $(3.104)_3$ are a system of nine equations. The nine unknowns are the six components (a_i, b_i) $(i = 1,2,3)$ and the three independent components of $\mathbb{\Lambda} \in \mathbb{S}\mathrm{kw}$. Therefore, in this constrained case, the equivalence between coaxiality of stress and strain and stationarity of the solutions of the remodelling equation is recovered thanks to the introduction of the multiplier $\mathbb{\Lambda}$. Indeed, if $(\mathbb{R}_p^*, \mathbb{R}_s^*)$ is a pair of rotations compatible with the constraint that makes stress and strain coaxial, then (3.105) is trivially satisfied. However, the reaction term $\mathbb{\Lambda}$ and the constraint equation guarantee that $(\mathbb{R}_p^*, \mathbb{R}_s^*)$ is also a stationary solution, as it is possible to find a value of $\mathbb{\Lambda}^*$ satisfying Eq. (3.106) once $\mathbf{a}^*$ and $\mathbf{b}^*$ are known.

When in-plane remodelling is considered, with $\mathbf{e}_3$ the orthogonal vector to the plane, we can set $\mathbb{\Omega}_p = (\theta_p - \theta_{p0}) \star \mathbf{e}_3$ and $\mathbb{\Omega}_s = (\theta_s - \theta_{s0}) \star \mathbf{e}_3$, where the operator $\star : \mathcal{V} \to \mathbb{S}\mathrm{kw}$ associates to each vector $\mathbf{w}$ a skew tensor $\mathbb{W}$ whose axial vector is $\mathbf{w}$, i.e. $(\star\mathbf{w})\mathbf{u} = \mathbf{w} \times \mathbf{u}$ for any $\mathbf{u} \in \mathcal{V}$. With this notation, we have $\mathbb{\Lambda} = \kappa \star \mathbf{e}_3$. As a consequence, the constraint

reduces to

$$\lambda_c(\theta_p,\theta_s) = (\theta_p - \theta_s) - (\theta_{p0} - \theta_{s0})\,, \tag{3.107}$$

whence the remodelling equations become

$$\begin{cases} 2m_p\,\dot{\theta}_p = (1+r)\,\varepsilon_1^2 F(\theta_p, r; k_4, k_{14}) + \frac{1}{2}\varepsilon_1^2 k_8\,[G(\theta_p,\theta_s,r) + H(\theta_p,\theta_s,r)] - 2\kappa \\ 2m_s\,\dot{\theta}_s = (1+r)\,\varepsilon_1^2 F(\theta_s, r; k_6, k_{16}) + \frac{1}{2}\varepsilon_1^2 k_8\,[G(\theta_s,\theta_p,r) + H(\theta_s,\theta_p,r)] + 2\kappa \\ \theta_p - \theta_s = \theta_{p0} - \theta_{s0}\,. \end{cases} \tag{3.108}$$

The constraint equation $(3.108)_3$ implies

$$\dot{\theta}_p - \dot{\theta}_s = 0$$

from which by summing and subtracting $(3.108)_1$ and $(3.108)_2$ we get

$$\begin{aligned} 2(m_p+m_s)\dot{\theta}_p = (1+r)\varepsilon_1^2\,[F(\theta_p,r;k_4,k_{14}) + F(\theta_s,r;k_6,k_{16})] \\ + \frac{1}{2}\varepsilon_1^2 k_8\,[H(\theta_p,\theta_s,r) + H(\theta_s,\theta_p,r)] \end{aligned} \tag{3.109}$$

and

$$\begin{aligned} 2(m_p-m_s)\dot{\theta}_p = (1+r)\varepsilon_1^2\,[F(\theta_p,r;k_4,k_{14}) - F(\theta_s,r;k_6,k_{16})] \\ + \frac{1}{2}\varepsilon_1^2 k_8\,[2G(\theta_p,\theta_s,r) + H(\theta_p,\theta_s,r) - H(\theta_s,\theta_p,r)] - 4\kappa, \end{aligned} \tag{3.110}$$

respectively, recalling (3.95). When the deformation is equibiaxial, $r=-1$ and by using the definitions of the functions F, G and H, Eq. (3.109) gives

$$2(m_p+m_s)\dot{\theta}_p = 0, \tag{3.111}$$

thus $\dot{\theta}_s = \dot{\theta}_p = 0$ and no evolution occurs as happened in the transversely isotropic case [72]. Moreover, Eq. (3.110) evaluated for $r=-1$ gives

$$\kappa = k_8\,\varepsilon_1^2 \cos^3(\theta_{p0} - \theta_{s0}) \sin(\theta_{p0} - \theta_{s0}) \tag{3.112}$$

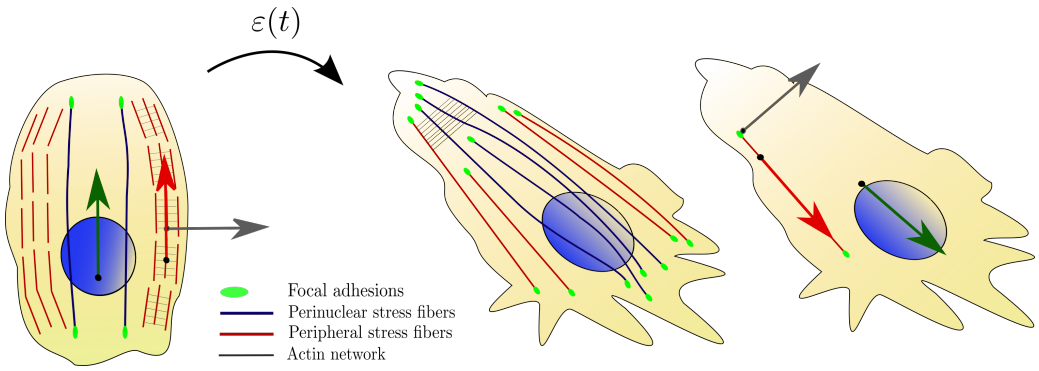

Fig. 3.10 Sketch of the cell structure and reorientation process. For comparison with experimental assays in [226], following [234], we consider the reorientation of the actin peripheral stress fibres (in red) which determine the alignment of the cell body, while the lateral protein network (in gray) is constrained to remain orthogonal to the SF. Instead, to compare our model with results in [308], we consider the peripheral stress fibres as the primary structure, whose orientation is changed according to $\mathbb{R}_p$, while the nucleus and the perinuclear stress fibres (in blue) that drive its orientation represent the secondary structure, evolving with $\mathbb{R}_s$.

and shows that the reaction κ is trivially constant. In particular, it is equal to zero either for fibres initially parallel, i.e., $\theta_{p0} - \theta_{s0} = k\pi$, or orthogonal, i.e., $\theta_{p0} - \theta_{s0} = \frac{\pi}{2} + k\pi$ ($k = 0, 1, ...$).

3.2.5 Comparison with Experimental Data

In this Section, we illustrate some applications of the proposed reorientation framework to the problem of cell alignment. This allows us both to discuss interesting implications of the model itself and to make a comparison with experimental data, showing the possibility of employing it to describe cytoskeletal remodelling. In particular, we will firstly consider a constrained case, in which the two fibre families cannot move with respect to each other: this may represent, for instance, the reorientation of actin stress fibres and lateral protein network. Then, we will focus on an unconstrained case, that may be relevant in the description of different stress fibre subtypes [308].

The Case of Constrained Reorientation

We consider here a case in which the two fibre families represent the cell aligned stress fibres and the orthogonal protein network, as sketched in Fig. 3.10. Such a choice mirrors the one made by Livne and coworkers [226] and ourselves [234] in Section 3.1. In the

following, we show that our model is able to recover the results in [226, 234] as a particular case, without the need of any phenomenological justification of the evolution equation.

As a starting point, following Section 3.1, we consider the cell monolayer as an hyperelastic anisotropic material, characterized by the strain energy function defined in Eq. (3.88). Then, we introduce the two assumptions also (implicitly) done in [226]: (1) the families of fibres are orthogonal in the reference configuration and constrained to remain orthogonal during remodelling; and (2) the fibres lie in the plane of unit normal $\mathbf{e}_3$. Finally, we consider a deformation of the substrate defined by $\mathbb{E} = \mathrm{diag}(\varepsilon_1, -r\varepsilon_1, 0)$.

In doing so, we are able to apply the constrained in-plane remodelling theory derived in Section 3.2.4 and to write the reorientation equations using (3.108). If we take into account that the fibres are orthogonal, i.e. $\theta_{p0} - \theta_{s0} = \pi/2$, the constraint becomes $\lambda_c(\theta_p, \theta_s) = (\theta_p - \theta_s) - \pi/2 = 0$, which also implies $\dot{\lambda}_c(\theta_p, \theta_s) = \dot{\theta}_p - \dot{\theta}_s = 0$. Moreover, the orthogonality of the fibres yields

$$G(\theta_p, \theta_s, r) = G(\theta_s, \theta_p, r) = 0 \quad \text{and} \quad H(\theta_p, \theta_s, r) = H(\theta_s, \theta_p, r) = 0,$$

and the remodelling equations are simplified as

$$\begin{cases} 2m_p\,\dot{\theta}_p = (1+r)\varepsilon_1^2 F(\theta_p, r; k_4, k_{14}) - 2\kappa\,, \\ 2m_s\,\dot{\theta}_s = (1+r)\varepsilon_1^2 F(\theta_s, r; k_6, k_{16}) + 2\kappa\,. \end{cases} \tag{3.113}$$

Summing up the two equations and exploiting the constraint, we can obtain an evolution equation for the primary cell orientation θ_p:

$$\widehat{m}\,\dot{\theta}_p = (1+r)\varepsilon_1^2 \left[\widehat{k}_p(\cos^2\theta_p - r\sin^2\theta_p) + k_m(1-r)\right]\sin 2\theta_p\,, \tag{3.114}$$

where

$$\widehat{m} := 2(m_p + m_s)\,, \qquad \widehat{k}_p := k_4 + k_6\,, \qquad k_m := k_{14} - k_{16} - k_6\,.$$

The stationary solutions of Eq. (3.114) can be readily identified: they correspond either to the cell being aligned with the principal directions of strain, i.e. $\theta_p^* = k\pi/2$, $k \in \mathbb{Z}$, or to the oblique orientations defined by

$$\cos^2\theta_p^* = 1 + \frac{k_m}{\widehat{k}_p} - \frac{1}{1+r}\left(1 + 2\frac{k_m}{\widehat{k}_p}\right) = \frac{1}{2} + \mathcal{K}\left(\frac{1}{2} - \frac{1}{1+r}\right), \tag{3.115}$$

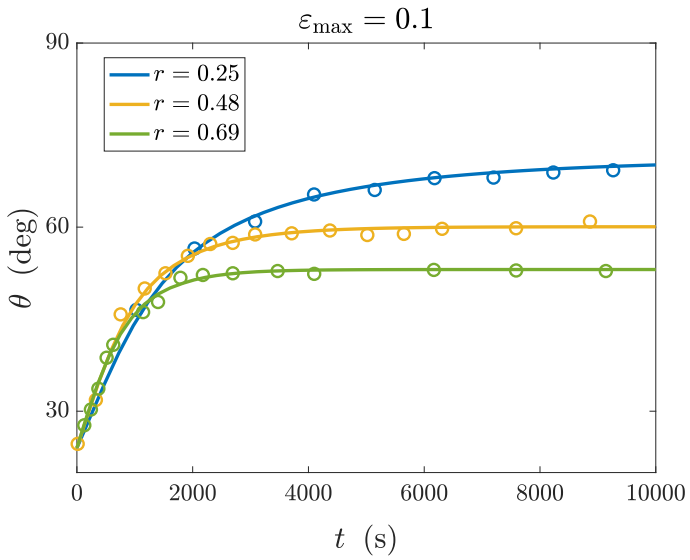

Fig. 3.11 Evolution of the cell orientation angle θ_p with maximum strain of 10%, following Eq. (3.114), for different values of the biaxiality ratio r. The curves show the best fitting of the model, while the dots represent experimental data taken from [226].

where $\mathcal{K} := 1 + 2k_m/\widehat{k}_p$. Such a result is coherent with our previously derived findings, recalling Eq. (3.22). However, in our model we did not postulate the evolution equation (3.114) as done for instance by Livne and coworkers [226], but rather derived it from a more general framework which lays on balance principles and thermodynamics. Clearly, the oblique stationary solutions only exist when $r \neq -1$ and the right-hand side of Eq. (3.115) has a value between 0 and 1; for details on the bifurcation analysis of the orientations, we refer the reader to Section 3.1.4.

The Lagrange multiplier κ, that represents the reaction needed to keep the fibres orthogonal, can be evaluated at stationarity through

$$4\kappa^* = (1+r)\varepsilon_1^2 \left[(k_4 - k_6)(\cos^2\theta_p^* - r\sin^2\theta_p^*) + (k_{14} + k_{16} + k_6)(1-r)\right] \sin 2\theta_p^*.$$

We observe that, when the cell is aligned with the principal strain directions, $\kappa^* = 0$. Indeed the same holds true when $r = -1$ (see Eq. (3.114)), i.e. in the case of equibiaxial deformation when no reorientation occurs. For oblique orientations, instead, we have

$$4\kappa^* = 2(1-r^2)\varepsilon_1^2 \frac{k_4 k_{16} + k_4 k_6 + k_6 k_{14}}{k_4 + k_6} \sin 2\theta_p^*,$$

which is in general different from zero provided that $r \neq 1$.

r	$k_m/\widehat{k}_p$	τ [s]
0.25	0.1594	7.3
0.48	0.2142	5.9
0.69	0.2596	5.7

Table 3.1 Constitutive parameters in Eq. (3.114) estimated from the fitting of experiments in [226].

We conclude this discussion by comparing the prediction of the constrained model with the data on cell reorientation in [226]. It can be seen from Eq. (3.114) that the three parameters $\widehat{k}_p, k_m$ and τ, where the latter is the characteristic time inside $\widehat{m}$, have to be calibrated. The results of this procedure, carried out through a nonlinear least square algorithm, are shown in Figure 3.11. The model matches accurately the evolution of the orientation angles seen in the experiments. The optimal parameters used for the fitting for $r \in \{0.25, 0.48, 0.69\}$ are listed in Table 3.1 and are indeed coherent with experiments in [226], where the authors found a value of the ratio $k_m/\widehat{k}_p = 0.13 \pm 0.04$ and a characteristic time $\tau = 6.6 \pm 0.4$ s.

It is worth noting that the evolution of the angle in Eq. (3.114) only depends on three constitutive parameters including a characteristic time. The evaluation of the other model coefficients, necessary to estimate the Lagrange multiplier κ^*, would require further experimental data.

Remark 3.6. In the general case of two plane fibre families constrained to remain orthogonal, namely such that $\mathbb{A} + \mathbb{B} = \breve{\mathbb{I}}$ with $\breve{\mathbb{I}}$ the identity tensor in the fibre plane, it can be easily shown that the stationarity requirement

$$[\frac{\partial \mathcal{W}}{\partial \mathbb{A}}, \mathbb{A}]^* + [\frac{\partial \mathcal{W}}{\partial \mathbb{B}}, \mathbb{B}]^* = \mathbb{O} \tag{3.116}$$

implies

$$[\mathbb{E}, (w_4^* - w_6^*)\mathbb{A}^* + (w_5^* - w_7^*)(\mathbb{A}^*\mathbb{E} + \mathbb{E}\mathbb{A}^*)] = \mathbb{O}, \tag{3.117}$$

which has the following consequences:

1. If $w_6 = w_7 = 0$ identically, meaning that there is a single fibre family, the relation $[\mathbb{E}, \mathbb{S}^*] = \mathbb{O}$ for a transversely isotropic material found in [72] is recovered.

2. If the remodelled direction **a** is along a principal direction of strain (and then so is **b** because they are orthogonal), the commutator on the l.h.s. of (3.117) is null.

Therefore, rotations that align the preferential orientations with the principal strain directions are always stationary solutions of the problem at hand.

3. If $\mathbf{a}$ is not aligned with a principal strain direction, there might be additional non-trivial solutions identified by the two conditions

$$w_4^*(\mathbb{E},\mathbb{A}^*) = w_6^*(\mathbb{E},\mathbb{A}^*) \quad \text{and} \quad w_5^*(\mathbb{E},\mathbb{A}^*) = w_7^*(\mathbb{E},\mathbb{A}^*).$$

It is also immediate to observe that the relation (3.117) is consistent with Eq. (3.12), as expected. The only difference lies in the presence of w_8 which does not appear here: this is due to the different definition of the invariant I_8 employed in the present Section, compared with the one used in Section 3.1. However, it is easily possible to show that, if the definition of I_8 given in Eq. (3.2) is instead adopted, then the result in Eq. (3.12) is completely recovered. Indeed, in this case the commutator between the strain tensor and the second Piola-Kirchhoff stress tensor can be written as

$$[\mathbb{E}, (w_4 - w_6)\mathbb{A} + (w_5 - w_7)(\mathbb{A}\mathbb{E} + \mathbb{E}\mathbb{A}) + w_8 \,\mathrm{Sym}(\mathbf{a}\otimes\mathbf{b})] = \mathbb{O}\,, \tag{3.118}$$

which is precisely equivalent to Eqs. (3.11)–(3.12).

The Case of Independent Reorientation

The complex interaction between the cell nucleus and the cytoplasm can be still captured by the proposed model in terms of changes in their relative orientation when cells are cyclically stretched. In [308], the mechanoadaptive organization of stress fibres and nuclei in epithelial cells under cyclic stretches is considered, highlighting that these two cellular components follow different orientation dynamics. In particular, epithelial cells on a plane substrate were stretched for 2 hours at 5%, 10% and 15% maximum strains whilst measuring the reorientation of the different stress fibre subtypes. It was seen that dorsal stress fibres, transverse arcs, and peripheral stress fibres were mainly involved in the cytoplasm response whereas perinuclear cap fibres were associated with the reorientation and elongation of the nucleus (see Fig. 3.10).

A sketch of the experimental set-up of [308] is shown in Fig. 3.12(a) where the coloured arrows are used to indicate the primary (red) and secondary (green) cell structures, i.e., cytoplasm and nucleus of the cell, respectively. In the experiments, the longitudinal strain ε_1 was controlled for 2 hours with the time history shown in inset 3.12(b) at three different

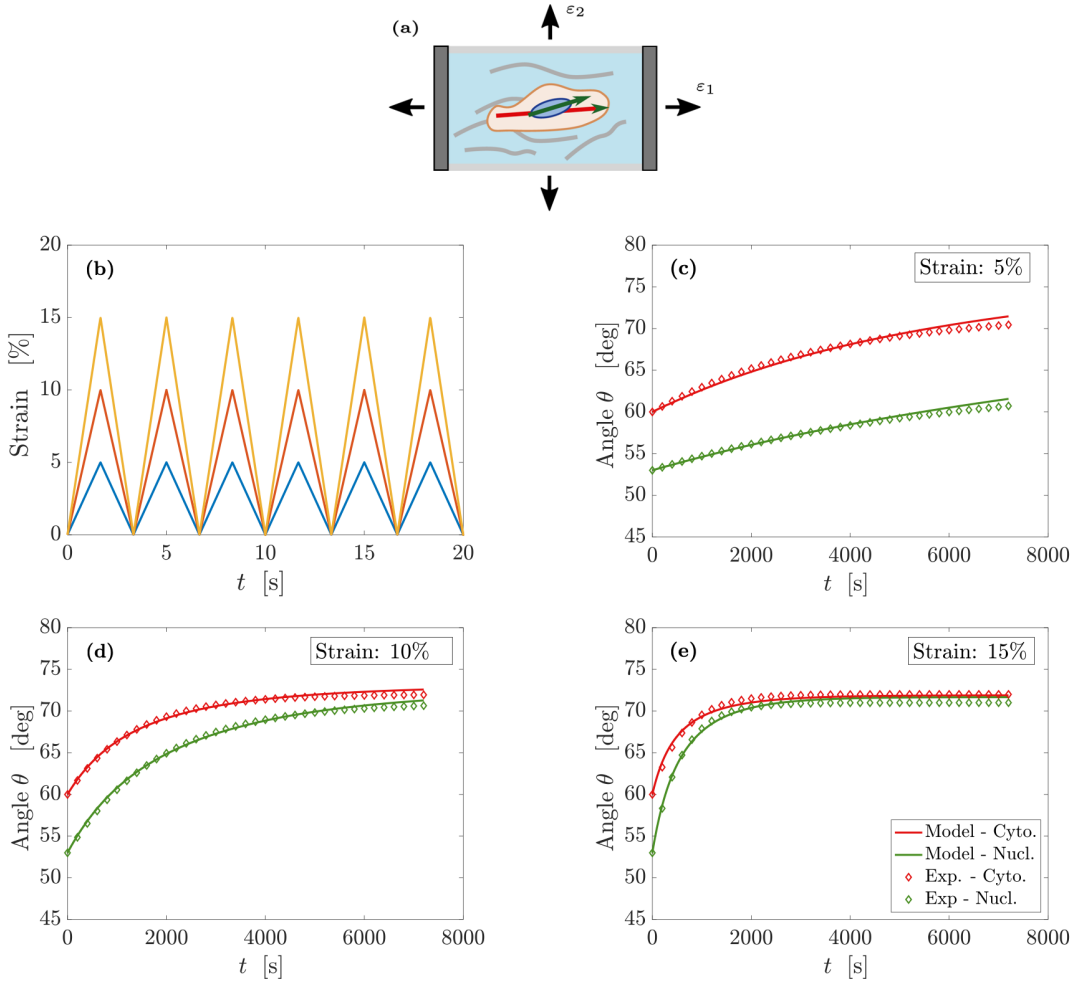

Fig. 3.12 (a): Sketch of the experiments in [308], where the substrate is deformed with a periodic strain. The peripheral (red) and the perinuclear (green) fibres represent the two fibre families. (b): Time history of the longitudinal strain ε_1 imposed to the substrate, with maximum amplitude of 5% (blue curve), 10% (red curve), and 15% (yellow curve). (c)–(e): Evolution of the orientation angles of cytoplasm and nucleus for a maximum strain of 5% (c), 10% (d) and 15% (e), compared with experimental results from [308]. The curves represent the best fitting obtained for the given data.

Table 3.2 Constitutive parameters in Eqs. (3.89)–(3.90) identified from the experiments in [308].

$\varepsilon_{\max}$	k_{14}/k_4	k_{16}/k_6	k_6/k_4	k_8/k_4	τ_p $[s]$	τ_s $[s]$
5%	26.5	3.3	9.75	55	128	313
10%	26.5	3.3	9.75	72	148	193
15%	26.5	3.3	9.75	76.25	128	133

level of maximum strain (5%, 10% and 15%); the lateral strain was also controlled in a way that $r = -\varepsilon_2/\varepsilon_1 = 0.49$ and the frequency of the deformation was set to 0.3 Hz. The plots in Fig. 3.12(c)-(e) were obtained by fitting the experimental data against Eqs. (3.89)-(3.90) (with $m_p = k_4\tau_p$ and $m_s = k_6\tau_s$), through a nonlinear least square algorithm implemented in MATLAB®. The corresponding best fit parameters are listed in Table 3.2. The stretch dependence for both the primary and secondary angles is well captured by the model for all the different values of applied strain and with very similar parameters. Interestingly, it can be observed that the main differences in the best fitting parameters are represented by k_8 and τ_s, which are related to the coupling between the fibre families and to the nucleus reorientation time, respectively. In particular, as the maximum applied strain increases, an increase in the coupling parameter also happens, leading to a corresponding decrease in the nucleus characteristic time. Therefore, the model predicts that the constitutive coupling between the fibre families becomes stronger as the applied deformation increases in magnitude. The decrease of the nucleus characteristic time for greater strains is also coherent with the experimental observations by Roshanzadeh and coworkers [308].

3.2.6 Discussion

Starting from a very general theory previously developed for transversely isotropic materials, in this Section we have proposed a remodelling framework to describe the reorientation of a material structure that features two families of fibres. The main novelty of our approach lies in the fact that the two preferential directions may change in time following different evolution dynamics, without being a priori constrained to keep the relative angle fixed. However, the fibres can be properly coupled by making appropriate constitutive choices, for instance concerning the hyperelastic strain energy density. The thermodynamically consistent structure of the model also offers an advantage over phenomenological approaches sometimes pursued in the literature.

After having derived the balance and remodelling equations, we thoroughly studied the stationary solutions of the latter. Interestingly, the addition of a fibre family which is able to reorient following its own dynamics leads to a generalisation of the well-known coaxiality result by Vianello. The equivalence between critical points of the elastic energy and coaxiality of strain and stress is then recovered by introducing a proper constraint between the two fibres, making them rotate without any change in their relative angle. Therefore, the case of two material structures that remodel with different rotation tensors does not turn out to be a simple generalisation of the transversely isotropic case, but rather provides a more complex enrichment of the reorientation theory for orthotropic materials.

The framework proposed in this Section remains very general and could therefore be readily adapted to describe materials like composites with two families of fibres which are engineered to reorient according to different stimuli. However, we chose to focus on biological applications of cell reorientation under external mechanical cues, in order to study the cytoskeletal remodelling in more detail. We found that our model is able to reproduce some experimental data from different groups [226, 308], both for constrained and unconstrained fibres, representing different structures of the cytoskeleton. In particular, when experiments by Livne and collaborators are considered [226], we recovered the preferential orientations derived in Section 3.1 as a particular case for orthogonal fibres. Then, we tested the behaviour of our model in a case where the fibres are not fixed to keep the initial angle, following experimental assays by Roshanzadeh et al. [308]. An interesting outcome in this case suggests that greater deformation magnitudes are associated with a stronger coupling between peripheral stress fibres and perinuclear cap fibres.

In summary, we have derived a system of equations capable of describing the remodelling of a material with two preferential directions, which can rotate independently but in a coupled way. From a theoretical viewpoint, we found that a generalisation of well-known results about coaxiality holds and is related to the stationary solutions of the system. Then, considering applications to cell layers under stretch, our results suggest the feasibility and flexibility of our framework for the description of cytoskeletal reorientation dynamics.

As a final remark, we recall that all the equations derived in this Section hold for a nonlinear elastic material, while no viscous effects have been incorporated.

3.3 Linear Viscoelastic Description

As discussed in Chapter 2, there are several mechanical factors that influence the process of cell reorientation under substrate stretching. Nevertheless, the mathematical models proposed in the previous Sections to investigate such a problem were mainly concerned with the relation between the cell orientation angle and the amplitude of the periodic deformation. Moreover, the important role of the biaxiality ratio r has been highlighted and analysed in detail. However, an additional relevant factor to be taken into account is the *frequency* of the applied stretch. As a matter of fact, as already pointed out in Section 2.1.2, in order to trigger a cellular response the period of the stretching cycle must be sufficiently small, or equivalently there is a lower frequency threshold [171, 190]. As specified in [190], this threshold seems to be cell-type dependent, leading to minimum frequencies that go from 0.01 Hz for rat embryonic fibroblasts to 0.1 Hz for human dermal fibroblasts. Furthermore, we recall that also an upper threshold seems to exist, above which there is no increase in the reorientation speed of the cells due to saturation of the molecular mechanisms.

The presence of these threshold effects cannot be covered by the purely elastic descriptions discussed above, and calls for the introduction of a characteristic response time that needs to be compared with the periodic deformation time scale. The existence of such a characteristic time might be related to the reorganisation of the acto-myosin cytoskeleton and to the remodelling of the ensemble of focal adhesions with the substrate. Indeed, it is known that the characteristic turnover times of both phenomena are of the order of tens of seconds, or even minutes (see, for instance, [68, 282, 284, 397]).

On the basis of these facts, in this Section we enrich the previous descriptions by proposing a simple viscoelastic model for cell preferential orientations, in order to account for reorganisation processes occurring inside the cell and between the cell and its microenvironment when a deformation is applied to the substrate. To our knowledge, previous viscoelastic descriptions of cell stress fibre dynamics have been mainly focused on the microscopic scale [205, 295], while here we treat the cell and the substrate as a continuum. In particular, we introduce an anisotropic viscoelastic framework that couples the evolution of the stress fibre orientation angle with the mechanical stress exerted on the cell as a consequence of cyclic stretching. Hence, the ensemble of cells lying on the substrate is considered as a Maxwell orthotropic fluid with a single relaxation time. We prove that, for high stretching frequencies, the cell cytoskeleton does not have enough time to reorganise and behaves elastically, while for slow frequencies the viscous character emerges and the

system behaves like a fluid. Furthermore, after having showed that the preferred angles are predicted by an energy minimization which mimics the one presented in Section 3.1, we perform an extensive bifurcation analysis, discussing the role of elastic parameters and finding the conditions under which a certain angle of cell orientation is stable. We find that also in this general set-up there exists a linear relationship between $\cos^2\theta_{eq}$ and a combination of parameters of the orthotropic elasticity tensor.

Finally, we perform some numerical simulations using the complete viscoelastic model, to study the reorientation dynamics in the high frequency and low frequency cases together with stress evolution. It is found that the cell orientation angle evolves toward the steady state predicted by the linear stability analysis, with a speed which depends on the elastic or viscous character of the system. Moreover, in accordance with the observation in [171, 190], simulations show that the speed of reorientation towards the equilibrium angle sensibly depends on the frequency of imposed oscillations. In particular, it presents a transition for values of the ratio of the oscillation period and the characteristic time of viscoelasticity close to 2π, so that the time required to observe reorientation is of the order of days for smaller frequencies, saturating to one hour for larger frequencies.

3.3.1 Viscoelastic Model

We consider a two-dimensional substrate seeded of cells that is stretched biaxially. While the response of the extracellular material is in general isotropic and elastic, the mechanical behaviour of the ensemble of cells can be regarded as anisotropic and viscoelastic. The viscoelastic character is due to the reorganization of the acto-myosin network inside the cell and to the rearrangement of focal adhesions, performed through repeated detachments and attachments of integrin bonds with the substrate, especially under stretch, to relax the perceived stress [293]. Instead, anisotropy derives from the fact that, when subject to a mechanical deformation, cells tend to build properly oriented actin stress fibers within their cytoskeleton [180, 378]. In addition, these SFs are linked by a network of proteins (such as fascin, fimbrin, α-actinin, filamin, ARP2-3 [75, 138, 310, 377]) that spans them orthogonally with respect to the fibre bundles or at well-defined angles, as in the case or ARP2-3, as sketched in Fig. 3.1. As a consequence, the cell responds differently to stretches and stresses along its major axis with respect to the transversal axis and to shear as well.

The main orientation of SFs, which will be identified by a unit vector $\mathbf{N}$, can change in time due to the mechanical cue. We will here consider, as in experiments, that the specimen

is subject to a biaxial stretch and take the x-axis aligned to the direction of maximal stretch. Then, the angle formed by $\mathbf{N}$ and the x-axis will be denoted by θ.

Resorting to Lagrangian mechanics, we can relate the evolution in time of the orientation angle θ with the changes in the virtual work $\mathcal{L}$ done by the stress acting on the cell due to SF alignment. Considering an overdamped regime, which corresponds to neglecting inertial effects, we can then write

$$0 = -\eta \frac{d\theta}{dt} - \frac{\partial \mathcal{L}}{\partial \theta}, \tag{3.119}$$

where $\mathcal{L} := \mathbb{T} : \mathbb{E}$, being $\mathbb{T}$ the excess Cauchy stress tensor and $\mathbb{E}$ the infinitesimal deformation tensor, is the work done by the stress, assuming that the mechanical behaviour is linear.

Remark 3.7. We choose to employ the same notation $\mathbb{E}$ to denote both the Green-Lagrange strain tensor and the infinitesimal deformation tensor. Indeed, in the linear elastic limit that we are studying in this Section they coincide. Therefore, unless otherwise stated, in the following $\mathbb{E}$ will refer to a small deformation.

Moreover, $\eta > 0$ is a viscous-like coefficient measuring cell resistance to realignment. Since we are interested in deformation tests, where a periodic stretch is imposed to the specimen, $\mathbb{E}$ is assumed to be independent of θ and externally imposed. It is then convenient to rearrange Eq. (3.119) to get the following evolution equation for $\theta(t)$:

$$\frac{d\theta}{dt}(t) = -\frac{1}{E\lambda_\theta} \frac{\partial \mathbb{T}}{\partial \theta}(t|\theta) : \mathbb{E}(t), \tag{3.120}$$

where we identified E as the characteristic Young modulus of the material and $\lambda_\theta := \eta/E$ as a parameter related to the time the cell takes to reorient itself. The notation $\mathbb{T}(t|\theta)$ reads as the stress at time t given the history of orientations θ.

Equation (3.120) implies that, for a given deformation $\mathbb{E}$, θ tends to assume a value such that the variation of $\mathbb{T}$ with respect to θ either vanishes or becomes orthogonal to $\mathbb{E}$.

Focusing on $\mathbb{T}$, we assume here that the stress in the elastic substrate and the viscoelastic cellular component embedded in it is given by

$$\mathbb{T}(t|\theta) = \int_{-\infty}^{t} \mathsf{C}(\theta(\tau); t-\tau)[\mathbb{E}(t) - \mathbb{E}(\tau)]\, \mathrm{d}\tau, \tag{3.121}$$

(see, for instance, [23] for the isotropic case and [287, 288] for the anisotropic case). We notice that the elements of the fourth-order tensor C are all bounded and that, in the

isotropic case, C reduces to the derivative of the so-called relaxation kernel (apart from the sign) times the identity tensor. The kernel C depends on the alignment direction, i.e. on the orientation angle θ, which during the history of deformation can evolve in time. On the other hand, the second part of the kernel dependence takes into account the weight of past orientations (at time τ) on the present state of stress and represents memory effects of the viscoelastic material. We will assume that such a dependence is exponential with a single relaxation time λ [287, 288], that is,

$$\mathsf{C}(\theta(\tau);t-\tau) = \frac{1}{\lambda}\mathsf{C}_0(\theta(\tau))e^{-(t-\tau)/\lambda}, \tag{3.122}$$

where $\mathsf{C}_0(\theta(\tau))$, which is the fourth-order elasticity tensor depending on the orientation direction θ at time τ, inherits from C the boundedness and regularity properties. Therefore, we can write

$$\mathbb{T}(t|\theta) = \int_{-\infty}^{t} \frac{1}{\lambda}e^{-(t-\tau)/\lambda}\mathsf{C}_0(\theta(\tau))[\mathbb{E}(t)-\mathbb{E}(\tau)]\,\mathrm{d}\tau\,. \tag{3.123}$$

As usual in rheology, for this type of kernels it is useful to differentiate (3.123) and to rewrite the constitutive equation in the following differential form:

$$\lambda\frac{d\mathbb{T}}{dt}(t|\theta) + \mathbb{T}(t|\theta) = \mathfrak{C}_0(t|\theta)\frac{d\mathbb{E}}{dt}(t)\,, \tag{3.124}$$

where

$$\mathfrak{C}_0(t|\theta) := \int_{-\infty}^{t} e^{-(t-\tau)/\lambda}\mathsf{C}_0(\theta(\tau))\,\mathrm{d}\tau = \int_0^{+\infty}\lambda e^{-s}\mathsf{C}_0(\theta(t-\lambda s))\,\mathrm{d}s\,, \tag{3.125}$$

is a functional on the exponentially weighted history of past orientations. We observe that, in the isotropic case, $\mathfrak{C}_0$ is twice the so-called elastic viscosity, i.e., the area under the relaxation kernel (times the identity tensor).

In Eq. (3.120) and (3.124) there are two intrinsic characteristic times that appear: λ refers to the viscous behaviour of cells due, for instance, to the continuous renewal of adhesion bonds with the substrate, while λ_θ is related to the characteristic time of reorganization of stress fibres and consequently to the change in cell orientation. It is known that both remodelling phenomena occur on time scales of seconds or even minutes [68, 282, 284, 397]. Now, given that in mechanical tests cells are often subject to cyclic strains, it is useful to discuss how the model behaves when the imposed oscillation period T is much shorter or longer than the characteristic times mentioned above. In order to do so, we observe that, for a periodic deformation $\mathbb{E}(t) = \mathbb{E}_0 e^{i\omega t}$, the expression of the stress

given by Eq. (3.123) can be rephrased as

$$\mathbb{T}(t|\theta) = \frac{1}{\lambda}\left[\int_{-\infty}^{t} e^{-(t-\tau)/\lambda}\,\mathsf{C}_0(\theta(\tau))\left(1-e^{-i\omega(t-\tau)/\lambda}\right)\,\mathrm{d}\tau\right]\mathbb{E}_0 e^{i\omega t}$$

$$= \left[\int_{0}^{+\infty} e^{-s}\,\mathsf{C}_0(\theta(t-\lambda s))\left(1-e^{-i\lambda\omega s}\right)\,\mathrm{d}s\right]\mathbb{E}_0 e^{i\omega t}\,. \tag{3.126}$$

High Frequency Regime

First of all, we consider a high frequency regime with $\lambda, \lambda_\theta \gg T = 2\pi/\omega$, so that the relaxation times are much longer than the oscillation period of the deformation, i.e., the reorganization process is slower than the imposed cyclic strain. In this case, it is useful to split the integral in Eq. (3.126) as

$$\mathbb{T}(t|\theta) = \left[\int_{0}^{+\infty} e^{-s}\mathsf{C}_0(\theta(t-\lambda s))\,\mathrm{d}s\right]\mathbb{E}_0 e^{i\omega t}$$
$$-\left[\int_{0}^{+\infty} e^{-s}\mathsf{C}_0(\theta(t-\lambda s))e^{-i\lambda\omega s}\,\mathrm{d}s\right]\mathbb{E}_0 e^{i\omega t}. \tag{3.127}$$

We observe that, as stated before, the coefficients of tensor $\mathsf{C}_0(\theta(t))$ are regular in θ. In particular, they are bounded as well as their derivatives. Hence, by Riemann-Lebesgue lemma, the second integral in the r.h.s. of Eq. (3.127), which can be regarded as the unilateral Fourier transform of the L^1 function $e^{-s}\mathsf{C}_0(\theta(t-\lambda s))$, vanishes in the limit of high frequencies.

As regards the first term, integrating by parts and exploiting Eq. (3.120) we have

$$\mathbb{T}(t|\theta) = \left[\mathsf{C}_0(\theta(t)) + \frac{\lambda}{E\lambda_\theta}\int_{0}^{+\infty} e^{-s}\frac{\partial \mathsf{C}_0}{\partial\theta}(\theta(t-\lambda s))\frac{\partial\mathbb{T}}{\partial\theta}(t-\lambda s|\theta) : \mathbb{E}_0 e^{i\omega(t-\lambda s)}\,\mathrm{d}s\right]\mathbb{E}_0 e^{i\omega t}$$

$$= \mathsf{C}_0(\theta(t))\mathbb{E}_0 e^{i\omega t} + \left[\frac{\lambda}{E\lambda_\theta}\int_{0}^{+\infty} e^{-s}\frac{\partial \mathsf{C}_0}{\partial\theta}(\theta(t-\lambda s))\frac{\partial\mathbb{T}}{\partial\theta}(t-\lambda s|\theta) : \mathbb{E}_0 e^{-i\lambda\omega s}\,\mathrm{d}s\right]\mathbb{E}_0 e^{i2\omega t}.$$

Provided that, denoting by $H(s)$ the Heaviside function, the function

$$f(s) = H(s)\frac{\partial \mathsf{C}_0}{\partial\theta}(\theta(t-\lambda s))\frac{\partial\mathbb{T}}{\partial\theta}(t-\lambda s|\theta) : \mathbb{E}_0 e^{-s} \quad \in L^1(\mathbb{R})\,,$$

as we expect because of the boundedness of the derivative of the coefficients in C_0, the integral in the stress expression corresponds to the Fourier transform of $f(s)$, which again

vanishes in the limit of high frequencies. Hence, in the high frequency regime we are left with

$$\mathbb{T}(t|\theta) \approx \mathsf{C}_0(\theta(t))\mathbb{E}_0 e^{i\omega t}. \tag{3.128}$$

Such a constitutive equation corresponds to an anisotropic linear elastic response of the material, where $\mathsf{C}_0(\theta(t))$ is the fourth-order elasticity tensor depending on the orientation θ. So, in the high frequency regime, Eq. (3.120) can be simplified to

$$\frac{d\theta}{dt} = -\frac{1}{\eta}\left[\frac{\partial \mathsf{C}_0}{\partial \theta}\mathbb{E}\right] : \mathbb{E} = -\frac{2}{E\lambda_\theta}\frac{\partial \mathcal{W}}{\partial \theta}, \tag{3.129}$$

where

$$\mathcal{W}(t,\theta) := \frac{1}{2}\mathbb{E}(t) : \mathsf{C}_0(\theta)\mathbb{E}(t), \tag{3.130}$$

is the elastic strain energy. Therefore, in this regime, the change in cell orientation is driven by the minimization of an elastic energy with respect to the orientation angle, coherently with previous models and experimental results [226, 234].

Low Frequency Regime

In a low frequency regime, in which the period of the cyclic strain imposed to the specimen is much longer than the characteristic time λ of cell relaxation, the reorientation process is faster than the externally applied oscillations. Therefore, taking into account the approximation $\lambda \ll T = 2\pi/\omega$, or equivalently $\lambda\omega \ll 1$, we have that

$$1 - e^{-i\lambda\omega s} \approx i\lambda\omega s,$$

and the stress can be expressed using Eq. (3.126) through

$$\mathbb{T}(t|\theta) \approx i\lambda\omega\left[\int_0^{+\infty} s e^{-s}\mathsf{C}_0(\theta(t-\lambda s))\,\mathrm{d}s\right]\mathbb{E}_0 e^{i\omega t}, \tag{3.131}$$

which, if we define

$$\overline{\mathsf{C}}_0(t|\theta) := \int_0^{+\infty} s e^{-s}\mathsf{C}_0(\theta(t-\lambda s))\,\mathrm{d}s,$$

shows an anisotropic viscous-like response characterized by the constitutive equation

$$\mathbb{T}(t|\theta) \approx \lambda\overline{\mathsf{C}}_0(t|\theta)\frac{d\mathbb{E}}{dt}(t). \tag{3.132}$$

Essentially, if the imposed oscillations are sufficiently slow, the system behaviour is similar to the one of a viscous fluid with anisotropy induced by oriented cells. Moreover, since we are mostly interested in steady orientations, given that $\mathsf{C}_0(\theta(t-\lambda s))$ is an analytic function on $\mathbb{R}$ it is possible to write

$$\mathsf{C}_0(\theta(t-\lambda s)) = \mathsf{C}_0(\theta(t)) + \mathsf{C}_0'(\theta(t))\frac{d\theta}{dt}(t)(-\lambda s) + \frac{1}{2}\left[\mathsf{C}_0''(\theta(t))\left(\frac{d\theta}{dt}(t)\right)^2 + \mathsf{C}_0'(\theta(t))\frac{d^2\theta}{dt^2}(t)\right](-\lambda s)^2 + \dots$$

and therefore, at the equilibrium orientations,

$$\mathsf{C}_0(\theta(t-\lambda s)) \approx \mathsf{C}_0(\theta(t)). \tag{3.133}$$

By means of this approximation, we can write the steady state oscillatory stress in the low frequency regime using Eq. (3.132) and Eq. (3.133) as

$$\mathbb{T}(t|\theta) \approx \lambda \mathsf{C}_0(\theta(t))\frac{d\mathbb{E}}{dt}(t)\,. \tag{3.134}$$

Comparing the latter with the stress in the high frequency case from Eq. (3.128), we observe that they essentially differ for a factor $\lambda\omega$, as will be highlighted by the simulations. Finally, recalling Eq. (3.120), we have that the angle θ tends to assume, as already stated, the configuration such that $\frac{\partial \mathbb{T}}{\partial \theta} \perp \mathbb{E}$, which in the low frequency limit writes as

$$\left(\frac{\partial \mathsf{C}_0}{\partial \theta}\frac{d\mathbb{E}}{dt}\right) \perp \mathbb{E}\,.$$

However, since the deformation is periodic, the last condition can be rephrased as

$$i\omega\left(\frac{\partial \mathsf{C}_0}{\partial \theta}\mathbb{E}_0\right) : \mathbb{E}_0 = 0 \qquad \Longrightarrow \qquad \frac{\partial \mathcal{W}}{\partial \theta} = 0\,,$$

where $\mathcal{W}$ is the elastic energy defined in (3.130). Therefore, we conclude that in the low frequency regime also in the viscoelastic case the steady cell configurations are predicted by a minimization with respect to the orientation angle θ of the energy introduced in the elastic case.

We remark however that, even though our model predicts that the equilibrium orientation of the cell is the same in both regimes, the time needed for reorientation is highly

influenced by the frequency. This leads therefore to final orientation angles of the cell that are in practice different in the two regimes of low and high frequencies, considering the time span of the biological experiment. Indeed, the reorientation time necessary to reach the predicted steady state for low frequencies is much longer than the actual experiment time scale, as will be shown in Section 3.3.3.

3.3.2 Bifurcation Analysis

In this Section, we study the equilibrium orientations of the cells and their bifurcations. Our goal is to describe the cell population subject to a periodic stretch through its elastic energy, since the steady orientation of the stress fibres is predicted by its minimization, as discussed above. This allows us to study in detail the equilibrium angles in terms of a very general strain energy, looking for those orientations which minimize it for a fixed deformation. Finally, we draw bifurcation diagrams in terms of the biaxiality ratio r of the deformation, putting in evidence the conditions under which the preferential orientations exist and are stable.

Elastic Energy and Deformation

We consider the most general elastic energy density $\mathcal{W}$ depending on the classical first three invariants I_1, I_2, and I_3, which represent the isotropic response of the material, and on the anisotropic invariants I_j, $j = 4,\dots,8$, defined in Eq. (3.2). Then, the general energy functional can be written as

$$\mathcal{W} = \mathcal{W}_i(\mathrm{I}_1,\mathrm{I}_2,\mathrm{I}_3) + \mathcal{W}_\ell(\mathrm{I}_1,\mathrm{I}_2,\mathrm{I}_3,\mathrm{I}_4,\mathrm{I}_5,\mathrm{I}_6,\mathrm{I}_7,\mathrm{I}_8) + \mathcal{W}_q(\mathrm{I}_4,\mathrm{I}_5,\mathrm{I}_6,\mathrm{I}_7,\mathrm{I}_8), \tag{3.135}$$

where $\mathcal{W}_i$ is the purely isotropic contribution, $\mathcal{W}_q$ is the purely anisotropic one and $\mathcal{W}_\ell$ includes a coupling between isotropic and anisotropic terms. However, since the invariants I_1, I_2, I_3 do not depend on the orientation angle, the inclusion of $\mathcal{W}_i$ will not influence the following discussion. Henceforth, the energy dependence upon the purely isotropic term will not be explicitly mentioned anymore, though one should recall that $\mathcal{W}_i$ might appear in an irrelevant way as an extra contribution in the energy that does not alter our results and conclusions.

Since we work here in the limit of small deformations, denoting by $\mathbb{E}$ the infinitesimal strain tensor one has

$$\mathrm{I}_4 \approx 1 + 2\mathbf{N}\cdot\mathbb{E}\mathbf{N}, \qquad \mathrm{I}_5 \approx 1 + 4\mathbf{N}\cdot\mathbb{E}\mathbf{N},$$
$$\mathrm{I}_6 \approx 1 + 2\mathbf{N}_\perp\cdot\mathbb{E}\mathbf{N}_\perp, \quad \mathrm{I}_7 \approx 1 + 4\mathbf{N}_\perp\cdot\mathbb{E}\mathbf{N}_\perp,$$
$$\mathrm{I}_8 \approx 2\mathbf{N}_\perp\cdot\mathbb{E}\mathbf{N},$$

recalling also the relationship between the invariants of $\mathbb{E}$ and $\mathbb{C}$ from Eq. (3.79) and neglecting terms of higher order. It follows that, in linear elasticity, it is impossible to discriminate the dependence on I_4 (resp. I_6) from the one on I_5 (resp. I_7), since they both merge in a dependence on $\mathbf{N}\cdot\mathbb{E}\mathbf{N}$ (resp. $\mathbf{N}_\perp\cdot\mathbb{E}\mathbf{N}_\perp$). As a consequence, working in a linear framework, from now on we will consider the following dependencies:

$$\mathcal{W}_q = \mathcal{W}_q\left(\hat{\mathrm{I}}_4, \hat{\mathrm{I}}_6, \mathrm{I}_8\right) \quad \text{and} \quad \mathcal{W}_\ell = \mathcal{W}_\ell\left(\hat{\mathrm{I}}_i\hat{\mathrm{I}}_4, \hat{\mathrm{I}}_i\hat{\mathrm{I}}_6, \hat{\mathrm{I}}_i\mathrm{I}_8\right), \ i = 1,2,3,$$

where we have defined

$$\begin{aligned} &\hat{\mathrm{I}}_1 := \mathrm{I}_1 - 2, && \hat{\mathrm{I}}_2 := \mathrm{I}_2 - 2, && \hat{\mathrm{I}}_3 := \mathrm{I}_3 - 1, \\ &\hat{\mathrm{I}}_4 := \mathrm{I}_4 - 1 \propto \mathbf{N}\cdot\mathbb{E}\mathbf{N}, && \hat{\mathrm{I}}_6 := \mathrm{I}_6 - 1 \propto \mathbf{N}_\perp\cdot\mathbb{E}\mathbf{N}_\perp. \end{aligned} \tag{3.136}$$

However, we anticipate here that, since we will be working with an energy which is quadratic in the deformation measures, the dependence on $\hat{\mathrm{I}}_2$ and $\hat{\mathrm{I}}_3$ inside $\mathcal{W}_\ell$ will be dropped later on.

Consider now a biaxial extension experiment. We assume that the deformation inside the specimen is homogeneous, so that in two dimensions the infinitesimal strain tensor writes

$$\mathbb{E} = \begin{pmatrix} \varepsilon & 0 \\ 0 & -r\varepsilon \end{pmatrix}, \tag{3.137}$$

where the parameter r is the *biaxiality ratio* that already appeared in previous discussions and was introduced in Eq. (2.1). We also observe that, as stated before, the maximum stretching is performed along the x-direction, which implies $1 + r > 0$. Finally, we recall that the equi-biaxial case, corresponding to $r = -1$, will not be discussed explicitly and is not interesting from the practical point of view. In fact, as discussed in Chapter 2, experimental evidence showed that, under equi-biaxial stretch, cells do not orient in a specific direction in the plane of the deformation [377].

Recalling that θ is the angle formed by the predominant cell orientation direction and the x-axis, then $\mathbf{N} = (\cos\theta, \sin\theta)$ and one has

$$\mathbf{N}\cdot\mathbb{E}\mathbf{N} = (\cos^2\theta - r\sin^2\theta)\varepsilon = [(r+1)\cos^2\theta - r]\varepsilon\,,$$
$$\mathbf{N}_\perp\cdot\mathbb{E}\mathbf{N}_\perp = [1-(r+1)\cos^2\theta]\varepsilon\,,$$
$$\mathbf{N}_\perp\cdot\mathbb{E}\mathbf{N} = -(r+1)\sin\theta\cos\theta\,\varepsilon\,,$$

and therefore, in the small deformation approximation, we can write both terms $\mathcal{W}_\ell$ and $\mathcal{W}_q$ of the elastic energy as functions of θ.

As regards $\mathcal{W}_q$, the most general elastic constitutive model for linear elasticity takes the following quadratic form:

$$\mathcal{W}_q\left(\hat{\mathrm{I}}_4, \hat{\mathrm{I}}_6, \mathrm{I}_8\right) = \frac{1}{2}K_\parallel(\mathbf{N}\cdot\mathbb{E}\mathbf{N})^2 + \frac{1}{2}K_\perp(\mathbf{N}_\perp\cdot\mathbb{E}\mathbf{N}_\perp)^2 + \frac{1}{2}K_s(\mathbf{N}_\perp\cdot\mathbb{E}\mathbf{N})^2$$
$$+K_{\parallel\perp}(\mathbf{N}\cdot\mathbb{E}\mathbf{N})(\mathbf{N}_\perp\cdot\mathbb{E}\mathbf{N}_\perp) + K_{\parallel s}(\mathbf{N}\cdot\mathbb{E}\mathbf{N})(\mathbf{N}_\perp\cdot\mathbb{E}\mathbf{N}) + K_{\perp s}(\mathbf{N}_\perp\cdot\mathbb{E}\mathbf{N}_\perp)(\mathbf{N}_\perp\cdot\mathbb{E}\mathbf{N})\,, \tag{3.138}$$

where $K_\parallel$ is a coefficient related to the stiffness to stretching in the direction of cell alignment, $K_\perp$ weighs the stiffness in the orthogonal direction, and K_s measures the response related to shear. The other coefficients are due to mixing effects among these three. In terms of θ, the purely anisotropic part of the energy can then be written as

$$\begin{aligned}\mathcal{W}_q(\theta) = \frac{1}{2}\varepsilon^2\Big\{ & K_\parallel\left[\xi(\theta)-r\right]^2 + K_\perp\left[1-\xi(\theta)\right]^2 + K_s\,\xi(\theta)\left[r+1-\xi(\theta)\right] \\ & + 2K_{\parallel\perp}\left[\xi(\theta)-r\right]\left[1-\xi(\theta)\right] - 2K_{\parallel s}\left[\xi(\theta)-r\right](r+1)\sin\theta\cos\theta \\ & - 2K_{\perp s}\left[1-\xi(\theta)\right](r+1)\sin\theta\cos\theta\Big\}\,,\end{aligned} \tag{3.139}$$

where for compactness we defined $\xi(\theta) := (r+1)\cos^2\theta$. We remark that, here and in the remainder of this Section, we have dropped the explicit energy dependence on t, since we are interested in the steady orientations of the cells which do not depend on time.

Moreover, we point out that we will take $K_{\parallel s} = K_{\perp s} = 0$ due to symmetry requirements on the energy. Indeed, for the problem at hand, biological observations suggest that the energy must be symmetric with respect to $\theta = 0$ and $\theta = \pi/2$, that is,

$$\mathcal{W}(-\theta) = \mathcal{W}(\pi-\theta) = \mathcal{W}(\theta) \qquad \forall\theta\,,$$

as was already imposed in Section 3.1. It is clear that, among the invariants appearing in the energy, the one which can lead to symmetry issues is I_8, because it gives rise to terms like $\sin\theta\cos\theta$ which do not preserve the above symmetries. Hence, it is reasonable to assume that $\mathcal{W}_q$ depends on I_8 only through its square, leading to $K_{\parallel s} = K_{\perp s} = 0$. For the sake of completeness, at the end of this Subsection we also discuss the case $K_{\parallel s}, K_{\perp s} \neq 0$, showing that their introduction provokes a symmetry breaking which is not biologically feasible, unless one needs to account for other directional cues.

Instead, concerning $\mathcal{W}_\ell$, we firstly drop the dependence on I_8 for the same symmetry reasons discussed above. Moreover, we observe that, in the linearised case, the contribution of $\hat{\mathrm{I}}_3$ is equivalent to the one of $\hat{\mathrm{I}}_1$. In fact, since $\mathbb{C} \approx \mathbb{I} + 2\mathbb{E}$, we have that

$$\hat{\mathrm{I}}_1 = \mathrm{tr}(\mathbb{C}) - 2 \approx 2\,\mathrm{tr}(\mathbb{E}) \approx \hat{\mathrm{I}}_3,$$

neglecting terms of higher order. Consequently, the dependence on $\hat{\mathrm{I}}_3$ can be dropped and merged with the one on $\hat{\mathrm{I}}_1$. Finally, since we are considering a quadratic approximation of the energy in the linear regime, the only admissible couplings between the other invariants are $\hat{\mathrm{I}}_1\hat{\mathrm{I}}_4$ and $\hat{\mathrm{I}}_1\hat{\mathrm{I}}_6$, because products involving $\hat{\mathrm{I}}_2$ would have a higher order. Therefore, the dependence on $\hat{\mathrm{I}}_2$ can be neglected as well, and the most general admissible expression of the coupling term becomes

$$\mathcal{W}_\ell\left(\hat{\mathrm{I}}_1, \hat{\mathrm{I}}_4, \hat{\mathrm{I}}_6\right) = 2K_{14}(\mathrm{tr}\mathbb{E})(\mathbf{N}\cdot\mathbb{E}\mathbf{N}) + 2K_{16}(\mathrm{tr}\mathbb{E})(\mathbf{N}_\perp\cdot\mathbb{E}\mathbf{N}_\perp)\,,$$

or, as a function of θ,

$$\mathcal{W}_\ell(\theta) = 2\varepsilon^2(1-r)\Big[(K_{14}-K_{16})\xi(\theta) + (K_{16} - rK_{14})\Big],$$

where K_{14} and K_{16} are coefficients that weigh the coupling between the three invariants involved.

To summarise, the energy as a function of θ that we consider is given by

$$\begin{aligned}\mathcal{W}(\theta) = \frac{1}{2}\varepsilon^2\Big\{&K_\parallel\left[\xi(\theta)-r\right]^2 + K_\perp\left[1-\xi(\theta)\right]^2 + K_s\,\xi(\theta)\left[r+1-\xi(\theta)\right]\\ &+ 2K_{\parallel\perp}\left[\xi(\theta)-r\right]\left[1-\xi(\theta)\right]\Big\} + 2\varepsilon^2(1-r)\Big[(K_{14}-K_{16})\xi(\theta) + (K_{16}-rK_{14})\Big].\end{aligned} \tag{3.140}$$

Since we want to study in more detail the equilibrium orientations and their stability, we take the first derivative of the overall energy with respect to θ and obtain

$$\begin{aligned}\mathcal{W}'(\theta) &= \mathcal{W}'_q(\theta)+\mathcal{W}'_\ell(\theta)\\ &= \varepsilon^2\Big\{K_\parallel\left[\xi(\theta)-r\right]+K_\perp\left[\xi(\theta)-1\right]+\left(\frac{1}{2}K_s+K_{\parallel\perp}\right)\left[r+1-2\xi(\theta)\right]\\ &\quad +2(K_{14}-K_{16})(1-r)\Big\}\xi'(\theta)\,. \end{aligned} \tag{3.141}$$

In order to rewrite the expression (3.141) in a more compact form, we define

$$\widehat{K}_\parallel := K_\parallel+4K_{14}\,,\qquad \widehat{K}_\perp := K_\perp+4K_{16}\,,\qquad K_m := \frac{1}{2}K_s+K_{\parallel\perp}+2K_{14}+2K_{16}\,, \tag{3.142}$$

so that

$$\begin{aligned}\mathcal{W}'(\theta) &= \varepsilon^2\Big\{\widehat{K}_\parallel\left[\xi(\theta)-r\right]+\widehat{K}_\perp\left[\xi(\theta)-1\right]+K_m\left[1+r-2\xi(\theta)\right]\Big\}\xi'(\theta)\\ &= \varepsilon^2\Big[A\xi(\theta)-B(r+1)+C\Big]\xi'(\theta)\,, \end{aligned} \tag{3.143}$$

setting

$$A := \widehat{K}_\parallel+\widehat{K}_\perp-2K_m\,,\qquad B := \widehat{K}_\parallel-K_m\,,\qquad C := \widehat{K}_\parallel-\widehat{K}_\perp. \tag{3.144}$$

Since, under mechanical stretch, the preferential direction of the cell is identified by the aligned stress fibres, coherently with [57] we will consider $\widehat{K}_\parallel > \widehat{K}_\perp$. As a consequence, the coefficient C is always positive, while the sign of A and B cannot be determined a priori, since it depends on the relative magnitude of the various coefficients involved.

Finally, to study the stability of the equilibrium orientations we will need to examine the sign of the second derivative of the energy, which reads

$$\mathcal{W}''(\theta) = \varepsilon^2\Big\{A\xi'(\theta)^2+\left[A\xi(\theta)-B(r+1)+C\right]\xi''(\theta)\Big\}\,. \tag{3.145}$$

Equilibrium Orientations and Stability

Recalling (3.143), the equilibrium orientations are given by

$$\theta\,:\,\xi'(\theta)=0\ \text{ i.e. }\ \theta=k\pi/2,\,k\in\mathbb{Z}\qquad\text{or}\qquad \theta\,:\,A\xi(\theta)-B(r+1)+C=0\,,$$

the latter meaning

$$\cos^2\theta = \frac{B}{A} - \frac{C}{A}\frac{1}{1+r} = \frac{1}{2} + \mathcal{K}\left(\frac{1}{2} - \frac{1}{1+r}\right), \tag{3.146}$$

where we have defined

$$\mathcal{K} := \frac{C}{A} = \frac{\widehat{K}_{\parallel} - \widehat{K}_{\perp}}{\widehat{K}_{\parallel} + \widehat{K}_{\perp} - 2K_m}. \tag{3.147}$$

So, in addition to the angles $\theta = k\frac{\pi}{2}$, one might have other four symmetric equilibrium angles given by Eq. (3.146) that depend only on the combination of parameters contained in $\mathcal{K}$. For simplicity, we will denote these configurations as *oblique* equilibria, while those with $\theta = k\pi$ will be referred to as *parallel* equilibria and those with $\theta = \frac{2k+1}{2}\pi$ as *perpendicular* equilibria, where the definition of parallel and perpendicular obviously refers to the stretching direction. We remark that the result found in Eq. (3.146) is coherent with the findings in Sections 3.1 and 3.2, and more specifically with Eqs. (3.22) and (3.115), up to an identification of the different coefficients. In particular, it is interesting to notice that the addition inside the energy of isotropic-anisotropic coupling terms, as done here through $\mathcal{W}_\ell$, does not modify the qualitative expression which defines the oblique angles. Indeed, it only affects the values of the coefficients, but a linear relation between the squared cosine and a parameter related to the deformation is still found.

As we shall see, the discussion about bifurcations will depend on the sign of $\mathcal{K}$ (i.e., whether A is positive or negative, having observed that $C > 0$) and on whether $|\mathcal{K}|$ is smaller or larger than 1. For this purpose it is useful to define

$$\begin{aligned}
\rho_{\parallel} &:= \frac{\mathcal{K}-1}{2\mathcal{K}} = \frac{K_m - \widehat{K}_{\perp}}{\widehat{K}_{\parallel} - \widehat{K}_{\perp}}, \\
\rho_{\perp} &:= \frac{\mathcal{K}+1}{2\mathcal{K}} = \frac{\widehat{K}_{\parallel} - K_m}{\widehat{K}_{\parallel} - \widehat{K}_{\perp}}, \\
\rho &:= \frac{\mathcal{K}+1}{\mathcal{K}-1} = \frac{\widehat{K}_{\parallel} - K_m}{K_m - \widehat{K}_{\perp}}.
\end{aligned} \tag{3.148}$$

Then, the existence of the oblique equilibrium angle depends on the value of the biaxiality ratio r. Namely, referring to Fig. 3.13, the equilibrium orientation defined by Eq. (3.146)

exists if

$$\begin{aligned}
&\rho_{\parallel} < \frac{1}{1+r} < \rho_{\perp} \quad \text{or} \quad \frac{1}{\rho} < r < \rho \quad \text{when} \quad \mathcal{K} > 1\,,\\
&0 < \frac{1}{1+r} < \rho_{\perp} \quad \text{or} \quad r > \frac{1}{\rho} \quad \text{when} \quad 0 < \mathcal{K} < 1\,,\\
&0 < \frac{1}{1+r} < \rho_{\parallel} \quad \text{or} \quad r > \rho \quad \text{when} \quad -1 < \mathcal{K} < 0\,,\\
&\rho_{\perp} < \frac{1}{1+r} < \rho_{\parallel} \quad \text{or} \quad \rho < r < \frac{1}{\rho} \quad \text{when} \quad \mathcal{K} < -1\,.
\end{aligned}$$

Looking at the stability of such an orientation, recalling Eq. (3.145) one readily has that the second derivative evaluated in this configuration gives $\mathcal{W}''(\theta) = \varepsilon^2 A \xi'(\theta)^2$, which is positive provided that $A > 0$. So, if the coefficient A is positive, or equivalently if $\mathcal{K} > 0$, the oblique equilibrium angle turns out to be stable. Otherwise, if the combination of elastic coefficients in A becomes negative, the oblique orientation is unstable.

If we look instead at parallel orientations, e.g., $\theta = 0$, we have that

$$\mathcal{W}''(0) = -2\varepsilon^2(r+1)\left[(A-B)(r+1)+C\right]. \tag{3.149}$$

Therefore, referring again to Fig. 3.13 and observing that $A - B = -\rho_{\parallel} C$, such an orientation is stable if

$$\frac{1}{1+r} < \rho_{\parallel}. \tag{3.150}$$

Consequently, if $\rho_{\parallel} > 0$ (i.e. if $\mathcal{K} < 0$ or $\mathcal{K} > 1$) the parallel orientation is stable under the condition (3.150), while if $\rho_{\parallel} < 0$ (i.e. if $0 < \mathcal{K} < 1$) it is always unstable.

Finally, the perpendicular orientations, e.g. $\theta = \pi/2$, are stable if

$$\mathcal{W}''\left(\frac{\pi}{2}\right) = -2\varepsilon^2(r+1)[B(r+1)-C] > 0, \tag{3.151}$$

leading to the condition

$$\frac{1}{1+r} > \rho_{\perp}, \tag{3.152}$$

or equivalently $r < 1/\rho$. However, if $\mathcal{K} \in (-1,0)$ the r.h.s. of (3.152) is negative. So, in this range the perpendicular orientation is always stable, while outside the aforementioned interval stability is granted whenever r satisfies (3.152).

The stability conditions discussed so far are summarised by the bifurcation diagrams reported in Fig. 3.13. Taken together, these results argue that, for the general quadratic orthotropic energy that we consider in a linear elastic regime, oblique equilibrium angles

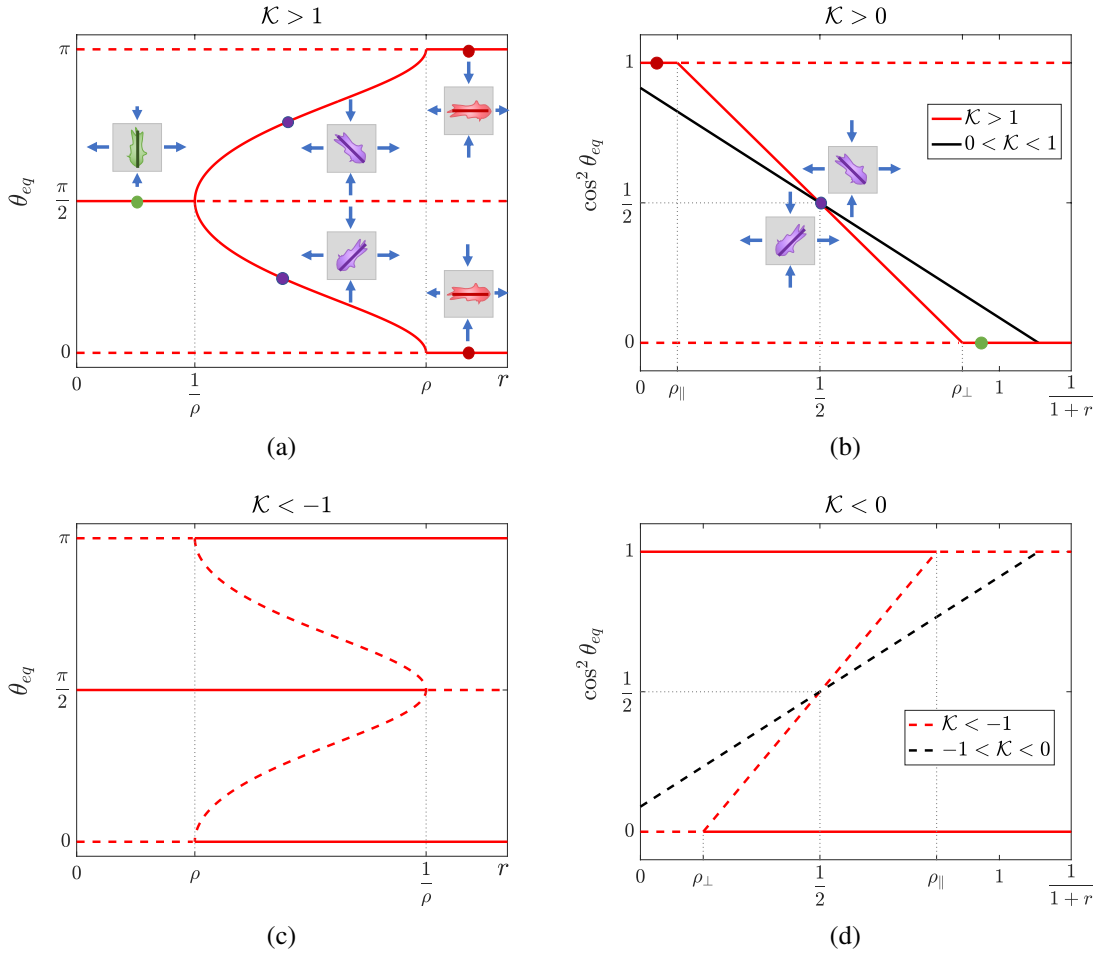

Fig. 3.13 Bifurcation diagrams for positive $\mathcal{K}$ (top) and negative $\mathcal{K}$ (bottom). In particular, (a) and (c) show the bifurcation diagrams in the parameter space (r, θ_{eq}), whereas (b) and (d) are plotted in the parameter space $((1+r)^{-1}, \cos^2\theta_{eq})$. The bifurcation values for the latter are obtained for $(1+r)^{-1} = \rho_\parallel = (K_m - \widehat{K}_\perp)/(\widehat{K}_\parallel - \widehat{K}_\perp)$ and $(1+r)^{-1} = \rho_\perp = (\widehat{K}_\parallel - K_m)/(\widehat{K}_\parallel - \widehat{K}_\perp)$. The insets and dots in (a) and (b) show representative cellular orientations: perpendicular (green), oblique (purple) and parallel (red).

follow a straight line in the $\left((1+r)^{-1}, \cos^2\theta\right)$ plane upon changes in the values of the biaxiality ratio. This is confirmed by experimental assays: in the set-up of the experiments by Livne et al. [226], collected data of the oblique orientation seem to align along a straight line with $\mathcal{K} = 1.26 \pm 0.08$. This is also coherent with the results for a nonlinear quadratic energy discussed in Section 3.1, suggesting that a model which considers the cell-substrate system as an anisotropic elastic material is able to recover experimental data.

More specifically, in Figs. 3.13a and 3.13c we show the bifurcation diagram in the (r, θ) plane for $\mathcal{K} > 1$ and $\mathcal{K} < -1$ respectively, while in Figs. 3.13b and 3.13d we report the straight lines in the $\left((1+r)^{-1}, \cos^2\theta\right)$ plane, for $\mathcal{K} > 0$ and $\mathcal{K} < 0$ respectively. It can be observed that, if $\mathcal{K} > 1$ as in Fig. 3.13a, there are two *supercritical* pitchfork bifurcation points for $r = 1/\rho$ and $r = \rho$. So, for any r there is only one stable equilibrium angle in the interval $\left[0, \frac{\pi}{2}\right]$, and its symmetric counterpart with respect to $\pi/2$ if $r \in \left(\rho^{-1}, \rho\right)$. Hence, by changing r one can smoothly pass from a configuration with the cell axis aligned along the stretching direction to a situation with such axis perpendicular to the main stretching direction. We observe however that the range of values tested in the experiments is $(1+r)^{-1} \in \left[\frac{1}{2}, 1\right]$, because the substrate is not compressed along y more than it is stretched along x, which would correspond to values of $r > 1$. At the same time, we have not found experiments where the specimen is simultaneously stretched along x and y, which would lead to negative values of r. We observe that, since for instance in [226] it is found that $\mathcal{K} \approx 1.26$, a constraint can be inferred among the three coefficients appearing in (3.147), or equivalently among the six parameters in (3.142). In particular, the fact that $\mathcal{K} > 1$ assures that K_m cannot be neglected, because otherwise $\mathcal{K}$ in (3.147) would always be smaller than 1. Starting from this observation and recalling that $\widehat{K}_{\parallel} > \widehat{K}_{\perp}$, we can make some considerations about the minimum number of coefficients necessary to satisfy the experimental values. For instance, if we neglect $\widehat{K}_{\perp}$, we find that $\mathcal{K}$ can be rewritten in terms of the ratio $K_m/\widehat{K}_{\parallel}$ as

$$\frac{1}{\mathcal{K}} \approx 1 - 2\frac{K_m}{\widehat{K}_{\parallel}}.$$

Therefore, since from experiments $1/\mathcal{K} \approx 0.794$ [226], we can argue that

$$\frac{K_m}{\widehat{K}_{\parallel}} = \frac{\frac{1}{2}K_s + K_{\parallel\perp} + 2K_{14}}{K_{\parallel} + 4K_{14}} \approx 0.103\,. \tag{3.153}$$

Hence, even though the contribution of K_m is smaller than the one of $\widehat{K}_{\parallel}$, the former parameter is fundamental to obtain a biologically relevant fitting.

Remark 3.8. From these calculations we can also observe that, if $K_{14} = 0$, then Eq. (3.153) yields

$$\frac{\frac{1}{2}K_s + K_{\parallel\perp}}{K_{\parallel}} \approx 0.103\,.$$

It is then clear that, if we now consider a transversely isotropic energy, for which $K_s = K_{\parallel\perp} = 0$, it is not possible to match the above condition. We already discussed such issue in Section 3.1. However, if $K_{14} \neq 0$, then Eq. (3.153) can be satisfied also in the transversely isotropic case by taking

$$\frac{2K_{14}}{K_{\parallel} + 4K_{14}} \approx 0.103 \quad \Longrightarrow \quad K_{14} \approx 0.065 K_{\parallel}\,.$$

If we consider now the case $\mathcal{K} < -1$, as in Fig. 3.13c, which might for instance occur if K_m is large with respect to $\widehat{K}_{\parallel}$ and $\widehat{K}_{\perp}$, then the pitchfork bifurcations become *subcritical* and one jumps from the parallel to the perpendicular equilibria, since the oblique one is always unstable. So, imagining to operate on K_m, when $2K_m$ passes from being smaller to being larger than $\widehat{K}_{\parallel} + \widehat{K}_{\perp}$, corresponding respectively to $\rho_{\parallel} < \rho_{\perp}$ and $\rho_{\parallel} > \rho_{\perp}$, there is a switch from supercritical to subcritical bifurcations. In Fig. 3.13d we also plot the case $-1 < \mathcal{K} < 0$, in which one has the same bistable behaviour for all the experimental values of r, while the oblique orientation loses its stability. This could be an explanation of why the oblique orientation might not be observed in the case $\mathcal{K} < 0$, that is $\widehat{K}_{\parallel} + \widehat{K}_{\perp} < 2K_m$. Differently from previous models, our bifurcation analysis includes this possibility, which however needs to be validated precisely through experimental data. Moreover, even though experiments are commonly performed in a range of biaxiality ratio $r \in [0,1]$, our model is able to foresee the behaviour of the cell even for values of $r > 1$, i.e. when the substrate is more compressed in the y-direction than it is stretched in the x-direction, a condition not tested yet experimentally.

The bifurcations we have found and discussed qualitatively in the high frequency regime can be also characterised from an analytical standpoint. We refer the reader to Appendix A and Proposition A.1 for the details.

We finally observe that the presence of pitchfork bifurcations is not surprising, since they often arise in one-dimensional dynamical systems that present some symmetries: this is indeed our case, since we took an energy functional which is even and symmetric with

respect to $\pi/2$ in order to match some biological considerations. As a matter of fact, the introduction of $K_{\parallel s}$ and $K_{\perp s}$, discussed in the following, leads to a symmetry breaking and therefore to the appearance of turning points.

The Asymmetric Case

To complete the overview about bifurcations and stability of the preferential orientations, we turn our attention to a more general case for which $K_{\perp s}, K_{\parallel s} \neq 0$ in the anisotropic energy (3.139). In particular, we will show that their introduction leads to a symmetry breaking bifurcation, which however does not seem to be observed in experiments.

If we do not neglect the contribution of the parameters $K_{\perp s}$ and $K_{\parallel s}$, the overall strain energy as a function of θ reads

$$\begin{aligned}\mathcal{W}(\theta) = \frac{1}{2}\varepsilon^2\Big\{ & K_{\parallel}[\xi(\theta)-r]^2 + K_{\perp}[1-\xi(\theta)]^2 + K_s\,\xi(\theta)[r+1-\xi(\theta)] \\ & + 2K_{\parallel\perp}[\xi(\theta)-r][1-\xi(\theta)] - 2K_{\parallel s}[\xi(\theta)-r](r+1)\sin\theta\cos\theta \\ & - 2K_{\perp s}[1-\xi(\theta)](r+1)\sin\theta\cos\theta\Big\} \\ & + 2\varepsilon^2(1-r)\Big[(K_{14}-K_{16})\xi(\theta) + (K_{16}-rK_{14})\Big], \end{aligned} \tag{3.154}$$

while its first derivative is

$$\begin{aligned}\mathcal{W}'(\theta) \;=\; & \varepsilon^2\Big\{\Big[K_{\parallel}\left[\xi(\theta)-r\right] + K_{\perp}\left[\xi(\theta)-1\right] + \left(\frac{1}{2}K_s + K_{\parallel\perp}\right)\left[r+1-2\xi(\theta)\right] \\ & - \left(K_{\parallel s}-K_{\perp s}\right)(r+1)\sin\theta\cos\theta + 2(K_{14}-K_{16})(1-r)\Big]\xi'(\theta) \\ & - \Big[K_{\parallel s}[\xi(\theta)-r] + K_{\perp s}[1-\xi(\theta)]\Big](r+1)(\cos^2\theta-\sin^2\theta)\Big\}. \end{aligned}$$

Before going further, we observe that, in order to have coherence with the experimental condition $\mathcal{W}'(\pi/4) = 0$ for $r = 1$ (which was automatically satisfied in the case $K_{\parallel s} = K_{\perp s} = 0$), the following constraint is necessary:

$$K_{\parallel s} = K_{\perp s}.$$

Hence, we have that the mixing contributions related to shear must be equal. Under this condition, the energy derivative rewrites as

$$\mathcal{W}'(\theta) = \varepsilon^2 \Big\{ [A\xi(\theta) - B(r+1) + C]\xi'(\theta) + K_{\|s}(r^2-1)(\cos^2\theta - \sin^2\theta) \Big\}, \quad (3.155)$$

where A, B and C are defined as in (3.144). Then, differently from Eq. (3.143), we have an additional contribution related to $K_{\|s}$.

In this situation, to derive the equilibrium orientations, we try to write them by making r explicit when imposing that $\mathcal{W}'(\theta) = 0$. Therefore, we have that the steady state angles satisfy

$$2[A(r+1)\cos^2\theta - B(r+1) + C]\sin\theta\cos\theta + (1-r)K_{\|s}(\cos^2\theta - \sin^2\theta) = 0,$$

that can be readily solved and yields

$$r = \frac{K_{\|s}\cos 2\theta + (A\cos^2\theta - B + C)\sin 2\theta}{K_{\|s}\cos 2\theta - (A\cos^2\theta - B)\sin 2\theta}. \quad (3.156)$$

Actually, as in the case $K_{\|s} = 0$, a more compact form only depending on a single parameter can be achieved working in terms of $\frac{1}{1+r}$. In fact, with this idea Eq. (3.156) becomes

$$\frac{1}{1+r} = \frac{C\sin 2\theta - A\sin 2\theta\cos 2\theta + 2K_{\|s}\cos 2\theta}{2(2K_{\|s}\cos 2\theta + C\sin 2\theta)} = \frac{1}{2}\left[1 - \frac{1}{\mathcal{K}}\frac{\sin 2\theta\cos 2\theta}{\sin 2\theta + 2\gamma\cos 2\theta}\right], \quad (3.157)$$

where $\mathcal{K}$ is defined in (3.147) and

$$\gamma := \frac{K_{\|s}}{C} = \frac{K_{\|s}}{\widehat{K}_{\|} - \widehat{K}_{\perp}}. \quad (3.158)$$

Thus, the introduction of the parameter $K_{\|s}$, related to the mixed contribution of stretch along the cell axis and shear, brings a new parameter γ into the equation for nontrivial equilibrium orientations. As expected, for $\gamma = 0$ we recover the symmetric situation described before in Eq. (3.146).

In order to make some theoretical considerations about stability and bifurcations, the first thing to notice is that if $\gamma \neq 0$ the graph in the $(\theta, (1+r)^{-1})$ plane given by (3.157) presents asymptotes when $\sin 2\theta + 2\gamma\cos 2\theta = 0$, namely if

$$\theta = -\frac{1}{2}\arctan 2\gamma + k\frac{\pi}{2},$$

and it has stationary points when $\tan^3 2\theta = 2\gamma$, i.e. whenever

$$\theta = \frac{1}{2}\arctan\sqrt[3]{2\gamma} + k\frac{\pi}{2}, \tag{3.159}$$

achieving in such points the values

$$\frac{1}{r+1} = \frac{1}{2}\left(1 \pm \frac{1}{\mathcal{K}\left(1+\sqrt[3]{4\gamma^2}\right)^{3/2}}\right).$$

Now we discuss the stability of the equilibrium orientations obtained by (3.157). In this case, recalling Eq. (3.145), the second derivative of the elastic energy can be written in general as

$$\mathcal{W}''(\theta) = \varepsilon^2\Big\{A\xi'(\theta)^2 + [A\xi(\theta) - B(r+1) + C]\xi''(\theta) + 4K_{\|s}(1-r^2)\sin\theta\cos\theta\Big\}.$$

Our goal is to study the sign of this derivative when evaluated in the equilibrium angles: in particular, since we consider $1+r>0$, we can focus on the stability condition given by the inequality

$$A\sin^2 2\theta - 2A\cos^2\theta\cos 2\theta + 2B\cos 2\theta - 2\frac{C}{1+r}\cos 2\theta + 2K_{\|s}\frac{1-r}{1+r}\sin 2\theta > 0.$$

Substituting Eq. (3.157) and dividing by $\cos^2 2\theta$ leads to

$$\frac{1}{\mathcal{K}}\tan^2 2\theta - \frac{1}{\mathcal{K}} + \frac{1}{\mathcal{K}}\frac{\sin 2\theta}{\sin 2\theta + 2\gamma\cos 2\theta}(1 - 2\gamma\tan 2\theta) > 0 \tag{3.160}$$

which is equivalent to

$$\frac{1}{\mathcal{K}}\frac{\tan^3 2\theta - 2\gamma}{\tan 2\theta + 2\gamma} > 0. \tag{3.161}$$

Therefore, if $\mathcal{K}>0$, the stable configurations are those with

$$\theta \in \left[\frac{1}{2}\arctan\sqrt[3]{2\gamma}, \frac{\pi}{2} - \frac{1}{2}\arctan 2\gamma\right] \cup \left[\frac{\pi}{2} + \frac{1}{2}\arctan\sqrt[3]{2\gamma}, \pi - \frac{1}{2}\arctan 2\gamma\right].$$

Instead, if $\mathcal{K}<0$, the angles corresponding to stable orientations for the cell are given by

$$\theta \in \left[0, \frac{1}{2}\arctan\sqrt[3]{2\gamma}\right] \cup \left[\frac{\pi}{2} - \frac{1}{2}\arctan 2\gamma, \frac{\pi}{2} + \frac{1}{2}\arctan\sqrt[3]{2\gamma}\right] \cup \left[\pi - \frac{1}{2}\arctan 2\gamma, \pi\right].$$

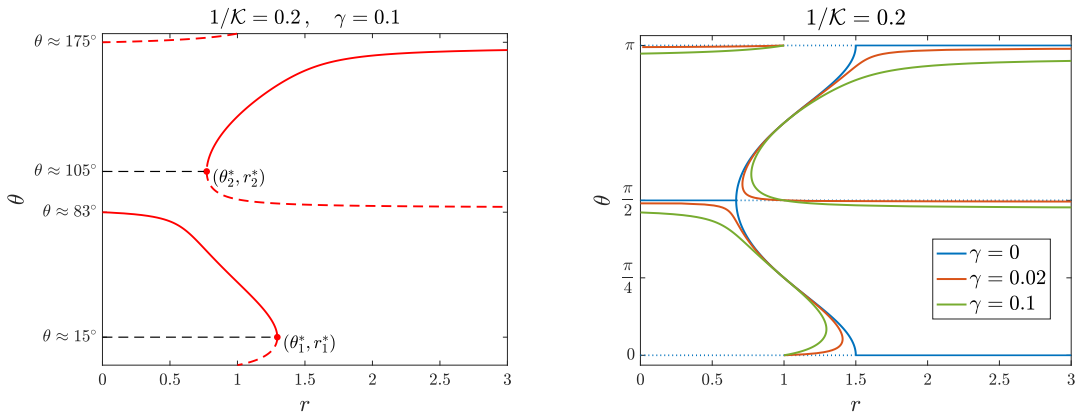

(a) (b)

Fig. 3.14 (a): Bifurcation diagram in the general case $K_{s\|} \neq 0$ for $1/\mathcal{K} = 0.2$, $\gamma = 0.1$. Differently from the symmetric case, here we have two turning points in (θ_1^*, r_1^*) and (θ_2^*, r_2^*). (b): The introduction of γ induces a symmetry breaking in the system, switching from pitchfork to saddle-node bifurcations.

Then, by combining the information given by the second derivative and the equation of the bifurcation curves, we can draw the bifurcation diagram of the system, shown in Figure 3.14a for the case $\mathcal{K} > 0$. In particular, we observe that for $r < r_2^*$ there are two equilibria, one stable and one unstable; however, when r crosses the critical value r_2^*, two new equilibria appear, of which one is stable and another one is unstable. Finally, we have another bifurcation for $r = r_1^*$, when the first two equilibria collide and annihilate each other. In order to give an idea of some numerical values, we reported in the plot in Fig. 3.14a some notable values of θ: more specifically, concerning the peculiar case we considered for $\mathcal{K}$ and γ, i.e. $\gamma = 0.1$ and $\mathcal{K} = 5$, for $r < r_2^*$ we have a stable orientation which is less than $\pi/2$.

The main difference from the symmetric case treated at the beginning of this Subsection lies in the type of bifurcations involved: here we have two *saddle-node bifurcations*. Hence, the introduction of the mixing parameter $K_{\|s}$ provokes the disappearance of the pitchfork bifurcations, while two *turning points* appear. The biggest consequence of this fact, which can be observed in Figure 3.14b, is that a symmetry breaking happens, leading for $\gamma \neq 0$ to equilibrium orientations that are not symmetric. This is due to the fact that the introduction of the coefficient $K_{\|s}$ brings into the energy a term proportional to $\sin\theta\cos\theta$, which is neither even nor symmetric with respect to $\pi/2$. Consequently, unlike the symmetric case previously discussed, one has $\mathcal{W}(-\theta) \neq \mathcal{W}(\theta)$ and $\mathcal{W}(\pi-\theta) \neq \mathcal{W}(\theta)$, but $\mathcal{W}(\pi-\theta) = \mathcal{W}(-\theta)$. However, this situation does not seem biologically meaningful,

because there is no reason why one of the two orientations corresponding to $-\theta$ or θ should be energetically preferable for the cell with respect to the other, unless one can envisage an internal (left-right) bias in the cell itself. Therefore, we can conclude that, from the biological point of view, in the problem at hand the assumption $K_{\parallel s} = 0$ is justified, since we expect to have symmetries in the system which would be broken if this coefficient is not null.

We conclude the discussion about the asymmetric case by remarking that the analytical conditions for a saddle-node bifurcation are actually satisfied, as we show in detail in Appendix A (see Proposition A.2).

3.3.3 Numerical Simulations

After having discussed the equilibrium orientations in Section 3.3.2, here we focus on the dynamics of cell reorientation in response to the viscoelastic model presented in Section 3.3.1, performing some numerical simulations. More specifically, we consider the system of equations which describes the time evolution of the Cauchy stress tensor $\mathbb{T}$ and the reorientation dynamics of the angle θ. As regards the former, its evolution is governed by the viscoelastic constitutive equation (3.124) described in Section 3.3.1; concerning the angle, as in Eq. (3.120) we assume that changes in orientation are driven by a dissipative process in which the cell tries to find the direction which minimizes the virtual work done by the Cauchy stress. Consequently, the system of equations is

$$\begin{cases} \dot{\theta} = -\dfrac{1}{\widehat{K}_{\parallel}\lambda_{\theta}} \dfrac{\partial \mathbb{T}}{\partial \theta} : \mathbb{E}\,, & \text{(3.162a)} \\[2ex] \dot{\mathbb{T}} + \dfrac{1}{\lambda}\mathbb{T} = \dfrac{1}{\lambda}\mathfrak{C}_0 \dot{\mathbb{E}}\,, & \text{(3.162b)} \end{cases}$$

where $\mathfrak{C}_0$ is the functional that accounts for the exponentially weighted history of past orientations defined in Eq. (3.125), depending on the elasticity tensor C_0. The components of C_0 can be written in terms of θ as

$$(\mathsf{C}_0)_{xxxx} = \widehat{K}_{\parallel}\cos^4\theta + \widehat{K}_{\perp}\sin^4\theta + 2K_m\sin^2\theta\cos^2\theta\,,$$

$$(\mathsf{C}_0)_{yyyy} = \widehat{K}_{\parallel}\sin^4\theta + \widehat{K}_{\perp}\cos^4\theta + 2K_m\sin^2\theta\cos^2\theta\,,$$

$$(\mathsf{C}_0)_{xxyy} = K_m - \frac{1}{2}K_s + (\widehat{K}_{\parallel} + \widehat{K}_{\perp} - 2K_m)\sin^2\theta\cos^2\theta\,.$$

We consider a specimen stretched in the x-direction uniformly with a fixed biaxiality ratio r, such that the infinitesimal deformation tensor is given by Eq. (3.137) with

$$\varepsilon(t) = \frac{1}{2}\varepsilon_0(1-\cos\omega t)\,,$$

for different angular frequencies. Compared to experiments, in the simulations we do not assume that the oscillation period is smaller or greater than the characteristic relaxation time λ or reorientation time λ_θ, in order to put in evidence both the elastic and the viscous behaviour of the system.

We now solve Eq. (3.162) for a range of values of r to check the theoretical predictions obtained through the bifurcation analysis. In particular, a numerical algorithm has been implemented using MATLAB®. As regards Eq. (3.162b), its discretisation was performed through the explicit Euler method. It is equivalent to two scalar equations for the components T_{xx}, T_{yy} of the Cauchy tensor $\mathbb{T}$. The integrals in the r.h.s. of (3.162b) have been approximated observing that, for instance in the case $r = 0$,

$$\begin{aligned}(\mathfrak{C}_0^{k+1})_{xxxx} &= \int_{-\infty}^{t_{k+1}} e^{-(t_{k+1}-\tau)/\lambda}\,(\mathsf{C}_0)_{xxxx}(\theta(\tau))\,\mathrm{d}\tau \\ &= e^{-(t_{k+1}-t_k)/\lambda}\,(\mathfrak{C}_0^{k})_{xxxx} + \int_{t_k}^{t_{k+1}} e^{-(t_{k+1}-\tau)/\lambda}\,(\mathsf{C}_0)_{xxxx}(\theta(\tau))\,\mathrm{d}\tau. \end{aligned} \tag{3.163}$$

Then, with an analogous procedure, all the integral terms can be evaluated from the value at the previous time instant plus the discretisation of the remaining integral in (3.163), which was performed through the trapezoidal rule. The generalization to the case $r \neq 0$ is then straightforward. Finally, concerning the virtual work term in Eq. (3.162a), the derivative of the stress with respect to θ was approximated using a centred finite difference. In all our simulations we take $\lambda = \lambda_\theta = 6.6\,\mathrm{s}$ and to have coherence with experimental data we consider a value of $\mathcal{K} = 1.26$ [226]. Instead, we focus on the effect of variations of r, ε_0 and ω to evaluate their impact on the reorientation dynamics of the cell.

In Figure 3.15a we show the evolution of the orientation angle in the high frequency case, starting from an initial condition $\theta(0) = \pi/6$, for different values of r. We see that the angle approaches the value obtained in Section 3.3.2 in the stationary case (identified by a coloured marker on the the right side of the plot) and reported in the bifurcation diagrams in Fig. 3.13. More specifically, for low values of r the final orientation is almost orthogonal to the direction of stretching. Increasing the biaxiality ratio r makes the equilibrium angle decrease, reaching the expected value given by the bifurcation diagrams. In particular,

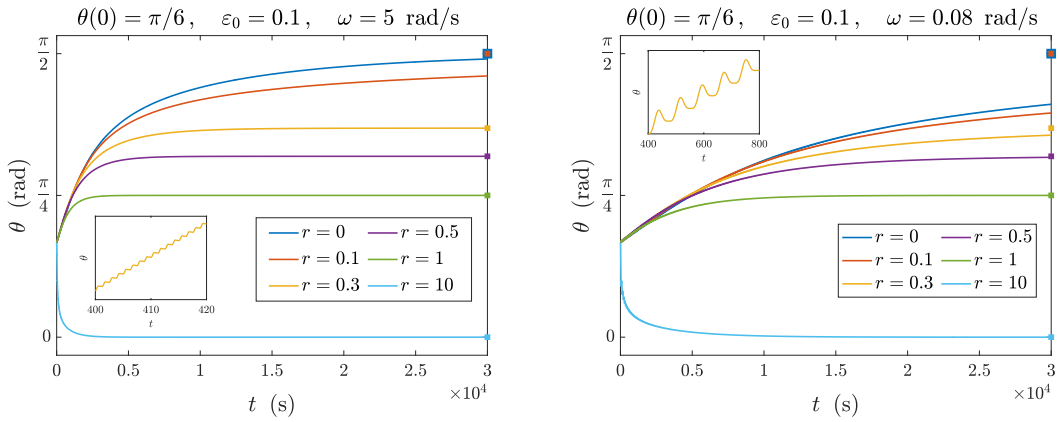

(a) (b)

Fig. 3.15 Evolution of θ according to (3.162) in the high frequency (a) and low frequency (b) cases, for $\mathcal{K} = 1.26$ and $\varepsilon_0 = 0.1$, while the biaxiality ratio r is varied. As initial condition, we take in both cases $\theta(0) = \pi/6$. The squares on the right of each plot highlight the steady orientations predicted by the bifurcation analysis. Moreover, all curves display an oscillatory behaviour, as shown in the insets for the specific case $r = 0.3$.

we observe that the steady angle is $\pi/4$ when $r = 1$, as predicted by the theory and by the experiments. For the sake of completeness, we also showed a case in which $r \gg 1$, even if no experimental data are available in this case: in this situation one has $\theta \to 0$, coherently with the study carried out in Section 3.3.2. Conversely, in Figure 3.15b, we report the plots of θ in the low frequency regime for the same initial condition, choosing $\omega = 0.08$ rad/s which is slightly above the experimental reorientation threshold of 0.06 rad/s suggested for experiments. The dynamics is coherent with model predictions: we have the same equilibria as in the high frequency case, even if the convergence towards the steady angle is slower due to the presence of viscous effects. As shown in the inset plots in Fig. 3.15a and Fig. 3.15b, all curves display an oscillatory behaviour as expected, since we are imposing a periodic deformation to the specimen. Hence, the orientation angle progressively increases through small oscillations until it reaches the predicted orientation. In particular, such oscillations are smaller in amplitude and faster in the elastic case, while they have a greater amplitude and are slower in the viscous limit.

To compare our results with reorientation frequencies and thresholds from Jungbauer et al. [190], we performed some simulations for their same experimental biaxiality ratio and amplitude, changing instead the value of ω. As shown in Fig. 3.16a, angular frequencies below a minimum threshold (which can be quantified in about 0.01 Hz $\approx$ 0.06 rad/s, coherently with experiments on some cell types [171, 190]) do not induce a significant or significantly fast response. In this case, the reorientation happens so slowly that it

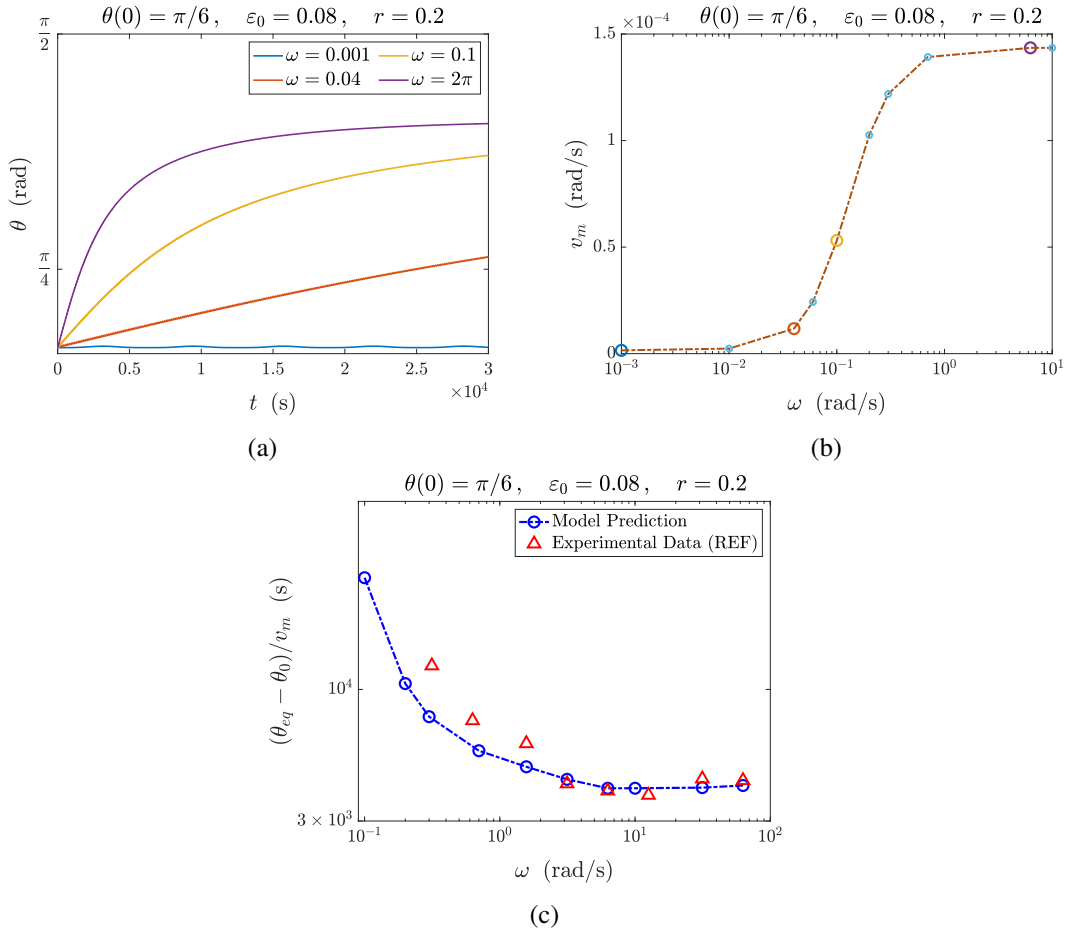

Fig. 3.16 (a): Evolution of θ according to Eq. (3.162) for a fixed biaxiality ratio and different angular frequencies. We observe that low frequencies (approximately below a minimum threshold of 0.06 rad/s, i.e., about 0.01 Hz, coherently with experimental results [171, 190]) do not induce a significant reorientation response. For higher frequencies, the preferential orientation becomes visible and the reorientation time decreases. (b): Average speed of reorientation v_m, computed in a suitable interval where the evolution curve is approximately linear, as a function of the imposed angular frequency in logarithmic scale. Recalling that we used $\lambda = \lambda_\theta = 6.6\,\mathrm{s}$, a transition occurs when $\lambda\omega = 1$, i.e., the inflection point in $\omega \approx 0.15$ rad/s. Then, there is a second threshold of about 2π rad/s, above which a further increase does not induce a significantly faster response [190]. The coloured dots match the values used in (a) for the curves. (c): Plot of the model characteristic time $\tau := (\theta_{eq} - \theta_0)/v_m$ as a function of the angular frequency in logarithmic scale, together with experimental results for rat embryonic fibroblasts (REF cells) taken from [190].

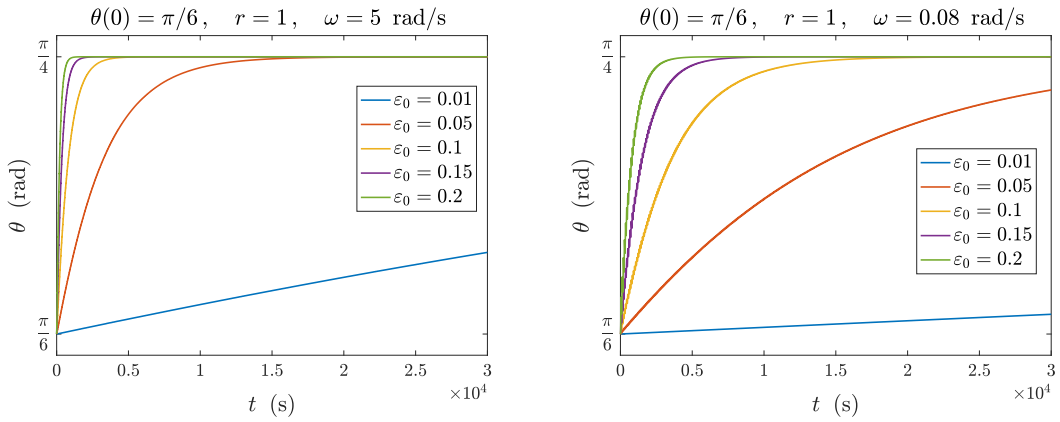

(a) (b)

Fig. 3.17 Evolution of θ according to (3.162). In (a) the high frequency and in (b) the low frequency cases are shown, for different values of the stretch amplitude ε_0 and fixed biaxiality ratio $r = 1$.

cannot be observed on time scales comparable with the cell cycle, and in the experimental case the process is destroyed by random fluctuations. Instead, higher frequencies induce reorientation, with a characteristic time that, coherently with [190], decreases with the frequency. This is true until ω reaches a second threshold of about 2π rad/s (i.e. 1 Hz), after which a further increase in the frequency does not substantially accelerate the reorientation process towards the expected equilibrium angle. This is confirmed and summarized by the results in Fig. 3.16b, where we report the average speed of reorientation v_m, calculated over a suitable interval where each curve can be approximated by a line, as a function of the frequency of the imposed deformation. We find that the speed of reorientation is very low when $\omega < 0.01$ rad/s, corresponding to evolution times of the order of days. Then, there is a sudden transition interval for $\omega \in [0.01, 1]$ rad/s with an inflection point close to $\omega \approx 0.15$ rad/s, i.e. when $\lambda\omega \approx 1$, related to the viscous-elastic transition in the material. Finally, for higher values of ω, the speed of reorientation saturates to values corresponding to experimental times of the order of an hour. To make a further comparison with experiments, we define the characteristic time of reorientation for our model as $\tau := (\theta_{eq} - \theta_0)/v_m$, assuming that the evolution curves for θ as a function of time are approximated by a saturating exponential. Then, in Fig. 3.16c we plot this characteristic time together with data for rat embryonic fibroblasts (REF cells) from [190]. As discussed before, such a time decreases with the frequency until a threshold, above which it remains almost constant, and the model predictions show a good agreement with experimental data.

In Figure 3.17 we studied instead the influence of the stretch amplitude ε_0, while the angular frequency is kept high in Fig. 3.17a and low in Fig. 3.17b, fixing $r = 1$ and

therefore $\theta_{eq} = \pi/4$. As one could expect, the equilibrium orientation for a given initial condition $\theta(0)$ and biaxiality ratio r is not altered by variations of ε_0 and remains equal to $\pi/4$ in this case. Changes in the amplitude only influence the speed of convergence towards the predicted equilibrium angle. Indeed, if we scale times with $1/\omega$, the stress tensor with $\widehat{K}_{\|}\varepsilon_0$, and the strain tensor with ε_0, the system (3.162) rewrites in dimensionless terms formally substituting $\widehat{K}_{\|}\lambda_\theta$ with $\widetilde{\Lambda}_\theta = \lambda_\theta\omega/\varepsilon_0^2$ and λ with $\widetilde{\Lambda} = \lambda\omega$. In formulas, defining $t = \widetilde{t}/\omega$, $\mathbb{T} = \widetilde{\mathbb{T}}\widehat{K}_{\|}\varepsilon_0$, $\mathbb{E} = \widetilde{\mathbb{E}}\varepsilon_0$ and $\mathfrak{C}_0 = \widetilde{\mathfrak{C}}_0\widehat{K}_{\|}\lambda$ yields

$$\begin{cases} \dfrac{d\theta}{d\widetilde{t}} = -\dfrac{1}{\widetilde{\Lambda}_\theta}\dfrac{\partial\widetilde{\mathbb{T}}}{\partial\theta} : \widetilde{\mathbb{E}}, & \text{(3.164a)} \\ \dfrac{d\widetilde{\mathbb{T}}}{d\widetilde{t}} + \dfrac{1}{\widetilde{\Lambda}}\widetilde{\mathbb{T}} = \widetilde{\mathfrak{C}}_0\dfrac{d\widetilde{\mathbb{E}}}{d\widetilde{t}}. & \text{(3.164b)} \end{cases}$$

As already discussed, the dimensionless group $\widetilde{\Lambda}_\theta$ is related to the time needed by the cell to re-orientate in terms of the oscillation frequency and amplitude, while $\widetilde{\Lambda}$ identifies the relative role of viscoelasticity. In particular, focusing on $\widetilde{\Lambda}_\theta$, if the amplitude of oscillation increases (e.g., doubles) the evolution of the orientation angle θ remains the same provided that the reorganization time λ_θ is suitably increased (e.g., quadruples). On the other hand, if λ_θ is kept constant, as done in Fig. 3.17, cells re-orient faster, and the re-orientation time scales like the square of the oscillation amplitude. However, to simplify the direct comparison with experimental results, we decided to perform all simulations using dimensional quantities.

Finally, in Figure 3.18 we report the evolution of the Cauchy stress components T_{xx} and T_{yy}, both normalized with respect to $\widehat{K}_{\|}$. In particular, Figs. 3.18a and 3.18b show the stresses in the high frequency case, for a fixed biaxiality ratio $r = 0.3$. It can be observed that, starting from a stress-free configuration, there is a first increase in both stress values up to a peak, after which relaxation begins and completes in about 100 seconds. Once the transient is passed, the stress components start to oscillate around zero, meaning that the system is behaving purely elastically. In the low frequency case, plotted in Fig. 3.18c and 3.18d, the response of the system is much slower, since the viscous component emerges visibly. Concerning the stress magnitude when the equilibrium orientation is reached, as predicted by the model, we observe that the stress components in the low frequency case differ from the ones in the high frequency case by a factor $\lambda\omega_{low} \approx 0.53$.

As a final observation, we stress that, in all simulations, we kept the characteristic times λ and λ_θ constant, to better identify the effects of the oscillation characteristics in

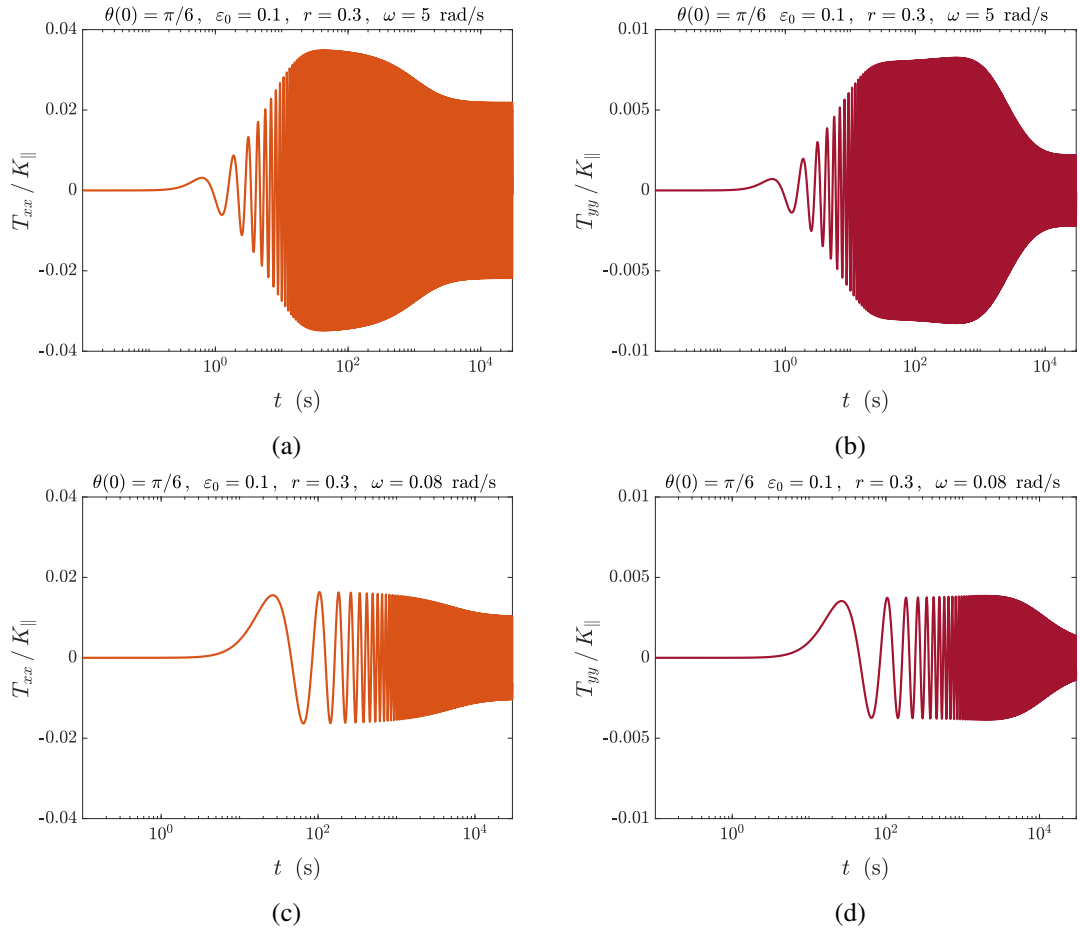

Fig. 3.18 Time evolution of the stress tensor components T_{xx} and T_{yy} (normalized w.r.t. $\widetilde{K}_{\|}$), for $r = 0.3$. In the top row, the high frequency case is reported, while in the bottom row the plots refer to the low frequency case. The time axis is reported in logarithmic scale to put in evidence the temporal behaviour of stress amplitudes.

terms of frequency and amplitude. However, the dynamics of adhesion to the substrate is more involved because the application of a stress on them has the consequence of both strengthening the bonds, due to an increased clustering of integrins, and prolonging their lifetime. In particular, two types of bonds are identified in the literature, called *catch* and *slip* bonds [206, 219, 368, 407, 408]. Increasing the applied deformation has the effect of increasing the applied force acting on the bonds and this causes a decrease (resp., an increase) of the lifetime of slip (resp., catch) bonds. So, the dependence of the adhesion bond lifetime, and therefore of λ, on the deformation is not constant and might actually not even be monotone, with a maximum corresponding to an applied force of the order of 10 pN. However, as discussed in Section 3.3.1, the inclusion of such a strain-dependence lifetime would not change the equilibrium configuration, but only the temporal behaviour

of the system. Conversely, a strengthening of the adhesion bond might change both, though we do not expect them to be relevant.

3.3.4 Discussion

In addition to parameters like the amplitude and the biaxiality ratio, the frequency of the applied periodic deformation is known to affect the process of cell reorientation. In particular, as pointed out in Chapter 2, higher frequencies are associated with a faster reorientation, provided that they exceed a minimum threshold value. Essentially, the comparison between the period of the cyclic strain and the characteristic time of cell bond turnover determines how fast cell realignment happens. Such an effect cannot be captured by the purely elastic descriptions employed in Sections 3.1 and 3.2.

Therefore, in this Section we have proposed a linear viscoelastic model of the system composed by cells and substrate, with anisotropy due to the presence of aligned stress fibres and lateral protein network. The model couples a Maxwell-type evolution equation for the stress tensor with the dynamics of the orientation angle, which is assumed to be driven by the stress-strain virtual work. We showed that our model is able to differentiate the behaviour of the system depending on the period of the applied cyclic stretch: if it is much shorter than the cell characteristic reorganisation times, then the response is elastic. On the other hand, if the frequency is low, viscous-like effects emerge and slow down the reorientation, until the whole process becomes too slow to be relevant. These differences can be put in evidence by taking the limit of the general constitutive equation in the high and low frequency cases.

Then, we thoroughly studied the stationary solutions of the evolution equation for the angle. Specifically, we focused on the bifurcations that occur when the biaxiality ratio of the deformation is changed. We observed the presence of supercritical pitchfork bifurcations when $\mathcal{K} > 1$, with the appearance of two specular oblique equilibria. Instead, such bifurcations become subcritical when $\mathcal{K} < -1$. Even if this case has not been tested experimentally, our model is in principle able to describe it. The presence of pitchfork bifurcations is coherent with the energy symmetries that we assumed for consistency with biological observations. For completeness, we also discussed what happens if the symmetry requirements are removed, showing that a symmetry breaking takes place.

Numerical simulations in the case $\mathcal{K} > 0$ confirmed the analytical predictions and showed an evolution towards a steady state angle which depends on the imposed biaxiality ratio, but not on the frequency. Instead, coherently with experimental results, the frequency

affects the speed of cytoskeletal reorientation. In particular, in the low frequency regime, convergence towards equilibrium is slowed down due to the presence of viscous effects, even if the theoretical stationary orientation is still predicted by energy minimization. Finally, we showed that our model is able to reproduce the presence of an upper frequency threshold, recovering the results by Jungbauer and collaborators [190].

Hence, our model seems consistent with previous experimental data and theories describing the behaviour of an ensemble of cells on a stretched substrate, also discussing the case of isotropic-anisotropic couplings in the energy and recovering once more the established linear relation between the squared cosine of the angle and a parameter related to the deformation.

Chapter 4

Mathematical Modelling of Axonal Cortex Contractility

Neurons constitute the main component of nervous tissue and represent a paramount example of electrically excitable cells, which are able to propagate signals to their neighbours. However, recent experimental results have shown that the axon of a neuron possesses a very mechanosensitive cytoskeleton, which is able to develop active contractility both in the axial and in the hoop directions. The fact that axons can regulate their longitudinal tension in an active way has been known for many years, but very recently the circumferential contractility has been put in evidence. Moreover, the same experiments appear to point towards the existence of a strong coupling between the axial and circumferential active contractions in the axonal cortex: this synergistic interplay does not seem trivial and it has not been fully clarified. To shed light on the active mechanics of the axon, in this Chapter we propose a mathematical model for the contractility of the cortex based on an active strain approach.

In detail, the structure of the Chapter is as follows. We begin in Section 4.1 with some biological background about the axon structure, which is fundamental for understanding the physical mechanisms of contraction. In Section 4.2, we propose a continuum model of the axon which takes into account both the axoplasm as a passive component and the cortex as an actively contracting coating. By using the Coleman-Noll procedure, we obtain the evolution equations for the coupled hoop and axial active stretches. Afterwards, in Section 4.3 we assume the axon to be an incompressible medium. In this case, the above mentioned equations reduce to a simple dynamical system whose equilibria can be studied analytically. This provides interesting qualitative observations and clearly allows to notice that a single

active stretch is not enough to reproduce the axonal behaviour. Then, in Section 4.4 we assume a more appropriate compressible constitutive equation and numerically solve the mathematical model. Comparisons are made between numerical and experimental results available in the literature from a quantitative viewpoint, showing a very good agreement. Finally, we summarise the main outcomes and remarks in Section 4.5.

The results of this Chapter led to the following publication:

D. Andrini, V. Balbi, G. Bevilacqua, G. Lucci, G. Pozzi, and D. Riccobelli. Mathematical modelling of axonal cortex contractility, *Brain Multiphysics* 3:100060 (2022).

4.1 Biological Background

The capability of neurons to transmit electrical signals and action potentials represents the foundational feature of the nervous system, which allows to control all actions in the body. In particular, as sketched in Fig. 4.1, the typical structure of a single neuron features a cell body, called *soma*, from which two types of cytoplasmic protrusions branch out. The *dendrites* are numerous extensions that receive signals from nearby neurons, whereas the *axon* is a single, slender protrusion that carries electro-chemical stimuli away towards neighbouring cells. The inner part of an axon, called *axoplasm*, constitutes the cytoplasmic part within an axon and contains several organelles as well as microtubules. The latter are cross-linked together, forming a network which confers the axoplasm an elastic behaviour. Then, the axoplasm is surrounded by a coating, called *cortex*, composed of F–actin, namely polymer microfilaments made of actin, interconnected together by myosin II molecular motors and spectrin, as sketched in Fig. 4.1. In particular, such a cortex is able to actively contract, thanks to the combined action of actin and myosin. In addition, the interplay between the microtubule network and the cortical actomyosin machinery is important for maintaining the cylindrical shape of the axon [279].

Many phenomena can alter such a delicate dynamic equilibrium. For instance, the disruption of the elastic component of the axoplasm during stretch can lead to bulging along the axon length. Such a process, called axonal *beading* or *pearling*, represents a hallmark of neuronal damage [91, 212]. However, axons can sustain large deformations, also up to 100%, if the strain is slowly and progressively imposed [356]. Under such conditions, the elastic deformation can even induce an axial growth of the axon itself thanks to the production of new microtubules [47, 60, 277, 404]. Conversely, rapid stretching

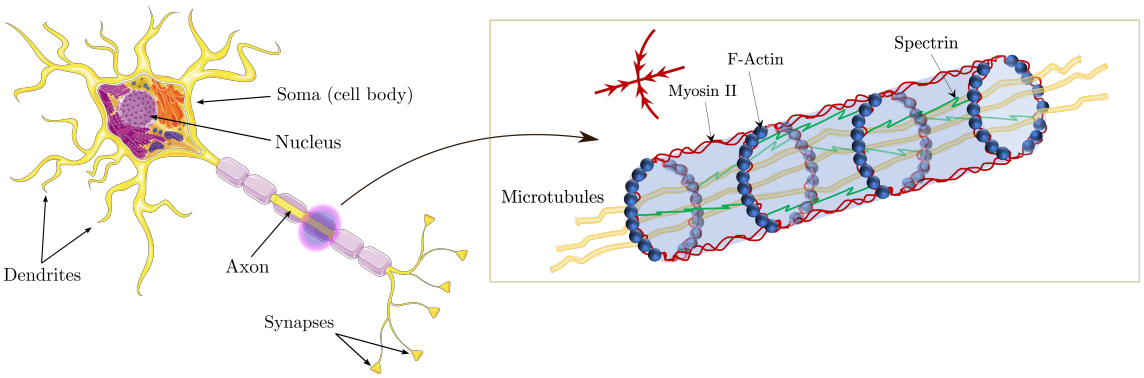

Fig. 4.1 Components of a neuron and microstructure of the axon. In the axonal cortex, F–actin is arranged in rings around the circumference of the axon. The myosin II motors both connect the actin rings and run along the length of the axon, creating a coupled contraction in the circumferential and the longitudinal directions. Adapted from [17, 318].

of the axon in the axial direction can lead to a damage of the cytoskeleton and to the depolymerisation of microtubules [29, 356], which consequently might provoke bulging.

Axonal beading has also been observed as a consequence of several pathological conditions, such as the Alzheimer's [334] and Parkinson's diseases [349], viral infections [184], and multiple sclerosis [272]. There is increasing evidence that all these conditions result in structural damage of the axon cytoskeleton. Indeed, it has been shown that beading can be explained by a mechanical instability triggered by both the reduction of axoplasm stiffness and the active contraction of the actin cortex [301]. Therefore, unveiling the mechanisms which underlie the mechanics of the axon, and in particular its cortical contraction, is of utmost importance to understand how axons maintain their structural stability.

In this respect, experimental observations show that actin filaments are arranged in a geometrically regular pattern, forming circles spaced at a constant distance of 180 nm – 190 nm along the axonal length, interconnected by spectrin and myosin II [393] (see Fig. 4.1). Such a microstructural organisation suggests that the actin cortex can generate an active tension in both the axial and the circumferential direction. Indeed, a sliding of the circular actin filaments might induce a hoop contraction, while myosin II is involved in longitudinal contractility [85, 86]. The fact that axons can actively maintain a certain axial tension has been known for long [85, 86, 119]. However, recent experiments have remarkably demonstrated that they are able to contract in an active manner also in the circumferential direction [119]. Furthermore, such experiments have linked hoop contractility to the self-regulation of the axon diameter following an externally imposed axial

stretch, microtubule depolymerisation or myosin II disruption [86, 119]. In these works, the authors suggest that such changes in diameter may be induced by the compressive force exerted on the axoplasm by the active contraction of the cortex [119]. Moreover, an active diameter reduction is as well observed when axons are axially stretched. All these interesting findings suggest a coupling between axial and hoop active tensions in the axon, whose nature is still not fully elucidated.

Motivated by these observations, in this Chapter we use tools of Continuum Mechanics to investigate the active contractility of the axon cytoskeleton, with a specific focus on the non-trivial coupling between the axial and circumferential active contractions. By means of an active strain approach, we show that cortex contractility induces a compression in the axoplasm and we derive the coupling between the active stretches in a thermodynamically consistent manner. Our mechanical model of the axon is able to describe the interplay between the deformation and the evolution of such stretches, showing a very good agreement with experimental data. Moreover, differently from previous approaches, we do not postulate the link between the axial and hoop active components of the deformation, but rather derive it from mechanical principles through the Mandel stress tensor.

4.2 Mathematical Model of Axonal Contractility

In this Section, we construct a mathematical model of actin cortex contraction, with the purpose of investigating the coupling between the axial and the circumferential contractility by means of Continuum Mechanics tools.

4.2.1 Notation and Kinematics

We model the axon as a continuum body with reference configuration

$$\Omega_0 = \{\, \mathbf{X} \in \mathcal{E} \;\mid\; R \in [0, R_o),\ \Theta \in [0, 2\pi),\ Z \in (Z_1, Z_2) \,\},$$

where we denote by (R, Θ, Z) the Lagrangian cylindrical coordinates of the material point $\mathbf{X} = (R\cos\Theta, R\sin\Theta, Z)$ belonging to the three-dimensional Euclidean space $\mathcal{E}$, with $(\mathbf{E}_R, \mathbf{E}_\Theta, \mathbf{E}_Z)$ being the corresponding vector basis. Due to the slenderness of the axon, whose length is much greater than the radius, in the following derivation we will consider the reference domain to be infinite along $\mathbf{E}_Z$.

In our model, the axon is composed of an inner part $\Omega_{0\mathrm{a}}$ and an outer coating $\Omega_{0\mathrm{c}}$, that represent the axoplasm and the actin cortex, respectively. More explicitly, we define

$$\Omega_{0\mathrm{a}} = \{\mathbf{X} \in \Omega_0 \mid 0 \leq R < R_\mathrm{i}\}, \quad \text{and} \quad \Omega_{0\mathrm{c}} = \{\mathbf{X} \in \Omega_0 \mid R_\mathrm{i} \leq R < R_\mathrm{o}\}, \tag{4.1}$$

where R_i is the internal radius of the axoplasm. Clearly, we have $\Omega_0 = \Omega_{0\mathrm{a}} \cup \Omega_{0\mathrm{c}}$.

Let $\boldsymbol{\chi} : \Omega_0 \times [t_0, t_1] \to \mathcal{E}$ be the motion of Ω_0, so that $\mathbf{x} = \boldsymbol{\chi}(\mathbf{X}, t)$ is the actual position vector of point $\mathbf{X}$ at time t. We denote by (r, θ, z) the triple of coordinates of $\mathbf{x}$ in a cylindrical reference frame where $(\mathbf{e}_r, \mathbf{e}_\theta, \mathbf{e}_z)$ is the corresponding vector basis. In addition, we set $\mathbb{F} = \mathrm{Grad}\,\boldsymbol{\chi}$ to be the deformation gradient and we resort to the active strain approach [12, 134] to model the active contraction of the cortex. Such a method was first developed to model muscle contraction [204, 265, 302, 348] and has been recently used to model axonal contractility [129, 301]. Following this approach, we assume a multiplicative decomposition of the deformation gradient $\mathbb{F}$ as follows:

$$\mathbb{F} = \mathbb{F}_\mathrm{e}\mathbb{F}_\mathrm{a},$$

where $\mathbb{F}_\mathrm{e}$ and $\mathbb{F}_\mathrm{a}$ account for the elastic and the inelastic active distortions, respectively. The tensor $\mathbb{F}_\mathrm{a}$ describes the contractility of the cortex and has to be constitutively prescribed (see Fig. 4.2). We also denote by J, J_e, and J_a the determinants of the tensors $\mathbb{F}$, $\mathbb{F}_\mathrm{e}$, and $\mathbb{F}_\mathrm{a}$, respectively, representing the local change of volume induced by the relative distortion field.

As shown in Fig. 4.1, the cortex of the axon has a highly organised structure whereby the F–actin rings, arranged along the circumference of the axon, are connected by the myosin II motors [86]. The myosin motors also run along the longitudinal direction and can generate an axial contraction. Spectrin filaments instead contribute to the structural integrity and the elasticity of axons. Given this specific microstructural organisation of the cortex, we can reasonably assume the following form for $\mathbb{F}_\mathrm{a}$:

$$\mathbb{F}_\mathrm{a} = \frac{1}{a_\Theta a_Z}\mathbf{E}_R \otimes \mathbf{E}_R + a_\Theta \mathbf{E}_\Theta \otimes \mathbf{E}_\Theta + a_Z \mathbf{E}_Z \otimes \mathbf{E}_Z, \tag{4.2}$$

for $\mathbf{X} \in \Omega_{0\mathrm{c}}$, where a_Θ and a_Z are the active stretches along the circumferential and the axial direction, respectively. In this way, the active strain tensor accounts for a pure remodelling of the cortex [117], i.e., $J_\mathrm{a} = 1$, without any volume modification (contrary to growth/resorption, which is treated for instance in Chapter 5).

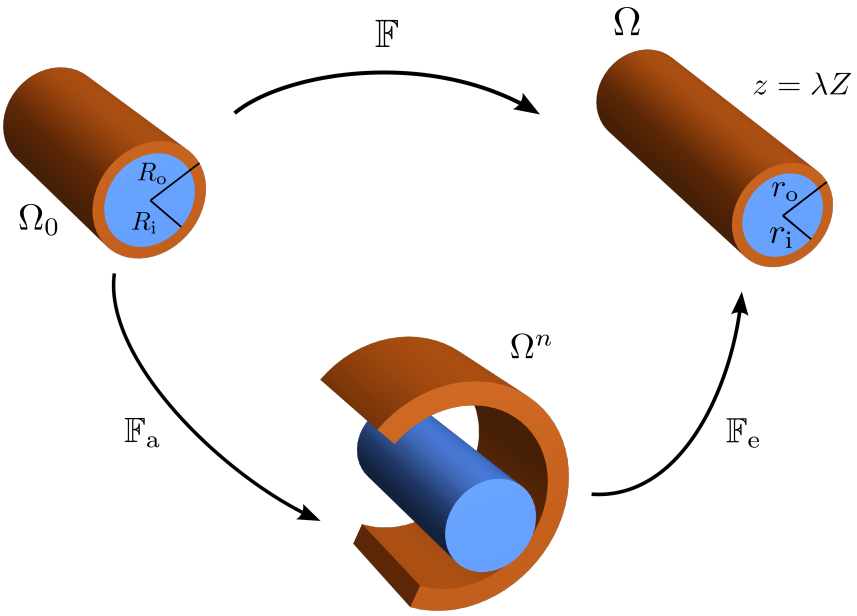

Fig. 4.2 Representation of the multiplicative decomposition of the deformation gradient $\mathbb{F} = \mathbb{F}_e\mathbb{F}_a$.

As already discussed, the active contraction is localised in the cortex. Hence, we model the axoplasm as a passive elastic material by setting $\mathbb{F}_a = \mathbb{I}$ therein. As for the cortex, we assume that the reference configuration Ω_{0c} corresponds to a relaxed condition in which all the active fibres are fully extended. Hence, a further reciprocal sliding of the actin and myosin filaments cannot take place without generating mechanical stress. Mathematically, this conditions translates into a unilateral constraint which forces the active stretches to be less than one, namely, $a_\Theta, a_Z \leq 1$.

4.2.2 Balance Equations and Boundary Conditions

In this Section, we specify the balance laws of the model, starting with the balance of linear momentum. In the absence of external body forces and by neglecting inertia, such a balance reduces to the following equation:

$$\mathrm{Div}\,\mathbb{P} = \mathbf{0}\,, \tag{4.3}$$

where $\mathbb{P}$ is the first Piola-Kirchhoff stress tensor and Div represents the divergence in material coordinates. Equivalently, the balance of the linear momentum can be recast in the actual configuration by requesting that $\nabla \cdot \mathbb{T} = \mathbf{0}$, where $\mathbb{T}$ is the Cauchy stress tensor

and $\nabla\cdot$ is the divergence operator in the actual reference frame. For later convenience, we also introduce the Mandel stress tensor, defined as

$$\mathbb{M} = \mathbb{F}_{\mathrm{e}}^{\mathrm{T}}\mathbb{P}\mathbb{F}_{\mathrm{a}}^{\mathrm{T}} = J\mathbb{F}_{\mathrm{e}}^{\mathrm{T}}\mathbb{T}\mathbb{F}_{\mathrm{e}}^{-\mathrm{T}}, \tag{4.4}$$

which is another measure of the stress commonly used in the theory of plasticity and remodelling [151, 235].

The momentum balance equation has to be complemented by proper boundary and interface conditions. We assume that the external boundary of the axon is free of traction, therefore

$$\mathbb{P}\mathbf{n}_* = \mathbf{0} \qquad \text{where } R = R_{\mathrm{o}}, \tag{4.5}$$

where $\mathbf{n}_*$ is the outward normal in the reference configuration. We also enforce the continuity of displacement and traction at the interface between the cortex and the axoplasm, namely

$$\begin{cases} \lim\limits_{R\to R_{\mathrm{i}}^-} \mathbf{u} = \lim\limits_{R\to R_{\mathrm{i}}^+} \mathbf{u}, \\ \lim\limits_{R\to R_{\mathrm{i}}^-} \mathbb{P}\mathbf{n}_* = \lim\limits_{R\to R_{\mathrm{i}}^+} \mathbb{P}\mathbf{n}_*. \end{cases} \tag{4.6}$$

We remark that, strictly speaking, one should impose only the continuity of the normal component of the displacement, so that $[\![\mathbf{u}\cdot\mathbf{n}_*]\!] = 0$, where $[\![\cdot]\!]$ denotes the jump across the interface $R = R_i$. However, due to the presence of adhesion molecules, it is physically reasonable to assume that no breakage or rotation between the cortex and the axoplasm occurs. Hence, we consider that also the tangential component is continuous.

Then, since the actin cortex is made of an active material, we must describe the active process underlying its contraction by introducing additional balance equations. Specifically, the active strain tensor (4.2) introduces two additional kinematic variables, which are a_Θ and a_Z. Changes in a_Θ and a_Z describe the microstructural reorganisation of the actin cortex and the subsequent active contraction. In particular, the cortex can undergo remodelling as a result of external stimuli, such as the presence of ATP molecules. In line with the theory developed in [107], we model such external stimuli by introducing two scalar fields, B_Θ and B_Z, that play the role of external forces driving cortical contractility in the hoop and in the axial direction, respectively. We label B_Θ and B_Z as *external* remodelling (or active) stresses. Such stresses induce an inelastic distortion of the material, i.e. they make the actin filaments undergo a microstructural reorganisation. The response of the material to the external stimuli (e.g. how much and how fast the actin filaments contract in the presence

of a given concentration of ATP) depends on how the cortex is organized. This material property of the cortex is modelled by the scalars C_Θ and C_Z, representing the resistance of the cortex to the contraction in the hoop and in the axial direction, respectively. Therefore, on the one hand B_Θ and B_Z represent the action of external entities, whereas C_Θ and C_Z are called *internal* remodelling (or active) stresses.

By following [107], we prescribe a balance between the remodelling stresses that drive the cortex contractility as follows:

$$\begin{cases} B_\Theta = C_\Theta, \\ B_Z = C_Z. \end{cases} \tag{4.7}$$

In the next Subsection, we provide the constitutive equations for the materials and we derive the evolution laws for the active stretches.

4.2.3 Thermodynamics Restrictions and Coleman-Noll Procedure

To derive the constitutive and evolution laws, we use the so-called Coleman-Noll [80] procedure. Specifically, we postulate the existence of a strain energy density function $\mathcal{W}$ and we write the Clausius-Duhem inequality [107]:

$$\int_{\mathcal{R}} \dot{\mathcal{W}} \, \mathrm{d}V \leq \int_{\mathcal{R}} \mathbb{P} : \dot{\mathbb{F}} \, \mathrm{d}V + \int_{\mathcal{R}\cap\Omega_{0c}} \left[C_\Theta \frac{\dot{a}_\Theta}{a_\Theta} + C_Z \frac{\dot{a}_Z}{a_Z} \right] \mathrm{d}V \,, \tag{4.8}$$

where $\mathcal{R}$ is a subdomain of Ω_0. The superposed dot denotes the time derivative, and $\mathbb{A} : \mathbb{B} = \mathrm{tr}(\mathbb{A}^{\mathrm{T}}\mathbb{B})$. We remark that the last integral in (4.8) represents the power of the internal remodelling forces and is performed on $\mathcal{R}\cap\Omega_{0c}$, since only the cortex can actively contract.

By following the equipresence principle [365], we postulate that the constitutive relations for $\mathcal{W}$, C_Θ, C_Z, and $\mathbb{P}$ depend on the same kinematic quantities. Here, we assume that

$$\mathcal{W} = \mathcal{W}(\mathbf{X}, \mathbb{F}, a_j, \dot{a}_j) \,, \qquad C_j = C_j(\mathbf{X}, \mathbb{F}, a_j, \dot{a}_j) \,, \qquad \mathbb{P} = \mathbb{P}(\mathbf{X}, \mathbb{F}, a_j, \dot{a}_j) \,,$$

where $j = \Theta, Z$. Under such assumptions, we can rewrite Eq. (4.8) as follows:

$$\int_{\mathcal{R}} \left(\frac{\partial \mathcal{W}}{\partial \mathbb{F}} - \mathbb{P} \right) : \dot{\mathbb{F}} \, \mathrm{d}V + \int_{\mathcal{R} \cap \Omega_{0c}} \sum_{j=\Theta,Z} \left(\frac{\partial \mathcal{W}}{\partial a_j} a_j - C_j \right) \frac{\dot{a}_j}{a_j} \, \mathrm{d}V + \int_{\mathcal{R} \cap \Omega_{0c}} \frac{\partial \mathcal{W}}{\partial \dot{a}_j} \ddot{a}_j \, \mathrm{d}V \leq 0 \,, \tag{4.9}$$

which must hold for any admissible process [80, 291]. Thus, from the arbitrariness of $\dot{\mathbb{F}}$ and $\ddot{a}_j$, we readily obtain

$$\mathbb{P} = \frac{\partial \mathcal{W}}{\partial \mathbb{F}}, \qquad \frac{\partial \mathcal{W}}{\partial \dot{a}_j} = 0 \,, \quad j = \Theta, Z \tag{4.10}$$

where the first relation is the classic expression of the first Piola-Kirchhoff stress tensor of a hyperelastic material, while the second one states that the energy $\mathcal{W}$ is independent of $\dot{a}_\Theta$ and $\dot{a}_Z$. If we consider every admissible $\dot{a}_j$, $j = \Theta, Z$, we can further enforce the Clausius-Duhem inequality (4.9). We then find that a constitutive law for C_Θ and C_Z satisfying (4.9) is given by[1]

$$C_j = \frac{\partial \mathcal{W}}{\partial a_j} a_j + \mu_c \tau_j \frac{\dot{a}_j}{a_j} + \Gamma_j a_j \,, \quad j = \Theta, Z, \tag{4.11}$$

where μ_c is the shear modulus of the cortex and τ_j is the characteristic time of axonal contractility. The additional variable Γ_j is the reactive term which enforces the unilateral constraint $a_j \leq 1$ and plays the role of a Lagrange multiplier. In physical terms, it can be interpreted as the force which prevents the actin and myosin filaments from sliding on each other beyond a certain threshold. More specifically, Γ_j satisfies the following relations, related to the Karush-Kuhn-Tucker conditions [312]:

$$\begin{cases} \Gamma_j (a_j - 1) = 0, \\ \Gamma_j \geq 0. \end{cases} \tag{4.12}$$

We observe that Γ_j is zero whenever $a_j \neq 1$. By using (4.7) and (4.11), we get

$$\dot{a}_j = \frac{a_j}{\mu_c \tau_j} \left(B_j - \frac{\partial \mathcal{W}}{\partial a_j} a_j - \Gamma_j a_j \right) , \tag{4.13}$$

[1] We stress that the restrictions on C_Θ and C_Z depend on the power of the remodelling forces postulated in (4.8). For an extensive discussion see [140], §14. In addition we remark that the dissipative term in (4.11) is just one of the admissible choices compatible with the Clausius-Duhem inequality, see [9].

for $j = \Theta, Z$. If $a_j = 1$, i.e. we are on the boundary of the unilateral constraint $a_j \leq 1$, and $\dot{a}_j\big|_{t=t_0} = 0$, from (4.13) we get

$$\Gamma_j a_j = B_j - \frac{\partial \mathcal{W}}{\partial a_j} a_j \,,$$

which holds whenever $\Gamma_j \geq 0$, namely when $B_j \geq a_j \frac{\partial \mathcal{W}}{\partial a_j}$. Conversely, if $B_j < a_j \frac{\partial \mathcal{W}}{\partial a_j}$, from (4.13) we observe that $\dot{a}_j\big|_{t=t_0}$ is negative, therefore $a_j(t) < 1$ in a neighbourhood of t_0, that is, a_j decreases from the maximum admissible value and therefore $\Gamma_j = 0$ again. In summary, when $a_j = 1$ the reactive term Γ_j is given by

$$\Gamma_j = \max\left\{0, \frac{B_j}{a_j} - \frac{\partial \mathcal{W}}{\partial a_j}\right\}. \tag{4.14}$$

As standard in the active strain approach [204, 348], we now make use the multiplicative decomposition of the deformation gradient to specialise the previously derived equations. Specifically, let $\mathcal{W}_0$ be the strain energy density of the passive material. We define the active free energy density as

$$\mathcal{W}(\mathbf{X}, \mathbb{F}, a_\Theta, a_Z) = \mathcal{W}_0(\mathbf{X}, \mathbb{F}\mathbb{F}_{\mathrm{a}}^{-1}). \tag{4.15}$$

With the newly defined energy density in the equation above, from (4.10) we get

$$\mathbb{P} = \frac{\partial \mathcal{W}_0}{\partial \mathbb{F}_{\mathrm{e}}} \mathbb{F}_{\mathrm{a}}^{-\mathrm{T}}, \tag{4.16}$$

while from Eq. (4.15) we obtain

$$\frac{\partial \mathcal{W}}{\partial a_j} = -\mathbb{M} : \left(\frac{\partial \mathbb{F}_{\mathrm{a}}}{\partial a_j} \mathbb{F}_{\mathrm{a}}^{-1}\right), \qquad \mathbb{M} = \mathbb{F}_{\mathrm{e}}^{\mathrm{T}} \frac{\partial \mathcal{W}_0}{\partial \mathbb{F}_{\mathrm{e}}}, \tag{4.17}$$

where $\mathbb{M}$ is the Mandel stress tensor defined in Eq. (4.4). If we introduce the tensors

$$\mathbb{I}_\Theta := \mathbf{E}_\Theta \otimes \mathbf{E}_\Theta - \mathbf{E}_R \otimes \mathbf{E}_R \,, \qquad \mathbb{I}_Z := \mathbf{E}_Z \otimes \mathbf{E}_Z - \mathbf{E}_R \otimes \mathbf{E}_R,$$

and combine (4.2) with (4.17), we get

$$\frac{\partial \mathcal{W}}{\partial a_j} a_j = -\mathbb{M} : \mathbb{I}_j. \tag{4.18}$$

Thus, by substituting (4.18) into (4.13) and enforcing (4.14), we finally get

$$\dot{a}_j = \begin{cases} \dfrac{a_j}{\mu_c \tau_j} \left(B_j + \mathbb{M} : \mathbb{I}_j \right), & \text{if } a_j < 1 \text{ or } B_j < -\mathbb{M} : \mathbb{I}_j, \\ 0, & \text{otherwise,} \end{cases} \tag{4.19}$$

where again $j = \Theta, Z$.

The evolution equations (4.19) for a_Θ and a_Z can be used to provide a physical interpretation of the external remodelling stress in (4.7). Similarly to the growth processes studied in [9, 107], B_Θ and B_Z represent the external forces that drive the active contraction of the cortex. We additionally observe that, when the linear combinations of the Mandel stress components $\mathbb{M} : \mathbb{I}_\Theta$ and $\mathbb{M} : \mathbb{I}_Z$ are equal to $-B_\Theta$ and $-B_Z$, respectively, the system is in chemo-mechanical equilibrium. Therefore, B_Θ and B_Z can be regarded as the equilibrium, or *homeostatic*, stresses towards which the system is led.

Despite sharing many similarities with the growth models developed in [9], our approach features an isochoric active strain tensor, namely, $J_a = 1$. As a consequence of this choice, the Mandel stress appears in Eq. (4.19) in place of the Eshelby stress (see for instance [9]). Secondly, $\mathbb{F}_a$ is not a generic tensor with positive determinant but belongs to the subset described by (4.2). Thus, only a particular combination of the Mandel stress components is involved in the evolution equations (4.19).

A similar approach has been recently adopted by Dehghany et al. in [99] to model F–actin contractility in axons. In their work, the authors used an approach inspired by smooth muscles models, such as those developed by Stålhand et al. [328]. With reference to these works, we underline that our model considers a more general form for the active strain tensor. In fact, instead of being prescribed *a priori*, the active strains a_Θ and a_Z are initially decoupled and their coupling is later provided by the Coleman-Noll procedure, through the Mandel stress tensor. In particular, the assumption of a linear relationship between a_Θ and a_Z such as $a_Z = \beta a_\Theta$ that was sometimes done previously can lead to some issues (for instance, the tensor $\mathbb{F}_a$ cannot be equal to the identity when $\beta \neq 1$). We will thoroughly analyse the assumption $a_\Theta = a_Z$ in the following, referring to it as the *monoparametric approach*.

4.2.4 Symmetry Assumptions

Experimental evidence [119] suggests that changes in the axonal external radius under contraction are invariant along $\mathbf{E}_Z$. We therefore assume the axon deformation to be

axisymmetric by enforcing the following simplified kinematics:

$$\boldsymbol{\chi}(\mathbf{X},t) = r(R,t)\mathbf{e}_r + \lambda Z\mathbf{e}_z\,, \tag{4.20}$$

with $\lambda \in (0,+\infty)$ being the imposed axial stretch along Z. Thus, the deformation gradient reads

$$\mathbb{F} = \frac{\partial r}{\partial R}\mathbf{e}_r \otimes \mathbf{E}_R + \frac{r}{R}\mathbf{e}_\theta \otimes \mathbf{E}_\Theta + \lambda \mathbf{e}_z \otimes \mathbf{E}_Z, \tag{4.21}$$

where $r(R,t) = R + u(R,t)$ with u representing the radial displacement. Under the assumption (4.20), the balance of linear momentum (4.3) takes the following form:

$$\frac{dP_{RR}}{dR} + \frac{P_{RR} - P_{\Theta\Theta}}{R} = 0\,, \tag{4.22}$$

where P_{RR} and $P_{\Theta\Theta}$ are the radial and the hoop components of the first Piola-Kirchhoff stress tensor, respectively. In terms of the Cauchy stress tensor the balance reads as follows:

$$\frac{dT_{rr}}{dr} + \frac{T_{rr} - T_{\theta\theta}}{r} = 0, \tag{4.23}$$

where T_{rr} and $T_{\theta\theta}$ are the radial and hoop components of $\mathbb{T}$. The balance of linear momentum must be solved with respect to the radial displacement u, either in material or spatial coordinates. Moreover, u must satisfy the homogeneous Dirichlet boundary condition $u(0,t) = 0$ to ensure the continuity of the deformation field along the Z-axis. By enforcing (4.20), the boundary condition (4.5) reduces to the scalar equation

$$P_{RR}|_{R=R_o} = 0\,, \qquad \text{or} \qquad T_{rr}|_{r=r_o} = 0\,, \tag{4.24}$$

depending on whether it is written in the reference or actual configuration; we have also introduced the notation $r_o = r(R_o,t)$. Eq. (4.22) endowed with the above mentioned boundary condition should be coupled with (4.19) to completely describe the axon dynamics.

4.3 Qualitative Analysis for an Incompressible Axon

In the following, we analyse the evolution equations (4.19) for the particular case where the axon is treated as an incompressible medium. Such a simplified assumption allows us

to provide analytical predictions on the existence and stability of the equilibrium solutions of (4.19).

To impose the incompressibility constraint, we require that

$$J_{\mathrm{e}} = \det \mathbb{F}_{\mathrm{e}} = 1$$

which, combined with the expression of the active strain tensor (4.2) and the multiplicative decomposition, implies that $J = \det \mathbb{F} = 1$ as well. The enforcement of the incompressibility constraint can be done by introducing a Lagrange multiplier p. More explicitly, we can introduce the extended strain energy density

$$\mathcal{W}_{\mathrm{ext}}(\mathbf{X}, \mathbb{F}, a_\Theta, a_Z, p) = \mathcal{W}(\mathbf{X}, \mathbb{F}, a_\Theta, a_Z) - p(J-1), \tag{4.25}$$

and then proceed as in the previous Section, by replacing $\mathcal{W}$ by $\mathcal{W}_{\mathrm{ext}}$ (see [117] for details). In particular, the Piola-Kirchhoff stress can be specified as

$$\mathbb{P} = \frac{\partial \mathcal{W}_0}{\partial \mathbb{F}_{\mathrm{e}}} \mathbb{F}_{\mathrm{a}}^{-\mathrm{T}} - p \mathbb{F}^{-\mathrm{T}}.$$

The Cauchy and the Mandel stress tensors instead are given by

$$\mathbb{T} = \frac{\partial \mathcal{W}_0}{\partial \mathbb{F}_{\mathrm{e}}} \mathbb{F}_{\mathrm{e}}^{\mathrm{T}} - p\mathbb{I}, \qquad \mathbb{M} = \mathbb{F}_{\mathrm{e}}^{\mathrm{T}} \frac{\partial \mathcal{W}_0}{\partial \mathbb{F}_{\mathrm{e}}} - p\mathbb{I}.$$

As a constitutive choice, we assume that both the cortex and the axoplasm are made of incompressible Neo-Hookean materials, i.e.

$$\mathcal{W}_0(\mathbb{F}_{\mathrm{e}}) = \frac{\mu}{2} \left(\mathbb{F}_{\mathrm{e}} : \mathbb{F}_{\mathrm{e}} - 3 \right), \qquad \mu = \begin{cases} \mu_{\mathrm{a}}, & R < R_{\mathrm{i}}, \\ \mu_{\mathrm{c}}, & R \geq R_{\mathrm{i}}, \end{cases} \tag{4.26}$$

where μ_{a} and μ_{c} represent the shear moduli of the axoplasm and of the cortex, respectively, and are both positive constants. By using the constitutive assumption (4.26), we can specialise the expressions of the Cauchy and the Mandel stress tensors:

$$\mathbb{T} = \mu \mathbb{F}_{\mathrm{e}} \mathbb{F}_{\mathrm{e}}^{\mathrm{T}} - p\mathbb{I}, \qquad \mathbb{M} = \mu \mathbb{F}_{\mathrm{e}}^{\mathrm{T}} \mathbb{F}_{\mathrm{e}} - p\mathbb{I}. \tag{4.27}$$

We now look for a radially symmetric solution in the form of (4.20) and we use the incompressibility constraint $J = 1$ to get $r(R,t) = R/\sqrt{\lambda}$, so that (4.21) becomes

$$\mathbb{F} = \frac{1}{\sqrt{\lambda}}\left(\mathbf{e}_r \otimes \mathbf{E}_R + \mathbf{e}_\theta \otimes \mathbf{E}_\Theta\right) + \lambda\, \mathbf{e}_z \otimes \mathbf{E}_Z\,. \tag{4.28}$$

The only unknown is therefore p, which can be obtained by the balance of linear momentum (4.23) as

$$p(r) = k_1, \qquad 0 \le r < r_i\,, \tag{4.29}$$

$$p(r) = k_2 + \frac{\left(a_\Theta^4 a_Z^2 - 1\right)\mu_c \log(r)}{a_\Theta^2 \lambda}, \qquad r_i \le r < r_o\,, \tag{4.30}$$

where $r_\mathrm{i} = r(R_\mathrm{i}, t)$. The constants k_1 and k_2 can be determined by using the interface and the boundary conditions (4.6)–(4.24) as follows:

$$k_1 = \frac{\mu_\mathrm{a}}{\lambda} + \frac{\mu_c\left[\log(r_i) - \log(r_o)\right]\left(a_\Theta^4 a_Z^2 - 1\right)}{a_\Theta^2 \lambda}, \tag{4.31}$$

$$k_2 = \frac{\mu_c\left[a_Z^2 a_\Theta^4 + \log(r_o) - a_Z^2 a_\Theta^4 \log(r_o)\right]}{a_\Theta^2 \lambda}. \tag{4.32}$$

The radial component of the Cauchy stress T_{rr} evaluated at the interface $r = r_\mathrm{i}$ can be computed by combining (4.27)–(4.32) as follows:

$$T_{rr}(r_i) = -\frac{\mu_c}{\lambda}\frac{\left(a_\Theta^4 a_Z^2 - 1\right)\left[\log(r_i) - \log(r_o)\right]}{a_\Theta^2}. \tag{4.33}$$

Thus, taking into account the expression of the Mandel stress tensor (4.27)–(4.28), the evolution equations (4.19) reduce to the following dynamical system:

$$\begin{cases} \dot{a}_\Theta = \dfrac{a_\Theta}{\mu_c \tau_\Theta}\left(B_\Theta + \dfrac{\mu_c(1 - a_\Theta^4 a_Z^2)}{\lambda a_\Theta^2}\right), \\[2ex] \dot{a}_Z = \dfrac{a_Z}{\mu_c \tau_Z}\left(B_Z + \dfrac{\mu_c\left(\lambda^3 - a_\Theta^2 a_Z^4\right)}{\lambda a_Z^2}\right), \end{cases} \tag{4.34}$$

where the first equation holds whenever $a_\Theta < 1$ or the right-hand side is negative, otherwise $\dot{a}_\Theta = 0$. Similarly, the second equation holds if either $a_Z < 1$ or the corresponding right-hand side is negative, otherwise $\dot{a}_Z = 0$.

4.3.1 Stability of the Equilibria

Throughout the rest of the Chapter, we will focus on the case where $B_\Theta = B_Z = B < 0$ is spatially constant, so that the external remodelling stresses are homogeneous and share the same value. As we will show in the following, we require B to be negative so that the cortex actively contracts. Moreover, since we are interested in uniaxial stretching of the axon, we focus on the range $\lambda \geq 1$.

By setting $\dot{a}_\Theta = \dot{a}_Z = 0$, we look for equilibrium solutions of (4.34). A subtraction of the two equations yields

$$a_\Theta^2 = \frac{a_Z^2}{\lambda^3}. \tag{4.35}$$

We can then substitute (4.35) into the second of equation (4.34) which gives the following condition to find the equilibria of the system:

$$f(a_Z) = \mu_c a_Z^6 - B\lambda^4 a_Z^2 - \mu_c \lambda^6 = 0. \tag{4.36}$$

We recall that $B < 0$ and $\lambda \geq 1$. Therefore, the function $f(a_Z)$ in (4.36) is strictly increasing and takes values of opposite sign at the endpoints of the interval $[0,1]$ whenever

$$\frac{B}{\mu_c} < \frac{1-\lambda^6}{\lambda^4}. \tag{4.37}$$

Hence, if such condition is satisfied, then the system has a unique equilibrium solution $(\bar{a}_\Theta, \bar{a}_Z)$. In particular, $\bar{a}_Z$ is obtained from (4.36) and $\bar{a}_\Theta = \bar{a}_Z/\lambda^{3/2}$ is given by (4.35).

To evaluate the stability of the equilibrium solutions, we compute the Jacobian matrix of the system (4.34) as follows:

$$\mathbb{J} = \begin{pmatrix} J_{11} & J_{12} \\ J_{21} & J_{22} \end{pmatrix}, \tag{4.38}$$

with

$$J_{11} = \frac{a_\Theta^2 \lambda B - \mu_c(1 - 3a_Z^2 a_\Theta^4)}{\lambda \mu_c \tau_\Theta a_\Theta^2}, \qquad J_{22} = \frac{a_Z^2 \lambda B - \mu_c(\lambda^3 - 3a_Z^4 a_\Theta^2)}{\lambda \mu_c \tau_Z a_Z^2}$$

$$J_{12} = -\frac{2a_Z a_\Theta^3}{\lambda \tau_\Theta}, \qquad J_{21} = -\frac{2a_Z^3 a_\Theta}{\lambda \tau_Z}.$$

A direct computation shows that, for all the admissible values of a_Θ and a_Z, we have $\mathrm{tr}\,\mathbb{J} < 0$ and $\det \mathbb{J} > 0$. Thus, the equilibrium solution $(\bar{a}_\Theta, \bar{a}_Z)$ is asymptotically stable. On

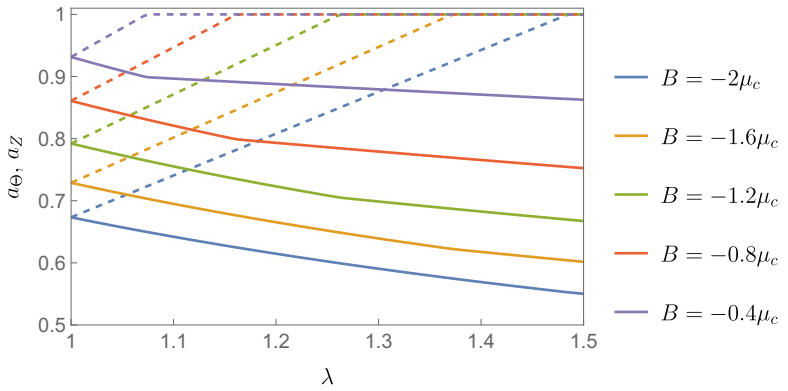

Fig. 4.3 Homeostatic active stretches $\bar{a}_\Theta$ (solid lines) and $\bar{a}_Z$ (dashed lines) plotted against the applied stretch λ for different values of B. The curves are obtained from (4.35), (4.36), and (4.40) for $B/\mu_c \in \{-2, -1.6, -1.2, -0.8, -0.4\}$.

the other hand, if (4.37) does not hold, i.e.

$$\frac{B}{\mu_c} \geq \frac{1-\lambda^6}{\lambda^4}, \tag{4.39}$$

we set $\bar{a}_Z = 1$, so that the first equation of (4.19) admits the equilibrium solution

$$\bar{a}_\Theta = \frac{1}{\sqrt{2}}\sqrt{\sqrt{\frac{B^2}{\mu_c^2}\lambda^2 + 4} + \frac{B\lambda}{\mu_c}}, \tag{4.40}$$

which always lies in $(0,1)$. Finally, we need to check that $B_Z + \mathbb{M} : \mathbb{I}_Z \geq 0$, so that $\bar{a}_Z = 1$ is a stationary solution of (4.19). It can be easily verified that such a condition is equivalent to (4.39). Moreover, such an equilibrium is always stable since the component J_{11} of the Jacobian matrix (4.38) is negative. The existence of asymptotically stable equilibria of (4.19) implies that, depending on the initial conditions, the system evolves towards the equilibrium points $\bar{a}_\Theta$ and $\bar{a}_Z$. These equilibrium values represent the homeostatic active stretches of the axon.

In Figure 4.3, we plot the stationary solutions $\bar{a}_\Theta$ and $\bar{a}_Z$ against the applied stretch λ, for different values of B. Starting from the same value for $\lambda = 1$, as evident from Eq. (4.35), the two homeostatic active stretches $\bar{a}_\Theta$ and $\bar{a}_Z$ exhibit opposite behaviours as λ increases. On the one hand, $\bar{a}_\Theta$ decreases with λ, leading to a stronger contraction in the circumferential direction which is generated by the actin molecular motors. On the other hand, a_Z increases until it reaches 1, meaning that there is no axial contraction.

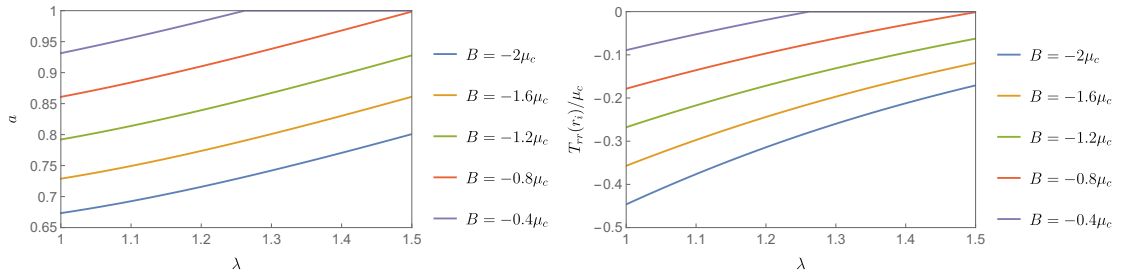

(a) (b)

Fig. 4.4 Monoparametric approach. (a): Homeostatic active stretch a versus the applied stretch λ. The value of a is computed by using (4.46). (b): Radial stress at the interface calculated from (4.47) for $R_\mathrm{i}/R_\mathrm{o} = 0.8$. In both cases, the curves are obtained with $B/\mu_\mathrm{c} \in \{-2, -1.6, -1.2, -0.8, -0.4\}$.

We remark that, when $\bar{a}_Z < 1$, the radial component of the Cauchy stress at the interface $r = r_\mathrm{i}$ given by Eq. (4.33) and evaluated at the equilibrium yields

$$\overline{T}_{rr}(r_i) = B \log\left(\frac{R_o}{R_i}\right), \tag{4.41}$$

which remarkably is independent of the applied stretch λ. Thus, as the axon is axially stretched, the cortex undergoes remodelling to maintain a constant compression in the axoplasm.

4.3.2 Monoparametric Active Stretch

In [99], the authors directly prescribe a coupling between a_Θ and a_Z, by assuming a linear relation between the two active stretches. In our case, enforcing $a_\Theta = a_Z = a$ we get

$$\mathbb{F}_\mathrm{a} = \frac{1}{a^2}\mathbf{E}_R \otimes \mathbf{E}_R + a(\mathbb{I} - \mathbf{E}_R \otimes \mathbf{E}_R). \tag{4.42}$$

The corresponding evolution equation for the active stretch a can be obtained by repeating the procedure exposed in Section 4.2. In such a case, the balance equations (4.7) for the remodelling stresses reduce to a single equation, namely $B = C$. The Clausius-Duhem inequality (4.8) reads instead

$$\int_{\mathcal{R}} \dot{\mathcal{W}}\, \mathrm{d}V \leq \int_{\mathcal{R}} \mathbb{P} : \dot{\mathbb{F}}\, \mathrm{d}V + 2\int_{\mathcal{R}\cap\Omega_{0\mathrm{c}}} C\frac{\dot{a}}{a}\, \mathrm{d}V.$$

Analogous computations to those performed above allow to find

$$\begin{cases} \mathbb{P} = \dfrac{\partial \mathcal{W}_0}{\partial \mathbb{F}_{\mathrm{e}}} \mathbb{F}_{\mathrm{a}}^{-\mathrm{T}}, \\ 2C = \mu_{\mathrm{c}} \tau \dfrac{\dot{a}}{a} - \mathbb{M} : \widehat{\mathbb{I}} + \Gamma, \end{cases} \tag{4.43}$$

where

$$\widehat{\mathbb{I}} := \mathbf{E}_\Theta \otimes \mathbf{E}_\Theta + \mathbf{E}_Z \otimes \mathbf{E}_Z - 2\mathbf{E}_R \otimes \mathbf{E}_R,$$

and Γ is the reactive term that enforces the unilateral constraint $a \leq 1$. Similarly to (4.19), the evolution equation for the active stretch reads as follows:

$$\dot{a} = \begin{cases} \dfrac{1}{\mu_{\mathrm{c}} \tau} \left(2B + \mathbb{M} : \widehat{\mathbb{I}} \right) a, & \text{if } a < 1 \text{ or } 2B < -\mathbb{M} : \widehat{\mathbb{I}}, \\ 0, & \text{otherwise.} \end{cases} \tag{4.44}$$

By assuming cylindrical symmetry as in (4.20), the differential equation can be specialised for the case $a < 1$ as

$$\dot{a} = \frac{a}{\mu_{\mathrm{c}} \tau} \left[2B + \frac{\mu_{\mathrm{c}} (\lambda^3 + 1 - 2a^6)}{\lambda a^2} \right], \tag{4.45}$$

which admits an equilibrium $\bar{a} < 1$ if

$$f(a) = 2\mu_{\mathrm{c}} a^6 - 2B\lambda a^2 - \mu_{\mathrm{c}} \left(\lambda^3 + 1 \right) = 0. \tag{4.46}$$

Since $f(0) < 0$, $f'(a) > 0$ for $B \leq 0$, and $f(a) \to +\infty$ as $a \to +\infty$, there exists one and only one $\bar{a} > 0$ such that $f(\bar{a}) = 0$. Such a root is acceptable if $\bar{a} < 1$, and this holds whenever $f(1) > 0$. It is straightforward to prove the asymptotic stability of $\bar{a}$. Otherwise, if $f(1) \leq 0$, then $2B + \mathbb{M} : \widehat{\mathbb{I}} \geq 0$ for $a = 1$ and the equilibrium solution is $\bar{a} = 1$.

To compute the stress components, we need to explicitly obtain the expression for p. By setting $a_\Theta = a_Z = a$ in (4.29)–(4.30), we get

$$\begin{aligned} p(r) &= \widehat{k}_1, && 0 \leq r < r_{\mathrm{i}}, \\ p(r) &= \widehat{k}_2 + \frac{(a^6 - 1)\mu_{\mathrm{c}} \log(r)}{\lambda a^2}, && r_{\mathrm{i}} \leq r < r_{\mathrm{o}}. \end{aligned}$$

If we impose the boundary and the interface conditions, (4.24) and (4.6) respectively, we find the two constants:

$$\widehat{k}_1 = \frac{\mu_a}{\lambda} + \frac{\mu_c}{\lambda}\frac{(a^6-1)\left[\log(r_i)-\log(r_o)\right]}{a^2}, \quad \text{and} \quad \widehat{k}_2 = \frac{\mu_c\left[a^6+\log(r_o)-a^6\log(r_o)\right]}{\lambda a^2}.$$

At the equilibrium, the radial stress at the interface is instead given by

$$\overline{T}_{rr}(r_i) = \frac{\mu_c(\bar{a}^6-1)}{\lambda\bar{a}^2}\log\left(\frac{R_o}{R_i}\right). \tag{4.47}$$

As shown in Fig. 4.4a, we observe that a is an increasing function of the axial stretch λ. Eventually, for large enough values of λ, the axon behaves as a passive material when a reaches 1. Differently, our approach with two active strains predicts an opposite behaviour for the hoop stretch, as reported in Figure 4.3. Such differences have important consequences on the stress distribution within the axon. In fact, while in our model the compression of the axoplasm is independent of λ, as shown in equation (4.41), in the monoparametric approach the radial stress at the interface relaxes as we increase λ and, eventually, becomes zero, see Figure 4.4b. This behaviour is the main drawback of such an approach since, as we will show in the next Section, axons actively decrease their radius upon stretching thanks to axoplasm compression.[2]

4.4 Active Regulation of Axon Diameter

In this Section, we investigate the role of cortex contractility in actively regulating the axon diameter. We then use experimental data from [119] to validate our numerical model. In these assays, the authors performed experiments on embryonic drosophila axons and measured variations in the diameter as a consequence of chemo-mechanical manipulations. In particular, different drugs were used to test the mechanical contribution of specific constituents: nocodazole was applied to depolymerise microtubules, while cytochalasin D was used to disrupt F–actin. The effect of these drugs on the axon is depicted in Fig. 4.5. Axons were then rapidly stretched and elongated by 20% from their initial length. To highlight the effect of each drug on the axon diameter, the authors also compared treated axons with control (untreated) axons.

[2] In the experiments of Fan et al. [119], to which we refer, the axial stretch is applied fast. We remark that if the towing is slow enough, axial stretch induces both an axial and radial growth of the axon [164].

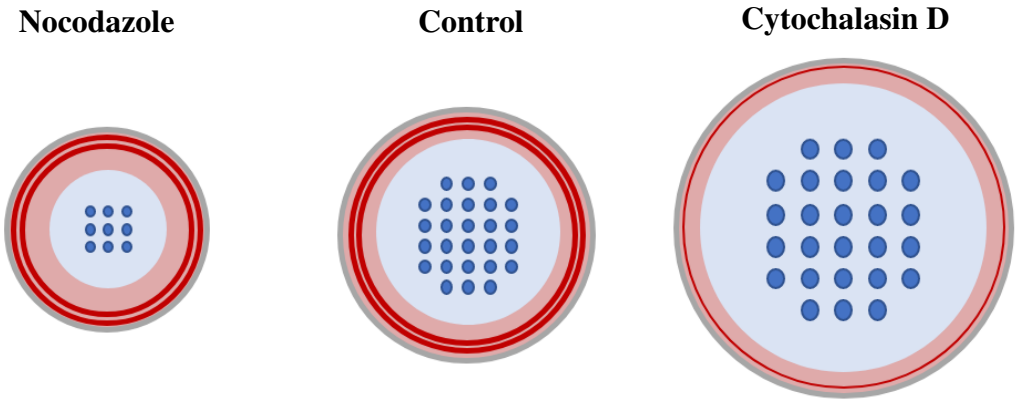

Fig. 4.5 Effect of drugs on the axon structure: red lines represent actin filaments while blue circles indicate microtubules. With respect to the control case (center), nocodazole depolymerises microtubules (left) leading to a reduction of the axon diameter, while cytochalasin D reduces the number of the actin filaments (right) and the axon can expand.

In order to replicate the experimental results, we relax the simplified assumption of incompressibility discussed in Section 4.3. To capture the effect of the active contractility on the axon radius, we thus rely on numerical simulations and obtain approximate solutions of the mathematical model. We then upgrade our model to include the effect of the different drugs on the mechanical response of the axon.

4.4.1 Damage

Experimental evidence shows that the axon stiffness decreases when samples are exposed to nocodazole and cytochalasin D [279]. We model the structural damage of the axon by introducing a scalar field $\alpha : \Omega_0 \times [t_0, t_1] \to [0,1]$ that describes the percentage of solid material depolymerised by the action of the drug or during the stretch. The free energy for the damaged axon can then be written as [142]:

$$\mathcal{W}(\mathbb{F}, \alpha) = (1-\alpha)\mathcal{W}_0(\mathbb{F}\mathbb{F}_a^{-1}), \tag{4.48}$$

where $\mathcal{W}_0$ is the strain energy density of the passive, sound axon. Initially, the axon is not damaged and therefore $\alpha(\mathbf{X}, t=0) = 0$. When nocodazole is applied, the actin cortex is not affected and only the microtubule network is damaged. Therefore, we propose the following simple phenomenological law for the damage of the axoplasm, which describes

an exponential degradation:

$$\alpha(\mathbf{X},t)=\begin{cases}\alpha_{\mathrm{n}}^{\infty}(1-e^{-t/\tau_{\mathrm{n}}}), & R<R_{\mathrm{i}},\\ 0, & R>R_{\mathrm{i}}.\end{cases} \tag{4.49}$$

Here, $\alpha_{\mathrm{n}}^{\infty}$ is a constant associated with the percentage of microtubules depolymerised in an infinite amount of time, while τ_{n} is the characteristic time for the action of nocodazole.

When cytochalasin D is applied, the contractility of the cortex is instead reduced and the actin filaments are depolymerised, thus damaging its elastic response [309]. Therefore, similarly to nocodazole, we assume that the damage field α follows a similar law:

$$\alpha(\mathbf{X},t)=\begin{cases}0, & R<R_{\mathrm{i}},\\ \alpha_{\mathrm{c}}^{\infty}(1-e^{-t/\tau_{\mathrm{c}}}), & R>R_{\mathrm{i}},\end{cases} \tag{4.50}$$

where $\alpha_{\mathrm{c}}^{\infty}$ and τ_{c} play the same role as $\alpha_{\mathrm{n}}^{\infty}$ and τ_{n} in (4.49). Furthermore, we postulate that cytochalasin D also reduces the contractility of the actin cortex by modulating the homeostatic stress in (4.7). For sake of simplicity, we take $B_{\Theta}=B_Z=B$ and we also assume that the contractions in the circumferential and axial direction share the same characteristic time, i.e. $\tau_{\Theta}=\tau_Z=\tau$ in (4.19). Here, we assume that the reduction of the external remodelling stress due to damage writes as follows:

$$B(\mathbf{X},t)=\left[1-\alpha(\mathbf{X},t)\right]^2 B_0,$$

where B_0 denotes the homeostatic stress in the intact axon. Finally, we also want to take into account the possible damage due to the deformation. In [119], Fan and co-authors observed that, when loads are removed, the final radius is smaller than the initial one. They concluded that this phenomenon was induced by the damage of the axoplasm. Indeed, a fast axial stretch can induce microtubule depolymerisation [356]. To model this phenomenon, we introduce an instantaneous damage in the axoplasm, i.e. we consider $\alpha(\mathbf{X},t)+\alpha_{\mathrm{s}}$ for $R<R_{\mathrm{i}}$, where α_{s} is a constant that represents the stretch-induced damage. If the axon is also damaged by nocodazole, the value of α_{s} will be smaller, since microtubules have been already impaired by the drug (see Table 4.1).

Symbol	Parameter description	Range	Value	References
R_o	Axon radius	$[1.45\,\mu m, 1.90\,\mu m]$	$1.5\,\mu m$	[119]
$R_o - R_i$	Cortex thickness	$[0.1\,\mu m, 0.5\,\mu m]$	$0.3\,\mu m$	[129, 218]
μ_c	Cortex shear modulus	$[0.1\,kPa, 10\,kPa]$	$1\,kPa$	[36, 102, 129, 402]
μ_a	Axoplasm shear modulus	$[0.1\,kPa, 10\,kPa]$	$1\,kPa$	[36, 102, 129, 402]
Λ_c	Cortex I Lame's coefficient	$[0.21\,kPa, +\infty]$	$100\,kPa$	[99, 129, 402]
Λ_a	Axoplasm I Lame's coefficient	$[0, 0.29\,kPa]$	$0.1\,kPa$	[99, 129]
B_0	External remodelling stress	—	$-1.6\,kPa$	Estimated
τ	Active contraction characteristic time	$\sim 10\,min$	$11.7\,min$	[119]
τ_n	Nocodazole characteristic time	$[8.5\,min, 83.4\,min]$	$20\,min$	[91]
τ_c	Cytochalasin D characteristic time	$\sim 10\,min$	$10\,min$	[119, 309]
α_n^∞	Nocodazole damage	—	0.65	Estimated
α_c^∞	Cytochalasin D damage	—	0.9	Estimated
α_s	Stretch-induced damage	—	0.1/0.75	Estimated

Table 4.1 Values of parameters involved in the model. The stretch-induced damage has been set equal to 0.75 in the control case and when cytochalasin D is applied. In the case of nocodazole-treated axons, such a parameter is decreased to 0.1 since the axoplasm is already damaged by the drug. With the exception of [129], the cortex is frequently treated as an almost incompressible medium, thus we have chosen a high value for Λ_c.

4.4.2 Constitutive Assumptions

For sake of simplicity, we neglect any anisotropy induced by the orientation of microtubules or actin filaments. We assume that both the axoplasm and the cortex are made of a compressible Neo-Hookean material. We therefore write the strain energy as follows:

$$\mathcal{W}_0(\mathbb{F}_e) = \frac{\mu}{2}(\mathbb{F}_e : \mathbb{F}_e - 2\log J_e - 3) + \frac{\Lambda}{2}(\log J_e)^2, \tag{4.51}$$

where μ and Λ are the Lamé coefficients of the intact axon. The axoplasm and the cortex are homogeneous, so that these coefficients are piecewise constant within the domain:

$$\mu = \begin{cases} \mu_a, & R < R_i, \\ \mu_c, & R > R_i, \end{cases} \qquad \Lambda = \begin{cases} \Lambda_a, & R < R_i, \\ \Lambda_c, & R > R_i. \end{cases}$$

In the next Section, we briefly present how the numerical simulations have been performed.

4.4.3 Initial Conditions and Numerical Implementation

In the experiments reported in [119], the axons are in their equilibrium state at the initial instant of time. Thus, we set $\lambda = 1$ and

$$\begin{cases} \alpha|_{t=0} = 0, \\ u|_{t=0} = u_0, \\ a_\Theta|_{t=0} = a_{\Theta 0}, \\ a_Z|_{t=0} = a_{Z0}, \end{cases}$$

as initial conditions, where u_0, $a_{\Theta 0}$, and a_{Z0} are the stationary solutions of (4.19) and (4.22). Such equilibrium state has to be determined by means of numerical computations.

Since the problem is independent of Z, we consider a cylindrical portion of the axon as follows:

$$\mathcal{B}_0 = \{\mathbf{X} \in \Omega_0 \mid 0 < Z < 1\}.$$

The strain energy of $\mathcal{B}_0$ is given by

$$\Psi(u) = \int_{\mathcal{B}_0} \mathcal{W}(\mathbb{F}, \alpha)\, \mathrm{d}V = \int_0^{R_0} 2\pi R\, \mathcal{W}(\mathbb{F}, \alpha)\, \mathrm{d}R, \tag{4.52}$$

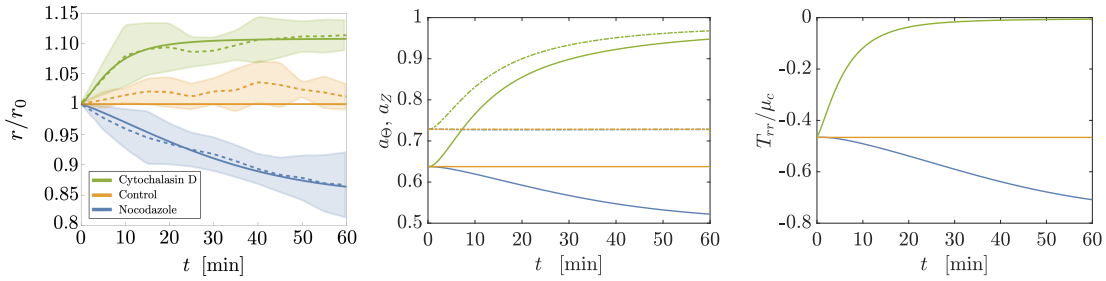

(a) (b) (c)

Fig. 4.6 Unstretched axons ($\lambda = 1$). Plots are reported for each treatment scenario: control (orange), nocodazole (blue) and cytochalasin D (green). (a): Comparison between the numerical result (continuous lines) and the experimental data reported in [119] (dashed lines) for the evolution of external radius. The latter is normalised with respect to r_0, the radius of the axon at equilibrium. The shaded regions indicate error bars in standard deviation relatively to the experimental data. (b): Plots of a_Θ (continuous lines) and a_Z (dashed-dotted lines) averaged over the cortex sectional area. (c): Evolution of radial stress T_{rr} at the interface $r = r_\mathrm{i}$, normalised with respect to the undamaged shear modulus of the cortex.

where we have used the cylindrical symmetry assumed in (4.20) and $\mathcal{W}$ is defined in (4.48). The function $u : (0, R_\mathrm{o}) \to \mathbb{R}$ satisfies the balance of linear momentum (4.22) and makes the functional (4.52) stationary (see [73] for details), i.e.,

$$\delta\Psi(u)[v] = 0 \quad \forall v \in V, \tag{4.53}$$

where v is a real scalar function on the interval $(0, R_\mathrm{o})$. Specifically, the functional space V is defined as

$$V = \{v \in H^1(0, R_\mathrm{o}) \mid v(0) = 0\},$$

where $H^1(0, R_\mathrm{o})$ denotes the space of square-integrable functions over $(0, R_\mathrm{o})$ admitting a square-integrable weak derivative.

The spatial computational domain $(0, R_\mathrm{o})$ is subdivided into 500 elements and the time step of the simulations is $\Delta t = 0.3$ minutes. Then, we solve Eq. (4.53) at each time step, whereas the time integration of the evolution equations (4.19) for a_Θ and a_Z is performed through the explicit Euler method. The numerical algorithm is implemented using the Python library FEniCS [8, 228].

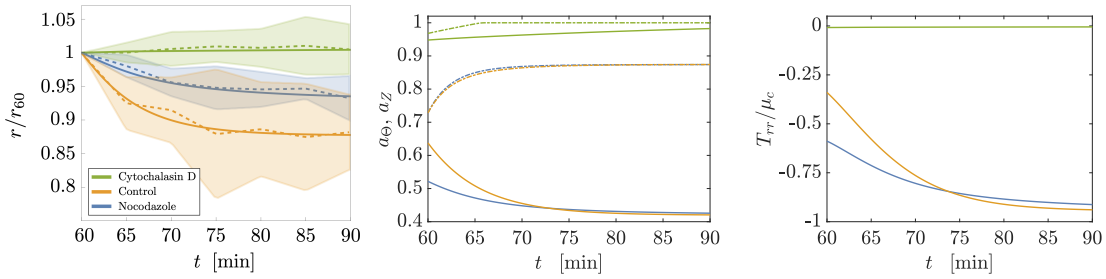

(a) (b) (c)

Fig. 4.7 Uniaxial stretch ($\lambda = 1.2$). Plots are reported for each treatment scenario: control (orange), nocodazole (blue) and cytochalasin D (green). (a): Comparison between the numerical result (continuous lines) and the experimental data reported in [119] (dashed lines) for the evolution of external radius. The latter is normalised with respect to r_{60}, the radius of the axon at $t = 60$ minutes, after the application of a fast stretch. The shaded regions indicate error bars in standard deviation relatively to the experimental data. (b): Plots of a_Θ (continuous lines) and a_Z (dashed-dotted lines) averaged over the cortex sectional area. (c): Evolution of radial stress T_{rr} at the interface $r = r_\mathrm{i}$, normalised with respect to the shear modulus of the sound cortex.

4.4.4 Results of the Simulations

In the following, we present and discuss the results of the numerical simulations. First, we analyse the effect of drugs in unstretched axons (i.e. $\lambda = 1$). Then, in accordance with the experimental procedure proposed in [119], we impose an elongation of the axon up to 20% of its initial length (i.e. $\lambda = 1.2$) and analyse its effect following a one-hour-long exposure to drugs. We refer to Table 4.1 for details on the choice of the model parameters.

Effect of Drugs on Unstretched Axons

First, we remark that untreated axons maintain the initial equilibrium state since they are not damaged, as evidenced by the orange curves in Fig. 4.6. In all the cases, the active contraction of the cortex induces a compressive stress on the axoplasm. The depolymerisation of microtubules due to nocodazole leads to a reduction of the radius and modifies the cortical stress state. Interestingly, the active remodelling forces induce a progressive decrease of a_Θ to restore the equilibrium state, as shown in Figure 4.6b. On the other hand, the axial active stretch a_Z does not undergo significant variations. The increase in the circumferential contraction results into a greater compression exerted by the cortex on the axoplasm (i.e. T_{rr} at the interface is negative and decreases, as shown in Figure 4.6c). In summary, the reduction of the axonal radius following nocodazole exposure is due to the coupling between microtubule depolymerisation and the circumferential active

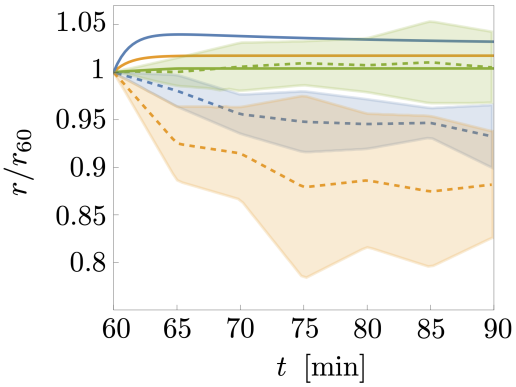

Fig. 4.8 Monoparametic approach: plot of the dimensionless radius r/r_{60} (where r_{60} is the radius of the axon at $t = 60$ minutes, when stretch is rapidly applied) as a function of time in the case of uniaxial stretch ($\lambda = 1.2$). The numerical results (continuous lines) are compared with the experimental data reported in [119] (dashed lines) for axons treated with nocodazole (blue), cytochalasin (green), and some untreated axons (orange). The shaded regions indicate error bars in standard deviation relatively to the experimental data. The monoparametric approach fails to reproduce the experimental data.

contraction. The longitudinal active stretch instead features an imperceptible deviation from the equilibrium configuration. Finally, cytochalasin D is responsible for a disruption of actin filaments in the cortex and the reduction of cortical remodelling stress. As a consequence, both the active stretches a_Θ and a_Z undergo a substantial increment which makes them close to 1 after one hour. In this case, the axoplasm behaves as a nearly passive material and the stress is almost completely relaxed (see Fig. 4.6c).

Uniaxial Stretch

To reproduce the stretch experiment, first of all the axon is exposed to one of the drugs for 60 minutes, after which a uniaxial stretch is imposed. We first consider the control case, i.e. the stretching of an untreated axon. The radius significantly reduces in time, as shown in Figure 4.7a. This is the result of cortex remodelling: while a_Z increases to balance the tension due to the axial stretch, a_Θ decreases, i.e. the active hoop contraction increases (see Figure 4.7b). Such a microstructural reorganisation increases axoplasm compression, as shown in Figure 4.7c. The changes in the axon diameter are amplified by the axoplasm damage, induced by the fast stretch.

The dynamics of nocodazole-treated axons under uniaxial stretching is similar, although the induced thinning is less pronounced when compared to the control case. We remark that axons treated with nocodazole are already damaged when stretch is applied. Therefore,

less microtubules are depolymerised as a result of the deformation, and the initial state is closer to the final equilibrium state, as depicted in Figure 4.7b. Instead, the evolution of a_Z is almost the same in both cases. Qualitatively similar trends are also observed in Figure 4.7c where we plot the radial stress T_{rr} at the interface as a function of time: radius reduction is correlated with an increased compression of the axoplasm.

Finally, we consider the stretching of axons exposed to cytochalasin D. In Figure 4.7a, we see that the radius is almost constant in time after the deformation. Indeed, as shown in Figure 4.7b, both the active stretches are close or equal to 1, so that the cortex behaves as nearly passive material. The constant diameter as result of F–actin depolymerisation supports our conjecture. In order to maintain a homeostatic stress state during stretching, the cortex actively reorganise itself and induces changes in the axon diameter.

In Section 4.3.2, based on the analysis performed in the incompressible case, we argued that imposing *a priori* a linear relation between the circumferential and the axial active stretches is not suitable to reproduce the experimental data in the case of the uniaxially stretched axon. This remains true also under the more realistic hypothesis of a compressible axon. Indeed, in Figure 4.8, we plot the dynamics of the axonal radius in all the three cases (control, nocodazole- and cytochalasin D-treated axons), obtained solving Eq. (4.44). We can see that the monoparametric model fails to fit the experimental curves and the reasons for that qualitatively rely on the considerations discussed in Section 4.3.2.

To better visualise how the stress profile affects the shape of the axon, in Figure 4.9 we show the actual transverse section at the final instant of time. Here, we plot the non-dimensional radial stress T_{rr}/μ_c. We observe that thinning of axons appears to be correlated with cortex thickening.

4.5 Discussion

In this Chapter, we have proposed a continuum model to predict the active contraction of the axonal cortex when the axon is subjected to chemo-mechanical stimuli. By modelling the axon as a continuum hyperelastic body, we have used the active strain approach to describe cortex contractility. The active contraction of the cortex is regulated by an extra balance law motivated by the work of DiCarlo and Quiligotti on growth [107]. In particular, Eq. (4.7) describes the equilibrium between the action of external active forces (modelled by B_Θ and B_Z) and the resistance of the material to remodelling, which we have called internal remodelling stresses and labelled as C_Θ and C_Z. We have then obtained thermodynamically

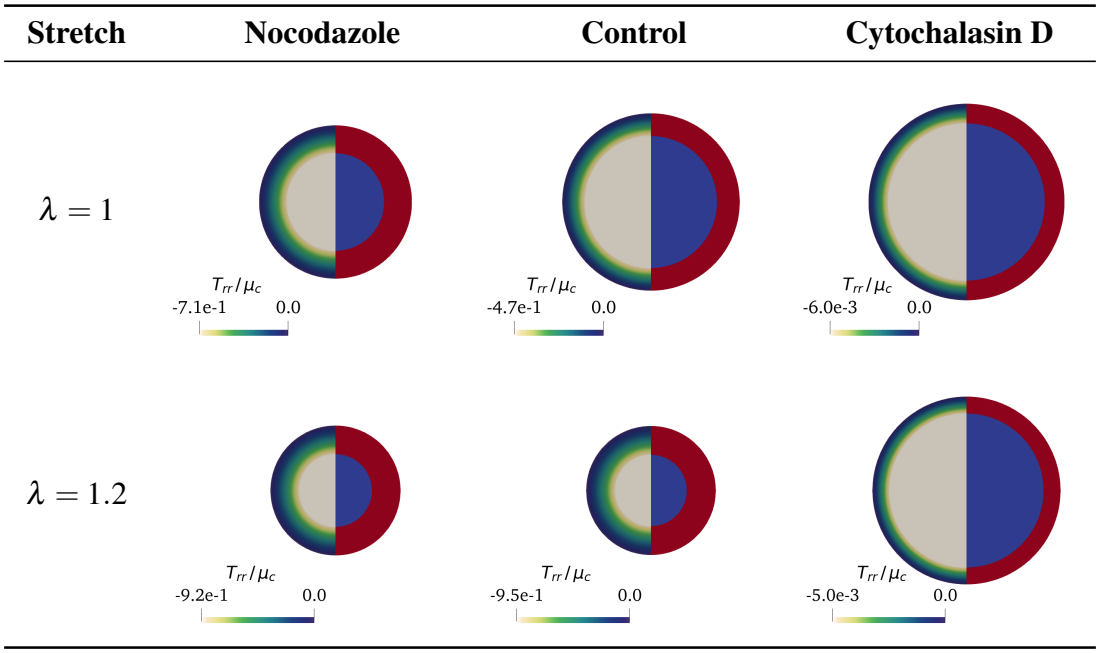

Fig. 4.9 Actual transverse section of the axon for $\lambda = 1$ (top) and $\lambda = 1.2$ (bottom) at $t = 60\,\text{min}$ and $t = 90\,\text{min}$, respectively. In each transverse section, on the left half we plot the dimensionless radial stress profile T_{rr}/μ_c, while on the right half we highlight the actual configurations of the axoplasm and of the cortex, represented as the blue and the red areas, respectively.

consistent constitutive laws by following the Coleman-Noll procedure. We extended the standard dissipation inequality for elastic bodies under isothermal conditions to account for the power of the cortex active contraction. More specifically, we have obtained the classic constitutive equation for the Piola-Kirchhoff stress tensor and some constitutive restrictions on C_Θ and C_Z. By using such constitutive laws, the remodelling balance in Eq. (4.7) becomes a system of differential equations that regulates the time evolution of the hoop and axial active stretches. Such equations exhibit some key features if compared with models of stress-modulated growth for biological tissues [9, 107]. Indeed, as can be seen in Eq. (4.19), the system evolves towards a steady state. Specific combinations of the Mandel stress tensor components associated with such equilibrium state are uniform throughout the cortex, namely $\mathbb{M} : \mathbb{I}_j = -B_j$. Thus, the axon reacts to external chemo-mechanical stimuli by regulating the active contraction to reach a homeostatic stress state.

To explore some qualitative characteristics of the model, we have at first assumed the axon to be incompressible. In this context, the evolution equations reduce to the nonlinear dynamical system (4.34). Through a linear stability analysis, we have proved the existence of a single asymptotically stable solution associated with the above mentioned homeostatic state.

Then, by means of a more suitable compressible constitutive model, we have implemented numerical simulations of axon dynamics and compared our results with the experiments reported in [119]. In our simulations, we have modelled the equilibrium behaviour of the axon followed by a uniaxial deformation of 20% stretch. We have reproduced three scenarios: a) control case, b) the disruption of F–actin filaments when axons are exposed to cytochalasin D and c) the depolymerisation of microtubules following the application of nocodazole. In our numerical model, the effect of the drugs is accounted for by introducing a damage function that modifies the energy functional, as we have discussed in Section 4.4.1. Moreover, since in experiments the axons are pulled at a high strain rate [119], we have assumed that microtubules are further damaged during the axial deformation [356].

The numerical results for all three scenarios are in very good quantitative agreement with the experimental results, as shown in Figures 4.6–4.7. Indeed, the diameter progressively increases when F–actin filaments are disrupted, while a decrease of the transverse section area with respect to the control case is observed when microtubules are depolymerised. We have shown that the diameter of axons is regulated by the compressive stress applied on the axoplasm by the cortex. Diameter reduction appears to be correlated with a thickening of the axonal cortex, as shown in Figure 4.9.

Our results support the hypothesis of a coupled mechanism between the axial and hoop active stretches [119]. The cortex undergoes a microstructural reorganisation to modulate its stress state and regulates axon diameter by compressing the axoplasm. Understanding such mechanism may represent a preliminary step towards a better comprehension of the physical causes which underlie axon morphological degeneration as a consequence of neurodegenerative diseases, viral infections, and traumatic strain injuries [91, 301].

Chapter 5

Solid and Fluid Stresses in Brain Tumour Growth

Moving from the cell scale to the tissue and organ scale, the main focus of this Chapter is to propose a mechanical framework for the description of brain tumour growth. Indeed, recent experimental findings seem to point towards a relevant role played by solid stresses induced by the proliferating tumour, in addition to fluid pressure. Such stresses may be important to understand the progression of the pathology and cannot be captured by classical models which are mainly based on diffusion equations. To provide a detailed mechanical description, we derive a model for brain tumour growth based on the theory of mixtures and on morphoelasticity. Moreover, our framework is able to incorporate patient-specific data obtained through medical imaging techniques. Simulations are therefore performed on realistic geometries which include the anisotropic features of brain tissue, properly modified to account for growth-induced deformations.

The Chapter is organised as follows. In Section 5.1 we provide a short review of brain tumour modelling and we discuss the role of solid stresses. Then, in Section 5.2 we derive the mathematical model and provide an estimate to all the parameters involved. After a discussion about the numerical implementation carried out in Section 5.3, we present the results of the simulations in Section 5.4. Finally, Section 5.5 is devoted to a summary and to the conclusions.

The contents of this Chapter have been published in the following article:

G. Lucci, A. Agosti, P. Ciarletta, and C. Giverso. Coupling solid and fluid stresses with brain tumour growth and white matter tracts deformation in a neuroimaging-informed model, *Biomechanics and Modeling in Mechanobiology* 21:1483–1509 (2022).

5.1 Mechanical Stresses in Brain Tumours

Despite the relevant advances in clinical practice supported by novel therapies and imaging techniques, the treatment of brain tumours remains not fully effective in many cases, due to cancer aggressiveness and to the intrinsically fragile nature of brain tissue. For this reason, in the last three decades, the mathematical modelling of brain tumour growth started to attract consistent research attention.

Indeed, mathematical and computational models can provide powerful instruments for investigating cancer progression, especially in those cases that are particularly difficult to be treated with current therapeutic protocols like brain tumours. Such models can be of help to understand the mechanisms of cancer progression, providing further support to clinical observations. At the same time, *in silico* findings might be employed to maximize the efficacy of the treatment and to approach personalised therapeutic strategies. To achieve these goals, mathematical models have become increasingly refined during the years: to give an overview, in Table 5.1 we summarise some of the main contributions that appear in the literature. For detailed and extensive reviews on brain cancer modelling, we refer the reader to [7, 118, 158, 240].

Specifically, at the microscopic and mesoscopic level, discrete computational approaches such as Cellular Automata (CA) or Agent-Based Models represent useful tools to explore invasive migration, phenotypic plasticity and early growth of brain tumours. Models based on Ordinary Differential Equations (ODE) might be employed to describe sub-cellular and molecular processes. At the macroscopic scale, continuum models are more suitable to describe brain tumour cell motility and spatial dynamics through Partial Differential Equations (PDE). The first works [341–345, 364, 391] used reaction-diffusion equations to model migration and proliferation of gliomas and paved the way for a number of subsequent studies. Multi-scale formulations bridging the gap between the microscopic and the macroscopic levels, grounded on Kinetic Models (KM) and their scaling [83, 84, 113–116, 176, 281, 340], also provided an interesting extension of purely diffusive, phenomenological descriptions. Another approach recently proposed to tackle the problem of brain tumour proliferation employs a Cahn-Hilliard-type (CH) equation to deal with the infiltrative nature of some brain tumours, showing a good agreement with real data [2–4, 82, 118].

Despite the ability of these models to qualitatively capture some peculiar features of the growth of a brain tumour, they do not account for some important mechanical aspects, such as the influence of the stress exerted by the healthy tissue on the tumour mass and

Type of Model	References	Mechanics	Imaging
CA	[26, 27, 44, 157, 194, 200, 357]	No	No
ODE	[31, 178]	No	No
ABM	[236–238]	No	No
ABM – PDE – RD	[132, 133]	No	No
PDE – RD	[306, 341–345, 347, 364, 391]	No	Yes (CT+MRI)
PDE – RD	[156, 187]	No	Yes (MRI+DTI)
PDE – ARD	[395]	No	No
PDE – ARD	[338]	No	Yes (DTI)
PDE – ARD – KM	[281, 340]	No	Yes (DTI)
ODE – PDE – ARD – KM	[83, 84, 113–116]	No	Yes (DTI)
PDE – ARD – CM	[42, 79, 163]	Yes (LE)	Yes (MRI+DTI)
PDE – CM	[18, 19, 110, 111, 211, 233]	Yes (NLE)	Yes (MRI+DTI)
PDE – CM	[242]	Yes (FL)	No
PDE – CH	[2–4, 82, 118, 221]	Yes (FL)	Yes (MRI+DTI)
HYB	[126, 202, 203, 315]	No	No
HYB	[355, 401]	No	No

Table 5.1 Summary of previous contributions concerning brain tumour modelling. The models are classified according to three criteria: (i) the mathematical framework employed to describe the growth of the tumour mass (first column); (ii) the inclusion of tumour and tissue mechanics with quantification of deformations and stresses (third column); (iii) the use of patient-specific imaging data to perform simulations (fourth column). Abbreviations: CA = Cellular Automaton; ABM = Agent-Based Model; ODE = Ordinary Differential Equations model; PDE-RD = Reaction-Diffusion equations; PDE-ARD = Advection-Reaction-Diffusion equations; PDE-KM = Kinetic model; PDE-CH = Cahn-Hilliard model; PDE-CM = Continuum-Mechanics-based model; HYB = Hybrid model; FL = Fluid; LE = Linear elasticity; NLE = Nonlinear elasticity.

vice versa. Indeed, not only the growth of the tumour might be limited by the surrounding tissue, as observed in many biological experiments *in vitro* [69, 101, 108, 161, 255], but also the presence of a neoplasm may be a critical clinical issue inside the healthy peripheral tissue subject to unnatural displacements. Although tumour growth can adversely impact the health of any hosting organ, this is especially devastating in the brain. As a matter of fact, compared with extra-cranial organs, the brain is unique because of its physical confinement due to the skull fixed volume, which can further amplify mechanical force effects. Furthermore, brain functions might be corrupted by mechanical forces: the tumour growth-induced deformation and compression is believed to be a major cause of the

neurological clinical symptoms and severe disabilities seen in patients with brain cancer, and represents a negative prognostic factor [128, 191, 331]. The identification of the importance of mechanical cues and their potential regulatory roles in the development and maintenance of neuronal structures [260] has led to the definition of a new field of research, named "neuromechanobiology", dealing with the effects of mechanical forces on normal neurophysiology and on neurological disorders [16, 45, 49, 260]. In this regard, understanding how injured and healthy brain fibre tracts deform and re-distribute in response to the growing tumour mass is a fundamental issue.

In particular, mechanical forces could be exerted either by the tumour-associated oedema or by the solid components of the malignant tissue, such as cells and extracellular matrix [317]. This kind of stress is often referred to as *solid stress* or *mass-effect*. Its origin and biological consequences are still poorly understood, with respect to the fluid pressure associated with oedema, a well-known mechanical abnormality in brain tumours [64, 141, 185, 317]. Although, recently, the origin and neurological effects of the solid stress have gained attention, details of their quantification *in vitro* and their biological impact on the physiology of the healthy brain surrounding the tumour remain unknown [191, 317]. Concerning these latter aspects, the tumour-generated solid stress consistently distorts the micro-anatomy of the neighbouring brain tissue and it compresses the blood vessels, generating a vascular collapse, as sketched in Fig. 5.1. Consequently, there is a reduction of peritumoural vascular perfusion, contributing to intratumoral hypoxia, inducing neuronal loss and hindering the delivery and efficacy of anti-cancer therapies [64, 269, 280, 317]. Since tumours of similar imaging volumes have been observed to give rise to different amounts and distributions of solid stresses [269, 331], it is relevant to evaluate deformations, stresses and displacement caused by their progression, in order to properly capture the correct area of the brain influenced by the cancer.

Motivated by these facts, some recent models employed the framework of Continuum Mechanics to provide a description of solid stresses. The first and simpler biomechanical models considered the brain as a linear elastic (LE) medium [42, 79, 163], while nonlinearly elastic (NLE) constitutive equations (e.g. Neo-Hookean or Mooney-Rivlin) have been employed in some successive descriptions [18, 19, 110, 111]. Nevertheless, in these latter works, the patient-specific anisotropy is not included and the effect of fibre deformations subsequent to tumour growth, as well as the impact on the diffusion of chemical species and on the motion of cells, have not been investigated.

Therefore, stimulated by the need to elaborate a more refined description of brain tumour mechanical impact, in this work we develop a mathematical model for cancer

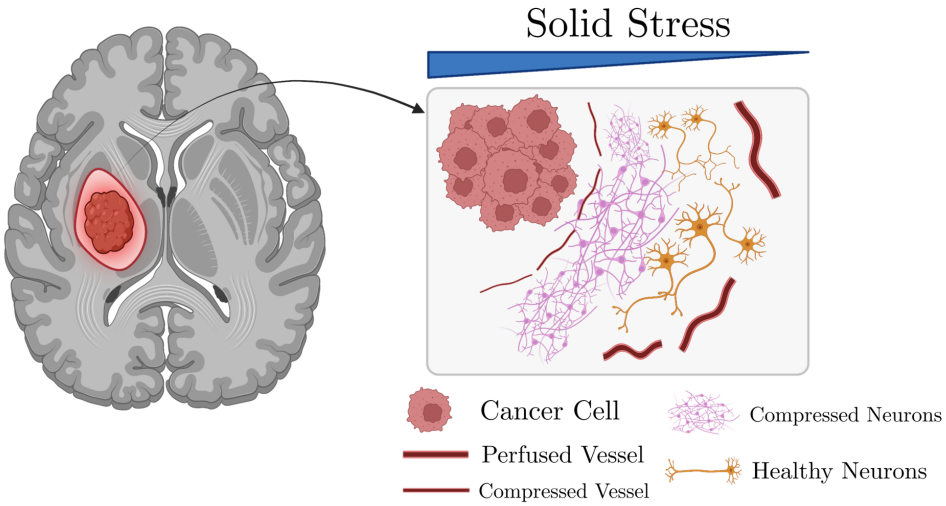

Fig. 5.1 Sketch of the solid stress effect in brain tumours, redrawn from [317]. In addition to compressing neurons, the presence of a solid mass may lead to reduced vessel perfusion. Created with [38].

growth and proliferation which includes brain hyperelasticity, in order to evaluate the effects of structural changes in the white matter and the nonlinear elastic deformations of brain tissue. In particular, we propose a macroscopic model based on the theory of mixtures and morphoelasticity.

5.2 Mathematical Model

In this Section, we derive a continuous mechanical theory for modelling the macroscopic brain tumour growth using a multiphase approach [46, 58] and the evolving natural configurations framework. Even though the general framework of the proposed model could be used, in principle, to describe the development of any kind of solid tumour, we specialise it to account for brain tumour evolution in a patient-specific setting. In particular, we consider both the healthy and the tumour brain tissues as saturated domains comprising two distinct phases, which represent the cell population (labelled with subscript "s") and the interstitial fluid (labelled with subscript "ℓ"). Moreover, the cancer and the host tissue are localized in different regions, denoted by a smooth approximation of an indicator function.

5.2.1 Kinematics and Growth Framework

At a given time t, we consider the current configuration of the brain as a three-dimensional domain $\Omega(t)$ and denote by $\Omega_{\mathrm{t}}(t)$ the subregion occupied by the growing tumour, while $\Omega_{\mathrm{h}}(t)$ stands for the subregion occupied by the healthy tissue, with $\Omega(t) = \Omega_{\mathrm{t}}(t) \cup \Omega_{\mathrm{h}}(t)$. In particular, the tumour region is identified by a smooth approximation of the indicator function $\chi_{\Omega_{\mathrm{t}}(t)}$ of the cancerous domain, which moves at the velocity of diseased cells. The smoothness of $\chi_{\Omega_{\mathrm{t}}(t)}$ allows to account for regions of coexistence of tumour cells and healthy cells near the cancer mass. Such a description is appropriate to describe solid and low-grade brain tumours, that are mostly localized and characterized by a superposition of healthy and diseased tissues only around the principal mass, without colonies of growing and invading cancer cells detached from the tumour bulk. In particular, we identify the tumour domain with the upper level set $\Omega_{\mathrm{t}}(t) = \{\mathbf{x} \in \mathbb{R}^3 : \chi_{\Omega_{\mathrm{t}}(t)}(\mathbf{x}) > 0.1\}$, where $\mathbf{x}$ is the spatial coordinate. Instead, we use the notation Ω^0, Ω^0_{t} and Ω^0_{h} for the reference configurations of the whole brain, the tumour and the host tissue, respectively. Coherently, the tumour domain in the reference configuration is $\Omega^0_{\mathrm{t}} = \{\mathbf{X} \in \mathbb{R}^3 : \chi_{\Omega^0_{\mathrm{t}}}(\mathbf{X}) > 0.1\}$, where $\mathbf{X}$ is the material coordinate. We remark that the tumour region Ω^0_{t} in the reference configuration does not evolve in time.

As mentioned above, brain tissue (both healthy and unhealthy) is regarded as a mixture of two phases: a solid one, with volume fraction ϕ_{s}, that represents the cellular component, and a liquid one, with volume fraction ϕ_ℓ, including all the fluid components of the brain. The solid and fluid phases are considered to saturate all the available space, so that the condition $\phi_{\mathrm{s}} + \phi_\ell = 1$ holds at any point in the domain $\Omega(t)$ and at any time instant. Following standard definitions in mixtures theory, by knowing the true density $\widehat{\rho}_\alpha$ of the material composing the α-phase, with $\alpha \in \{\mathrm{s}, \ell\}$, it is possible to define the partial phase density $\rho_\alpha = \widehat{\rho}_\alpha \phi_\alpha$. Then, we can introduce the displacement vector field $\mathbf{u}_{\mathrm{s}}$ of the solid phase, which defines the deformation of the body mapping the reference configuration to the current one, and the related deformation gradient $\mathbb{F}_{\mathrm{s}} = \mathbb{I} + \mathrm{Grad}\,\mathbf{u}_{\mathrm{s}}$.

Furthermore, it is well known that a tissue undergoing growth, such as the one in the tumour region, experiences inelastic distortions and residual stresses [140, 307, 323]. To account for this fact from the mechanical point of view, a possible way is to employ a multiplicative decomposition of the deformation gradient [10, 107]: the tensor $\mathbb{F}_{\mathrm{s}}$ of the cellular population can therefore be split into two contributions, yielding

$$\mathbb{F}_{\mathrm{s}} = \mathbb{F}_{\mathrm{e}}\,\mathbb{F}_{\mathrm{g}}. \tag{5.1}$$

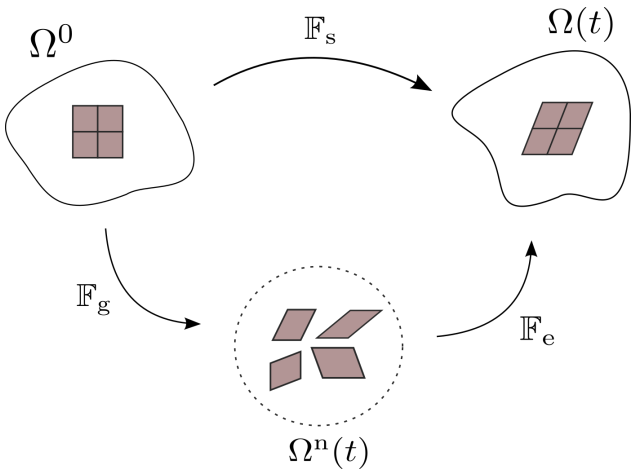

Fig. 5.2 Schematics of the multiplicative decomposition of the deformation gradient for brain tumour growth.

In Eq. (5.1), $\mathbb{F}_e$ is the purely elastic contribution to the overall deformation gradient, whereas $\mathbb{F}_g$ represents the inelastic distortions related to growth. The tensor $\mathbb{F}_g$ determines the so-called *evolving natural state* $\Omega^n(t)$ of the body undergoing growth processes, where each material particle is allowed to grow freely and independently of the other ones. Hence, the natural state of the material is stress-free: the transition between the reference configuration and the natural state is then described by tensor $\mathbb{F}_g$, while the subsequent elastic accommodation is included in $\mathbb{F}_e$, because the state defined by $\mathbb{F}_g$ is not in general compatible. We also recall that, throughout the path between the natural state and the current configuration, mass is assumed to be preserved, so that the growth contribution is entirely carried by $\mathbb{F}_g$. A sketch of the multiplicative decomposition of the deformation gradient is reported in Fig. 5.2.

A consequence of Eq. (5.1) is that the volumetric part of the deformation gradient, $J_s := \det \mathbb{F}_s$, can be written as

$$J_s = J_e J_g, \tag{5.2}$$

with $J_e := \det \mathbb{F}_e$ and $J_g := \det \mathbb{F}_g$. Since the overall deformation gradient $\mathbb{F}_s$ is assumed to be non-singular and $J_g \geq 1$, since we are considering growth processes, from Eq. (5.2) it follows that each tensor introduced in Eq. (5.1) is non-singular as well. Finally, we introduce the elastic right Cauchy-Green deformation tensor $\mathbb{C}_e := \mathbb{F}_e^T \mathbb{F}_e$ and its isochoric part $\overline{\mathbb{C}}_e := J_e^{-2/3} \mathbb{C}_e$.

5.2.2 Balance Equations

The multiphase approach we employ to describe tumour growth is based on the theory of mixtures and consists of a set of mass and momentum balance equations. First of all, we assume that the mixture is saturated and that both phases of the mixture have constant true densities, so that the materials composing the phases are incompressible. Then, since cells are mainly composed of water, we assume that the true densities of both phases are equal, i.e., $\widehat{\rho}_{\mathrm{s}} = \widehat{\rho}_{\ell}$, and that external body forces (such as the gravitational force) as well as inertial effects are negligible. These hypotheses are reasonable when dealing with biological problems [14, 58], since the motion of cells and interstitial fluid is very slow. Next, we write the balance equations for the cellular phase, with volume fraction ϕ_{s} moving with velocity $\mathbf{v}_{\mathrm{s}}$, and for the liquid phase, with volume fraction ϕ_{ℓ} moving with velocity $\mathbf{v}_{\ell}$. As mentioned above, we remark that the boundary between the tumour and the healthy domain is advected with the velocity of the cell phase $\mathbf{v}_{\mathrm{s}}$. We assume that in the tumour region $\Omega_{\mathrm{t}}(t)$ cells proliferate, whereas in the domain occupied by the healthy tissue $\Omega_{\mathrm{h}}(t)$ the proliferation of cells is compensated by natural cell death, so that the net rate of growth Γ_{s} is equal to zero. Finally, assuming that the mixture is closed, the mass increase in the cellular phase happens at the expense of the liquid phase, so that the mass balances of the cellular and fluid phases read:

$$\frac{\partial \phi_{\mathrm{s}}}{\partial t} + \nabla \cdot (\phi_{\mathrm{s}} \mathbf{v}_{\mathrm{s}}) = \Gamma_{\mathrm{s}} \chi_{\Omega_{\mathrm{t}}(t)}\,, \tag{5.3}$$

$$\frac{\partial \phi_{\ell}}{\partial t} + \nabla \cdot (\phi_{\ell} \mathbf{v}_{\ell}) = \Gamma_{\ell} \chi_{\Omega_{\mathrm{t}}(t)} = -\Gamma_{\mathrm{s}} \chi_{\Omega_{\mathrm{t}}(t)}\,. \tag{5.4}$$

The net rate of tumour growth Γ_{s} is influenced by many different factors, such as the availability of nutrients and the solid stress [10, 11, 13, 241]. In a first approximation, one can assume that the amount of nutrients, denoted by its concentration c_n, along with the availability of space, are the main factors regulating cell growth, so that the following constitutive equation for the growth term holds:

$$\Gamma_{\mathrm{s}}(\phi_{\mathrm{s}}, c_n) = \gamma \phi_{\mathrm{s}} (\phi_{\max} - \phi_{\mathrm{s}}) \, (c_n - c_0)_+\,, \tag{5.5}$$

where $(\cdot)_+$ denotes the positive part of its argument and γ is a positive coefficient. That way, the proliferation rate depends affinely on the available concentration of nutrients c_n, provided that it is greater than a hypoxia threshold c_0. Conversely, when $c_n \leq c_0$ the growth rate becomes zero and tumour expansion arrests. Moreover, in Eq. (5.5) we have

that growth depends on the fraction of cells that is already present - which is reasonable since cell population grows by duplication; finally, we have a factor $(\phi_{\max} - \phi_s)$, whose presence is explained by the necessity to decrease the proliferation rate as the cellular phase fills all the available space for the solid constituent $\phi_{\max}$: this accounts for the phenomenon of contact inhibition of growth. More complex relations for Γ_s including explicitly the role of stresses may also be considered [241, 242, 335]. Indeed, several studies have dealt with the effect of mechanical stresses on tumour growth *in vitro*, by embedding tumour spheroids either in agarose matrices of varying concentrations or in a culture medium with biocompatible polymers able to exert a mechanical stress, such as Dextran [69, 101, 161, 255]. These studies showed that tumour growth is impaired by the compressive forces generated by the resistance of the surrounding tissue/matrix and that the mechanical stress has a strong impact on cancer progression. In light of these observations, we will also take into account an expression for the tumour proliferation rate that involves growth inhibition due to compressive stresses [241], namely,

$$\Gamma_s(\phi_s, c_n, \Sigma) = \gamma \phi_s (\phi_{\max} - \phi_s) (c_n - c_0)_+ \left(1 - \frac{\delta_1 \Sigma_+}{\Sigma_+ + \delta_2}\right), \tag{5.6}$$

where $\Sigma := -\mathrm{tr}(\mathbb{T}_s)/3$ is a measure of compression, related to the spherical part of the constitutive Cauchy stress tensor of the solid phase. The presence of the positive part means that, if the tissue is in compression, then growth is slowed down, while traction does not inhibit tumour proliferation. The constitutive definition of the stress $\mathbb{T}_s$ as a function of the deformation will be provided in the next Subsection. Instead, δ_1 and δ_2 are parameters quantifying the inhibition of growth: in particular, $\delta_1 < 1$ regulates the maximum amount of inhibition due to stress, while δ_2 describes how fast the reduction of Γ_s happens in response to compressive stresses. A plot of the stress inhibition contribution to the growth rate for different values of the parameters δ_1, δ_2 is shown in Fig. 5.3.

In order to insert in the model the growth terms (5.5) and (5.6), it is necessary to introduce an equation describing the evolution of the nutrients in the domain. We assume that these chemicals are transported by the fluid phase and can diffuse into it; at the same time, they are taken by the growing tumour and uniformly supplied by the vasculature. We introduce the hypothesis that the nutrients' uptake by the healthy tissue is negligible compared to the one by the tumour tissue. Biologically, this is equivalent to saying that the nutrients absorbed by the host tissue are immediately replaced by the vasculature. Hence, if we denote by c_n the concentration of available nutrients normalized with respect to the

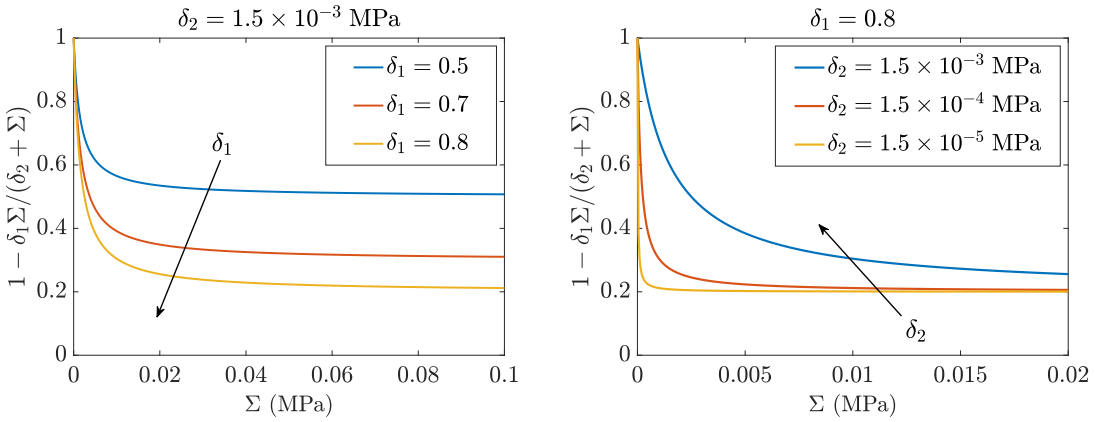

Fig. 5.3 Stress inhibition component in the growth rate (5.6) as a function of the compressive stress measure Σ, for different values of the parameters δ_1 and δ_2. In (a) we fix $\delta_2 = 1.5 \times 10^{-3}$ MPa and change δ_1, which governs the maximum amount of stress inhibition. In (b) we have $\delta_1 = 0.8$ fixed and vary δ_2, which modifies the sensitivity of Γ_s to variations in Σ.

physiological concentration, so that $c_n \in [0,1]$, the mass balance of nutrients in $\Omega(t)$ reads

$$\frac{\partial}{\partial t}(\phi_\ell c_n) + \nabla \cdot (\phi_\ell c_n \mathbf{v}_\ell) = \nabla \cdot (\phi_\ell \mathbb{D} \nabla c_n) + \Gamma_\ell c_n \chi_{\Omega_t(t)} + G_n \chi_{\Omega_t(t)}\,, \tag{5.7}$$

where $\mathbb{D}$ is the diffusion tensor. The use of a tensor in the diffusion term allows to account for the structural anisotropy of brain tissue [187], that induces fluids to diffuse preferentially along certain directions. Actually, the tensor $\mathbb{D}$, that can be obtained through DTI imaging and subsequent modification (see Section 5.2.4), describes how water diffuses along specific directions. However, if we consider that the main nutrient for cells is oxygen which is carried by water molecules, we can take the same tensor as a descriptor of the diffusion values of nutrients. The term $\Gamma_\ell c_n$ accounts for the variation of the chemical concentration due to absorption/production of the liquid in which the chemical is dissolved. Instead, G_n models the supply of chemicals due to the presence of the blood as well as the consumption of nutrients by the cells in the tissue that occurs without net variation of the liquid amount. This last term could represent the transport of oxygen through the walls of the capillaries, either without exchange of fluids, or with the possible excess of fluid due to the presence of leaky vessels in the tumour region automatically balanced by the venous capillaries and the lymphatic system (not explicitly included in the model). Thus, the exchanged fluid does not contribute to the growth/absorption of the constituent and the system remains closed with respect to the fluid and solid phases [22]. Then, G_n is multiplied by the indicator function of the tumour region, since this term is null in

the healthy tissue where the nutrient supply is perfectly balanced in the physiological condition, whereas in the cancer region we have an higher consumption of nutrients due to the pathological proliferation of cells. Specifically, we will consider the following form for G_n:

$$G_n(\phi_s, \phi_\ell, c_n) = -\zeta \phi_s \phi_\ell c_n + S_n(1 - c_n)\phi_\ell \,. \tag{5.8}$$

This expression describes the fact that nutrients are consumed by the tumour with a constant rate ζ: the uptake depends on the volumetric fractions of cells and liquid in the tumour region, as well as on the available concentration of nutrients. Concurrently, nutrients are supplied by the vasculature at a constant rate S_n as long as their concentration is below the physiological value, i.e. $c_n < 1$, and they are dispersed in the liquid phase. The whole expression is multiplied by the tumour indicator function in Eq. (5.7), since, as mentioned above, in the healthy region we assume that production and absorption of nutrients are reciprocally balanced. By using standard calculus techniques and recalling the mass balance equation of the fluid phase (5.4) and the functional formulation of G_n assumed in (5.8), Eq. (5.7) can be rephrased as

$$\frac{\partial c_n}{\partial t} + \mathbf{v}_\ell \cdot \nabla c_n = \frac{1}{\phi_\ell} \nabla \cdot (\phi_\ell \mathbb{D} \nabla c_n) + [-\zeta \phi_s c_n + S_n(1 - c_n)]\, \chi_{\Omega_t(t)}. \tag{5.9}$$

As regards the momentum balances, we recall that, in a saturated mixture, the partial Cauchy stress tensor associated with the α-th phase of the mixture can be written as

$$\widetilde{\mathbb{T}}_\alpha = -\phi_\alpha\, p\mathbb{I} + \mathbb{T}_\alpha, \tag{5.10}$$

where $\mathbb{T}_\alpha$ is referred to as *effective* (or extra-) stress, and the purely hydrostatic contribution $-\phi_\alpha\, p\mathbb{I}$ indicates the amount of pressure sustained by the α-th phase. We underline that, in the present theory, p plays the role of a Lagrange multiplier related to the mixture incompressibility. Moreover, in the following we will neglect both the inertial effects and the momentum exchange rates between phases associated with the mass sources/sinks Γ_α, $\alpha \in \{s, \ell\}$. These assumptions are reasonable in the context of biological growth, which is a process that takes place on long time scales with small velocities for both the phases of the mixture [136]. Then, taking into account these observations, the momentum balance

for each phase reads

$$-p\nabla\phi_s - \phi_s\nabla p + \nabla\cdot\mathbb{T}_s + \widetilde{\mathbf{m}}_{s\ell} = \mathbf{0}, \tag{5.11}$$

$$-p\nabla\phi_\ell - \phi_\ell\nabla p + \nabla\cdot\mathbb{T}_\ell + \widetilde{\mathbf{m}}_{\ell s} = \mathbf{0}, \tag{5.12}$$

where the term $\widetilde{\mathbf{m}}_{\alpha\beta}$ represents the force acting on the α-th phase due to the other phase β. In particular, following thermodynamical prescriptions, the latter can be decomposed as $\widetilde{\mathbf{m}}_{\alpha\beta} = p\nabla\phi_\alpha + \overline{\mathbf{m}}_{\alpha\beta}$, highlighting the non-dissipative and dissipative contributions, respectively [136, 154]. Coherently with the hypotheses usually made to deduce Darcy's law, we require that the extra-stress of the fluid phase $\mathbb{T}_\ell$ is negligible with respect to the pressure gradient and to the dissipative interaction forces between fluid and solid phase, that can be assumed in the form $\overline{\mathbf{m}}_{\ell s} = -\bar{m}u\phi_\ell^2\mathbb{K}^{-1}(\phi_\ell)(\mathbf{v}_\ell - \mathbf{v}_s)$ [136], where $\mathbb{K}$ is a permeability tensor. As a consequence, from Eq. (5.12) the classical Darcy's law as a momentum balance for the fluid phase is retrieved:

$$\mathbf{v}_\ell = \mathbf{v}_s - \frac{\mathbb{K}(\phi_\ell)}{\bar{\mu}\phi_\ell}\nabla p, \tag{5.13}$$

where $\mathbf{v}_\ell$ is the velocity of the liquid, $\mathbf{v}_s$ is the velocity of the cellular phase, $\bar{\mu}$ is the dynamic viscosity of the fluid component and $\mathbb{K}$ is the permeability tensor. Then, the momentum balance for the mixture as a whole can be obtained by summing the balances in Eqs. (5.11)–(5.12), taking into account the saturation condition $\phi_s + \phi_\ell = 1$ and the action-reaction principle $\overline{\mathbf{m}}_{s\ell} = -\overline{\mathbf{m}}_{\ell s}$:

$$-\nabla p + \nabla\cdot\mathbb{T}_s = \mathbf{0}. \tag{5.14}$$

Remark 5.1. The action-reaction condition applies in principle to the interaction forces between phases, i.e., $\widetilde{\mathbf{m}}_{s\ell} + \widetilde{\mathbf{m}}_{\ell s} = \mathbf{0}$. However, since the non-dissipative contributions to $\widetilde{\mathbf{m}}_{s\ell}$ and $\widetilde{\mathbf{m}}_{\ell s}$ are given by $p\nabla\phi_s$ and $p\nabla\phi_\ell$, respectively, it follows from the saturation condition that the constraint also holds for the dissipative parts, leading to $\overline{\mathbf{m}}_{s\ell} + \overline{\mathbf{m}}_{\ell s} = \mathbf{0}$.

To model the presence of white and grey matter fibres in the brain tissue and account for the consequent anisotropy in fluid motion, we will take the permeability tensor as

$$\mathbb{K}(\phi_\ell) = \bar{\mu}\hat{k}(\phi_\ell)\mathbb{A}, \tag{5.15}$$

where $\mathbb{A}$ denotes the *tensor of preferential directions* [82] derived through DTI imaging, whose construction will be described in Section 5.2.4 and 5.3. This approach allows to model preferential fluid and nutrients motion along the fibre tracts in the brain, taking into account the anisotropic structure of the tissue. Instead, the coefficient $\hat{k}(\phi_\ell)$ is given by the exponential Holmes–Mow expression [165, 261], as it is often done for soft tissues [106, 148]:

$$\hat{k}(\phi_\ell) = k(J_e) = k_0 \left(\frac{J_e - \phi_{sn}}{1 - \phi_{sn}} \right)^{\alpha_0} e^{m(J_e^2 - 1)/2}, \tag{5.16}$$

where α_0 and m are model parameters, k_0 is a reference value for k taken in the natural state, and ϕ_{sn} is the volume fraction of the solid phase in the natural state. An estimate of all parameters will be provided in Section 5.2.4.

5.2.3 Constitutive Equations for the Stresses

To close the system of mass and momentum balance equations, derived in the previous Subsection, it is necessary to determine an appropriate evolution law for the Cauchy stress tensor $\mathbb{T}_s$ associated with the cellular population, both in the diseased and in the healthy region, i.e.,

$$\mathbb{T}_s = \mathbb{T}_s^t \chi_{\Omega_t(t)} + \mathbb{T}_s^h (1 - \chi_{\Omega_t(t)}) \qquad \text{in } \Omega(t), \tag{5.17}$$

where $\mathbb{T}_s^t$ is the Cauchy stress tensor associated with the tumour cells and $\mathbb{T}_s^h$ is the Cauchy stress tensor associated with the healthy cells. This is a relevant part of the mathematical model, since our primary aim is to study how brain tumour growth influences mechanically the surrounding tissues and to quantify the entity of stress and deformation as a consequence of abnormal proliferation. In this respect, we remark that several difficulties arise when dealing with experimental settings involving brain tissue and the definition of a realistic constitutive equation is a non trivial problem that is still debated [53, 62]. Most of the brain biomechanical studies performed in the last fifty years have been conducted *in vitro* on excised samples of brains (either from humans, when available, or from animals) with different experimental protocols, that make the results difficult to be compared. Moreover, *in vitro* tests need to be generalized to *in vivo* conditions, providing additional complications. Novel techniques and protocols have been recently proposed in the literature to carry out *in vivo* non-destructive and non-invasive investigations. In particular, Magnetic Resonance Elastography (MRE) emerged as the most promising non-invasive imaging technique to measure the mechanical parameters of biological soft tissues by coupling a mechanical excitation, which promotes elastic wave propagation

in the soft medium, to a Magnetic Resonance Imaging (MRI) device for visualizing it [62]. However, nowadays, the use of MRE does not offer enough information to establish nonlinear, finite strain constitutive models for realistic computational simulations [53] and the use of *in vitro* experiments to characterize the brain and tumour elastic properties in a nonlinear regime (such as the one occurring during tumour growth) is still the most established.

In the context of *in vitro* experiments, a first important issue put forward by experimental studies [54, 97, 141] concerns the anisotropy of brain tissue. Despite the intrinsic microstructural anisotropy due to the presence of nerve tracts, the human brain tissue seems nearly isotropic from a mechanical viewpoint and no significant directional dependency affecting the mechanical behaviour can be observed, even in highly anisotropic regions of the brain. Therefore, the brain can be considered isotropic as far as mechanics is concerned, whereas anisotropy cannot be neglected when dealing with the diffusion of substances and with fluids and cell motion [54].

As regards the constitutive characterization, the vast majority of experimental results agree upon the highly nonlinear and viscoelastic nature of brain tissue [54, 97, 141], under different loading conditions [253, 296–298] and even with multiple loading modes [54]. However, for the purposes of our work, we are interested in brain response under small strain rates induced by cell proliferation. Therefore, the rate dependent response can be neglected without introducing significant errors [10]. To describe the elastic response, several models have been proposed in the literature [97] and there is a common agreement that the generalized Ogden model [275] is suitable to represent the mechanical behaviour of soft brain tissue. In particular, the Mooney-Rivlin model, which is a particular case of the generalized Ogden energy, turns out to be an appropriate choice from the experimental point of view [30, 105, 252].

We further remark that the fitting of the experimental data to get a quantitative estimation of the behaviour of the brain is generally obtained under the assumption of incompressibility of the sample described as a solid, without taking into account the contribution of the liquid encapsulated inside it. However, brain tissues have an exceptionally high water content *in vivo* [53] and are better represented by a mixture of at least two constituents, a liquid and a solid phase. As stated before, the constituents composing the mixture are said to be incompressible if their true densities $\widehat{\rho}^{\alpha}$ are constants. The bulk density ρ^{α} does not need to be constant even if the α-constituent is incompressible. Thus, the elastic determinant J_{e} is not constrained to be equal to 1. The variation of J_{e} leads instead to a deformation of the pores, that in turn induces volumetric solid stresses. To take

into account the experimental observations on the mechanical behaviour of the brain under isochoric conditions and the existence of a volumetric stress due to variations of J_e, the strain energy density function for both the solid tumour mass $\mathcal{W}^t_{sn}$ and the healthy brain tissue $\mathcal{W}^h_{sn}$, expressed per unit volume of the natural state $\Omega^n(t)$, is additively split into an isochoric part, $\widehat{\mathcal{W}}^{\omega i}_{sn}$, and a volumetric part, $\widehat{\mathcal{W}}^{\omega v}_{sn}$:

$$\mathcal{W}^{\omega}_{sn}(\mathbb{C}_e) = \widehat{\mathcal{W}}^{\omega}_{sn}(\overline{\mathbb{C}}_e, J_e) = \widehat{\mathcal{W}}^{\omega i}_{sn}(\overline{\mathbb{C}}_e) + \widehat{\mathcal{W}}^{\omega v}_{sn}(J_e)\,, \tag{5.18}$$

with $\omega \in \{t,h\}$. We remark that many of the strain energy density functions used to represent brain tissues, such as the Mooney-Rivlin model used hereafter, can be naturally written in the separable form of Eq. (5.18). Furthermore, even in those cases in which the contribution related to J_e cannot be naturally decoupled from the one related to $\overline{\mathbb{C}}_e$, for small variations of J_e (i.e., in the case of approximately elastically incompressible materials [151]), it is always possible to approximate the strain energy density function with such a separable form.

Then, even though, in principle, the mechanical model for the tumour tissue might be taken as totally different from the one describing the elastic behaviour of the healthy tissue [333], in the following we assume the same functional form for the strain energy density functions both in the tumour and in the healthy region, with possibly varying mechanical parameters. Specifically, following [30, 105], we take a Mooney-Rivlin model for the isochoric strain energy density function, i.e., for $\omega \in \{t,h\}$

$$\widehat{\mathcal{W}}^{\omega i}_{sn}(\overline{\mathbb{C}}_e) = \frac{1}{2}\mu_1^{\omega}\left(I_{1,\overline{\mathbb{C}}_e} - 3\right) + \frac{1}{2}\mu_2^{\omega}\left(I_{2,\overline{\mathbb{C}}_e} - 3\right)\,, \tag{5.19}$$

where $I_{1,\overline{\mathbb{C}}_e} = \mathrm{tr}(\overline{\mathbb{C}}_e)$, $I_{2,\overline{\mathbb{C}}_e} = \frac{1}{2}\left[\left(\mathrm{tr}\,\overline{\mathbb{C}}_e\right)^2 - \mathrm{tr}\left(\overline{\mathbb{C}}_e^2\right)\right]$ are respectively the first and second principal invariant of $\overline{\mathbb{C}}_e$. The material parameters of the cancer tissue, μ_1^t and μ_2^t, are in general different from the ones employed to describe the healthy brain tissue, μ_1^h and μ_2^h. For what concerns the volumetric part $\widehat{\mathcal{W}}^{\omega v}_{sn}$, with $\omega \in \{t,h\}$, we take the following form [151, 169, 292]:

$$\widehat{\mathcal{W}}^{\omega v}_{sn}(J_e) = \frac{1}{2}\kappa^{\omega}\left(\log J_e\right)^2\,, \tag{5.20}$$

where κ^{ω} is the elastic parameter associated with the response of the tumour and healthy tissue to volumetric deformations. Other functional forms for $\widehat{\mathcal{W}}^{\omega v}_{sn}(J_e)$ taking into account

the concept of the compaction point [109] or the existence of a maximum cell volume fraction [58] could alternatively be used.

Once a proper constitutive form for the strain energy density function $\mathcal{W}_{\rm sn}^{\omega}$ is chosen, it is possible to compute the constitutive part of the solid phase stress tensor inside the tumour and the healthy regions:

$$\mathbb{T}_{\rm s}^{\omega} = 2J_{\rm e}^{-1}\mathbb{F}_{\rm e}\frac{\partial \widehat{\mathcal{W}}_{\rm sn}^{\omega}(\overline{\mathbb{C}}_{\rm e}, J_{\rm e})}{\partial \mathbb{C}_{\rm e}}\mathbb{F}_{\rm e}^{\rm T} = J_{\rm e}^{-1}\mathbb{F}_{\rm e}\mathbb{S}_{\rm sn}^{\omega}\mathbb{F}_{\rm e}^{\rm T}\,, \tag{5.21}$$

where $\mathbb{S}_{\rm sn}^{\omega}$ is the solid phase second Piola-Kirchhoff stress tensor associated with the natural state, in the $\omega \in \{\mathrm{t},\mathrm{h}\}$ domain.

By classical computations [151] one obtains

$$\begin{aligned}\mathbb{S}_{\rm sn}^{\omega} &= 2J_{\rm e}^{-2/3}\left(\underline{\underline{\mathbb{I}}} - \frac{1}{3}\overline{\mathbb{C}}_{\rm e}^{-1}\otimes\overline{\mathbb{C}}_{\rm e}\right) : \frac{\partial \widehat{\mathcal{W}}_{\rm sn}^{\omega}(\overline{\mathbb{C}}_{\rm e}, J_{\rm e})}{\partial \overline{\mathbb{C}}_{\rm e}} + J_{\rm e}\frac{\partial \widehat{\mathcal{W}}_{\rm sn}^{\omega}(\overline{\mathbb{C}}_{\rm e}, J_{\rm e})}{\partial J_{\rm e}}\mathbb{C}_{\rm e}^{-1} \\ &= 2J_{\rm e}^{-2/3}\left(\underline{\underline{\mathbb{I}}} - \frac{1}{3}\overline{\mathbb{C}}_{\rm e}^{-1}\otimes\overline{\mathbb{C}}_{\rm e}\right) : \frac{\partial \widehat{\mathcal{W}}_{\rm sn}^{\omega{\rm i}}(\overline{\mathbb{C}}_{\rm e})}{\partial \overline{\mathbb{C}}_{\rm e}} + J_{\rm e}\frac{\partial \widehat{\mathcal{W}}_{\rm sn}^{\omega{\rm v}}(J_{\rm e})}{\partial J_{\rm e}}\mathbb{C}_{\rm e}^{-1}\,,\end{aligned} \tag{5.22}$$

where $\underline{\underline{\mathbb{I}}}$ is the symmetric fourth-order identity tensor, with components $\underline{\underline{\mathbb{I}}}_{ijkl} = \frac{1}{2}(\delta_{ik}\delta_{jl} + \delta_{il}\delta_{jk})$, and the tensor product $\mathbb{A}\otimes\mathbb{B}$ of two second-order tensors is defined for any second-order tensor $\mathbb{H}$ by $(\mathbb{A}\otimes\mathbb{B}) : \mathbb{H} = (\mathbb{B} : \mathbb{H})\mathbb{A}$.

As a consequence of Eqs. (5.18) and (5.21), the Cauchy stress tensor of the solid phase is decomposed into a deviatoric part $\mathbb{T}_{\rm s}^{\omega{\rm d}}$, for which we have $\mathrm{tr}(\mathbb{T}_{\rm s}^{\omega{\rm d}}) = 0$, and a spherical component $\mathbb{T}_{\rm s}^{\omega{\rm v}}$, with $\omega \in \{\mathrm{t},\mathrm{h}\}$, i.e.,

$$\begin{aligned}\mathbb{T}_{\rm s}^{\omega} &= 2J_{\rm e}^{-1}\left[J_{\rm e}^{-2/3}\mathbb{F}_{\rm e}\frac{\partial \widehat{\mathcal{W}}_{\rm sn}^{\omega{\rm i}}(\overline{\mathbb{C}}_{\rm e})}{\partial \overline{\mathbb{C}}_{\rm e}}\mathbb{F}_{\rm e}^{\rm T} - \frac{1}{3}\left(\overline{\mathbb{C}}_{\rm e} : \frac{\partial \widehat{\mathcal{W}}_{\rm sn}^{\omega{\rm i}}(\overline{\mathbb{C}}_{\rm e})}{\partial \overline{\mathbb{C}}_{\rm e}}\right)\mathbb{I}\right] + \frac{\partial \widehat{\mathcal{W}}_{\rm sn}^{\omega{\rm v}}(J_{\rm e})}{\partial J_{\rm e}}\mathbb{I} \\ &= \mathbb{T}_{\rm s}^{\omega{\rm d}} + \mathbb{T}_{\rm s}^{\omega{\rm v}}\,.\end{aligned} \tag{5.23}$$

The constitutive expressions of the Cauchy stress tensors $\mathbb{T}_{\rm s}^{\rm t}$ and $\mathbb{T}_{\rm s}^{\rm h}$ must be accompanied by equations defining $\mathbb{F}_{\rm s}$ and $\mathbb{F}_{\rm g}$. However, the deformation gradient tensor $\mathbb{F}_{\rm s}$, which is entirely determined by the motion of the cell phase, is not an additional unknown for the model, whereas $\mathbb{F}_{\rm g}$ has to be determined by solving appropriate evolution equations. The evolution of $\mathbb{F}_{\rm g}$ can be obtained self-consistently by working out Eq. (5.3) (see, for instance, [136, 145, 241]). In particular, we assume that the orientation of the mitotic spindle of cell division, which could be affected by external mechanical cues and by the

mechanical behaviour of the tissue (here taken as isotropic), is not influenced by brain fibre alignment, so that growth deformations are isotropic as well. Therefore, the inelastic tensor can be written as

$$\mathbb{F}_g = g\mathbb{I}, \tag{5.24}$$

with g a scalar field whose evolution is given by an ordinary differential equation [10, 145]:

$$\frac{\dot{g}}{g} = \frac{1}{3}\frac{\Gamma_s}{\phi_s}\chi_{\Omega_t^0} \qquad \text{in } \Omega^0. \tag{5.25}$$

We remark that, even if the multiplicative decomposition of the deformation gradient is actually needed only inside the tumour region, for simplicity we assume its validity everywhere in the domain. This allows to have all quantities defined on both the tumour and the healthy tissue. Thus, as a consequence of Eqs. (5.24)–(5.25), we will have $\mathbb{F}_g = \mathbb{I}$ outside the cancer domain.

5.2.4 Parameters Estimation

A fundamental passage to complete the mathematical model and focus on its numerical implementation consists in assessing the values of the parameters that appear in the system. This is both a challenging and delicate task: since our goal is to simulate tumour progression and its mechanical impact, the choice of the parameters is crucial to have a realistic and reliable outcome. At the same time, when working in the field of mathematical biology, accurate estimations of the parameters are often hard to obtain. This is particularly true for the brain, which is very difficult to be investigated experimentally [141]. In this Section, we review the literature so as to assign a value, or at least a range of values, to the parameters introduced in our model, in order to test its qualitative behaviour.

First of all, we deal with the material parameters μ_1^t, μ_2^t, μ_1^h, μ_2^h that appear in the Mooney–Rivlin energy densities. We take as a reference the work by Balbi et al. [30], who analysed the constitutive behaviour of brain matter considering a Mooney–Rivlin-type energy, for which they propose as mean values for the material parameters $\mu_1^h = 153$ Pa and $\mu_2^h = 297$ Pa. We consider these values as references for the healthy tissue mechanics. As regards tumour tissue, several experimental studies have assessed that it is in general stiffer than the healthy one. Stewart et al. [333] showed that human brain tumours like gliomas and meningiomas are two–five times stiffer than normal brain tissue; Chauvet et al. [65] and Miroshnikova et al. [254] proved a significant increase in stiffness for high-grade gliomas, more than ten times the healthy reference value [3, 79]. Therefore, for our main

simulations we take the material parameters in the tumour region as ten times greater than the ones in the healthy region. However, some works estimate the stiffness of brain tumours to be either the same order as the healthy tissue or even softer [269, 339]. Hence, to compare the growth velocities, we will also consider a case in which the parameters differ by four times and a case in which the tumour and the host tissue are assigned the same mechanical parameters, equal to the ones of the normal brain.

For what concerns the volumetric moduli κ^{t} and κ^{h}, as mentioned above they penalize volumetric changes in the solid skeleton. However, their estimation is difficult, since most of the experimental works and subsequent modelling do not consider the brain as a mixture. In some previous works on biological tissues considered as porous media, the coefficient related to the volume excess stress is evaluated using the Young modulus [2, 58, 82], which is very low for the brain [3, 53, 79]. The work by Prevost et al. [292], which uses a volumetric brain tissue response comparable to the one of the present work, estimates a range of $2 \cdot 10^2 - 2 \cdot 10^4$ Pa for the volumetric modulus. Therefore, following these observations and taking into account that the brain is very soft, we choose $\kappa^{\mathrm{t}} = 1.4 \cdot 10^{-3}$ MPa and $\kappa^{\mathrm{h}} = 1.4 \cdot 10^{-4}$ MPa, looking forward to further experimental confirmation.

As regards the parameters involved in the growth rate Γ_{s} proposed in Eq. (5.5), we estimate them as done in other recent works on brain tumours [2, 82]. In particular, the cell proliferation constant γ is taken as the inverse of typical doubling times for *in vitro* glioma cells, that vary from 24 to 48 hours. Thus, a range $0.5 - 1$ day^{-1} can be considered appropriate for γ [126]. Since proliferation depends significantly on nutrients availability, also smaller values seem however admissible [82]. For this reason, in the following we will consider the minimum value inside the mentioned interval, i.e. $\gamma = 0.5$ day^{-1}. The hypoxia threshold c_0 is estimated in the literature as ranging from 0.15 to 0.5 [126, 131, 355]: we will consider an intermediate value of $c_0 = 0.3$ in simulations. Moreover, we need to estimate the nutrients consumption rate ζ and the nutrients supply rate S_n appearing in Eq. (5.8). As far as the former is concerned, following the approach by Colombo et al. [82] it can be estimated as $\zeta = 8640$ days^{-1}. For the estimation of the nutrients supply rate S_n, we rely on the value of 10^4 days^{-1} proposed in [61], as done also in [2, 82]. When we consider the stress-inhibited proliferation rate defined in Eq. (5.6), the parameters governing the impairment of growth due to compression δ_1 and δ_2 have to be estimated as well. Referring to [241], in our simulations we will consider $\delta_1 = 0.8 - 0.9$, while we will choose $\delta_2 = 10^{-3} - 10^{-4}$ MPa to investigate different sensitivities to growth inhibition.

Regarding the estimate of ϕ_{sn}, that is, the cell volumetric fraction in the natural state, it is usually assumed to be a constant given from the outset [10, 145]. Different values

appear in the literature: Colombo et al. [82] and Agosti et al. [2] in their model considered a value of $\phi_{sn} = 0.39$, which they derived as the complementary value of the extra-cellular space studied in [48] and amounting at up to 61%. In our simulations, coherently with the constraint $\phi_{max} = 0.85$ lower than 1, we set $\phi_{sn} = 0.3$.

Finally, we need an estimate for the parameters which appear in the permeability tensor expression from Eq. (5.16), and in particular inside $\hat{k}(\phi_\ell)$. Given its definition and the spatial and temporal scales we employ in our model, this function has unit of measure $\text{mm}^2/(\text{MPa} \cdot \text{day})$. As usually done for the Holmes–Mow permeability in soft tissues [106, 148], the values $\alpha_0 = 0.0848$ and $m = 4.638$ are considered. Concerning the reference permeability k_0, values found in the literature for the brain cover a range of $10^4 - 10^5$ $\text{mm}^2/(\text{MPa} \cdot \text{day})$. For instance, Mascheroni et al. [241] consider a value of $4.2 \cdot 10^4$ $\text{mm}^2/(\text{MPa} \cdot \text{day})$ for the fluid phase in glioma tumour spheroids, modelled as mixtures. Instead, Basser [33] proposed values of $k_0 = 4.31 \times 10^5$ $\text{mm}^2/(\text{MPa} \cdot \text{day})$ and $k_0 = 6.47 \times 10^5$ $\text{mm}^2/(\text{MPa} \cdot \text{day})$ for the permeability of white and grey matter, respectively. Coherently, Smith and Humphrey [324] reported a range of $1.47 \times 10^5 - 2.67 \times 10^5$ $\text{mm}^2/(\text{MPa} \cdot \text{day})$, while a conversion of the value used by Jin et al. [188] leads to 7.8×10^4 $\text{mm}^2/(\text{MPa} \cdot \text{day})$. Finally, in Asgari et al. [21] a value of 1.72×10^5 $\text{mm}^2/(\text{MPa} \cdot \text{day})$ was employed. Therefore, we choose to consider an intermediate value of $k_0 = 2.17 \times 10^5$ $\text{mm}^2/(\text{MPa} \cdot \text{day})$.

We report the complete list of parameters, alongside their description, their values and the main references, in Table 5.2.

To complete the parameters overview, we need to provide a definition for the diffusion tensor $\mathbb{D}$ and for the tensor of preferential directions $\mathbb{A}$, influencing the permeability $\mathbb{K}$. To do so, we take advantage of the mechanical description included in the present model to progressively modify these tensors as time evolves. Indeed, the unnatural displacement induced by the neoplasm alters the direction of brain fibres in the surroundings, which should be taken into account in the description of both diffusion and fluid motion. It has been experimentally observed, by analysing both the DTI and the MRI scans of glioma patients, that volumetric and diffusion alterations can be recorded not only in the tumour region, but also in the surrounding healthy tissue. Consequently, structural and connectivity abrasions of brain areas might happen even distant from the brain tumour. These damage often underlies the pathogenesis of several neurological symptoms seen in glioma patients [45]. Since our model explicitly evaluates the deformation and the displacement caused by the tumour, we are able to track these changes and to exploit them to modify tissue anisotropy.

Param.	**Description**	**Value**	**Ref.**
μ_1^{t}	Mooney-Rivlin parameter (tumour)	1.53×10^{-3} MPa	[65, 254]
μ_2^{t}	Mooney-Rivlin parameter (tumour)	2.97×10^{-3} MPa	[65, 254]
κ^{t}	Volumetric modulus (tumour)	1.40×10^{-3} MPa	[292]
μ_1^{h}	Mooney-Rivlin parameter (healthy)	1.53×10^{-4} MPa	[30]
μ_2^{h}	Mooney-Rivlin parameter (healthy)	2.97×10^{-4} MPa	[30]
κ^{h}	Volumetric modulus (healthy)	1.40×10^{-4} MPa	[292]
γ	Cell proliferation constant	0.5 day^{-1}	[126]
c_0	Hypoxia threshold	0.3	[131]
ζ	Nutrients consumption rate	8640 day^{-1}	[126]
S_n	Nutrients supply rate	10^4 day^{-1}	[82]
δ_1	Growth inhibition parameter	$0.8 - 0.9$	[241]
δ_2	Growth inhibition parameter	$10^{-3} - 10^{-4}$ MPa	[241]
ϕ_{sn}	Cell volume fraction (natural state)	0.3	[136]
$\phi_{\max}$	Maximum cell volume fraction	0.85	-
α_0	Holmes–Mow parameter	0.0848	[106, 148]
m	Holmes–Mow parameter	4.638	[106, 148]
k_0	Reference permeability	2.17×10^5 mm^2 MPa^{-1} day^{-1}	[21, 33, 188, 324]

Table 5.2 Values of model parameters for brain tumour growth.

In detail, we start from a diffusion tensor $\mathbb{D}_0$ considered at the initial time instant, which can be inferred directly from DTI imaging data after a proper computational processing described in Section 5.3. Since we consider oxygen as the main nutrients source, it seems appropriate to employ these data in the nutrients balance equation, given that the DTI scan actually quantifies the diffusion of water inside the brain. Then, we can write

$$\mathbb{D}_0 = \lambda_1 \mathbf{e}_1^0 \otimes \mathbf{e}_1^0 + \lambda_2 \mathbf{e}_2^0 \otimes \mathbf{e}_2^0 + \lambda_3 \mathbf{e}_3^0 \otimes \mathbf{e}_3^0, \tag{5.26}$$

where we have put in evidence the descending order eigenvalues $\lambda_1 > \lambda_2 > \lambda_3$ of the diffusion tensor and the corresponding orthogonal eigenvectors $\mathbf{e}_1^0, \mathbf{e}_2^0, \mathbf{e}_3^0$, all evaluated at the initial time.

Concerning $\mathbb{A}_0$, i.e. the initial value of tensor $\mathbb{A}$, its construction is also performed using DTI data, to evaluate the preferential directions determined by the presence of white

matter tracts. In particular, we assume that $\mathbb{A}_0$ has the same eigenvectors as the diffusion tensor, but increased anisotropy along the preferential directions of motion inside the brain, as described in [2, 4, 187]. To enhance anisotropy without modifying the preferred directions, a control parameter ς is introduced and $\mathbb{A}_0$ is defined as

$$\widehat{\mathbb{A}}_0 = a_1(\varsigma)\lambda_1 \mathbf{e}_1^0 \otimes \mathbf{e}_1^0 + a_2(\varsigma)\lambda_2 \mathbf{e}_2^0 \otimes \mathbf{e}_2^0 + \lambda_3 \mathbf{e}_3^0 \otimes \mathbf{e}_3^0, \tag{5.27a}$$

$$\mathbb{A}_0 = \frac{1}{\mathrm{A}_{av}} \widehat{\mathbb{A}}_0, \qquad \mathrm{A}_{av} = \frac{1}{3}\mathrm{tr}(\widehat{\mathbb{A}}_0). \tag{5.27b}$$

In Eq. (5.27a), the functions $a_i(\varsigma)$, $i = 1, 2$ are given by

$$a_1(\varsigma) = \varsigma \mathrm{a}_l + \varsigma \mathrm{a}_p + \mathrm{a}_s, \tag{5.28}$$

$$a_2(\varsigma) = \mathrm{a}_l + \varsigma \mathrm{a}_p + \mathrm{a}_s, \tag{5.29}$$

where the coefficients a_l, a_p, a_s are the *linear*, *planar* and *spherical* anisotropy indices, respectively, defined as [187, 281, 386]:

$$\mathrm{a}_l = \frac{\lambda_1 - \lambda_2}{\lambda_1 + \lambda_2 + \lambda_3}, \quad \mathrm{a}_p = \frac{2(\lambda_2 - \lambda_3)}{\lambda_1 + \lambda_2 + \lambda_3}, \quad \mathrm{a}_s = \frac{3\lambda_3}{\lambda_1 + \lambda_2 + \lambda_3}. \tag{5.30}$$

The definition of these coefficients stems from the three simplest modes of diffusion. Indeed, when $\lambda_1 \gg \lambda_2 \approx \lambda_3$, then $\mathrm{a}_l \approx 1$ and diffusion preferentially happens linearly along the direction of the eigenvector $\mathbf{e}_1^0$. On the other hand, if $\lambda_1 \approx \lambda_2 \gg \lambda_3$, the diffusion process is mainly confined into the plane spanned by $\mathbf{e}_1^0$ and $\mathbf{e}_2^0$, leading to the planar coefficient $\mathrm{a}_p \approx 1$. Finally, in the case of spherical diffusion, all the eigenvalues of $\mathbb{D}_0$ have the same order of magnitude and $\mathrm{a}_s \approx 1$. Since, in general, the diffusion tensor will feature a combination of all these modes, it can be decomposed as [386]:

$$\mathbb{D}_0 = (\lambda_1 - \lambda_2)\mathbb{D}_l + (\lambda_2 - \lambda_3)\mathbb{D}_p + \lambda_3 \mathbb{D}_s,$$

where $\mathbb{D}_l := \mathbf{e}_1^0 \otimes \mathbf{e}_1^0$, $\mathbb{D}_p := \mathbf{e}_1^0 \otimes \mathbf{e}_1^0 + \mathbf{e}_2^0 \otimes \mathbf{e}_2^0$ and $\mathbb{D}_s := \mathbf{e}_1^0 \otimes \mathbf{e}_1^0 + \mathbf{e}_2^0 \otimes \mathbf{e}_2^0 + \mathbf{e}_3^0 \otimes \mathbf{e}_3^0$. Therefore, the coefficients a_l, a_p, a_s are related to the components of $\mathbb{D}_0$ with respect to the tensor basis $\{\mathbb{D}_l, \mathbb{D}_p, \mathbb{D}_s\}$. The scaling factors and trace normalization are introduced to guarantee that the coefficients range between 0 and 1, while keeping their sum equal to one. Concerning the definition of the anisotropy coefficients appearing in Eq. (5.28), they are employed to introduce changes in anisotropy through the parameter ς, as done in [187]. In particular, the case $\varsigma = 1$ corresponds to no increase in anisotropy, since $\mathrm{a}_l + \mathrm{a}_p + \mathrm{a}_s = 1$, while $\varsigma > 1$

enhances anisotropy along the directions of the eigenvectors according to the values of the coefficients of anisotropy.

Once we have built the starting tensors $\mathbb{D}_0$ and $\mathbb{A}_0$, their modification subsequent to growth and deformation is done taking into account that, as far as diffusion is concerned, it is relevant to consider just the reorientation of the preferential directions. Their extension or compression, in principle, does not affect nutrients diffusion and cell motility. Therefore, we deform the eigenvectors according to the deformation gradient $\mathbb{F}_s$, but we normalize them to account for the fact that only the direction of the fibres is changing (see Fig. 5.4). Hence, for the modified diffusion tensor we write

$$\mathbb{D} = \lambda_1 \frac{\mathbb{F}_s \mathbf{e}_1^0 \otimes \mathbb{F}_s \mathbf{e}_1^0}{|\mathbb{F}_s \mathbf{e}_1^0|^2} + \lambda_2 \frac{\mathbb{F}_s \mathbf{e}_2^0 \otimes \mathbb{F}_s \mathbf{e}_2^0}{|\mathbb{F}_s \mathbf{e}_2^0|^2} + \lambda_3 \frac{\mathbb{F}_s \mathbf{e}_3^0 \otimes \mathbb{F}_s \mathbf{e}_3^0}{|\mathbb{F}_s \mathbf{e}_3^0|^2}, \tag{5.31}$$

where we observe that

$$\left|\mathbb{F}_s \mathbf{e}_i^0\right|^2 = \mathbb{F}_s \mathbf{e}_i^0 \cdot \mathbb{F}_s \mathbf{e}_i^0 = \mathbf{e}_i^0 \cdot \mathbb{C}_s \mathbf{e}_i^0, \quad i = 1,2,3, \quad \mathbb{C}_s = \mathbb{F}_s^{\mathrm{T}} \mathbb{F}_s.$$

We remark that, in defining the modified diffusion tensor, we choose to keep the trace of the initial tensor, and therefore the mean diffusivity along the principal directions, unchanged. As a consequence of these assumptions, the pull-back $\mathbb{D}^*$ of the modified diffusion tensor $\mathbb{D}$ to the reference configuration does not coincide with $\mathbb{D}_0$ and the volume of the diffusion ellipsoid is not preserved in general, as highlighted in Fig. 5.4.

The modified tensor of preferential directions $\mathbb{A}$ can be defined using the same procedure as

$$\mathbb{A} = a_1(\varsigma)\lambda_1 \frac{\mathbb{F}_s \mathbf{e}_1^0 \otimes \mathbb{F}_s \mathbf{e}_1^0}{\mathbf{e}_1^0 \cdot \mathbb{C}_s \mathbf{e}_1^0} + a_2(\varsigma)\lambda_2 \frac{\mathbb{F}_s \mathbf{e}_2^0 \otimes \mathbb{F}_s \mathbf{e}_2^0}{\mathbf{e}_2^0 \cdot \mathbb{C}_s \mathbf{e}_2^0} + \lambda_3 \frac{\mathbb{F}_s \mathbf{e}_3^0 \otimes \mathbb{F}_s \mathbf{e}_3^0}{\mathbf{e}_3^0 \cdot \mathbb{C}_s \mathbf{e}_3^0}. \tag{5.32}$$

5.3 Numerical Implementation

To perform simulations and solve our equations numerically, we need to introduce a spatially and temporally discrete formulation of the continuous problems. Therefore, in this Section we briefly describe the procedures to generate the patient-specific mesh used for the computation. We then introduce the Lagrangian formulation of the model, that allows to solve the problem in the reference configuration, and finally we report the finite element and time discretization of the problem.

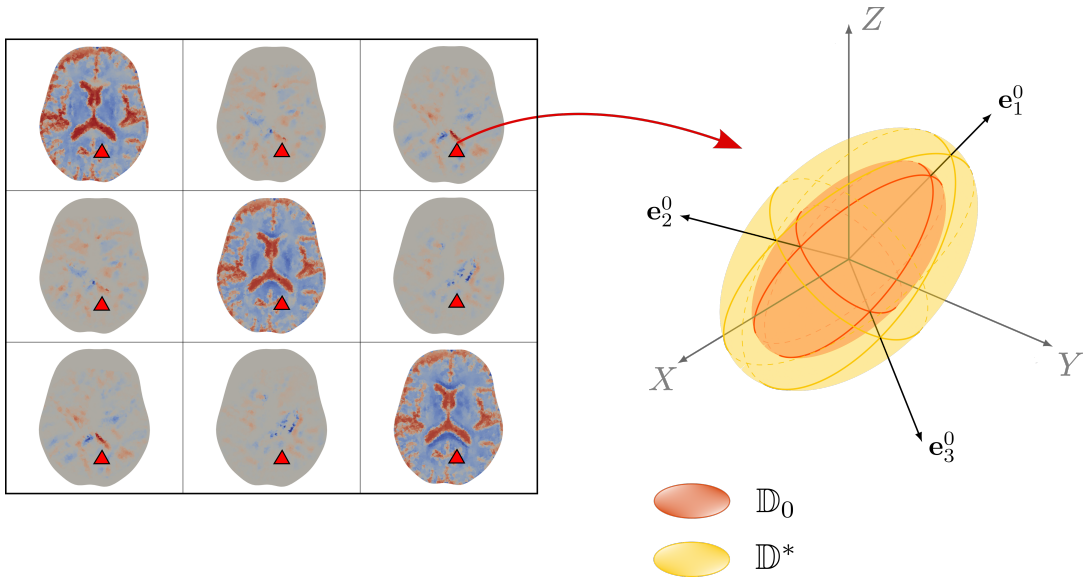

Fig. 5.4 Computational reconstruction and modification of the components of the diffusion tensor taken from DTI data. The initial tensor $\mathbb{D}_0$ is built using medical imaging data (as explained in Section 5.3) and the values of the six components of the symmetric diffusion tensor are assigned to each mesh cell. In particular, on the left we show a sample of the components of the tensor $\mathbb{D}_0$ as they appear on a transverse (horizontal) brain section, with higher values of the diffusion coefficients plotted in red. For a fixed representative cell sketched by the red triangle, on the right we draw the red ellipsoid representing the preferential directions and values of diffusion at the initial time instant, i.e. the eigenvectors and eigenvalues of $\mathbb{D}_0$, respectively. The initial eigenvectors are modified according to the deformation of the tissue, in order to obtain the time and spatially dependent tensor $\mathbb{D}$, given by Eq. (5.31). In the Figure, we report $\mathbb{D}_0$ and the pullback $\mathbb{D}^* := J_s \mathbb{F}_s^{-1} \mathbb{D} \mathbb{F}_s^{-T}$ of the modified diffusion tensor (in yellow), which are both defined in the reference configuration. We observe that $\mathbb{D}^*$ has the same eigenvectors as $\mathbb{D}_0$ but different eigenvalues, due to the normalization and volumetric changes.

5.3.1 Mesh Creation and Preprocessing

The computational mesh used for the numerical simulations is built starting from MRI and DTI clinical data of a patient affected by a brain tumour gently provided by the Istituto Neurologico Carlo Besta (Milan). The main advantage of MRI lies in its efficiency for the detection of brain tumours and to highlight different tissue types composing the brain. Nevertheless, MRI does not provide any information about the microstructural architecture of the tissue. Therefore, the values of $\mathbb{D}_0$ and $\mathbb{A}_0$ are derived from DTI data, which quantify the diffusivity of water molecules and allow to visualise the orientation of white matter tracts.

To construct the mesh, first of all a segmentation of the grey-scale MRI image is performed through the software package Slicer3D [121] in order to recreate the brain

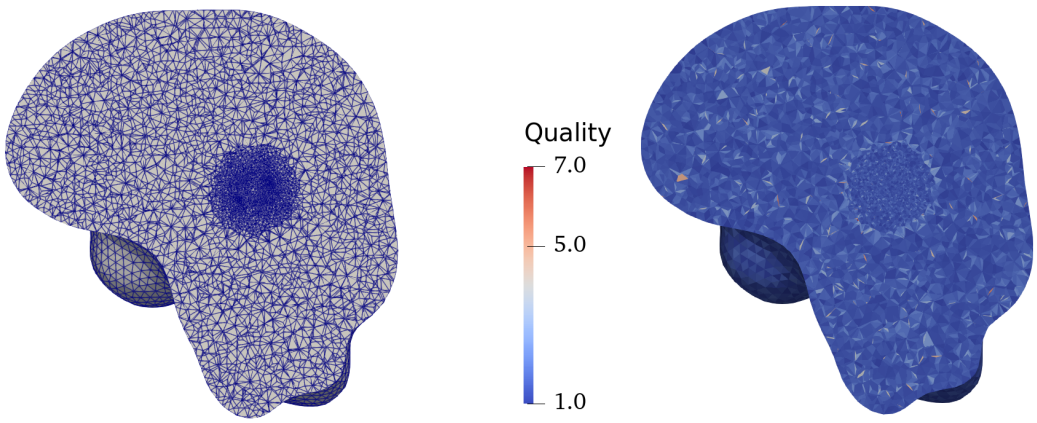

(a) (b)

Fig. 5.5 (a): Tetrahedral mesh generated within the brain domain, reconstructed from neuroimaging data, and properly refined in the tumour region; (b): Mesh quality in terms of tetrahedral aspect ratio.

geometry and boundary. After the segmentation, the computational mesh is built using TetGen [322], which is able to generate tetrahedral meshes of any 3D domain, and properly refined inside and around the tumour region. The resulting mesh and its quality evaluated in terms of aspect ratio of its elements are reported in Fig. 5.5. In particular, we verified that almost all elements ($> 95\%$) had an aspect ratio smaller than five.

Finally, to incorporate diffusion data, we assign to each mesh cell six piecewise constant fields, each one associated with one independent component of the tensor $\mathbb{D}_0$. In particular, each cell is assigned the value of the tensor component of the voxel containing the cell barycentre, as shown in Fig. 5.4. The same process is also carried out for the components of the tensor of preferential directions $\mathbb{A}_0$. For further details, we refer the reader to [2, 82, 233].

5.3.2 Lagrangian Formulation

Since we solve our equations in the reference configuration, we rewrite the model in material coordinates. In the following, unless otherwise specified, we will use the same symbols to denote the variables in the spatial and material description, and also omit the explicit spatial dependence.

By classical computations [10, 135, 145, 241], using a superimposed dot to denote the material time derivative, it is possible to derive the following complete set of equations,

holding in the fixed reference domain Ω^0:

$$J_\mathrm{s}\phi_\mathrm{s} = J_\mathrm{g}\phi_\mathrm{sn}\,, \qquad \phi_\mathrm{s} + \phi_\ell = 1\,, \tag{5.33a}$$

$$\dot{J}_\mathrm{s} = \mathrm{Div}\left[\frac{\mathbb{K}^*}{\bar{\mu}}\mathrm{Grad}\,p\right], \tag{5.33b}$$

$$\mathrm{Div}\left[-J_\mathrm{s}p\mathbb{F}_\mathrm{s}^{-\mathrm{T}} + \mathbb{P}_\mathrm{s}\right] = \mathbf{0}\,, \tag{5.33c}$$

$$\dot{g} = g\frac{\Gamma_\mathrm{s}}{3\phi_\mathrm{s}}\chi_{\Omega_\mathrm{t}^0}\,, \tag{5.33d}$$

$$J_\mathrm{s}\phi_\ell\dot{c}_n - \frac{\mathbb{K}^*}{\bar{\mu}}\mathrm{Grad}\,p\cdot\mathrm{Grad}\,c_n - \mathrm{Div}\left[\phi_\ell\mathbb{D}^*\mathrm{Grad}\,c_n\right] = J_\mathrm{s}G_n\chi_{\Omega_\mathrm{t}^0}, \tag{5.33e}$$

where $\mathbb{K}^* := J_\mathrm{s}\bar{\mu}k(J_\mathrm{e})\mathbb{F}_\mathrm{s}^{-1}\mathbb{A}\mathbb{F}_\mathrm{s}^{-\mathrm{T}}$, $\mathbb{D}^* := J_\mathrm{s}\mathbb{F}_\mathrm{s}^{-1}\mathbb{D}\mathbb{F}_\mathrm{s}^{-\mathrm{T}}$, and $\mathbb{D}$, $\mathbb{A}$ are the tensors modified according to the deformation, as reported in Eqs. (5.31)–(5.32). We remark that the pull-backs $\mathbb{D}^*$ and $\mathbb{A}^* = J_\mathrm{s}\mathbb{F}^{-1}\mathbb{A}\mathbb{F}^{-\mathrm{T}}$ of $\mathbb{D}$ and $\mathbb{A}$ have the same eigenvectors as their initial counterparts $\mathbb{D}_0$ and $\mathbb{A}_0$, but the eigenvalues are rescaled because of the normalization of the deformed eigenvectors and volumetric changes (see Eq. (5.31) and Fig. 5.4). Instead, $\mathbb{P}_\mathrm{s}$ is the constitutive part of the first Piola-Kirchhoff stress tensor of the solid phase, $\mathbb{P}_\mathrm{s} = J_\mathrm{s}\mathbb{T}_\mathrm{s}\mathbb{F}_\mathrm{s}^{-\mathrm{T}}$.

We notice that the system (5.33) is closed, since it constitutes a set of eight scalar equations and features eight scalar unknowns, namely the displacement vector field of the solid phase $\mathbf{u}_\mathrm{s}(\mathbf{X},t)$ and the scalar fields $\phi_\mathrm{s}(\mathbf{X},t)$, $\phi_\ell(\mathbf{X},t)$, $g(\mathbf{X},t)$, $c_n(\mathbf{X},t)$ and $p(\mathbf{X},t)$. The fluid velocity $\mathbf{v}_\ell(\mathbf{X},t)$ can be derived using Eq. (5.13). We remark that, since all the equations are pulled back on the reference configuration using the deformation field of the solid phase, the indicator function $\chi_{\Omega_\mathrm{t}^0}$ does not evolve in space and time, so it is not an additional unknown for the model and an evolution equation is not needed.

The system of equations (5.33) allows therefore to determine all the unknown fields, $\forall\mathbf{X}\in\Omega^0$ and $\forall t\in(0,T)$, provided that proper initial and boundary conditions are prescribed. Since in our simulations the external boundary $\partial\Omega^0$ stands for the cranial skull, we consider the following set of boundary conditions:

$$\mathbf{u}_\mathrm{s} = \mathbf{0} \quad \text{on} \quad \partial\Omega^0, \forall t\in(0,T)\,, \tag{5.34a}$$

$$p = 0 \quad \text{on} \quad \partial\Omega^0, \forall t\in(0,T)\,, \tag{5.34b}$$

$$c_n = 1 \quad \text{on} \quad \partial\Omega^0, \forall t\in(0,T)\,. \tag{5.34c}$$

In particular, the first boundary condition stems from the rigidity of the skull, which cannot be displaced, and it represents the most natural constraint on the solid deformation. Instead, conditions (5.34b)–(5.34c) correspond to fixing both the pressure and the nutrients concentration on the boundary of the brain. They represent a fairly reasonable assumption when the tumour is placed sufficiently far from the skull and its growth does not have a direct impact on the values of the variables at the boundary, which may then be fixed at reference values.

However, in some cases brain tumours may appear near the brain boundary, leading to the generation of high stresses and extremely asymmetric growth patterns due to the rigid constraint that the skull imposes. To investigate such a situation using our mathematical and computational model, we also performed two sets of simulations with different boundary conditions. Indeed, if the cancer mass is positioned in close proximity to the skull, zero-flux Neumann boundary conditions might be appropriate. In fact, it is enough to impose that the fluid and the chemicals cannot flow out of the boundary, without necessarily forcing them to attain specific values. Therefore, we performed two simulations near the skull, using both the Dirichlet boundary conditions (5.34) and the following set of conditions:

$$\mathbf{u}_s = \mathbf{0} \qquad \text{on} \qquad \partial\Omega^0, \forall t \in (0,T)\,, \tag{5.35a}$$

$$\mathbb{K}^* \operatorname{Grad} p \cdot \mathbf{n}_* = 0 \qquad \text{on} \qquad \partial\Omega^0, \forall t \in (0,T)\,, \tag{5.35b}$$

$$\mathbb{D}^* \operatorname{Grad} c_n \cdot \mathbf{n}_* = 0 \qquad \text{on} \qquad \partial\Omega^0, \forall t \in (0,T)\,, \tag{5.35c}$$

where $\mathbf{n}_*$ is the outer normal vector to the boundary $\partial\Omega^0$. In this case, we keep the fixed null displacement and impose zero normal flux conditions on p and c_n.

Concerning initial conditions, at the beginning of the tumour growth process it is reasonable to assume that the displacement and the pressure are equal to zero everywhere in the domain; meanwhile, we take the scalar field g related to the growth component of the deformation gradient as equal to 1 everywhere in the domain at $t = 0$. Enforcing the condition that the variation of body mass is due to cell proliferation, it is possible to show [10, 145] that the solid volumetric fraction in the natural state ϕ_{sn} is constant in time and, thus, equal to the $\phi_s(\mathbf{X}, 0)$. In particular, in the following we will consider ϕ_{sn} homogeneous in space. Finally the initial nutrients concentration is uniformly set to $c_n = 1$

everywhere. To sum up, we have the following set of initial conditions:

$$\mathbf{u}_s(\mathbf{X},0) = \mathbf{0} \qquad \forall \mathbf{X} \in \Omega^0 \tag{5.36a}$$
$$p(\mathbf{X},0) = 0 \qquad \forall \mathbf{X} \in \Omega^0 \tag{5.36b}$$
$$g(\mathbf{X},0) = 1 \qquad \forall \mathbf{X} \in \Omega^0 \tag{5.36c}$$
$$\phi_s(\mathbf{X},0) = \phi_{sn} \qquad \forall \mathbf{X} \in \Omega^0 \tag{5.36d}$$
$$c_n(\mathbf{X},0) = 1 \qquad \forall \mathbf{X} \in \Omega^0. \tag{5.36e}$$

5.3.3 Finite Element Discretization

To perform numerical simulations, we here introduce the spatially discrete formulation of a proper continuous variational formulation of the system (5.33). We make use of linear tetrahedron $\mathbb{P}_1$ elements, so we introduce the following finite element spaces:

$$\mathbf{V}_h := \{\mathbf{q}_h \in \left[C^0(\overline{\Omega^0})\right]^3 : \mathbf{q}_h|_K \in [\mathbb{P}_1(K)]^3 \ \ \forall K \in \mathcal{T}_h\,,\ \mathbf{q}_h|_{\partial\Omega^0} = \mathbf{0}\} \subset \mathbf{H}^{\mathbf{1}}_{\mathbf{0}}(\Omega^0)\,, \tag{5.37}$$

$$W_{h0} := \{q_h \in C^0(\overline{\Omega^0}) : q_h|_K \in \mathbb{P}_1(K) \ \ \forall K \in \mathcal{T}_h\,,\ q_h|_{\partial\Omega^0} = 0\} \subset H^1_0(\Omega^0)\,, \tag{5.38}$$

$$W_{h1} := \{q_h \in C^0(\overline{\Omega^0}) : q_h|_K \in \mathbb{P}_1(K) \ \ \forall K \in \mathcal{T}_h\,,\ q_h|_{\partial\Omega^0} = 1\} \subset H^1(\Omega^0)\,, \tag{5.39}$$

where $\mathcal{T}_h$ is a conforming decomposition of the domain Ω^0 into tetrahedra K. Then, we are able to define our fully discrete variational problem as follows: for $k = 1,\dots,N$, given $(\mathbf{u}_h^k, p_h^k, c_h^k) \in \mathbf{V}_h \times W_{h0} \times W_{h1}$ find $(\mathbf{u}_h, p_h, c_h) \in \mathbf{V}_h \times W_{h0} \times W_{h1}$ such that for all test functions $(\boldsymbol{\nu}_h, w_h, q_h) \in \mathbf{V}_h \times W_{h0} \times W_{h0}$

$$(J_s(\mathbf{u}_h), w_h) + \Delta t \left(\operatorname{Grad} w_h, \frac{\mathbb{K}^*}{\bar{\mu}} \operatorname{Grad} p_h\right) = \left(J_s^k(\mathbf{u}_h^k), w_h\right), \tag{5.40}$$

$$-(\mathbb{P}(\mathbf{u}_h, p_h), \operatorname{Grad} \boldsymbol{\nu}_h) = \mathbf{0}\,, \tag{5.41}$$

$$(J_s(\mathbf{u}_h)c_h, q_h) - \Delta t \left(\frac{\mathbb{K}^*}{\bar{\mu}\phi_\ell} \operatorname{Grad} p_h \cdot \operatorname{Grad} c_h, q_h\right) + \Delta t\,(\operatorname{Grad} q_h, \mathbb{D}^* \operatorname{Grad} c_h) =$$
$$= \left(J_s(\mathbf{u}_h)c_h^k, q_h\right) + \Delta t \left(J_s(\mathbf{u}_h)\frac{G_n(c_h)}{\phi_\ell}, q_h\right), \tag{5.42}$$

where, in order to have a lighter notation, we have dropped the unnecessary superscripts and denoted by the same symbol $(\cdot,\cdot)$ the standard scalar product on the spaces $L^2(\Omega^0)$,

$L^2(\Omega^0;\mathbb{R}^3)$ and $L^2(\Omega^0;\mathbb{R}^{3\times 3})$. Finally, we have indicated by $\mathbb{P} = -J_s p \mathbb{F}_s^{-T} + \mathbb{P}_s$ the first Piola-Kirchhoff stress tensor. We remark that, since we are working in a Lagrangian configuration, also the tensors $\mathbb{K}^*$ and $\mathbb{D}^*$ depend on $\mathbf{u}_h$. The time discretization of Eqs. (5.40)–(5.42) consists in a semi-implicit Euler scheme, which is solved by a Newton's method with a sufficiently small time step $\Delta t = 0.1$ days.

Once we have obtained the discrete formulation of the partial differential equations, the last step is to introduce a proper discretization of the other equations involved, namely the ordinary differential equation for g (5.33d) and the relations (5.33a). Concerning the former, it can be easily discretized in time using the explicit Euler method. Then, we have

$$g^{k+1}(\mathbf{X}_j) = g^k(\mathbf{X}_j)\left(1 + \Delta t \frac{\Gamma_s^k(\mathbf{X}_j)}{3\,\phi_s^k(\mathbf{X}_j)}\chi_{\Omega_t^0}\right) \qquad j = 1,\dots,M \tag{5.43}$$

where $\mathbf{X}_j$ are the grid nodes and M is the number of spatial nodes in the discretization. The first equation of (5.33a) is simply discretized as follows:

$$J_s^{k+1}(\mathbf{X}_j)\phi_s^{k+1}(\mathbf{X}_j) = J_g^{k+1}(\mathbf{X}_j)\phi_{sn} \quad \Rightarrow \quad \phi_s^{k+1}(\mathbf{X}_j) = \frac{J_g^{k+1}(\mathbf{X}_j)}{J_s^{k+1}(\mathbf{X}_j)}\phi_{sn}\,,\ j = 1,\dots,M. \tag{5.44}$$

Given the discretized form of all the necessary equations, we implemented our code using the open source computing software for solving partial differential equations called *FEniCS* [8, 228]. Such a software provides a high-level Python and C++ interface for solving PDEs through the finite element method. In particular, FEniCS code is attractive since it remains very close to the mathematical formulation, allowing the user to write down a program which closely resembles the variational form of equations. It also comes with built-in classes specifically dedicated to the resolution of nonlinear variational problems, which in our case is an important feature.

5.4 Results

To test the model and its implementation, we perform some numerical simulations on a realistic brain geometry, constructed from medical imaging data following the procedure described in Section 5.3. As specified before, we use the finite element method to solve the equations and we consider an initial tumour radius of about 7 mm. Then, we simulate the progression of the tumour for 45 days in different conditions. In particular, in Section 5.4.1 we compare the results of tumour evolution using both the growth laws given in Eqs. (5.5)

and (5.6), the latter including the effect of solid stress inhibition on cell proliferation. Then, in Section 5.4.2 we report the results concerning the modification of DTI data as a consequence of growth-induced deformations. Finally, in Section 5.4.3 we consider the case of a tumour growing near the skull and compare the two different sets of boundary conditions discussed in Eqs. (5.34)–(5.35).

5.4.1 Stress Inhibition of Tumour Growth

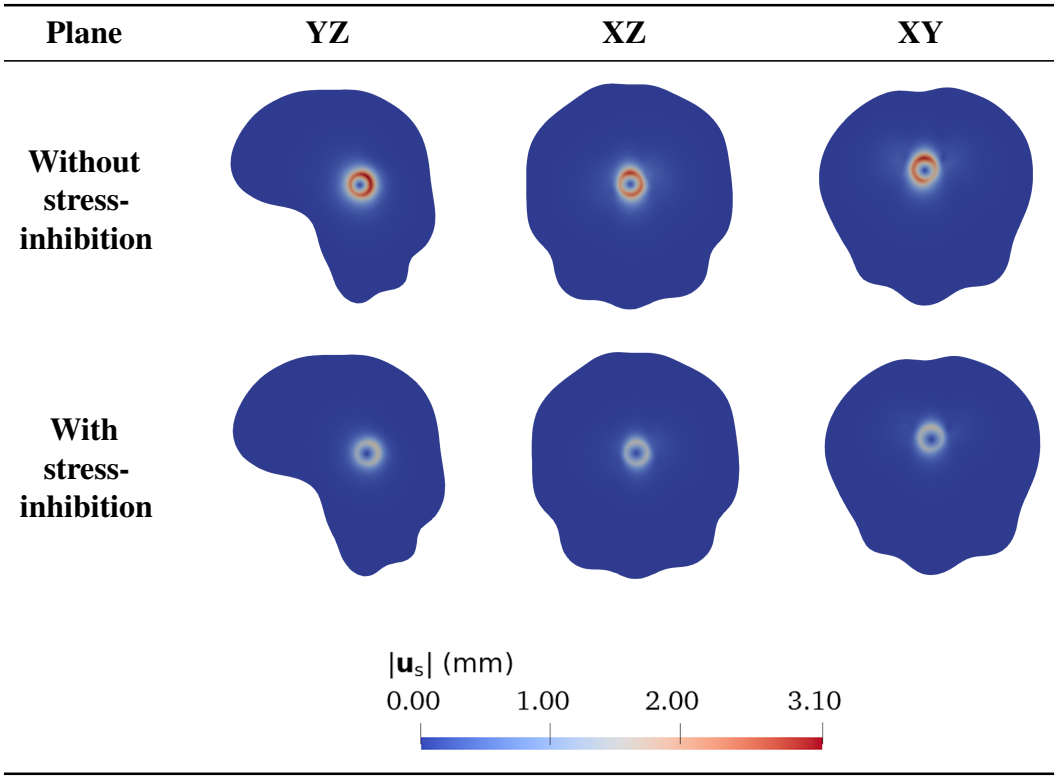

Fig. 5.6 Comparison between the displacement magnitude $|\mathbf{u}_s|$ after $t = 45$ days of tumour growth in the brain, clipped along a sagittal (first column), an axial (second column), and coronal (third column) plane centred within the tumour. In the first row, the case without stress inhibition is reported, while the second row shows a case of stress-inhibited growth. After a month and a half, the maximum displacement induced by the tumour without any inhibition due to stress amounts at 3.1 mm, while in the inhibited case it is about 1.7 mm.

Results in terms of displacements, cell volume fraction, pressure, and the chosen measure of stress are shown in Figs. 5.6–5.8 along three sagittal, axial, and coronal planes centred within the tumour. Specifically, in order to highlight the displacement induced by the growing mass, in Fig. 5.6 we report the magnitude $|\mathbf{u}_s|$ of the displacement vector $\mathbf{u}_s$. The comparison between the case without stress inhibition, in which the rate of

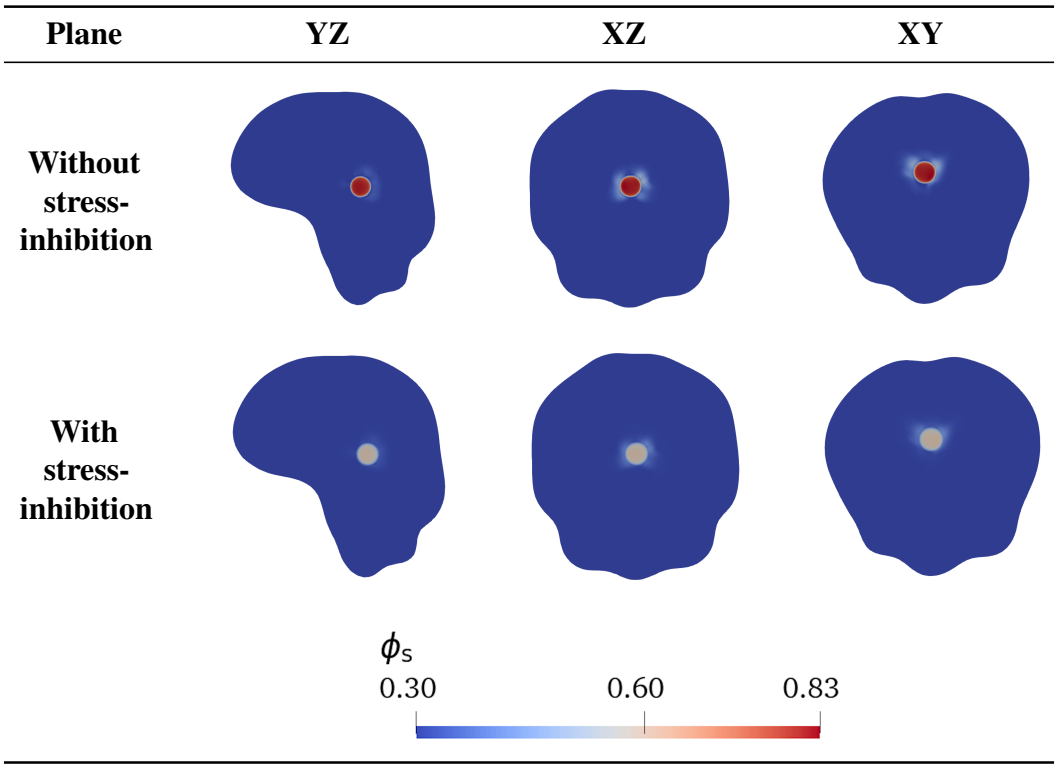

Fig. 5.7 Comparison between the solid volume fraction ϕ_s after $t = 45$ days of tumour growth in the brain, clipped along a sagittal (first column), an axial (second column), and coronal (third column) plane centred within the tumour. In the first row, the case without stress inhibition is reported, while the second row shows a case of stress-inhibited growth.

proliferation is taken as defined in Eq. (5.5), and the stress-inhibited case using Eq. (5.6) is put in evidence. It can be observed that, in the case without stress inhibition, the maximum value of the displacement amounts at 3.1 mm; moreover, such a value is not uniform around the tumour and along the three cutting planes: in the XZ-plane, for instance, the maximum displacement is about 2.9 mm. This is a consequence of the patient-specific anisotropy included in the model thanks to the diffusion and permeability tensors. The presence of fibres influences the movement of fluid and nutrients diffusion, which in turn affect the growth, leading to a displacement around the tumour mass which is greater along certain directions. The second row of Fig. 5.6 shows instead the displacement magnitude in the stress-inhibited case, i.e., when the proliferation term defined in Eq. (5.6) is chosen with parameters $\delta_1 = 0.8$ and $\delta_2 = 10^{-4}$ MPa. It can be noticed that compression strongly inhibits the growth of the tumour, reducing therefore the amount of deformation around its placement; in particular, the maximum displacement is about 1.7 mm, which is almost a half of the one attained in the case without stress inhibition. This result highlights once

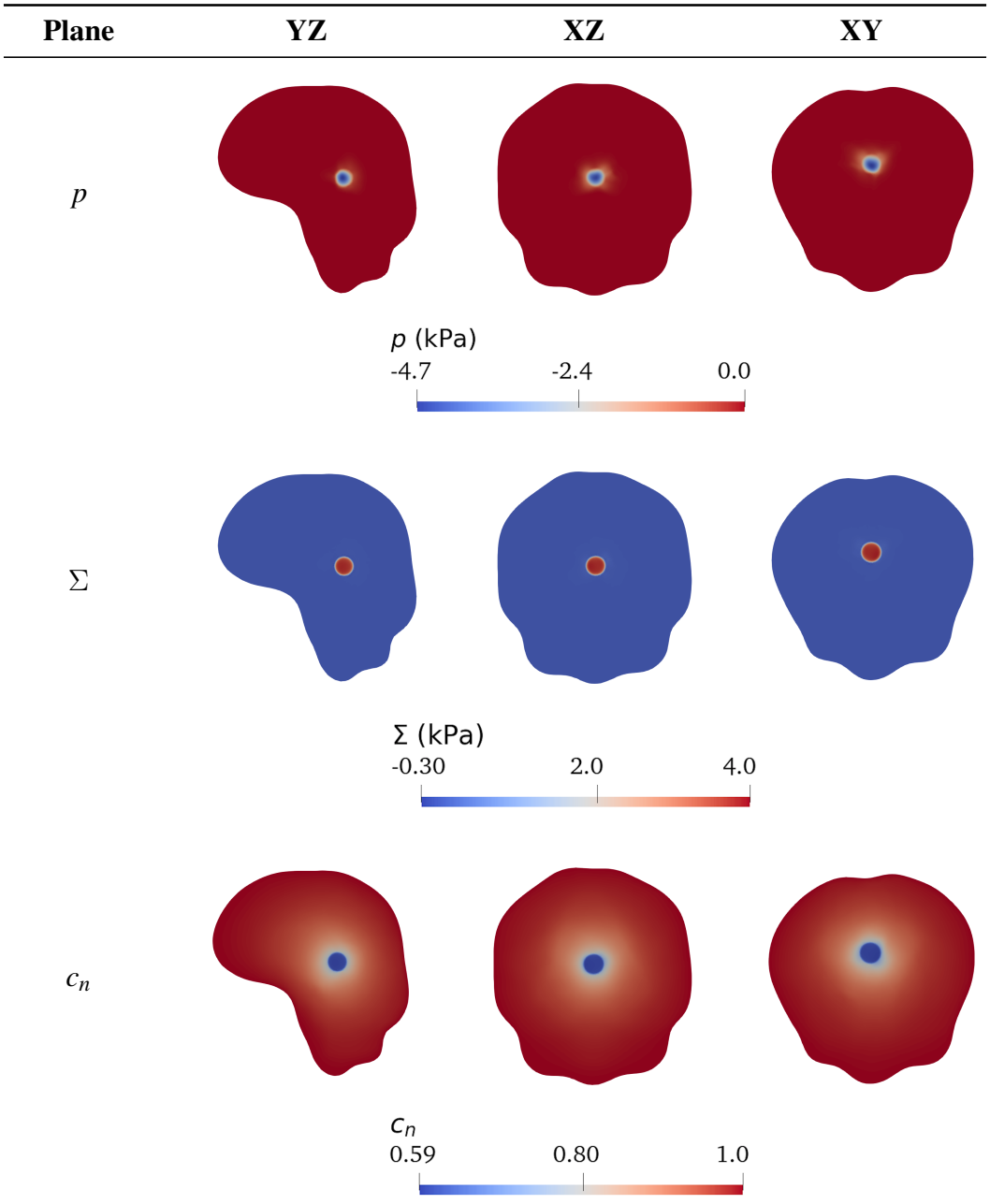

Fig. 5.8 Comparison between variables during tumour growth in the brain, clipped along a sagittal (first column), an axial (second column) and coronal (third column) plane centred within the tumour, at time $t = 45$ days. In the first row the fluid pressure p is reported, while the second row shows the stress measure $\Sigma = -\frac{1}{3}\mathrm{tr}(\mathbb{T}_s)$ and the third row shows the concentration of nutrients c_n.

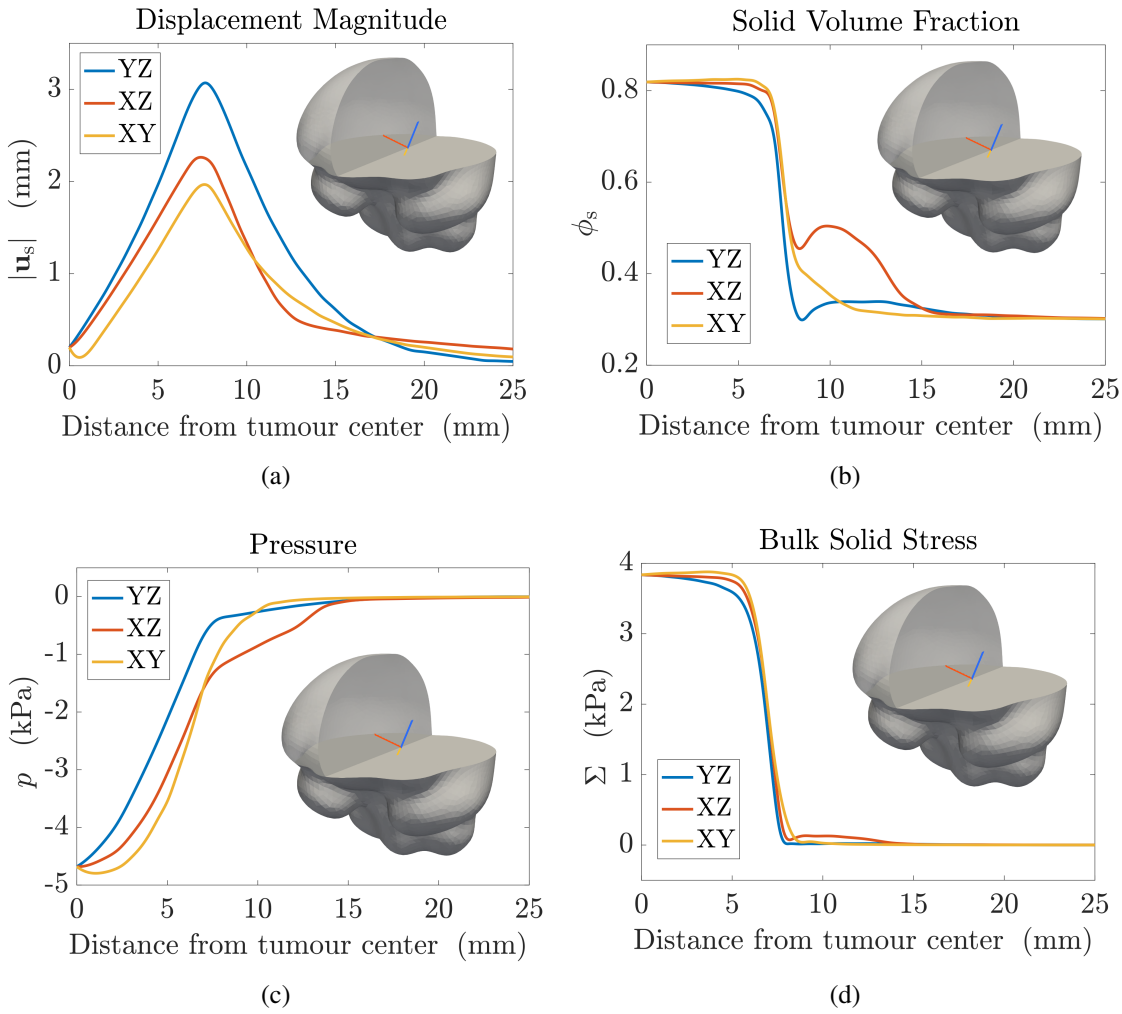

Fig. 5.9 Comparison between variables during tumour growth in the brain, along three representative rays in different planes originating from the tumour center, at time $t = 45$ days. In the insets, the chosen rays are depicted on the 3D brain mesh. (a): displacement magnitude $|\mathbf{u}_s|$; (b): solid volume fraction ϕ_s; (c): pressure p; (d): bulk solid stress Σ.

more the importance of having a model which is able to include mechanical features of tumour growth, both to evaluate the impact of the mass on the healthy tissue and to correctly predict tumour evolution.

Moreover, the cellular proliferation inside the tumour region leads to an increase in the volumetric fraction of the solid phase, as shown in the first row of Fig. 5.7. After a month and a half of growth without stress inhibition, ϕ_s has almost reached the saturation value of 0.85 inside the tumour domain. Then, it starts to substantially increase also in the surrounding healthy region, due to the compression exerted by the growing mass. On the other hand, if growth becomes sensitive to compressive stresses, the value achieved

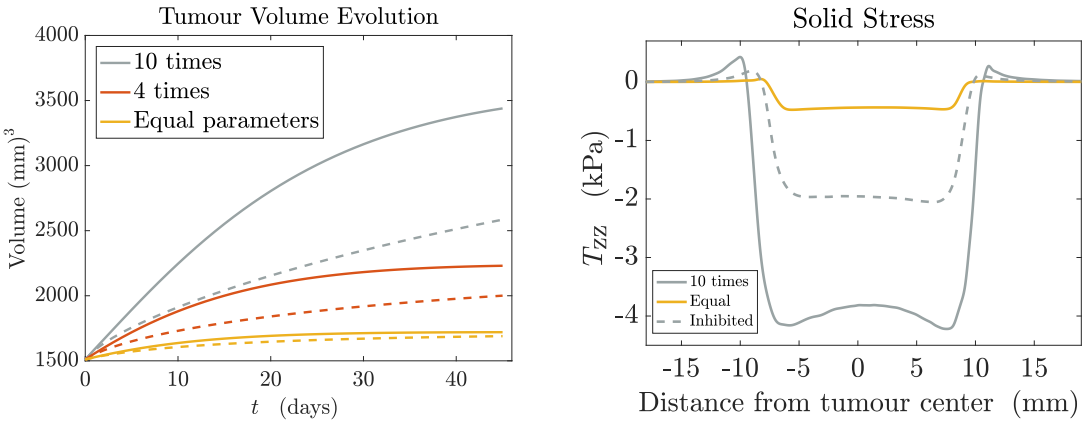

(a) (b)

Fig. 5.10 (a): Tumour volume evolution over time, for different values of the elastic parameters in the tumour region. In particular, the tumour is taken as ten times stiffer than the host tissue (grey curves), four times stiffer (red curves) and equal to the healthy tissue (yellow curves). Solid lines correspond to the cases without stress inhibition on growth, while dashed lines refer to the simulations with stress inhibition ($\delta_1 = 0.8$, $\delta_2 = 10^{-4}$ MPa). (b): T_{zz} component of the solid Cauchy stress tensor along a ray that crosses the tumour diameter, for the case of a tumour which is ten times stiffer (grey curves) and as stiff as the healthy tissue (yellow curve).

by the solid fraction is much smaller after the same period of simulation and the changes in volume fraction around the tumour are slightly perceivable. This is consistent with the fact that stress is slowing down tumour proliferation, as observed also in biological experiments [69, 101, 161, 255].

As regards some other relevant variables of the model, in the first row of Fig. 5.8 we show the final values of the fluid pressure p, which is negative inside the cancer region, since the fluid is consumed during the uncontrolled cellular proliferation. In the second row of Fig. 5.8 we plot the value of $\Sigma = -\frac{1}{3}\mathrm{tr}(\mathbb{T}_s)$, that coincides with the trace of the volumetric solid Cauchy stress, recalling Eq. (5.23), and it is a stress measure of the compression used in our model to account for stress-inhibition of growth. As expected, Σ is positive inside the tumour, meaning that there is a compression in this area, and negative in zones around the tumour boundary, where the tissue is in traction. The existence of gradients of compression and tension, moving from the tumour towards the surrounding brain tissue is confirmed by biological tests combined with a simple finite element model [269, 317].

Finally, as regards the concentration of nutrients shown in the third row of Fig. 5.8, it is almost maintained at the physiological value of 1 in the whole healthy region of the

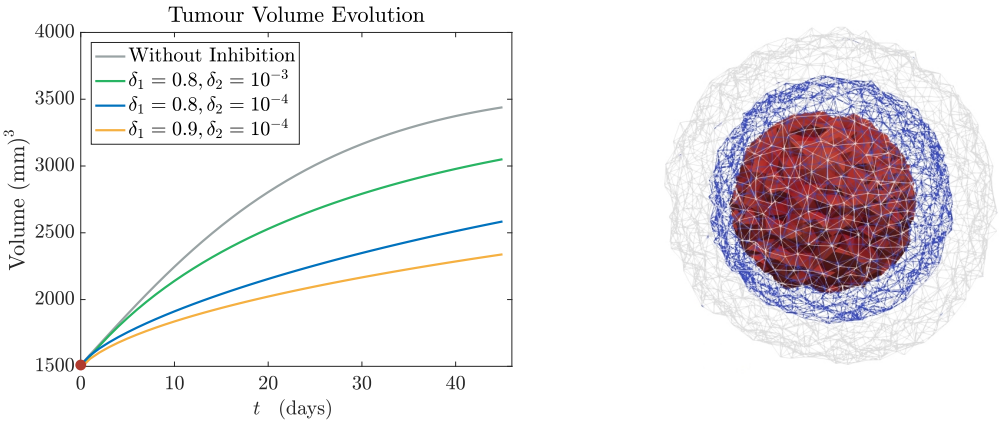

(a) (b)

Fig. 5.11 (a): Tumour volume evolution, as a function of time, in the case with and without stress inhibition of growth, for different values of the parameters δ_1 and δ_2 appearing in Eq. (5.6). The red marker identifies the initial volume of the tumour. (b): Initial tumour configuration (red), corresponding to the volume at $t = 0$; final configuration for the case without stress inhibition (grey) and for the stress-inhibited case with $\delta_1 = 0.8$, $\delta_2 = 10^{-4}$ MPa (blue), corresponding to the final volumes in the line plot (a).

brain, while it substantially decreases inside the tumour, where proliferating neoplastic cells are consuming the nutrients faster than they are supplied.

In addition to the maps representing the relevant variables on the three-dimensional brain domain, in Fig. 5.9 we report some line plots along three representative rays originating from the tumour center and lying in different orthogonal planes. This allows to evaluate spatial evolutions of the variables, moving away from the tumour centre. It can be observed that the displacement magnitude presents a peak at the tumour boundary and then vanishes as we move away from the cancer domain. However, the region of healthy tissue affected by the unnatural displacement may reach a distance up to 25 mm, which is significant for a tumour of 7 mm of starting radius. Moreover, the plot in Fig. 5.9a shows that the displacement is not uniform in the three planes, which highlights again the anisotropic growth pattern. Instead, as already shown before, the solid volume fraction ϕ_s in Fig. 5.9b displays a non-monotonic behaviour along some rays, due to the fact that the solid phase is growing and compressing the surrounding healthy tissue. Looking at Fig. 5.9c, the pressure increases when moving from the tumour center to the healthy tissue, while the bulk solid stress decreases, coherently with the observation that the maximum compression is experienced inside the cancer proliferation domain (Fig. 5.9d).

To compare our results with biological data, we computed the tumour volume evolution for three different values of its elastic parameters: results are shown in Fig. 5.10a. It can be seen that there is an initial stage where the tumour volume grows approximately linearly: then, growth starts to slow down due to saturation. In detail, when the tumour is ten times stiffer than the healthy tissue, the final volume after 45 days amounts at 3.5 cm^3. Moreover, we observe a volume doubling time (VDT) of about 25 days and a specific growth rate (SGR, defined as $(\log 2)/\mathrm{VDT}$) of 2.8%/day. These results are indicative of a very fast growth and are in the range of experimental data by Stensjøen et al. [332], who reported a median VDT of 29.8 days, and by Ellingson et al. [112] where a median VDT of 21.1 days (with average of 41.0 ± 28.2 days) is found. Additionally, the SGR ranges from a median of 1.2–2.2%/day in [332] to an average of 5.9 ± 2.0%/day in [112]. We remark however that these quantities are usually obtained in medical assays by assuming that growth is exponential, which in some cases might be an oversimplification.

Moreover, even if the tumour in our simulations is highly non-spherical due to anisotropy as discussed before, we computed an average velocity of radial expansion (VRE) to make a comparison with other experimental results. In detail, starting from the tumour volume, we computed its equivalent radius considering it as a sphere and evaluated the expansion velocity along the radial coordinate. Our simulations suggest an average VRE of approximately $v_r \approx 18.4$ mm/year, which is biologically feasible [112, 332, 346, 374] even if there is a high clinical variability from patient to patient and in some cases the VRE is even greater. In particular, growth is faster in the first period, when the tumour is still localized and the cell volume fraction is far from the saturation limit. Instead, if we consider a softer tumour, which is only four times stiffer than the surrounding brain tissue, its growth is significantly slower: over the same time span of 45 days, the final cancer volume is about 2.2 cm^3, with a relative change in volume of 49%. In this case, the average VRE amounts at $v_r \approx 8$ mm/year, indicative of a slower growth. In the case in which the mechanical parameters inside the tumour region are equal to the ones of the healthy tissue [269, 339], volume growth is very slow compared to the other situations: the final volume of the mass amounts at 1.7 cm^3 and the relative volume change is less than 15%. For each choice of the mechanical parameters, in Fig. 5.10a we report as dashed lines the corresponding simulation with stress inhibition of growth, setting $\delta_1 = 0.8$ and $\delta_2 = 10^{-4}$ MPa. As expected, the sensitivity of volume growth to compressive stresses increases with the difference in mechanical parameters between the tumour and the host tissue. Overall, the results underline the importance of accounting for

the mechanical features of tumour growth, since stiffer cancer masses are more effective in displacing the surrounding healthy tissue and can progress faster.

Furthermore, we compare our model outcomes with experimental data provided in [269, 317, 335]. In particular, the profiles of the Cauchy stress component T_{zz} across the tumour diameter and the surrounding tissue, reported in Fig. 5.10b are in qualitative agreement with the experimental results and finite element estimates provided in [269]. It can be observed that the stress has a peak near the interface between the tumour and the healthy tissue, where tension accumulates. Then, there is a high compression zone inside the tumour, with a slight decrease at the tumour center. Moreover, if the tumour is ten times stiffer than the host tissue, the modulus of the considered component of the Cauchy stress is significantly higher compared with the case in which the two tissues are mechanically equivalent. In spite of this, the tension and compression values for both T_{zz} and Σ predicted by our model are overall higher when we consider the mechanical parameters of the tumour ten times greater than the ones of the healthy tissue. On the other hand, if we take equal material parameters we obtain results both qualitatively and quantitatively comparable with the ones reported in [269, 317], where stresses between -0.1 and 0.1 kPa are recorded for tumours in mice. These discrepancies may be due to the fact that the stress values are highly dependent on the material model and on the chosen constitutive characterization, and most experimental and computational models, including [269, 317], are based on linear elasticity, while we employ a nonlinear elastic framework. Moreover, in our case we deal with a tumour that has a radius of about 7 mm, which is almost twice as much as the one used in the experimental set-up of [269]. Since it has been shown that solid stress increases with tumour radius [269], our stress results may be feasible from a biological viewpoint, though further investigation about stress for *in vivo* tumours is needed as well as an accurate estimation of the mechanical parameters and tumour stiffness. We also find that the tumour solid stress predicted by our model is within the range of residual stresses estimated for cancer spheroids in [335], namely between 1.3 and 13.3 kPa, though these results are not brain-specific. In addition, solid stress values are again shown to be higher in modulus in the tumour interior, where there is a consistent amount of compression that slows down the growth of the cancer. Notwithstanding Stylianopoulos et al. [335] reported that the interstitial fluid pressure increases inside the tumour bulk as a consequence of vascular collapse (not modelled in our framework), our predictions suggest that the pressure is decreased, in accordance with other works using mixture models [135, 136]. Moreover, we did not take into account the

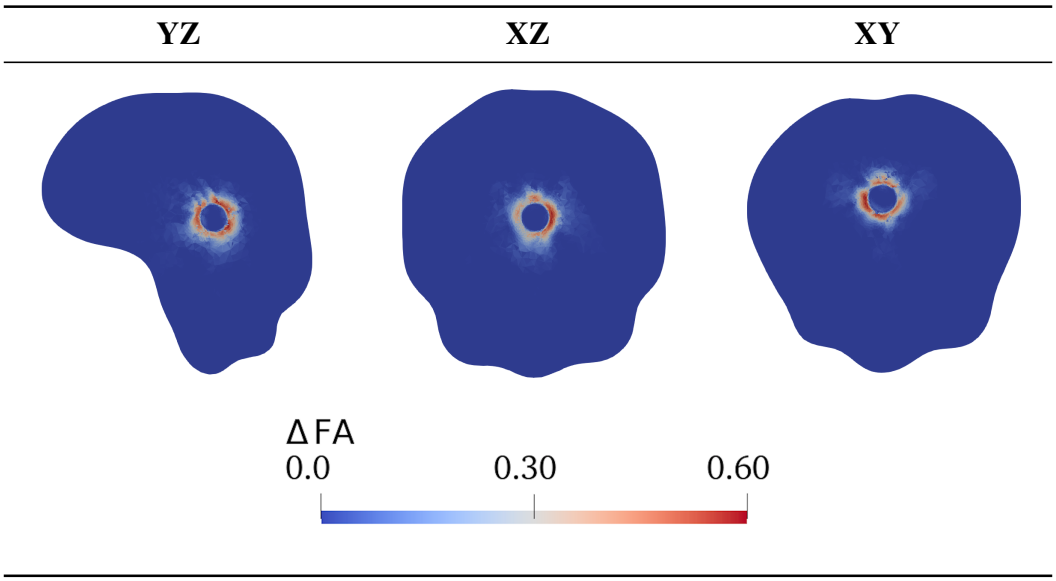

Fig. 5.12 Variation of the fractional anisotropy (FA) after 45 days of tumour growth. It can be noted that, around the tumour zone, there is an increase in the tissue anisotropy.

possibility of reduced perfusion due to cancer growth, which is an effect often reported in the literature [317, 335], but it would be interesting to consider it in future research.

Finally, we investigated the role of cancer cell sensitivity to stress-inhibition in the progression of the disease. To do so, in Fig. 5.11 we compare the evolution of the tumour volume for different grades of stress inhibition (regulated by the parameters δ_1 and δ_2), with respect to the case without stress inhibition. In particular, in Fig. 5.11a we show the volume evolution of the cancer in the case without stress inhibition and in three stress-inhibited cases, varying both the parameters δ_1 and δ_2. Specifically, if we increase the impact of compression by decreasing δ_2 while keeping $\delta_1 = 0.8$ fixed, the volume growth becomes consistently slower and reduces the velocity of cancer expansion. This can be also seen in Fig. 5.11b, where the three-dimensional configuration of the tumour is shown at the initial time instant and at $t = 45$ days, for the case without stress inhibition and for a strongly stress-inhibited case. An evaluation of the velocities of radial expansion yields $v_r = 15.1$ mm/year if $\delta_1 = 0.8$, $\delta_2 = 10^{-3}$ MPa and $v_r = 11.2$ mm/year if $\delta_1 = 0.8$, $\delta_2 = 10^{-4}$ MPa. Instead, keeping $\delta_2 = 10^{-4}$ MPa fixed and increasing δ_1 also leads to a slower growth, even if the volume reduction due to inhibition is smaller.

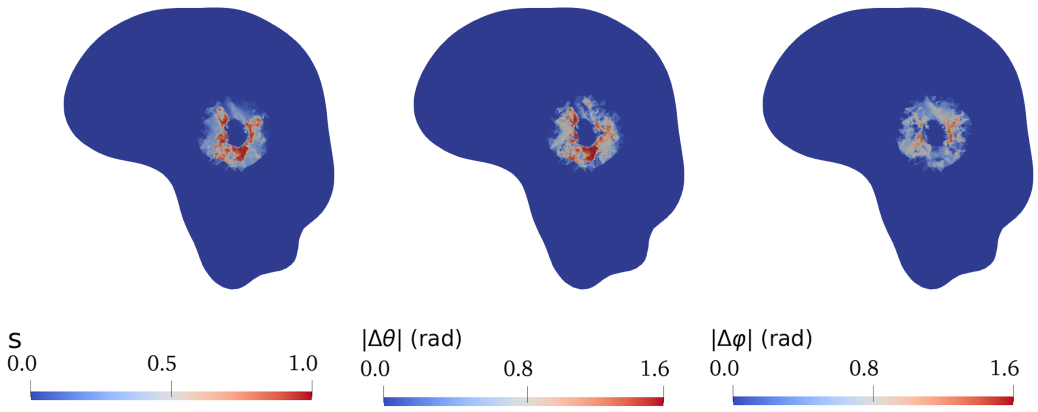

Fig. 5.13 Variation during tumour growth (from $t = 0$ to $t = 45$ days) of the eigenvector associated with the greatest eigenvalue of the diffusion tensor $\mathbb{D}$, quantified in terms of the scalar index s (left) and the absolute variations of the azimuthal angle $|\Delta\theta|$ (center) and polar angle $|\Delta\varphi|$ (right).

5.4.2 Modification of DTI Data

In this Section, we show some results related to the DTI data modification due to tumour growth. Indeed, the expansion of the mass and the induced displacement alter the fibre tracts in the surroundings, leading to changes in diffusion and preferential directions. To quantify these changes, we recall that, given $\lambda_1 > \lambda_2 > \lambda_3$ the descending order eigenvalues of the diffusion tensor, the fractional anisotropy (FA) is a scalar parameter defined by [281, 340]:

$$\mathrm{FA} := \sqrt{\frac{1}{2}\frac{(\lambda_1-\lambda_2)^2+(\lambda_2-\lambda_3)^2+(\lambda_1-\lambda_3)^2}{\lambda_1^2+\lambda_2^2+\lambda_3^2}}. \tag{5.45}$$

A fractional anisotropy of 0 identifies an isotropic medium, where the eigenvalues are all coincident and the diffusion ellipsoid is actually a sphere, with no preferential direction. Instead, a FA value of 1 indicates the existence of a totally preferred direction, making diffusion to occur only along one of the eigenvectors. In order to provide an estimate of how the diffusion tensor is changed in time as a consequence of the tumour-induced deformation, in Fig. 5.12 we report the difference $\Delta\mathrm{FA} = \mathrm{FA}_f - \mathrm{FA}_i$ of fractional anisotropy between the final and initial diffusion tensors. It can be noted that, in the region surrounding the growing cancer, there is an increase in diffusive anisotropy up to 60%. Variations in FA are also non-uniform in the tumour area, highlighting zones which are significantly affected by changes in anisotropy and others which instead maintain their initial preferential directions. It is also worth to observe that most of the tumour bulk displays no change in FA with respect to the initial value, computed from medical images. Indeed, DTI data extracted

from patients are often altered by the tumour, which displaces or even destroys the fibres as it grows, reducing anisotropy inside the tumour bulk, as pointed out in other works [340]. Since at the beginning of the simulations the tumour has already a size of some millimetres, the most significant changes in anisotropy happen around the tumour domain, where the cancer mass dislocates the surrounding white matter fibres and the displacements are higher.

Since the fractional anisotropy only gives a scalar measure related to the eigenvalues, we also investigated the variation in the eigenvector direction $\mathbf{e}_1^0$ associated with the greatest eigenvalue λ_1 of the diffusion tensor $\mathbb{D}_0$. To do so, first of all we computed in each mesh cell the direction of the eigenvector $\mathbf{e}_1^f$ associated with the greatest eigenvalue of the diffusion tensor $\mathbb{D}$ at the final time step. In fact, thanks to the modification of the initial tensor $\mathbb{D}_0$, we can keep track of the preferential directions of diffusion, which may vary in each cell due to tumour growth and subsequent deformation. Then, we calculated the value of

$$s := 1 - |\mathbf{e}_1^0 \cdot \mathbf{e}_1^f|,$$

that is a measure related to the scalar product between the initial and final eigenvectors. In particular, $s = 0$ denotes zones where the eigenvector does not change as a consequence of the deformation, while $s = 1$ identifies regions with the greatest modifications in the direction of $\mathbf{e}_1^0$ due to tumour growth. As shown in Fig. 5.13, the greatest variations occur in cells located at the border of the tumour region and in the surrounding healthy area. However, the scalar index s does not provide details about the change in orientation of the eigenvectors. Therefore, we expressed the eigenvectors $\mathbf{e}_1^0$ and $\mathbf{e}_1^f$ using spherical coordinates (r, θ, φ), where $r > 0$ is the distance from the origin, $\theta \in (-\pi, \pi]$ is the azimuthal angle and $\varphi \in (0, \pi]$ is the polar angle, so that $\mathbf{e}_1^0 = (r^0, \theta^0, \varphi^0)$ and $\mathbf{e}_1^f = (r^f, \theta^f, \varphi^f)$. Then, we calculated the absolute differences $|\Delta\theta| = |\theta^f - \theta^0|$ and $|\Delta\varphi| = |\varphi^f - \varphi^0|$ between the angles θ and φ, respectively, at final and initial time instants. Since we are interested in the preferential axis of diffusion and not in its orientation, we identified azimuthal angles and polar angles differing by multiples of π and rescaled the angles variation between 0 and $\pi/2$. These variations were only computed in anisotropic regions, where $\mathbb{D}$ is not spherical and therefore it is meaningful to evaluate changes in the eigenvector associated with the greatest eigenvalue. Results for $|\Delta\theta|$ and $|\Delta\varphi|$ are shown in Fig. 5.13: there are regions, both inside and outside the tumour domain, in which the two angles defining the spherical coordinates of $\mathbf{e}_1^0$ vary, leading therefore to changes in the preferential direction of nutrients diffusion, in qualitative agreement with medical observations [45].

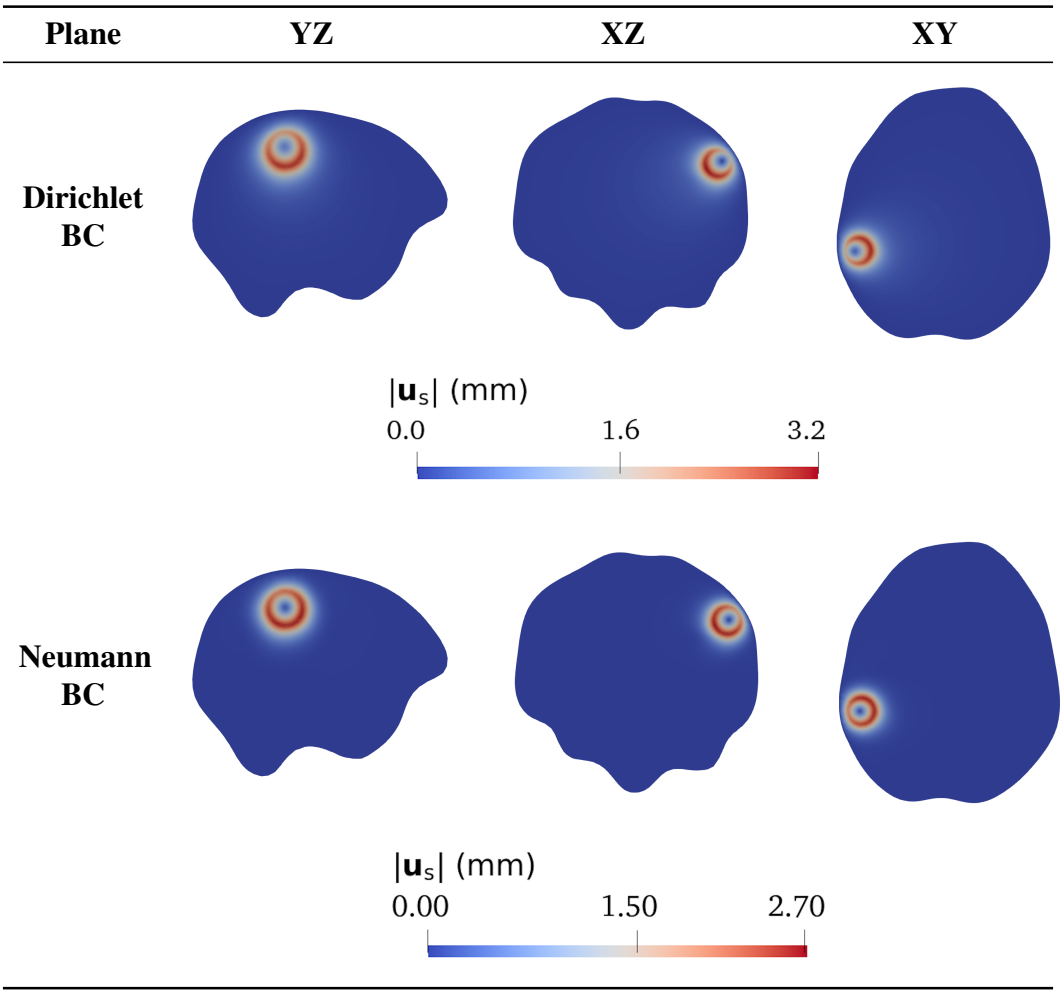

Fig. 5.14 Comparison between the displacement magnitude $|\mathbf{u}_s|$ after $t = 35$ days of tumour growth near the skull, clipped along a sagittal (first column), an axial (second column) and coronal (third column) plane centred within the tumour. In the first row, the case with Dirichlet boundary conditions as from Eqs. (5.34) is reported, while the second row shows the case with zero-flux boundary conditions for the pressure and concentration of nutrients, as stated in Eqs. (5.35).

5.4.3 Simulations of a Tumour Close to the Boundary

Lastly, we investigated a situation in which the tumour is placed near the boundary of the brain, in order to evaluate the effect of different boundary conditions. In particular, we performed two sets of simulations. In the first case, we used Dirichlet boundary conditions on $\mathbf{u}_s$, p, and c_n, as we did before when the tumour was far from the boundary. Such conditions are reasonable when the cancer mass does not reach the skull, where we can assume that all variables have fixed values. However, in the case of a tumour close to the boundary, Neumann boundary conditions might be more appropriate and physically

motivated. Therefore, to make a comparison, we performed a simulation in which we use the set of boundary conditions defined in Eq. (5.35).

The results are shown in Figs. 5.14–5.15 for the displacement magnitude and the nutrients' concentration, respectively. As expected, the presence of the fixed skull generates a pronounced asymmetry in the tumour growth pattern, that can be seen clearly in the displacement plot, especially in the case of Dirichlet boundary conditions (5.34). Moreover, when zero-flux conditions (5.35c) on c_n are imposed, the concentration of nutrients decreases more around the tumour region, since there is no supply coming from the boundary as in the Dirichlet case.

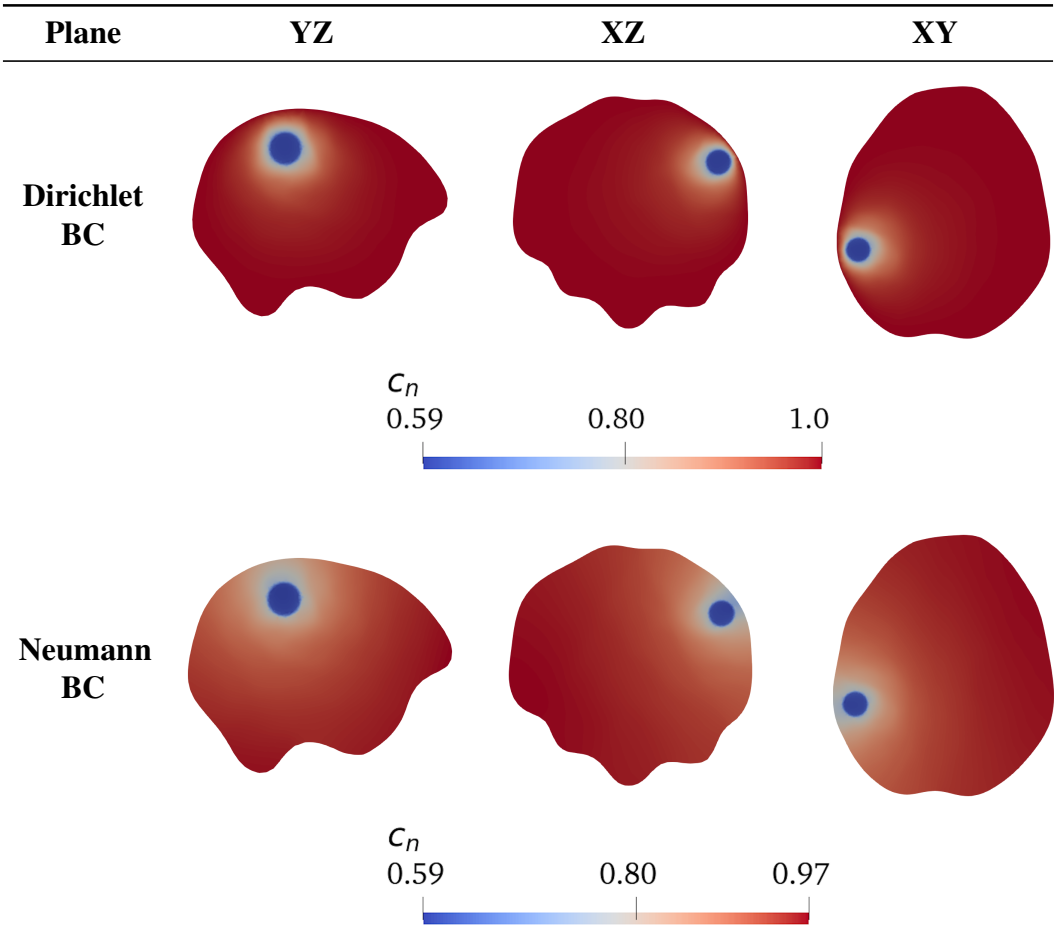

Fig. 5.15 Comparison between the concentration of nutrients c_n after $t = 35$ days of tumour growth in the brain, clipped along a sagittal (first column), an axial (second column) and coronal (third column) plane centred within the tumour. In the first row, the case with Dirichlet boundary conditions as from Eqs. (5.34) is reported, while the second row shows the case with zero-flux boundary conditions for the pressure and concentration of nutrients, as stated in Eqs. (5.35).

5.5 Discussion

Mechanical compression is a common abnormality of brain tumours that has been shown to be responsible for the severe neurological defects of brain cancer patients and to represent a negative prognostic factor [128, 191]. To refine previous mathematical descriptions of brain tumour growth and account for this mechanical impact, in this Chapter we have proposed a model that explicitly features hyperelastic deformations of brain tissue and incorporates medical imaging data coming from DTI and MRI.

Using the well-established framework of Continuum Mechanics, we described the brain and the cancer mass as saturated biphasic mixtures, comprising a solid and a fluid phase, which are both relevant in a hydrated soft tissue like the brain. This enables us to evaluate deformations and stresses caused by the proliferation of tumour cells, as well as the displacement induced on the surrounding healthy tissue. In particular, thanks to the multiphase approach, the model is able to distinguish the stress contribution associated with the fluid from the one associated with the solid mass, and therefore it could be useful in understanding the biological implications and the extent of the so-called mass-effect [64, 141, 185, 191, 317]. The mechanical description included in the present model allows to account for growth inhibition due to excessive compression, thanks to the definition of a proliferation term embedding a proper stress measure. Moreover, by numerically computing the deformation field, it is possible to modify the diffusion and permeability tensors, taking into account the displacement of the brain tissue. This is a clear advantage for simulations of brain tumour growth, since it allows to consider changes in the DTI data without the need of repeating the clinical screening exams multiple times.

Chapter 6

Conclusions and Perspectives

It is becoming increasingly clear that a deeper understanding of biological systems throughout all scales requires an interdisciplinary effort. In this respect, the contribution of mathematical models and numerical simulations appears rich of potentialities: they can be suitably used to support experimental researches and to capture the essential mechanisms behind complex phenomena. A reproduction of these systems through equations and simulations, although intrinsically incomplete, turns out to be an extremely flexible tool to accelerate the research process in the fields of biology, biomedicine, and engineering science in general. Moreover, the development of new models represents also a challenge from the mathematical point of view, since it requires to build novel frameworks upon well-established theories.

Motivated by these facts, in this Thesis we addressed the problem of describing structural reorganisations, growth, and active responses of cells and tissues, with particular emphasis on their mechanical behaviour. Indeed, the importance of mechanics have been underscored more and more also at the cellular scale, leading to the development of a totally new field called mechanobiology. Furthermore, biological organisms are by their nature capable of dynamically adapting to their environment and to grow. These two characteristics add difficulties in the modelling process and have to be properly taken into account. Specifically, we focused on the following open issues:

- the mathematical modelling of cell cytoskeletal reorganisation as a consequence of external mechanical stimuli;
- the description of active contractility in axons;
- the evaluation of the mechanical impact of a tumour growing in the brain.

More in detail, in Chapter 2 we have provided a thorough review of the experimental and modelling literature about the cellular response to mechanical cues. In particular, we analysed the phenomenon of cell reorientation under cyclic stretching of the substrate, which is extremely relevant in a number of physiological tissues: blood vessels, the heart, the lungs, the intestine, and muscles are all constantly subject to periodic deformations, just to mention a few examples. Moreover, understanding how a cell orients as a reaction to environmental alterations is extremely relevant in tissue engineering, where the aim is to build artificial tissues in a faithful way, and also in medicine, since some pathologies appear related to issues in cell mechanotransduction. We summarised the main features of the numerous experiments performed from the 1980s until today, trying to capture the relevant factors that are involved in cell reorientation on smooth 2D substrates, on grooved substrates and in 3D matrices.

Then, in Chapter 3, we proposed three models with the aim of investigating more deeply the reorientation of the cell cytoskeleton. First of all, in Section 3.1, we approached the problem within the framework of nonlinear elasticity, in order to evaluate possible effects of finite deformations. The system composed by cells and their substrate was treated as an anisotropic elastic solid, for which we introduced an energy that generalises the one previously employed in the literature for linear elasticity. We found that, for a large class of elastic energies, it is possible to find a relation between the angle and the deformation which is a generalisation of the one put forward by Livne et al. [226] in their very relevant work. The existence of such a relation might provide an explanation of why experimental data obtained outside the linear elastic regime are still fitted well by a linear model. Then, we analysed the effect of intrinsically nonlinear terms within the energy, showing that their impact is not fundamental to capture the experimentally observed behaviour.

Afterwards, to introduce the dynamic remodelling of the cell cytoskeleton during the reorientation process, in Section 3.2 we built a thermodynamically consistent model of fibre realignment in a hyperelastic material. This framework consists of the usual balances for a continuum body complemented by a system of equations describing the evolution of two fibre structures, which may evolve following independent rotations. The stationary solutions of such a system are then studied, showing an extension of a well-known result about coaxiality of stress and strain if the two fibre families are allowed to reorganise independently. The case with a fixed angle between fibres is then recovered by introducing an appropriate constraint between the two rotations. Then, the model is applied to the problem of cytoskeletal reorientation under mechanical stimuli, showing a good agreement with experiments both for constrained and unconstrained fibres.

At the end of Chapter 3, in Section 3.3, we proposed a simple linear viscoelastic model, to account for the frequency effect seen in experiments. Indeed, as discussed in Chapter 2, the frequency of the cyclic deformation might impact on the speed of cell reorientation, and some thresholds to initiate the cellular response also exist. Therefore, we considered a Maxwell-like viscoelastic model with anisotropy induced by the presence of cells and stress fibres, and studied its behaviour in both high and low frequency regimes. In particular, for high frequencies, the equilibrium solutions can be predicted by the critical points of an energy akin to the one introduced in Section 3.1. We studied the stability of such equilibrium solutions and their bifurcations in detail. Finally, we performed some numerical simulations, which were in agreement with the existence of experimental frequency thresholds.

Another problem related to cellular mechanics and response to mechanical stimuli is the contractility of axons, which we studied in Chapter 4. In fact, experimental evidence suggests that the axonal cortex, i.e. the external coating of axons, is able to actively contract and exert compression on the inner part. This capability seems also related to the regulation of the axon diameter evidenced in experiments. To describe these phenomena, we followed an active strain approach to develop a model of active contractility, in which the coupling between the circumferential and axial active stretches is derived through a thermodynamically based procedure. Then, we implemented a numerical framework to simulate the stretching of axons and drug-induced alterations of their cytoskeletal structure. The variations of the diameter that we found appear in agreement with experimental data and suggest that the coupling of contractility in two different directions and the compressive stress exerted by the cortex are very relevant.

Finally, in Chapter 5 we moved to the tissue scale and analysed the mechanical impact of a growing tumour inside the brain. In particular, we focused on the effect of solid stresses, which have been shown to be detrimental for patients: their negative repercussions are even amplified in brain tissue, which is extremely soft and confined by the skull. To investigate these effects, we proposed a mathematical model based on mixture theory, to account for solid and fluid components, and morphoelasticity, to describe growth distortions. Moreover, we considered the healthy brain tissue and the tumour as hyperelastic solids with different mechanical parameters, so as to evaluate the displacement and stress induced by the growing cancer mass. Since we explicitly evaluated the deformations following tumour growth, we were also able to exploit them to compute alterations in the preferential directions of diffusion and fluid motion. Simulations to test the model behaviour were then

performed on a realistic brain geometry, built from imaging data, and the results underlined the relevance of a mechanical description of brain tumour growth.

The mathematical modelling of biological systems is however in constant expansion and numerous challenges still remain open. With respect to the problems examined in this Thesis, in our models of cell reorientation we did not feature explicitly the adhesion between cells and substrates, for the sake of simplicity. However, it is known that the link between a cell and its environment, due to focal adhesions, is fundamental in the transduction of mechanical signals both outside-in and inside-out. Even if the modelling becomes more complicated, it might be worth to investigate adhesion effects. This purpose should probably be pursued by considering a more detailed description of viscoelasticity, for instance accompanied by a multiplicative decomposition of the deformation gradient together with a proper evolution of the material symmetry group. Moreover, it could be interesting to employ our framework to evaluate the role of microtubules in reorientation, which is not fully elucidated. In this respect, a model that describes a dragged reorientation of a family of fibres performed by another family could provide insights and represents a stimulating mathematical challenge. For what concerns the modelling of axons, future developments should be focused on the electrical coupling with mechanics, which we neglected for simplicity. Indeed, the active contractility might be influenced by the action potential crossing the axon. In addition, it could be important to introduce mechanical anisotropy due to the presence of microtubules arranged in the axial direction: such an issue could also be related to a more refined description of axonal damage as a consequence of imposed stretch. Finally, the brain modelling framework could be improved by considering first of all anisotropic growth distortions, which may drive the proliferation of the tumour mass along brain fibres. Then, a further step could be represented by the implementation of therapeutic protocols, representing a difficult problem for clinicians. The inclusion of realistic patient-specific mechanical parameters, obtained through Magnetic Resonance Elastography, also represents a very intriguing possibility, though this imaging technique is still under development.

In conclusion, we have shown that the mathematical modelling of biological structures can be fruitfully employed to get insight into the wide variety of phenomena that are observed. The intrinsically nonlinear, multiphysical, and strongly coupled behaviour of cells and tissues poses challenging tasks, which however could take advantage of a mathematically based description.

References

[1] R. Abbott, A. Howe, H. Langevin, and J. Iatridis. Live free or die: Stretch-induced apoptosis occurs when adaptive reorientation of annulus fibrosus cells is restricted. *Biochemical and Biophysical Research Communications*, 421:361–366, 2012.

[2] A. Agosti, C. Cattaneo, C. Giverso, D. Ambrosi, and P. Ciarletta. A computational framework for the personalized clinical treatment of glioblastoma multiforme. *ZAMM - Journal of Applied Mathematics and Mechanics*, 98:2307–2327, 2018.

[3] A. Agosti, P. Ciarletta, H. Garcke, and M. Hinze. Learning patient-specific parameters for a diffuse interface glioblastoma model from neuroimaging data. *Mathematical Methods in the Applied Sciences*, 43:8945–8979, 2020.

[4] A. Agosti, C. Giverso, E. Faggiano, A. Stamm, and P. Ciarletta. A personalized mathematical tool for neuro-oncology: A clinical case study. *International Journal of Non-Linear Mechanics*, 107:170–181, 2018.

[5] W. Ahmed, T. Wolfram, A. Goldyn, K. Bruellhoff, B. Rioja, M. Moller, J. Spatz, T. Saif, J. Groll, and R. Kemkemer. Myoblast morphology and organization on biochemically micropatterned hydrogel coatings under cyclic mechanical strain. *Biomaterials*, 31:250–258, 2010.

[6] B. Alberts, A. Johnson, J. Lewis, M. Raff, K. Roberts, and P. Walter. *Molecular Biology of the Cell (5th Edition)*. Garland Science, 2008.

[7] J. Alfonso, K. Talkenberger, M. Seifert, B. Klink, A. Hawkins-Daarud, K. Swanson, H. Hatzikirou, and A. Deutsch. The biology and mathematical modelling of glioma invasion: A review. *Journal of the Royal Society Interface*, 14:1–20, 2017.

[8] M. Alnaes, J. Blechta, J. Hake, A. Johansson, B. Kehlet, A. Logg, C. Richardson, J. Ring, M. Rognes, and G. Wells. The FEniCS Project Version 1.5. *Archive of Numerical Software*, 3:9–23, 2015.

[9] D. Ambrosi and F. Guana. Stress-modulated growth. *Mathematics and Mechanics of Solids*, 12:319–342, 2007.

[10] D. Ambrosi and F. Mollica. On the mechanics of a growing tumor. *International Journal of Engineering Science*, 40:1297–1316, 2002.

[11] D. Ambrosi and F. Mollica. The role of stress in the growth of a multicell spheroid. *Journal of Mathematical Biology*, 48:477–499, 2004.

[12] D. Ambrosi and S. Pezzuto. Active stress vs. active strain in mechanobiology: Constitutive issues. *Journal of Elasticity*, 107(2):199–212, 2011.

[13] D. Ambrosi, S. Pezzuto, D. Riccobelli, T. Stylianopoulos, and P. Ciarletta. Solid tumors are poroelastic solids with a chemo-mechanical feedback on growth. *Journal of Elasticity*, 129:107–124, 2017.

[14] D. Ambrosi and L. Preziosi. On the Closure of Mass Balance Models for Tumor Growth. *Mathematical Models and Methods in Applied Sciences*, 12(5):737–754, 2002.

[15] D. Ambrosi and L. Preziosi. Cell adhesion mechanisms and stress relaxation in the mechanics of tumours. *Biomechanics and Modeling in Mechanobiology*, 8:397–413, 2009.

[16] C. Amidei and D. S. Kushner. Clinical implications of motor deficits related to brain tumors. *Neuro-Oncology Practice*, 2(4):179–184, 2015.

[17] D. Andrini, V. Balbi, G. Bevilacqua, G. Lucci, G. Pozzi, and D. Riccobelli. Mathematical modelling of axonal cortex contractility. *Brain Multiphysics*, 3:100060, 2022.

[18] S. Angeli, K. Emblem, P. Due-Tonnessen, and T. Stylianopoulos. Towards patient-specific modeling of brain tumor growth and formation of secondary nodes guided by DTI-MRI. *NeuroImage: Clinical*, 20:664–673, 2018.

[19] S. Angeli and T. Stylianopoulos. Biphasic modeling of brain tumor biomechanics and response to radiation treatment. *Journal of Biomechanics*, 49:1524–1531, 2016.

[20] S. Asano, S. Ito, M. Morosawa, K. Furuya, K. Naruse, M. Sokabe, E. Yamaguchi, and Y. Hasegawa. Cyclic stretch enhances reorientation and differentiation of 3D culture model of human airway smooth muscle. *Biochemistry and Biophysics Reports*, 16:32–38, 2018.

[21] M. Asgari, D. de Zelicourt, and V. Kurtcuoglu. Glymphatic solute transport does not require bulk flow. *Scientific Reports*, 6:38635, 2016.

[22] S. Astanin and L. Preziosi. Multiphase models of tumour growth. In N. Bellomo, M. Chaplain, and E. De Angelis, editors, *Selected Topics in Cancer Modelling: Genesis - Evolution - Immune Competition - Therapy*. Birkhäuser, 2008.

[23] G. Astarita and G. Marrucci. *Principles of Non-Newtonian Fluid Mechanics*. McGraw-Hill, 1974.

[24] H. Atcha, C. Davis, N. Sullivan, T. Smith, S. Anis, W. Dahbour, Z. Robinson, A. Grosberg, and W. Liu. A low-cost mechanical stretching device for uniaxial strain of cells: A platform for pedagogy in mechanobiology. *Journal of Biomechanical Engineering*, 140:081005, 2018.

[25] H. Atcha, V. Meli, C. Davis, K. Brumm, S. Anis, J. Chin, K. Jiang, M. Pathak, and W. Liu. Crosstalk between CD11b and Piezo1 mediates macrophage responses to mechanical cues. *Frontiers in Immunology*, 140:689397, 2018.

[26] M. Aubert, M. Badoual, C. Christov, and B. Grammaticos. A model of glioma cell migration on collagen and astrocytes. *Journal of Royal Society Interface*, 5:75–83, 2008.

[27] M. Aubert, M. Badoual, S. Fereol, C. Christov, and B. Grammaticos. A cellular automaton model for the migration of glioma cells. *Physical Biology*, 3:93–100, 2006.

[28] Y. Başar, M. Itskov, and A. Eckstein. Composite laminates: Nonlinear interlaminar stress analysis by multi-layer shell elements. *Computer Methods in Applied Mechanics and Engineering*, 185:367–397, 2000.

[29] A. C. Bain and D. F. Meaney. Tissue-level thresholds for axonal damage in an experimental model of central nervous system white matter injury. *Journal of Biomechanical Engineering*, 122(6):615–622, 2000.

[30] V. Balbi, A. Trotta, M. Destrade, and A. Annaidh. Poynting effect of brain matter in torsion. *Soft Matter*, 15:5147–5153, 2019.

[31] S. Banerjee, S. Khajanchi, and S. Chaudhuri. A mathematical model to elucidate brain tumor abrogation by immunotherapy with T11 Target Structure. *PLoS ONE*, 10:e0123611, 2015.

[32] V. Barron, C. Brougham, K. Coghlan, E. McLucas, D. O'Mahoney, C. Stenson-Cox, and P. McHugh. The effect of physiological cyclic stretch on the cell morphology, cell orientation and protein expression of endothelial cells. *Journal of Materials Science: Materials in Medicine*, 18:1973–1981, 2007.

[33] P. Basser. Interstitial pressure, volume, and flow during infusion into brain tissue. *Microvascular Research*, 44:143–165, 1992.

[34] C. Bellows, A. Melcher, and J. Aubin. Association between tension and orientation of periodontal ligament fibroblasts and exogenous collagen fibres in collagen gels in vitro. *Journal of Cell Science*, 58:125–138, 1982.

[35] M. Ben Amar and A. Goriely. Growth and instability in elastic tissues. *Journal of the Mechanics and Physics of Solids*, 53:2284–2319, 2005.

[36] R. Bernal, P. A. Pullarkat, and F. Melo. Mechanical properties of axons. *Physical Review Letters*, 99(1):018301, 2007.

[37] A. Bilby, L. Gardner, and A. Stroh. Continuous distributions of dislocations and the theory of plasticity. In *Proceedings of the Ninth International Congress of Applied Mechanics*. 1957.

[38] BioRender. https://biorender.com/.

[39] I. Bischofs and U. Schwarz. Cell organization in soft media due to active mechanosensing. *PNAS*, 100:9274–9279, 2003.

[40] F. Boccafoschi, M. Bosetti, S. Gatti, and M. Cannas. Dynamic fibroblast cultures: Response to mechanical stretching. *Cell Adhesion & Migration*, 1:124–128, 2007.

[41] R. Boerboom, M. Rubbens, N. Driessen, C. Bouten, and F. Baaijens. Effect of strain magnitude on the tissue properties of engineered cardiovascular constructs. *Annals of Biomedical Engineering*, 36(2):244–253, 2008.

[42] P.-Y. Bondiau, O. Clatz, M. Sermesant, P.-Y. Marcy, H. Delingette, M. Frenay, and N. Ayache. Biocomputing: numerical simulation of glioblastoma growth using diffusion tensor imaging. *Physics in Medicine and Biology*, 53:879–893, 2008.

[43] N. Bono, D. Pezzoli, L. Levesque, C. Loy, G. Candiani, G. Fiore, and D. Mantovani. Unraveling the role of mechanical stimulation on smooth muscle cells: A comparative study between 2D and 3D models. *Biotechnology and Bioengineering*, 113:2254–2263, 2016.

[44] K. Bottger, H. Hatzikirou, A. Chauviere, and A. Deutsch. Investigation of the migration/proliferation dichotomy and its impact on avascular glioma invasion. *Mathematical Modelling of Natural Phenomena*, 7:105–135, 2012.

[45] B. L. J. Bouwen, K. J. Pieterman, M. Smits, C. M. F. Dirven, Z. Gao, and A. J. P. E. Vincent. The impacts of tumor and tumor associated epilepsy on subcortical brain structures and long distance connectivity in patients with low grade glioma. *Frontiers in Neurology*, 9:1004, 2018.

[46] R. Bowen. Theory of mixtures. In A. Eringen, editor, *Continuum Physics - Volume 3*. Academic Press, 1976.

[47] D. Bray. Axonal growth in response to experimentally applied mechanical tension. *Developmental Biology*, 102(2):379–389, 1984.

[48] M. Bruehlmeier, U. Roelcke, P. Blauenstein, J. Missimer, P. Schubiger, J. Locher, R. Pellikka, and S. Ametamey. Measurement of the Extracellular Space in Brain Tumors Using ^{7}6Br-Bromide and PET. *Journal of Nuclear Medicine*, 44:1210–1218, 2003.

[49] N. Bryniarska-Kubiak, A. Kubiak, M. Lekka, and A. Basta-Kaim. [the emerging role of mechanical and topographical factors in the development and treatment of nervous system disorders: Dark and light sides of the force. *Pharmacological Reports*, pages 1626–1641.

[50] R. Buck. The longitudinal orientation of structures in the subendothelial space of rat aorta. *American Journal of Anatomy*, 156:1–14, 1979.

[51] R. Buck. Reorientation response of cells to repeated stretch and recoil of the substratum. *Experimental Cell Research*, 127:470–474, 1980.

[52] R. Buck. Behaviour of vascular smooth muscle cells during repeated stretching of the substratum in vitro. *Atherosclerosis*, 46:217–223, 1983.

[53] S. Budday, T. C. Ovaert, G. A. Holzapfel, P. Steinmann, and E. Kuhl. Fifty shades of brain: A review on the mechanical testing and modeling of brain tissue. *Archives of Computational Methods in Engineering*, 27(4):1187–1230, 2020.

[54] S. Budday, G. Sommer, C. Birkl, C. Langkammer, J. Haybaeck, J. Kohnert, M. Bauer, F. Paulsen, P. Steinmann, E. Kuhl, and G. Holzapfel. Mechanical characterization of human brain tissue. *Acta Biomaterialia*, 48:319–340, 2017.

[55] A. Buskermolen, H. Suresh, S. Shishvan, A. Vigliotti, A. DeSimone, N. Kurniawan, C. Bouten, and V. Deshpande. Entropic forces drive cellular contact guidance. *Biophysical Journal*, 116:1994–2008, 2019.

[56] D. Butcher, T. Alliston, and V. Weaver. A tense situation: forcing tumour progression. *Nature Reviews Cancer*, 9:108–122, 2009.

[57] J. Butler, I. Tolic-Norrelykke, B. Fabry, and J. Fredberg. Traction fields, moments, and strain energy that cells exert on their surroundings. *American Journal of Physiology - Cell Physiology*, 282:C595–C605, 2002.

[58] H. Byrne and L. Preziosi. Modelling solid tumour growth using the theory of mixtures. *Mathematical Medicine and Biology*, 20:341–366, 2003.

[59] J. Cha, S.-N. Park, S. Noh, and H. Suh. Time-dependent modulation of alignment and differentiation of smooth muscle cells seeded on a porous substrate undergoing cyclic mechanical strain. *Artificial Organs*, 30(4):250–258, 2006.

[60] S. Chada, P. Lamoureux, R. E. Buxbaum, and S. R. Heidemann. Cytomechanics of neurite outgrowth from chick brain neurons. *Journal of Cell Science*, 110(10):1179–1186, 1997.

[61] C. Chatelain, T. Balois, P. Ciarletta, and M. Ben Amar. Emergence of microstructural patterns in skin cancer: A phase separation analysis in a binary mixture. *New Journal of Physics*, 13:115013, 2011.

[62] S. Chatelin, A. Constantinesco, and R. Willinger. Fifty years of brain tissue mechanical testing: From in vitro to in vivo investigations. *Biorheology*, 47:255–276, 2010.

[63] A. Chatterjee, P. Kondaiah, and N. Gundiah. Stress fiber growth and remodeling determines cellular morphomechanics under uniaxial cyclic stretch. *Biomechanics and Modeling in Mechanobiology*, 21:553–567, 2022.

[64] V. P. Chauhan, Y. Boucher, C. R. Ferrone, S. Roberge, J. D. Martin, T. Stylianopoulos, N. Bardeesy, R. A. DePinho, T. P. Padera, L. L. Munn, and R. K. Jain. Compression of pancreatic tumor blood vessels by hyaluronan is caused by solid stress and not interstitial fluid pressure. *Cancer Cell*, 1(26):14–15, 2014.

[65] D. Chauvet, M. Imbault, L. Capelle, M. Demene, M. Mossad, C. Karachi, A.-L. Boch, J.-L. Gennisson, and M. Tanter. In vivo measurement of brain tumor elasticity using intraoperative shear wave elastography. *Ultraschall in der Medizin*, 37:584–590, 2016.

[66] B. Chen, R. Kemkemer, M. Deibler, J. Spatz, and H. Gao. Cyclic stretch induces cell reorientation on substrates by destabilizing catch bonds in focal adhesions. *PLoS ONE*, 7:e48346, 2012.

[67] K. Chen, A. Vigliotti, M. Bacca, R. McMeeking, V. Deshpande, and J. Holmes. Role of boundary conditions in determining cell alignment in response to stretch. *PNAS*, 115(5):986–991, 2018.

[68] Y. Chen, A. Pasapera, A. Koretsky, and C. Waterman. Orientation-specific responses to sustained uniaxial stretching in focal adhesion growth and turnover. *PNAS*, 110:E2352–E2361, 2013.

[69] G. Cheng, J. Tse, R. K. Jain, and L. L. Munn. Micro-Environmental Mechanical Stress Controls Tumor Spheroid Size and Morphology by Suppressing Proliferation and Inducing Apoptosis in Cancer Cells. *PLOS ONE*, 4(2):1–11, 2009.

[70] J. Ciambella, G. Lucci, P. Nardinocchi, and L. Preziosi. Passive and active fiber reorientation in anisotropic materials. *International Journal of Engineering Science*, 176:103688, 2022.

[71] J. Ciambella and P. Nardinocchi. Magneto-induced remodelling of fibre-reinforced elastomers. *International Journal of Non-Linear Mechanics*, 117:103230, 2019.

[72] J. Ciambella and P. Nardinocchi. Torque-induced reorientation in active fibre-reinforced materials. *Soft Matter*, 15:2081–2091, 2019.

[73] P. G. Ciarlet. *Mathematical Elasticity: Three-Dimensional Elasticity*. Society for Industrial and Applied Mathematics, Philadelphia, PA, 2021.

[74] P. Ciarletta, L. Foret, and M. Ben Amar. The radial growth phase of malignant melanoma: multi-phase modelling, numerical simulations and linear stability analysis. *Journal of the Royal Society Interface*, 8:345–368, 2011.

[75] G. Civelekoglu-Scholey, A. Wayne Orr, I. Novak, J.-J. Meister, M. Schwartz, and A. Mogilner. Model of coupled transient changes of Rac, Rho, adhesions and stress fibers alignment in endothelial cells responding to shear stress. *Journal of Theoretical Biology*, 232:569–585, 2005.

[76] P. Clark, P. Connolly, A. Curtis, J. Dow, and C. Wilkinson. Topographical control of cell behaviour: I. Simple step cues. *Development*, 99(3):439–448, 1987.

[77] P. Clark, P. Connolly, A. Curtis, J. Dow, and C. Wilkinson. Topographical control of cell behaviour: II. Multiple grooved substrata. *Development*, 108:439–448, 1990.

[78] P. Clark, P. Connolly, A. Curtis, J. Dow, and C. Wilkinson. Cell guidance by ultrafine topography in vitro. *Journal of Cell Science*, 99:73–77, 1991.

[79] O. Clatz, M. Sermesant, P. Bondiau, H. Delingette, S. Warfield, G. Malandain, and N. Ayache. Realistic simulation of the 3-D growth of brain tumors in MR images coupling diffusion with biomechanical deformation. *IEEE Transactions on Medical Imaging*, 24:1334–1346, 2005.

[80] B. Coleman and W. Noll. The thermodynamics of elastic materials with heat conduction and viscosity. *Archive for Rational Mechanics and Analysis*, 13:167–178, 1963.

[81] A. Collinsworth, C. Torgan, S. Nagda, R. Rajalingam, W. Kraus, and G. Truskey. Orientation and length of mammalian skeletal myocytes in response to a unidirectional stretch. *Cell and Tissue Research*, 302:243–251, 2000.

[82] M. Colombo, C. Giverso, E. Faggiano, C. Boffano, F. Acerbi, and P. Ciarletta. Towards the personalized treatment of Glioblastoma: Integrating patient-specific clinical data in a continuous mechanical model. *PLoS ONE*, 10:e0132887, 2015.

[83] M. Conte, L. Gerardo-Giorda, and M. Groppi. Glioma invasion and its interplay with nervous tissue and therapy: A multiscale model. *Journal of Theoretical Biology*, 486:110088, 2020.

[84] M. Conte and C. Surulescu. Mathematical modeling of glioma invasion: acid- and vasculature mediated go-or-grow dichotomy and the influence of tissue anisotropy. *Applied Mathematics and Computation*, 407:126305, 2021.

[85] A. R. Costa, R. Pinto-Costa, S. Castro Sousa, and M. Mendes Sousa. The regulation of axon diameter: From axonal circumferential contractility to activity-dependent axon swelling. *Frontiers in Molecular Bioscience*, 11:319, 2018.

[86] A. R. Costa, S. C. Sousa, R. Pinto-Costa, J. C. Mateus, C. D. Lopes, A. C. Costa, D. Rosa, D. Machado, L. Pajuelo, X. Wang, et al. The membrane periodic skeleton is an actomyosin network that regulates axonal diameter and conduction. *Elife*, 9:e55471, 2020.

[87] P. Dartsch and E. Betz. Cellular and cytoskeletal response of vascular cells to mechanical stimulation. In H. Planck, M. Dauner, and M. Renardy, editors, *Medical Textiles for Implantation*, pages 193–218, Berlin, Heidelberg, 1990. Springer.

[88] P. Dartsch and H. Hammerle. Orientation response of arterial smooth muscle cells to mechanical stimulation. *European Journal of Cell Biology*, 41:339–346, 1986.

[89] P. Dartsch, H. Hammerle, and E. Betz. Orientation of cultured arterial smooth muscle cells growing on cyclically stretched substrates. *Acta Anatomica*, 125:108–113, 1986.

[90] S. Das, A. Ippolito, P. McGarry, and V. Deshpande. Cell reorientation on a cyclically strained substrate. *PNAS Nexus*, 1:1–15, 2022.

[91] A. Datar, J. Ameeramja, A. Bhat, R. Srivastava, A. Mishra, R. Bernal, J. Prost, A. Callan-Jones, and P. A. Pullarkat. The roles of microtubules and membrane tension in axonal beading, retraction, and atrophy. *Biophysical Journal*, 117(5):880–891, 2019.

[92] R. De. A general model of focal adhesion orientation dynamics in response to static and cyclic stretch. *Communications Biology*, 1:81, 2018.

[93] R. De and S. Safran. Dynamical theory of active cellular response to external stress. *Physical Review E*, 78:031923–031940, 2008.

[94] R. De, A. Zemel, and S. Safran. Do cells sense stress or strain? Measurement of cellular orientation can provide a clue. *Biophysical Journal*, 94:L29–L31, 2008.

[95] R. De and S. Zemel, A. Safran. Dynamics of cell orientation. *Nature Physics*, 3:655–659, 2007.

[96] N. De Jonge, F. Kanters, F. Baaijens, and C. Bouten. Strain-induced collagen organization at the micro-level in fibrin-based engineered tissue constructs. *Annals of Biomedical Engineering*, 41(4):763–774, 2013.

[97] R. de Rooij and E. Kuhl. Constitutive Modeling of Brain Tissue: Current Perspectives. *Applied Mechanics Reviews*, 68:1–16, 2016.

[98] S. Deguchi, T. Ohashi, and M. Sato. Tensile properties of single stress fibers isolated from cultured vascular smooth muscle cells. *Journal of Biomechanics*, 39:2603–2610, 2006.

[99] M. Dehghany, R. Naghdabadi, S. Sohrabpour, Y. Li, and Y. Hu. A thermodynamically consistent electro-chemo-mechanical theory for modeling axonal swelling. *Journal of the Mechanics and Physics of Solids*, 145:104113, 2020.

[100] M. Deibler, J. Spatz, and R. Kemkemer. Actin fusion proteins alter the dynamics of mechanically induced cytoskeleton rearrangement. *PLoS ONE*, 6:e22941, 2011.

[101] M. Delarue, F. Montel, D. Vignjevic, J. Prost, J. F. Joanny, and G. Cappello. Compressive stress inhibits proliferation in tumor spheroids through a volume limitation. *Biophysical Journal*, 107(8):1821–1828, 2014.

[102] T. J. Dennerll, P. Lamoureux, R. E. Buxbaum, and S. R. Heidemann. The cytomechanics of axonal elongation and retraction. *Journal of Cell Biology*, 109(6):3073–3083, 1989.

[103] V. Deshpande, R. McMeeking, and A. Evans. A bio-chemo-mechanical model for cell contractility. *PNAS*, 103:14015–14020, 2006.

[104] V. Deshpande, R. McMeeking, and A. Evans. A model for the contractility of the cytoskeleton including the effects of stress-fibre formation and dissociation. *Proceedings of the Royal Society A*, 463:787–815, 2007.

[105] M. Destrade, M. Gilchrist, J. Murphy, B. Rashid, and G. Saccomandi. Extreme softness of brain matter in simple shear. *International Journal of Non-Linear Mechanics*, 75:54–58, 2015.

[106] S. Di Stefano, M. Carfagna, M. Knodel, K. Hashlamoun, S. Federico, and A. Grillo. Anelastic reorganisation of fibre-reinforced biological tissues. *Computing and Visualization in Science*, 20:95–109, 2019.

[107] A. DiCarlo and S. Quiligotti. Growth and balance. *Mechanics Research Communications*, 29(6):449–456, 2002.

[108] M. Dolega, G. Zurlo, M. Le Goff, M. Greda, C. Verdier, J.-F. Joanny, G. Cappello, and P. Recho. Mechanical behavior of multi-cellular spheroids under osmotic compression. *Journal of the Mechanics and Physics of Solids*, 147:104205, 2021.

[109] W. Ehlers and G. Eipper. Finite elastic deformations in liquid-saturated and empty porous solids. *Transport in Porous Media*, 34:179–191, 1999.

[110] W. Ehlers, M. M. Rehm, P. Schröder, D. Stöhr, and A. Wagner. Multiphasic modelling and computation of metastatic lung-cancer cell proliferation and atrophy in brain tissue based on experimental data. *Biomechanics and Modeling in Mechanobiology*, 21:277–315, 2022.

[111] W. Ehlers and A. Wagner. Multi-component modelling of human brain tissue: A contribution to the constitutive and computational description of deformation, flow and diffusion processes with application to the invasive drug-delivery problem. *Computer Methods in Biomechanics and Biomedical Engineering*, 18:861–879, 2015.

[112] B. Ellingson, H. Nguyen, A. Lai, R. Nechifor, O. Zaw, W. Pope, W. Yong, P. Nghiemphu, L. Liau, and T. Cloughesy. Contrast-enhancing tumor growth dynamics of preoperative, treatment-naive human glioblastoma. *Cancer*, 122:1718–1727, 2016.

[113] C. Engwer, T. Hillen, M. Knappitsch, and C. Surulescu. Glioma follow white matter tracts: A multiscale DTI-based model. *Journal of Mathematical Biology*, 71:551–582, 2015.

[114] C. Engwer, A. Hunt, and C. Surulescu. Effective equations for anisotropic glioma spread with proliferation: A multiscale approach and comparisons with previous settings. *Mathematical Medicine and Biology*, 33:435–459, 2016.

[115] C. Engwer, M. Knappitsch, and C. Surulescu. A multiscale model for glioma spread including cell-tissue interactions and proliferation. *Mathematical Biosciences and Engineering*, 13:443–460, 2016.

[116] C. Engwer and M. Wenske. Estimating the extent of glioblastoma invasion. *Journal of Mathematical Biology*, 82:10, 2021.

[117] M. Epstein. Mathematical characterization and identification of remodeling, growth, aging and morphogenesis. *Journal of the Mechanics and Physics of Solids*, 84:72–84, 2015.

[118] J. Falco, A. Agosti, I. Vetrano, A. Bizzi, F. Restelli, M. Broggi, M. Schiariti, F. DiMeco, P. Ferroli, P. Ciarletta, and F. Acerbi. In silico mathematical modelling for glioblastoma: A critical review and a patient-specific case. *Journal of Clinical Medicine*, 10:2169, 2021.

[119] A. Fan, A. Tofangchi, M. Kandel, G. Popescu, and T. Saif. Coupled circumferential and axial tension driven by actin and myosin influences in vivo axon diameter. *Scientific Reports*, 7(1), 2017.

[120] U. Faust, N. Hampe, W. Rubner, N. Kirchgessner, S. Safran, B. Hoffmann, and R. Merkel. Cyclic stress at mHz frequencies aligns fibroblasts in direction of zero strain. *PLoS ONE*, 6:e28963, 2011.

[121] A. Fedorov, R. Beichel, J. Kalpathy-Cramer, J. Finet, J.-C. Fillion-Robin, S. Pujol, C. Bauer, D. Jennings, F. Fennessy, M. Sonka, J. Buatti, S. Aylward, J. Miller, S. Pieper, and R. Kikinis. 3D Slicer as an Image Computing Platform for the Quantitative Imaging Network. *Magnetic*

Resonance Imaging, 30:1323–1341, 2012.

[122] Z. Feng, Y. Wagatsuma, M. Kikuchi, T. Kosawada, T. Nakamura, D. Sato, N. Shirasawa, T. Kitajima, and M. Umezu. The mechanisms of fibroblasts-mediated compaction of collagen gels and the mechanical niche around individual fibroblasts. *Biomaterials*, 35:8078–8091, 2014.

[123] C. Fink, S. Ergun, D. Kralisch, U. Remmers, J. Weil, and T. Eschenhagen. Chronic stretch of engineered heart tissue induces hypertrophy and functional improvement. *FASEB Journal*, 14:669–679, 2000.

[124] J. Foolen, V. Deshpande, F. Kanters, and F. Baaijens. The influence of matrix integrity on stress-fiber remodeling in 3D. *Biomaterials*, 33:7508–7518, 2012.

[125] J. Foolen, M. Janssen-van den Broek, and F. Baaijens. Synergy between Rho signaling and matrix density in cyclic stretch-induced stress fiber organization. *Acta Biomaterialia*, 10:1876–1885, 2014.

[126] H. Frieboes, J. Lowengrub, S. Wise, X. Zheng, P. Macklin, E. Bearer, and V. Cristini. Computer simulations of glioma growth and morphology. *NeuroImage*, 37:S59–S70, 2007.

[127] Y. Fung. Elasticity of soft tissues in simple elongation. *American Journal of Physiology*, 213:1532–1544, 1967.

[128] E. S. Gamburg, W. F. Regine, R. A. Patchell, J. M. Strottmann, M. Mohiuddin, and A. B. Young. The prognostic significance of midline shift at presentation on survival in patients with glioblastoma multiforme. *International Journal of Radiation Oncology, Biology, Physics*, 48(5):1359–1362, 2000.

[129] J. A. García-Grajales, A. Jérusalem, and A. Goriely. Continuum mechanical modeling of axonal growth. *Computer Methods in Applied Mechanics and Engineering*, 314:147–163, 2017.

[130] R. Gauvin, R. Parentau-Bareil, D. Larouche, H. Marcoux, F. Bisson, A. Bonnet, F. Auger, S. Bolduc, and L. Germain. Dynamic mechanical stimulations induce anisotropy and improve the tensile properties of engineered tissues produced without exogenous scaffolding. *Acta Biomaterialia*, 7:3294–3301, 2011.

[131] P. Gerlee and A. Anderson. An evolutionary hybrid cellular automaton model of solid tumour growth. *Journal of Theoretical Biology*, 246:583–603, 2007.

[132] P. Gerlee and S. Nelander. The impact of phenotypic switching on glioblastoma growth and invasion. *PLoS Computational Biology*, 8:e1002556, 2012.

[133] P. Gerlee and S. Nelander. Travelling wave analysis of a mathematical model of glioblastoma growth. *Mathematical Biosciences*, 276:75–81, 2016.

[134] G. Giantesio, A. Musesti, and D. Riccobelli. A comparison between active strain and active stress in transversely isotropic hyperelastic materials. *Journal of Elasticity*, 137(1):63–82, 2018.

[135] C. Giverso and L. Preziosi. Influence of the mechanical properties of the necrotic core on the growth and remodelling of tumour spheroids. *International Journal of Non-Linear Mechanics*, 108:20–32, 2019.

[136] C. Giverso, M. Scianna, and A. Grillo. Growing avascular tumours as elasto-plastic bodies by the theory of evolving natural configurations. *Mechanics Research Communications*, 68:31–39, 2015.

[137] A. Goldyn, P. Kaiser, J. Spatz, C. Ballestrem, and R. Kemkemer. The kinetics of force-induced cell reorganization depend on microtubules and actin. *Cytoskeleton*, 67:241–250, 2010.

[138] E. Goley and M. Welch. The ARP 2/3 complex: An actin nucleator comes of age. *Nature Reviews Molecular Cell Biology*, 7:713–726, 2006.

[139] Z. Goli-Malekabadi, M. Tafazzoli-Shadpour, M. Rabbani, and M. Janmaleki. Effect of uniaxial stretch on morphology and cytoskeleton of human mesenchymal stem cells: Static vs. dynamic loading. *Biomedizinische Technik*, 56:259–265, 2011.

[140] A. Goriely. *The Mathematics and Mechanics of Biological Growth*. Springer, 2017.

[141] A. Goriely, M. Geers, G. Holzapfel, J. Jayamohan, A. Jerusalem, S. Sivaloganathan, W. Squier, J. van Dommelen, S. Waters, and E. Kuhl. Mechanics of the brain: perspectives, challenges, and opportunities. *Biomechanics and Modeling in Mechanobiology*, 14:931–965, 2015.

[142] P. Grammenoudis, D. Reckwerth, and C. Tsakmakis. Continuum damage models based on energy equivalence: Part I - Isotropic material response. *International Journal of Damage Mechanics*, 18:31–63, 2009.

[143] A. Greiner, S. Biela, H. Chen, J. Spatz, and R. Kemkemer. Temporal responses of human endothelial and smooth muscle cells exposed to uniaxial cyclic tensile strain. *Experimental Biology and Medicine*, 240:1298–1309, 2015.

[144] A. Greiner, H. Chen, J. Spatz, and R. Kemkemer. Cyclic tensile strain controls cell shape and directs actin stress fiber formation and focal adhesion alignment in spreading cells. *PLoS ONE*, 8:e77328, 2013.

[145] A. Grillo, C. Giverso, M. Favino, M. Krause, M. Lampe, and G. Wittum. Mass transport in porous media with variable mass. In J. Delgado, A. Barbosa de Lima, and M. Vazquez da Silva, editors, *Numerical Analysis of Heat and Mass Transfer in Porous Media*. Springer, 2012.

[146] A. Grillo, G. Wittum, A. Tomic, and S. Federico. Remodelling in statistically oriented fibre-reinforced materials and biological tissues. *Mathematics and Mechanics of Solids*, 20:1107–1129, 2015.

[147] C. Guimaraes, L. Gasperini, A. Marques, and R. Reis. The stiffness of living tissues and its implications for tissue engineering. *Nature Reviews Materials*, 5:351–370, 2020.

[148] H. Guo, M. Shah, and R. Spilker. A finite element implementation for biphasic contact of hydrated porous media under finite deformation and sliding. *Proceedings of the Institution of Mechanical Engineers, Part H: Journal of Engineering in Medicine*, 228:225–236, 2014.

[149] M. Gupta, B. Sarangi, J. Deschamps, Y. Nematbakhsh, A. Callan-Jones, F. Margadant, R.-M. Mège, C. Lim, R. Voituriez, and B. Ladoux. Adaptive rheology and ordering of cell cytoskeleton govern matrix rigidity sensing. *Nature Communications*, 6:7525, 2015.

[150] M. Gurtin. *An Introduction to Continuum Mechanics*. Academic Press, 1981.

[151] M. Gurtin, E. Fried, and L. Anand. *The Mechanics and Thermodynamics of Continua*. Cambridge University Press, 2010.

[152] L. Gérémie, E. Ilker, M. Bernheim-Dennery, C. Cavaniol, J.-L. Viovy, D. Vignjevic, J.-F. Joanny, and S. Descroix. Evolution of a confluent gut epithelium under on-chip cyclic stretching. *Physical Review Research*, 4:023032, 2022.

[153] A. Harris, P. Wild, and D. Stopak. Silicone rubber substrata: A new wrinkle in the study of cell locomotion. *Science*, 208:177–179, 1980.

[154] S. Hassanizadeh. Derivation of basic equations of mass transport in porous media. Part 2. Generalized Darcy's and Fick's laws. *Advances in Water Resources*, 9:207–222, 1986.

[155] W. Haston, J. Shields, and P. Wilkinson. The orientation of fibroblasts and neutrophils on elastic substrata. *Experimental Cell Research*, 146:117–126, 1983.

[156] L. Hathout, V. Patel, and P. Wen. A 3-dimensional DTI MRI-based model of GBM growth and response to radiation therapy. *International Journal of Oncology*, 49:1081–1087, 2016.

[157] H. Hatzikirou, D. Basanta, M. Simon, K. Schaller, and A. Deutsch. Go or grow: The key to the emergence of invasion in tumour progression? *Mathematical Medicine and Biology*, 29:49–65, 2012.

[158] H. Hatzikirou, A. Deutsch, C. Schaller, M. Simon, and K. Swanson. Mathematical Modelling of Glioblastoma Tumour Development: A Review. *Mathematical Models and Methods in Applied Sciences*, 15(11):1779–1794, 2005.

[159] K. Hayakawa, A. Hosokawa, K. Yabusaki, and T. Obinata. Orientation of smooth muscle-derived A10 cells in culture by cyclic stretching: Relationship between stress fiber rearrangement and cell reorientation. *Zoological Science*, 17:617–624, 2000.

[160] K. Hayakawa, N. Sato, and T. Obinata. Dynamic reorientation of cultured cells and stress fibers under mechanical stress from periodic stretching. *Experimental Cell Research*, 268:104–114, 2001.

[161] G. Helmlinger, P. A. Netti, H. C. Lichtenbeld, R. J. Melder, and R. K. Jain. Solid stress inhibits the growth of multicellular tumor spheroids. *Nature Biotechnology*, 8(15):778–783, 1997.

[162] A. Hill. The heat of shortening and the dynamic constants of muscle. *Proceedings of the Royal Society B*, 126:136–195, 1938.

[163] C. Hogea, C. Davatzikos, and G. Biros. An image-driven parameter estimation problem for a reaction–diffusion glioma growth model with mass effects. *Journal of Mathematical Biology*, 56:793–825, 2008.

[164] M. A. Holland, K. E. Miller, and E. Kuhl. Emerging brain morphologies from axonal elongation. *Annals of Biomedical Engineering*, 43(7):1640–1653, 2015.

[165] M. Holmes and V. Mow. The nonlinear characteristics of soft gels and hydrated connective tissues in ultrafiltration. *Journal of Biomechanics*, 23:1145–1156, 1990.

[166] G. Holzapfel and T. Gasser. A viscoelastic model for fiber-reinforced composites at finite strains: Continuum basis, computational aspects and applications. *Computer Methods in Applied Mechanics and Engineering*, 190:4379–4403, 2001.

[167] G. Holzapfel, T. Gasser, and R. Ogden. A new constitutive framework for arterial wall mechanics and a comparative study of material models. *Journal of Elasticity*, 61:1–48, 2000.

[168] G. Holzapfel and R. Ogden. Constitutive modelling of passive myocardium: a structurally based framework for material characterization. *Philosophical Transactions of the Royal Society A*, 367:3445–3475, 2009.

[169] C. Horgan and G. Saccomandi. Constitutive models for compressible nonlinearly elastic materials with limiting chain extensibility. *Journal of Elasticity*, 77:123–138, 2004.

[170] G. Houtchens, M. Foster, T. Desai, E. Morgan, and J. Wong. Combined effects of microtopography and cyclic strain on vascular smooth muscle cell orientation. *Journal of Biomechanics*, 41:762–769, 2008.

[171] H.-J. Hsu, C.-F. Lee, and R. Kaunas. A dynamic stochastic model of frequency-dependent stress fiber alignment induced by cyclic stretch. *PLoS ONE*, 4:e4853, 2009.

[172] H.-J. Hsu, C.-F. Lee, A. Locke, S. Vanderzyl, and R. Kaunas. Stretch-induced stress fiber remodeling and the activations of JNK and ERK depend on mechanical strain rate, but not FAK. *PLoS ONE*, 5:e12470, 2010.

[173] J.-J. Hu, J. Humphrey, and A. Yeh. Characterization of engineered tissue development under biaxial stretch using nonlinear optical microscopy. *Tissue Engineering: Part A*, 15(7):1553–1564, 2009.

[174] S. Hu, L. Eberhard, J. Chen, J. Love, J. Butler, J. Fredberg, G. Whitesides, and N. Wang. Mechanical anisotropy of adherent cells probed by a three-dimensional magnetic twisting device. *American Journal of Physiology - Cell Physiology*, 287:C1184–C1191, 2004.

[175] C. Huang, K. Miyazaki, S. Akaishi, A. Watanabe, H. Hyakusoku, and R. Ogawa. Biological effects of cellular stretch on human dermal fibroblasts. *Journal of Plastic, Reconstructive & Aesthetic Surgery*, 66:e351–e361, 2013.

[176] A. Hunt and C. Surulescu. A multiscale modeling approach to glioma invasion with therapy. *Vietnam Journal of Mathematics*, 45:221–240, 2016.

[177] D. Q. Huynh. Metrics for 3D rotations: Comparison and analysis. *Journal of Mathematical Imaging and Vision*, 35(2):155–164, 2009.

[178] K. Iarosz, F. Borges, A. Batista, M. Baptista, R. Siqueira, R. Viana, and S. Lopes. Mathematical model of brain tumour with glia–neuron interactions and chemotherapy treatment. *Journal of Theoretical Biology*, 368:113–121, 2015.

[179] T. Iba and B. Sumpio. Morphological response of human endothelial cells subjected to cyclic strain in vitro. *Microvascular Research*, 42:245–254, 1991.

[180] D. Ingber. Mechanobiology and diseases of mechanotransduction. *Annals of Medicine*, 35:564–577, 2003.

[181] M. Itskov. A generalized orthotropic hyperelastic material model with application to incompressible shells. *International Journal for Numerical Methods in Engineering*, 50:1777–1799, 2001.

[182] C. Ives, S. Eskin, and L. McIntire. Mechanical effects on endothelial cell morphology: In vitro assessment. *In Vitro Cellular & Developmental Biology*, 22(9):500–507, 1986.

[183] M. Iwaki, S. Ito, M. Morioka, S. Iwata, Y. Numaguchi, M. Ishii, M. Kondo, H. Kume, K. Naruse, M. Sokabe, and Y. Hasegawa. Mechanical stretch enhances IL-8 production in pulmonary microvascular endothelial cells. *Biochemical and Biophysical Research Communications*, 389:531–536, 2009.

[184] H. Jacomy, G. Fragoso, G. Almazan, W. E. Mushynski, and P. J. Talbot. Human coronavirus OC43 infection induces chronic encephalitis leading to disabilities in BALB/C mice. *Virology*, 349(2):335–346, 2006.

[185] R. K. Jain, J. D. Martin, and T. Stylianopoulos. The role of mechanical forces in tumor growth and therapy. *Annual Review of Biomedical Engineering*, 16:321–346, 2014.

[186] K. Jansen, D. Donato, H. Balcioglu, T. Schmidt, E. Danen, and G. Koenderink. A guide to mechanobiology: Where biology and physics meet. *Biochimica et Biophysica Acta*, 1853:3043–3052, 2015.

[187] S. Jbabdi, E. Mandonnet, H. Duffau, L. Capelle, K. Swanson, M. Pelegrini-Issac, R. Guillevin, and H. Benali. Simulation of Anisotropic Growth of Low-Grade Gliomas Using Diffusion Tensor Imaging. *Magnetic Resonance in Medicine*, 54:616–624, 2005.

[188] B.-J. Jin, A. Smith, and A. Verkman. Spatial model of convective solute transport in brain extracellular space does not support a 'glymphatic' mechanism. *Journal of General Physiology*, 148(6):489–501, 2016.

[189] Y. Jin, L. Liu, F. Yu, X. Shi, J. Guo, B. Che, Y. Duan, J. Li, Y. Pan, M. Luo, and L. Deng. Emergent differential organization of airway smooth muscle cells on concave and convex tubular surface. *Frontiers in Molecular Biosciences*, 8:717771, 2021.

[190] S. Jungbauer, H. Gao, J. Spatz, and R. Kemkemer. Two characteristic regimes in frequency-dependent dynamic reorientation of fibroblasts on cyclically stretched substrates. *Biophysical Journal*, 95:3470–3478, 2008.

[191] M. Kalli, C. Voutouri, A. Minia, V. Pliaka, C. Fotis, L. G. Alexopoulos, and T. Stylianopoulos. Mechanical Compression Regulates Brain Cancer Cell Migration Through MEK1/Erk1 Pathway Activation and GDF15 Expression. *Frontiers in Oncology*, 9:992, 2019.

[192] K. Kanda and T. Matsuda. Behavior of arterial wall cells cultured on periodically stretched substrates. *Cell Transplantation*, 2:475–484, 1993.

[193] K. Kanda and T. Matsuda. Mechanical stress-induced orientation and ultrastructural change of smooth muscle cells cultured in three-dimensional collagen lattices. *Cell Transplantation*, 3(6):481–492, 1994.

[194] A. Kansal, S. Torquato, G. Harsh IV, E. Chiocca, and T. Deisboeck. Simulated Brain Tumor Growth Dynamics Using a Three-Dimensional Cellular Automaton. *Journal of Theoretical Biology*, 203:367–382, 2000.

[195] S. Katzman, A. Barrera, R. Higgins, J. Talley, and J. Hurst-Kennedy. Fundamentals of Cell Biology. University System of Georgia, 2019. https://alg.manifoldapp.org/projects/fundamentals-of-cell-biology.

[196] R. Kaunas and H.-J. Hsu. A kinematic model of stretch-induced stress fiber turnover and reorientation. *Journal of Theoretical Biology*, 257:320–330, 2009.

[197] R. Kaunas, H.-J. Hsu, and S. Deguchi. Sarcomeric model of stretch-induced stress fiber reorganization. *Cell Health and Cytoskeleton*, 3:13–22, 2011.

[198] R. Kaunas, P. Nguyen, S. Usami, and S. Chien. Cooperative effects of Rho and mechanical stretch on stress fiber organization. *PNAS*, 102(44):15895–15900, 2005.

[199] R. Kaunas, S. Usami, and S. Chien. Regulation of stretch-induced JNK activation by stress fiber orientation. *Cellular Signaling*, 18:1924–1931, 2006.

[200] E. Khain, M. Katakowski, S. Hopkins, A. Szalad, X. Zheng, F. Jiang, and M. Chopp. Collective behavior of brain tumor cells: The role of hypoxia. *Physical Review E*, 83:031920, 2011.

[201] B.-S. Kim, J. Nikolovski, J. Bonadio, and D. Mooney. Cyclic mechanical strain regulates the development of engineered smooth muscle tissue. *Nature Biotechnology*, 17:979–983, 1999.

[202] Y. Kim, K. Hang, G. Powathil, H. Kim, D. Trucu, W. Lee, S. Lawler, and M. Chaplain. Role of extracellular matrix and microenvironment in regulation of tumor growth and LAR-mediated invasion in glioblastoma. *PLoS ONE*, 13:e0204865, 2018.

[203] Y. Kim, G. Powathil, H. Kang, D. Trucu, H. Kim, S. Lawler, and M. Chaplain. Strategies of eradicating glioma cells: A multi-scale mathematical model with miR451-AMPK-mTOR Control. *PLoS ONE*, 10:e0114370, 2015.

[204] V. Kondaurov and L. Nikitin. Finite strains of viscoelastic muscle tissue. *Journal of Applied Mathematics and Mechanics*, 51(3):346–353, 1987.

[205] D. Kong, B. Ji, and L. Dai. Stability of adhesion clusters and cell reorientation under lateral cyclic tension. *Biophysical Journal*, 95:4034–4044, 2008.

[206] F. Kong, A. Garcia, A. Mould, M. Humphries, and C. Zhu. Demonstration of catch bonds between an integrin and its ligand. *Journal of Cell Biology*, 185:1275–1284, 2009.

[207] T. Kreis, B. Geiger, and J. Schlessinger. Mobility of micro-injected rhodamine actin within living chicken gizzard cells determined by fluorescence photobleaching recovery. *Cell*, 29:835–845, 1982.

[208] E. Kröner. Allgemeine Kontinuumstheorie der Versetzungen und Eigenspannungen. *Archive for Rational Mechanics and Analysis*, 4:273–334, 1959.

[209] S. Kumar, I. Maxwell, A. Heisterkamp, T. Polte, T. Lele, M. Salanga, E. Mazur, and D. Ingber. Viscoelastic retraction of single living stress fibers and its impact on cell shape, cytoskeletal

organization, and extracellular matrix mechanics. *Biophysical Journal*, 90:3762–3773, 2006.

[210] K. Kurpinski, J. Chu, C. Hashi, and S. Li. Anisotropic mechanosensing by mesenchymal stem cells. *PNAS*, 103(44):16095–16100, 2006.

[211] S. Kyriacou, C. Davatzikos, S. Zinreich, and R. Bryan. Nonlinear elastic registration of brain images with tumor pathology using a biomechanical model. *IEEE Transactions on Medical Imaging*, 18:580–592, 1999.

[212] G. E. Lang, S. L. Waters, D. Vella, and A. Goriely. Axonal buckling following stretch injury. *Journal of Elasticity*, 129(1):239–256, 2017.

[213] K. Lazopoulos and A. Pirentis. Substrate stretching and reorganization of stress fibers as a finite elasticity problem. *International Journal of Solids and Structures*, 44:8285–8296, 2007.

[214] K. Lazopoulos and D. Stamenovic. A mathematical model of cell reorientation in response to substrate stretching. *MCB*, 3:43–48, 2006.

[215] C.-F. Lee, C. Haase, S. Deguchi, and R. Kaunas. Cyclic stretch-induced stress fiber dynamics – Dependence on strain rate, Rho-kinase and MLCK. *Biochemical and Biophysical Research Communications*, 401:344–349, 2010.

[216] E. Lee. Elastic-plastic deformation at finite strains. *Journal of Applied Mechanics*, 36:1–6, 1969.

[217] E. Lee, J. Holmes, and K. Costa. Remodeling of engineered tissue anisotropy in response to altered loading conditions. *Annals of Biomedical Engineering*, 36(8):1322–1334, 2008.

[218] P. Letourneau. Actin in axons: Stable scaffolds and dynamic filaments. In E. Koenig, editor, *Cell Biology of the Axon*. Springer Berlin Heidelberg, 2009.

[219] Z. Li, H. Lee, and C. Zhu. Molecular mechanisms of mechanotransduction in integrin-mediated cell-matrix adhesion. *Experimental Cell Research*, 349:85–94, 2016.

[220] J. Lin, X. Li, J. Yin, and J. Qian. Effect of cyclic stretch on neuron reorientation and axon outgrowth. *Frontiers in Bioengineering and Biotechnology*, 8:597867, 2020.

[221] J. Lipkova, B. Menze, B. Wiestler, P. Koumoutsakos, and J. Lowengrub. Modelling glioma progression, mass effect and intracranial pressure in patient anatomy. *Journal of the Royal Society Interface*, 19:20210922, 2022.

[222] B. Liu, M.-J. Qu, K.-R. Qin, H. Li, Z.-K. Li, B.-R. Shen, and Z.-L. Jiang. Role of cyclic strain frequency in regulating the alignment of vascular smooth muscle cells in vitro. *Biophysical Journal*, 94:1497–1507, 2008.

[223] C. Liu, S. Baek, J. Kim, E. Vasko, R. Pyne, and C. Chan. Effect of static pre-stretch induced surface anisotropy on orientation of mesenchymal stem cells. *Cellular and Molecular Bioengineering*, 7(1):106–121, 2014.

[224] H. Liu, G. A. Holzapfel, B. H. Skallerud, and V. Prot. Anisotropic finite strain viscoelasticity: Constitutive modeling and finite element implementation. *Journal of the Mechanics and Physics of Solids*, 124:172–188, 2019.

[225] I.-S. Liu. On representations of anisotropic invariants. *International Journal of Engineering Science*, 20(10):1099 – 1109, 1982.

[226] A. Livne, E. Bouchbinder, and B. Geiger. Cell reorientation under cyclic stretching. *Nature Communications*, 5:3938, 2014.

[227] W. Loesberg, X. Walboomers, J. van Loon, and J. Jansen. The effect of combined cyclic mechanical stretching and microgrooved surface topography on the behaviour of fibroblasts. *Journal of Biomedical Materials Research - Part A*, 75(3):723–732, 2005.

[228] A. Logg, K.-A. Mardal, G. Wells, et al. *Automated Solution of Differential Equations by the Finite Element Method*. Springer, 2012.

[229] N. Loy and L. Preziosi. A Statistical Mechanics approach to describe cell re-orientation under stretch. *arXiv Preprint*, https://arxiv.org/abs/2108.00894, 2021.

[230] L. Lu, Y. Feng, W. Hucker, S. Oswald, G. Longmore, and F.-P. Yin. Actin stress fiber pre-extension in human aortic endothelial cells. *Cytoskeleton*, 65:281–294, 2008.

[231] L. Lu, S. Oswald, H. Ngu, and F.-P. Yin. Mechanical properties of actin stress fibers in living cells. *Biophysical Journal*, 95:6060–6071, 2008.

[232] A. Lucantonio, P. Nardinocchi, and L. Teresi. Transient analysis of swelling-induced large deformations in polymer gels. *Journal of the Mechanics and Physics of Solids*, 61:205–218, 2013.

[233] G. Lucci, A. Agosti, P. Ciarletta, and C. Giverso. Coupling solid and fluid stresses with brain tumour growth and white matter tract deformations in a neuroimaging-informed model. *Biomechanics and Modeling in Mechanobiology*, 21:1483–1509, 2022.

[234] G. Lucci and L. Preziosi. A nonlinear elastic description of cell preferential orientations over a stretched substrate. *Biomechanics and Modeling in Mechanobiology*, 20:631–649, 2021.

[235] J. Mandel. Thermodynamics and plasticity. In J. J. Delgado Domingos, M. N. R. Nina, and J. H. Whitelaw, editors, *Foundations of Continuum Thermodynamics*, chapter 15, pages 283–304. Macmillan Education UK, 1973.

[236] Y. Mansury and T. Deisboeck. The impact of "search precision" in an agent-based tumor model. *Journal of Theoretical Biology*, 224:325–337, 2003.

[237] Y. Mansury and T. Deisboeck. Modelling tumours as complex biosystems: An agent-based approach. In J. Kresh and T. Deisboeck, editors, *Complex Systems Science: The Emergence of a New Approach in Biomedicine*. Kluwer, 2004.

[238] Y. Mansury, M. Kimura, J. Lobo, and T. Deisboeck. Emerging Patterns in Tumor Systems: Simulating the Dynamics of Multicellular Clusters with an Agent-based Spatial Agglomeration Model. *Journal of Theoretical Biology*, 219:343–370, 2002.

[239] T. Mao, Y. He, Y. Gu, Y. Yang, Y. Yu, X. Wang, and J. Ding. Critical frequency and critical stretching rate for reorientation of cells on a cyclically stretched polymer in a microfluidic chip. *AMS Applied Materials & Interfaces*, 13:13934–13948, 2021.

[240] N. Martyrosian, E. Rutter, W. Ramey, E. Kostelich, Y. Kuang, and M. Preul. Mathematically modeling the biological properties of gliomas: A review. *Mathematical Biosciences and Engineering*, 12:879–905, 2015.

[241] P. Mascheroni, M. Carfagna, A. Grillo, D. Boso, and B. Schrefler. An avascular tumor growth model based on porous media mechanics and evolving natural states. *Mathematics and Mechanics of Solids*, 23:686–712, 2018.

[242] P. Mascheroni, S. Stigliano, M. Carfagna, D. Boso, L. Preziosi, P. Decuzzi, and B. Schrefler. Predicting the growth of glioblastoma multiforme spheroids using a multiphase porous media model. *Biomechanics and Modeling in Mechanobiology*, 15:1215–1228, 2016.

[243] J. Mason, D. Ramseth, D. Chanter, T. Moon, D. Goodman, and B. Mendzelevski. Electrocardiographic reference ranges derived from 79,743 ambulatory subjects. *Journal of Electrocardiology*, 40:228–234, 2007.

[244] L. Matheson, N. Fairbank, G. Maksym, J. Santerre, and R. Labow. Characterization of the Flexcell™ Uniflex™ cyclic strain culture system with U937 macrophage-like cells. *Biomaterials*, 27:226–233, 2006.

[245] A. Mathur, W. Reichert, and G. Truskey. Flow and high affinity binding affect the elastic modulus of the nucleus, cell body and the stress fibers of endothelial cells. *Annals of*

Biomedical Engineering, 35:1120–1130, 2007.

[246] A. Matsugaki, N. Fujiwara, and T. Nakano. Continuous cyclic stretch induces osteoblast alignment and formation of anisotropic collagen fiber matrix. *Acta Biomaterialia*, 9:7227–7235, 2013.

[247] T. Matsumoto, P. Delafontaine, K. Schnetzer, B. Tong, and R. Nerem. Effect of uniaxial cyclic stretch on the morphology of monocytes/macrophages in culture. *Journal of Biomechanical Engineering*, 118:420–422, 1996.

[248] T. Matsumoto, J.-I. Sasaki, E. Alsberg, H. Egusa, H. Yatani, and T. Sohmura. Three-dimensional cell and tissue patterning in a strained fibrin gel system. *PLoS One*, 2:e1211, 2007.

[249] E. McEvoy, V. Deshpande, and P. McGarry. Transient active force generation and stress fibre remodelling in cells under cyclic loading. *Biomechanics and Modeling in Mechanobiology*, 18:921–937, 2019.

[250] A. Menzel. A fibre reorientation model for orthotropic multiplicative growth. *Biomechanics and Modeling in Mechanobiology*, 6:303–320, 2007.

[251] J. Merodio and R. Ogden. Material instabilities in fiber-reinforced nonlinearly elastic solids under plane deformation. *Archives of Mechanics*, 54:525–552, 2002.

[252] L. Mihai, S. Budday, G. Holzapfel, E. Kuhl, and A. Goriely. A family of hyperelastic models for human brain tissue. *Journal of the Mechanics and Physics of Solids*, 106:60–79, 2017.

[253] K. Miller, K. Chinzei, G. Orssengo, and P. Bednarz. Mechanical properties of brain tissue in-vivo: experiment and computer simulation. *Journal of Biomechanics*, 33:1369–1376, 2000.

[254] Y. Miroshnikova, J. Mouw, J. Barnes, M. Pickup, J. Lakins, Y. Kim, K. Lobo, A. Persson, G. Reis, T. McKnight, E. Holland, J. Phillips, and V. Weaver. Tissue mechanics promote iDH1-dependent HIF1α-tenascin C feedback to regulate glioblastoma aggression. *Nature Cell Biology*, 18:1336–1346, 2016.

[255] F. Montel, M. Delarue, J. Elgeti, D. Vignjevic, G. Cappello, and J. Prost. Isotropic stress reduces cell proliferation in tumor spheroids. *New Journal of Physics*, 14(5):055008, 2012.

[256] M. Moretti, A. Prina-Mello, A. Reid, V. Barron, and P. Prendergast. Endothelial cell alignment on cyclically-stretched silicone surfaces. *Journal of Materials Science: Materials in Medicine*, 15:1159–1164, 2004.

[257] A. Moriel, A. Livne, and E. Bouchbinder. Cellular orientational fluctuations, rotational diffusion and nematic order under periodic driving. *Soft Matter*, 18:7091–7102, 2022.

[258] M. Morioka, H. Parameswaran, K. Naruse, M. Kondo, M. Sokabe, Y. Hasegawa, B. Suki, and S. Ito. Microtubule dynamics regulate cyclic stretch-induced cell alignment in human airway smooth muscle cells. *PLoS One*, 6:e26384, 2011.

[259] Y. Morita, S. Watanabe, Y. Ju, and S. Yamamoto. In vitro experimental study for the determination of cellular axial strain threshold and preferential axial strain from cell orientation behavior in a non-uniform deformation field. *Cell Biochemistry and Biophysics*, 67:1249–1259, 2013.

[260] C. T. Motz, V. Kabat, T. Saxena, R. V. Bellamkonda, and C. Zhu. Neuromechanobiology: An expanding field driven by the force of greater focus. *Advanced Healthcare Materials*, 19(10):e2100102, 2021.

[261] V. Mow, S. Kuei, W. Lai, and C. Armstrong. Biphasic creep and stress relaxation of articular cartilage in compression: Theory and experiments. *Journal of Biomechanical Engineering*, 102:73–84, 1980.

[262] M. C. Murphy, J. Huston 3rd, and R. L. Ehman. MR elastography of the brain and its application in neurological diseases. *Neuroimage*, 187:176–183, 2019.

[263] S. Na, G. Meininger, and J. Humphrey. A theoretical model for F-actin remodeling in vascular smooth muscle cells subjected to cyclic stretch. *Journal of Theoretical Biology*, 246:87–99, 2007.

[264] K. Nagayama, Y. Kimura, N. Makino, and T. Matsumoto. Strain waveform dependence of stress fiber reorientation in cyclically stretched osteoblastic cells: effects of viscoelastic compression of stress fibers. *American Journal of Physiology - Cell Physiology*, 302:C1469–C1478, 2012.

[265] P. Nardinocchi and L. Teresi. On the active response of soft living tissues. *Journal of Elasticity*, 88(1):27–39, 2007.

[266] C. Neidlinger-Wilke, E. Grood, L. Claes, and R. Brand. Fibroblast orientation to stretch begins within three hours. *Journal of Orthopaedic Research*, 20:953–956, 2002.

[267] C. Neidlinger-Wilke, E. Grood, J. H.-C. Wang, R. Brand, and L. Claes. Cell alignment is induced by cyclic changes in cell length: studies of cells grown in cyclically stretched substrates. *Journal of Orthopaedic Research*, 19:286–293, 2001.

[268] H. Ngu, Y. Feng, L. Lu, S. Oswald, G. Longmore, and F. C.-P. Yin. Effect of focal adhesion proteins on endothelial cell adhesion, motility and orientation response to cyclic strain. *Annals of Biomedical Engineering*, 38:208–222, 2010.

[269] H. Nia, H. Liu, G. Seano, M. Datta, D. Jones, N. Rahbari, J. Incio, V. Chauhan, K. Jung, J. Martin, V. Askoxylakis, T. Padera, D. Fukumura, Y. Boucher, F. Hornicek, A. Grodzinsky, J. Baish, L. Munn, and R. Jain. Solid stress and elastic energy as measures of tumour mechanopathology. *Nature Biomedical Engineering*, 1:0004, 2017.

[270] V. Niediek, S. Born, N. Hampe, N. Kirchgeßner, R. Merkel, and B. Hoffmann. Cyclic stretch induces reorientation of cells in a src family kinase- and p130Cas-dependent manner. *European Journal of Cell Biology*, 91:118–128, 2012.

[271] A. Nieponice, T. Maul, J. Cumer, L. Soletti, and D. Vorp. Mechanical stimulation induces morphological and phenotypic changes in bone marrow-derived progenitor cells within a three-dimensional fibrin matrix. *Journal of Biomedical Materials Research - Part A*, 81(3):523–530, 2007.

[272] I. Nikić, D. Merkler, C. Sorbara, M. Brinkoetter, M. Kreutzfeldt, F. M. Bareyre, W. Brück, D. Bishop, T. Misgeld, and M. Kerschensteiner. A reversible form of axon damage in experimental autoimmune encephalomyelitis and multiple sclerosis. *Nature Medicine*, 17(4):495–499, 2011.

[273] D. Nolan, A. Gower, M. Destrade, R. Ogden, and J. McGarry. A robust anisotropic hyperelastic formulation for the modelling of soft tissue. *Journal of the Mechanical Behavior of Biomedical Materials*, 39:48–60, 2014.

[274] C. Obbink-Huizer, C. Oomens, S. Loerakker, J. Foolen, C. Bouten, and F. Baaijens. Computational model predicts cell orientation in response to a range of mechanical stimuli. *Biomechanics and Modeling in Mechanobiology*, 13:227–236, 2014.

[275] R. Ogden. Large deformation isotropic elasticity - On the correlation of theory and experiment for incompressible rubberlike solids. *Proceedings of the Royal Society of London A*, 326:565–584, 1972.

[276] R. Ogden. Nonlinear elasticity, anisotropy, material stability and residual stresses in soft tissue. In G. Holzapfel and R. Ogden, editors, *Biomechanics of Soft Tissue in Cardiovascular Systems*, pages 65–108. Springer, 2003.

[277] H. Oliveri and A. Goriely. Mathematical models of neuronal growth. *Biomechanics and Modeling in Mechanobiology*, (21):89–118, 2022.

[278] T. Olsson and A. Klarbring. Residual stresses in soft tissue as a consequence of growth and remodeling: application to an arterial geometry. *European Journal of Mechanics - A/Solids*, 27:959–974, 2008.

[279] H. Ouyang, E. Nauman, and R. Shi. Contribution of cytoskeletal elements to the axonal mechanical properties. *Journal of Biological Engineering*, 7(1), 2013.

[280] T. P. Padera, B. R. Stoll, J. B. Tooredman, D. Capen, E. di Tomaso, and R. K. Jain. Cancer cells compress intratumour vessels. *Nature*, 427(6976):695–695, 2004.

[281] K. Painter and T. Hillen. Mathematical modelling of glioma growth: The use of Diffusion Tensor Imaging (DTI) data to predict the anisotropic pathways of cancer invasion. *Journal of Theoretical Biology*, 323:25–39, 2013.

[282] A. Palamidessi, E. Frittoli, N. Ducano, N. Offenhauser, S. Sigismund, H. Kajiho, D. Parazzoli, A. Oldani, M. Gobbi, G. Serini, P. Di Fiore, G. Scita, and L. Lanzetti. The GTPase-activating protein RN-3 controls focal adhesion turnover and cell migration. *Current Biology*, 23:2355–2364, 2013.

[283] S. Park, I. Kim, Y. Lee, J. Shin, C.-R. Kim, J. Kim, Y.-I. Yang, and J.-W. Shin. Biological responses of ligament fibroblasts and gene expression profiling on micropatterned silicone substrates subjected to mechanical stimuli. *Journal of Bioscience and Bioengineering*, 102(5):402–412, 2006.

[284] A. Pasapera, I. Schneider, E. Rericha, D. Schlaepfer, and C. Waterman. Myosin II activity regulates vinculin recruitment to focal adhesions through FAK-mediated paxillin phosphorylation. *Journal of Cell Biology*, 188:877–890, 2010.

[285] P. Pedersen. On optimal orientation of orthotropic materials. *Structural Optimization*, 1:101–106, 1989.

[286] P. Pedersen. Bounds on elastic energy in solids of orthotropic materials. *Structural Optimization*, 2:55–63, 1990.

[287] H. Pettermann, C. Cheyrou, and A. DeSimone. Modeling and simulation of anisotropic linear viscoelasticity. *Mechanics of Time-Dependent Materials*, 25:679–689, 2020.

[288] H. Pettermann and A. DeSimone. An anisotropic linear thermo-viscoelastic constitutive law. *Mechanics of Time-Dependent Materials*, 22:877–890, 2018.

[289] S. Pezzuto, D. Ambrosi, and A. Quarteroni. An orthotropic active–strain model for the myocardium mechanics and its numerical approximation. *European Journal of Mechanics - A/Solids*, 48:83–96, 2014.

[290] A. Pirentis, E. Peruski, A. Iordan, and D. Stamenovic. A model for stress fiber realignment caused by cytoskeletal fluidization during cyclic stretching. *Cellular and Molecular Bioengineering*, 4:67–80, 2011.

[291] P. Podio-Guidugli. *Continuum Thermodynamics*. Springer, 2019.

[292] T. Prevost, A. Balakrishnan, S. Suresh, and S. Socrate. Biomechanics of brain tissue. *Acta Biomaterialia*, 7:83–95, 2011.

[293] L. Preziosi and G. Vitale. A multiphase model of tumour and tissue growth including cell adhesion and plastic re-organisation. *Mathematical Models and Methods in the Applied Sciences*, 21:1901–1932, 2011.

[294] L. Prodanov, J. te Riet, E. Lamers, M. Domanski, R. Luttge, J. van Loon, J. Jansen, and X. Walboomers. The interaction between nanoscale surface features and mechanical loading and its effect on osteoblast-like cells behavior. *Biomaterials*, 31:7758–7765, 2010.

[295] J. Qian, H. Liu, Y. Lin, W. Chen, and H. Gao. A mechanochemical model of cell reorientation on substrates under cyclic stretch. *PLoS ONE*, 8:e65864, 2013.

[296] B. Rashid, M. Destrade, and M. Gilchrist. Mechanical characterization of brain tissue in compression at dynamic strain rates. *Journal of the Mechanical Behavior of Biomedical Materials*, 10:23–38, 2012.

[297] B. Rashid, M. Destrade, and M. Gilchrist. Mechanical characterization of brain tissue in simple shear at dynamic strain rates. *Journal of the Mechanical Behavior of Biomedical Materials*, 28:71–85, 2013.

[298] B. Rashid, M. Destrade, and M. Gilchrist. Mechanical characterization of brain tissue in tension at dynamic strain rates. *Journal of the Mechanical Behavior of Biomedical Materials*, 33:43–54, 2014.

[299] N. Reynolds, E. McEvoy, J. Panadero Perez, R. Coleman, and J. McGarry. Influence of multi-axial dynamic constraint on cell alignment and contractility in engineered tissues. *Journal of the Mechanical Behavior of Biomedical Materials*, 1112:104024, 2020.

[300] J. Rhodin. Fine structure of vascular walls in mammals, with special reference to smooth muscle component. *Physiological Reviews*, 42:48–81, 1962.

[301] D. Riccobelli. Active elasticity drives the formation of periodic beading in damaged axons. *Physical Review E*, 104(2), 2021.

[302] D. Riccobelli and D. Ambrosi. Activation of a muscle as a mapping of stress–strain curves. *Extreme Mechanics Letters*, 28:37–42, 2019.

[303] B. Rihel, J.-H. Park, I. Kwon, and J. Lim. Mechanical Stretching for Tissue Engineering: Two-Dimensional and Three-Dimensional Constructs. *Tissue Engineering Part B: Reviews*, 18:288–300, 2012.

[304] T. Ristori, A. Vigliotti, F. Baaijens, S. Loerakker, and V. Deshpande. Prediction of cell alignment on cyclically strained grooved substrates. *Biophysical Journal*, 111:2274–2285, 2016.

[305] A. Ritchie, S. Wijaya, W. Ong, S. Zhong, and K. Chian. Dependence of alignment direction on magnitude of strain in esophageal smooth muscle cells. *Biotechnology and Bioengineering*, 102(6):1703–1711, 2009.

[306] R. Rockne, E. Alvord Jr., J. Rockhill, and K. Swanson. A mathematical model for brain tumor response to radiation therapy. *Journal of Mathematical Biology*, 58:561–578, 2009.

[307] E. Rodriguez, A. Hoger, and A. McCulloch. Stress-dependent finite growth in soft elastic tissues. *Journal of Biomechanics*, 27:455–467, 1994.

[308] A. Roshanzadeh, T. Nguyen, K. Nguyen, D.-S. Kim, B.-K. Lee, D.-W. Lee, and E.-S. Kim. Mechanoadaptive organization of stress fiber subtypes in epithelial cells under cyclic stretches and stretch release. *Scientific Reports*, 10:18684, 2020.

[309] C. Rotsch and M. Radmacher. Drug-induced changes of cytoskeletal structure and mechanics in fibroblasts: An atomic force microscopy study. *Biophysical Journal*, 78(1):520–535, 2000.

[310] I. Rouiller, X.-P. Xu, K. Amann, C. Egile, S. Nickell, D. Nicastro, R. Li, T. Pollard, N. Volkmann, and D. Hanein. The structural basis of actin filament branching by the Arp2/3 complex. *Journal of Cell Biology*, 180:887–895, 2008.

[311] M. Rubbens, A. Driessen-Mol, R. Boerboom, M. Koppert, H. van Assen, B. TerHaar Romeny, F. Baaijens, and C. Bouten. Quantification of the temporal evolution of collagen orientation in mechanically conditioned engineering cardiovascular tissues. *Annals of Biomedical Engineering*, 37(7):1263–1272, 2009.

[312] A. Ruszczynski. *Nonlinear Optimization*. Princeton University Press, 2006.

[313] G. Saccomandi and M. Vianello. A universal relation characterizing transversely hemitropic hyperelastic materials. *Mathematics and Mechanics of Solids*, 2:181–188, 1997.

[314] S. Safran and R. De. Nonlinear dynamics of cell orientation. *Physical Review E*, 80:060901 (R), 2009.

[315] L. Sander and T. Deisboeck. Growth patterns of microscopic brain tumours. *Physical Review E*, 66:051901, 2002.

[316] U. Schwarz and S. Safran. Elastic interactions of cells. *Physical Review Letters*, 88:048102, 2002.

[317] G. Seano, H. T. Nia, K. E. Emblem, M. Datta, J. Ren, S. Krishnan, J. Kloepper, M. C. Pinho, W. W. Ho, M. Ghosh, V. Askoxylakis, G. B. Ferraro, L. Riedemann, E. R. Gerstner, T. T. Batchelor, P. Y. Wen, N. U. Lin, A. J. Grodzinsky, D. Fukumura, P. Huang, J. W. Baish, T. P. Padera, L. L. Munn, and R. K. Jain. Solid stress in brain tumours causes neuronal loss and neurological dysfunction and can be reversed by lithium. *Nature Biomedical Engineering*, 3(3):230–245, 2019.

[318] Servier. Servier Medical Art, Licensed under a Creative Commons Attribution 3.0 Unported License (https://creativecommons.org/licenses/by/3.0/).

[319] C. Sgarra and M. Vianello. Rotations which make strain and stress coaxial. *Journal of Elasticity*, 47:217–224, 1997.

[320] V. Shirinsky, A. Antonov, K. Birukov, A. Sobolevsky, Y. Romanov, N. Kabaeva, G. Antonova, and V. Smirnov. Mechano-chemical control of human endothelium orientation and size. *J. Cell Biol.*, 109:331–339, 1989.

[321] S. Shishvan, A. Vigliotti, and V. Deshpande. The homeostatic ensemble for cells. *Biomechanics and Modeling in Mechanobiology*, 17:1631–1662, 2018.

[322] H. Si. TetGen, a Delaunay-Based Quality Tetrahedral Mesh Generator. *ACM Transactions on Mathematical Software*, 41(2), 2015.

[323] R. Skalak. Growth as a finite displacement field. In D. Carlson and R. Shield, editors, *Proceedings of the IUTAM Symposium on Finite Elasticity*, pages 347–355, Dordrecht, 1981. Springer.

[324] J. Smith and J. Humphrey. Interstitial transport and transvascular fluid exchange during infusion into brain and tumor tissue. *Microvascular Research*, 73:58–73, 2007.

[325] P. Smith, L. Deng, J. Fredberg, and G. Maksym. Mechanical strain increases cell stiffness through cytoskeletal filament reorganization. *American Journal of Physiology - Lung Cellular and Molecular Physiology*, 285:L456–L463, 2003.

[326] V. Sottiurai, P. Kollros, S. Glagov, C. Zarins, and M. Mathews. Morphologic alterarion of cultured arterial smooth muscle cells by cyclic stretching. *Journal of Surgical Research*, 35:490–497, 1983.

[327] A. J. M. Spencer. Constitutive theory for strongly anisotropic solids. In A. J. M. Spencer, editor, *Continuum theory of the mechanics of fibre-reinforced composites*, pages 1–32. Springer, Wien, Austria, 1984.

[328] J. Stålhand, A. Klarbring, and G. Holzapfel. A mechanochemical 3D continuum model for smooth muscle contraction under finite strains. *Journal of Theoretical Biology*, 268(1):120–130, 2011.

[329] D. Stamenovic, K. Lazopoulos, A. Pirentis, and B. Suki. Mechanical stability determines stress fiber and focal adhesion orientation. *Cellular and Molecular Bioengineering*, 2:475–485, 2009.

[330] P. Standley, A. Camaratta, B. Nolan, C. Purgason, and M. Stanley. Cyclic stretch induces vascular smooth muscle cell alignment via NO signaling. *American Journal of Physiology -*

Heart and Circulatory Physiology, 283:H1907–H1914, 2002.

[331] T. Steed, J. Treiber, M. Brandel, K. Patel, A. Dale, B. Carter, and C. Chen. Quantification of glioblastoma mass effect by lateral ventricle displacement. *Scientific Reports*, 8:2827, 2018.

[332] A. Stensjøen, O. Solheim, K. Kvistad, A. Haberg, O. Salvesen, and E. Berntsen. Growth dynamics of untreated glioblastomas in vivo. *Neuro-Oncology*, 17(10):1402–1411, 2015.

[333] D. Stewart, A. Rubiano, K. Dyson, and C. Simmons. Mechanical characterization of human brain tumors from patients and comparison to potential surgical phantoms. *PLoS ONE*, 12:e0177561, 2017.

[334] G. B. Stokin, C. Lillo, T. L. Falzone, R. G. Brusch, E. Rockenstein, S. L. Mount, R. Raman, P. Davies, E. Masliah, D. S. Williams, et al. Axonopathy and transport deficits early in the pathogenesis of Alzheimer's disease. *Science*, 2005.

[335] T. Stylianopoulos, J. Martin, M. Snuderl, F. Mperkis, S. Jain, and R. Jain. Coevolution of solid stress and interstitial fluid pressure in tumors during progression: Implications for vascular collapse. *Cancer Research*, 73:3833–3841, 2013.

[336] B. Sumpio and A. Banes. Response of porcine aortic smooth muscle cells to cyclic tensional deformation in culture. *Journal of Surgical Research*, 44:696–701, 1988.

[337] B. Sumpio, A. Banes, W. Link, and G. Johnson. Enhanced collagen production by smooth muscle cells during repetitive mechanical stretching. *Archives of Surgery*, 123:1233–1236, 1988.

[338] S. Suveges, K. Hossain-Ibrahim, J. Steele, R. Eftimie, and D. Trucu. Mathematical modelling of glioblastomas invasion within the brain: A 3D multi-scale moving-boundary approach. *Mathematics*, 9:2214, 2021.

[339] S. Svensson, E. Fuster-Garcia, A. Latysheva, J. Fraser-Green, W. Nordhøy, O. Darwish, I. Hovden, S. Holm, E. Vik-Mo, R. Sinkus, and K. Emblem. Decreased tissue stiffness in glioblastoma by MR elastography is associated with increased cerebral blood flow. *European Journal of Radiology*, 147:110136, 2022.

[340] A. Swan, T. Hillen, J. Bowman, and A. Murtha. A patient-specific anisotropic diffusion model for brain tumour spread. *Bulletin of Mathematical Biology*, 80:1259–1291, 2018.

[341] K. Swanson, E. Alvord Jr., and J. Murray. A quantitative model for differential motility of gliomas in grey and white matter. *Cell Proliferation*, 33:317–329, 2000.

[342] K. Swanson, E. Alvord Jr., and J. Murray. Quantifying efficiency of chemotherapy of brain tumors with homogeneous and heterogeneous drug delivery. *Acta Biotheoretica*, 50:223–237, 2002.

[343] K. Swanson, E. Alvord Jr., and J. Murray. Virtual brain tumours (gliomas) enhance the reality of medical imaging and highlight inadequacies of current therapy. *British Journal of Cancer*, 86:14–18, 2002.

[344] K. Swanson, E. Alvord Jr., and J. Murray. Virtual resection of gliomas: effect of extent of resection on recurrence. *Mathematical and Computer Modelling*, 37:1177–1190, 2003.

[345] K. Swanson, C. Bridge, J. Murray, and E. Alvord Jr. Virtual and real brain tumors: using mathematical modeling to quantify glioma growth and invasion. *Journal of the Neurological Sciences*, 216:1–10, 2003.

[346] K. Swanson, H. Harpold, D. Peacock, R. Rockne, C. Pennington, L. Kilbride, R. Grant, J. Wardlaw, and E. Alvord Jr. Velocity of radial expansion of contrast-enhancing gliomas and the effectiveness of radiotherapy in individual patients: a proof of principle. *Clinical Oncology*, 20:301–308, 2008.

[347] K. Swanson, R. Rockne, J. Claridge, M. Chaplain, E. Alvord Jr., and A. Anderson. Quantifying the role of angiogenesis in malignant progression of gliomas: In silico modeling

integrates imaging and histology. *Cancer Research*, 71:7366–7375, 2011.

[348] L. A. Taber and R. Perucchio. Modeling heart development. *Journal of Elasticity and the Physical Science of Solids*, 61(1):165–197, 2000.

[349] P. Tagliaferro and R. E. Burke. Retrograde axonal degeneration in Parkinson disease. *Journal of Parkinson's disease*, 6(1):1–15, 2016.

[350] A. Takayama, T. Nagamine, and K. Kotani. Aging is independently associated with an increasing normal respiratory rate among an older adult population in a clinical setting: A cross-sectional study. *Geriatrics & Gerontology International*, 19:1179–1183, 2019.

[351] T. Takemasa, K. Sugimoto, and K. Yamashita. Amplitude-dependent stress fiber reorientation in early response to cyclic strain. *Experimental Cell Research*, 230:407–410, 1997.

[352] T. Takemasa, T. Yamaguchi, Y. Yamamoto, K. Sugimoto, and K. Yamashita. Oblique alignment of stress fibers in cells reduces the mechanical stress in cyclically deforming fields. *European Journal of Cell Biology*, 77:91–99, 1998.

[353] C. Tamiello, C. Bouten, and F. Baaijens. Competition bewteen cap and basal actin fiber orientation in cells subjected to contact guidance and cyclic strain. *Scientific Reports*, 5:8752, 2015.

[354] C. Tamiello, A. Buskermolen, F. Baaijens, J. Broers, and C. Bouten. Heading in the right direction: Understanding cellular orientation responses to complex biophysical environments. *Cellular and Molecular Bioengineering*, 9:12–37, 2016.

[355] M. Tanaka, W. Debinski, and I. Puri. Hybrid mathematical model of glioma progression. *Cell Proliferation*, 42:637–646, 2009.

[356] M. D. Tang-Schomer, A. R. Patel, P. W. Baas, and D. H. Smith. Mechanical breaking of microtubules in axons during dynamic stretch injury underlies delayed elasticity, microtubule disassembly, and axon degeneration. *The FASEB Journal*, 24(5):1401–1410, 2009.

[357] M. Tektonidis, H. Hatzikirou, A. Chauviere, M. Simon, K. Schaller, and A. Deutsch. Identification of intrinsic *in vitro* cellular mechanisms for glioma invasion. *Journal of Theoretical Biology*, 287:131–147, 2011.

[358] L. Terracio, B. Miller, and T. Borg. Effects of cyclic mechanical stimulation of the cellular components of the heart: In vitro. *In Vitro Cellular & Developmental Biology*, 24(1):53–58, 1988.

[359] C. Thodeti, B. Matthews, A. Ravi, A. Mammoto, K. Ghosh, A. Bracha, and D. Ingber. TRPV4 channels mediate cyclic strain-induced endothelial cell reorientation through integrin-to-integrin signaling. *Circulation Research*, 104:1123–1130, 2009.

[360] A. Throm Quinlan, L. Sierad, A. Capulli, L. Firstenberg, and K. Billiar. Combining dynamic stretch and tunable stiffness to probe cell mechanobiology in vitro. *PLoS One*, 6:e23272, 2011.

[361] S. Tojkander, G. Gateva, and P. Lappalainen. Actin stress fibers - assembly, dynamics and biological roles. *Journal of Cell Science*, 125:1855–1864, 2012.

[362] A. Tondon, H.-J. Hsu, and R. Kaunas. Dependence of cyclic stretch-induced stress fiber reorientation on stretch waveform. *Journal of Biomechanics*, 45:728–735, 2012.

[363] A. Tondon and R. Kaunas. The direction of stretch-induced cell and stress fiber orientation depends on collagen matrix stress. *PLOS One*, 9:e89592, 2014.

[364] P. Tracqui, C. Cruywagen, D. Woodward, G. Bartoo, J. Murray, and E. Alvord Jr. A mathematical model of glioma growth: the effect of chemotherapy on spatio-temporal growth. *Cell Proliferation*, 28:17–31, 1995.

[365] C. Truesdell and W. Noll. The Non-Linear Field Theories of Mechanics. *Handbuch der Physik*, 2:1–541, 1965.

[366] N. Tulloch, V. Muskheli, M. Razumova, F. Korte, M. Regnier, K. Hauch, L. Pabon, H. Reinecke, and C. Murry. Growth of engineered human myocardium with mechanical loading and vascular coculture. *Circulation Research*, 109:47–59, 2011.

[367] Y. Ujihara, M. Nakamura, M. Soga, K. Koshiyama, H. Miyazaki, and S. Wada. Computational studies on strain transmission from a collagen gel construct to a cell and its internal cytoskeletal filaments. *Computers in Biology and Medicine*, 56:20–29, 2015.

[368] F. Vernerey and U. Akalp. Role of catch bonds in actomyosin mechanics and cell mechanosensitivity. *Physical Review E*, 94:012403, 2016.

[369] F. Vernerey and M. Farsad. A constrained mixture approach to mechano-sensing and force generation in contractile cells. *Journal of the Mechanical Behavior of Biomedical Materials*, 4:1683–1699, 2011.

[370] M. Vianello. Optimization of the stored energy and coaxiality of strain and stress in finite elasticity. *Journal of Elasticity*, 44:193–202, 1996.

[371] A. Vigliotti, R. McMeeking, and V. Deshpande. Simulation of the cytoskeletal response of cells on grooved or patterned substrates. *Journal of the Royal Society Interface*, 12:20141320, 2015.

[372] A. Vigliotti, W. Ronan, F. Baaijens, and V. Deshpande. A thermodynamically motivated model for stress-fiber reorganization. *Biomechanics and Modeling in Mechanobiology*, 15:761–789, 2016.

[373] T. Wakatsuki and E. Elson. Reciprocal interactions between cells and extracellular matrix during remodeling of tissue constructs. *Biophysical Chemistry*, 100:593–605, 2003.

[374] C. Wang, J. Rockhill, M. Mrugala, D. Peacock, A. Lai, K. Jusenius, J. Wardlaw, T. Cloughesy, A. Spence, R. Rockne, E. Alvord Jr, and K. Swanson. Prognostic significance of growth kinetics in newly diagnosed glioblastomas revealed by combining serial imaging with a novel biomathematical model. *Cancer Research*, 69:9133–9140, 2009.

[375] H. Wang, W. Ip, R. Boissy, and E. Grood. Cell orientation response to cyclically deformed substrates: experimental validation of a cell model. *Journal of Biomechanics*, 28(12):1543–1552, 1995.

[376] J. H.-C. Wang. Substrate deformation determines actin cytoskeleton reorganization: A mathematical modeling and experimental study. *Journal of Theoretical Biology*, 202:33–41, 2000.

[377] J. H.-C. Wang, P. Goldschmidt-Clermont, J. Wille, and F. C.-P. Yin. Specificity of endothelial cell reorientation in response to cyclic mechanical stretching. *Journal of Biomechanics*, 34:1563–1572, 2001.

[378] J. H.-C. Wang, P. Goldschmidt-Clermont, and F. C.-P. Yin. Contractility affects stress fiber remodeling and reorientation of endothelial cells subjected to cyclic mechanical stretching. *Annals of Biomedical Engineering*, 28:1165–1171, 2000.

[379] J. H.-C. Wang and E. Grood. The strain magnitude and contact guidance determine orientation response of fibroblasts to cyclic substrate strains. *Connective Tissue Research*, 41(1):29–36, 2000.

[380] J. H.-C. Wang, E. Grood, J. Florer, and R. Wenstrup. Alignment and proliferation of MC3T3-E1 osteoblasts in microgrooved silicone substrata subjected to cyclic stretching. *Journal of Biomechanics*, 33:729–735, 2000.

[381] J. H.-C. Wang, G. Yang, and Z. Li. Controlling cell responses to cyclic mechanical stretching. *Annals of Biomedical Engineering*, 33(3):337–342, 2005.

[382] J. H.-C. Wang, G. Yang, Z. Li, and W. Shen. Fibroblasts responses to cyclic mechanical stretching depend on cell orientation to the stretching direction. *Journal of Biomechanics*, 37:573–576, 2004.

[383] S. Wang, D. Lu, Z. Zhang, X. Jia, and L. Yang. Effects of mechanical stretching on the morphology of extracellular polymers and the mRNA expression of collagens and small leucine-rich repeat proteoglycans in vaginal fibroblasts from women with pelvic organ prolapse. *PLoS ONE*, 13:e0193456, 2018.

[384] S. Wang, Z. Zhang, D. Lu, and Q. Xu. Effects of mechanical stretching on the morphology and cytoskeleton of vaginal fibroblasts from women with pelvic organ prolapse. *International Journal of Molecular Sciences*, 16:9406–9419, 2015.

[385] Z. Wei, V. Deshpande, R. McMeeking, and A. Evans. Analysis and interpretation of stress fiber organization in cells subject to cyclic stretch. *Journal of Biomechanical Engineering*, 130:031009–1 – 031009–9, 2008.

[386] C.-F. Westin, S. Maier, H. Mamata, A. Nabavi, F. Jolesz, and R. Kikinis. Processing and visualization for diffusion tensor MRI. *Medical Image Analysis*, 6:93–108, 2002.

[387] G. White, M. Gimbrone Jr, and K. Fujiwara. Factors influencing the expression of stress fibers in vascular endothelial cells in situ. *Journal of Cell Biology*, 97:416–424, 1983.

[388] J. Wille, C. Ambrosi, and F. C.-P. Yin. Comparison of the effects of cyclic stretching and compression of endothelial cell morphological responses. *Journal of Biomechanical Engineering*, 126:545–551, 2004.

[389] J. Wille, E. Elson, and R. Okamoto. Cellular and matrix mechanics of bioartificial tissues during continuous cyclic stretch. *Annals of Biomechanical Engineering*, 34(11):1678–1690, 2006.

[390] A. Wong, T. Pollard, and I. Herman. Actin filament stress fibers in vascular endothelial cells in vivo. *Science*, 219:867–869, 1983.

[391] D. Woodward, J. Cook, P. Tracqui, C. Cruywagen, J. Murray, and E. Alvord Jr. A mathematical model of glioma growth: the effect of extent of surgical resection. *Cell Proliferation*, 29:269–288, 1996.

[392] G. Xu, B. Li, X. Feng, and H. Gao. A tensegrity model of cell reorientation on cyclically stretched substrates. *Biophysical Journal*, 111:1478–1486, 2016.

[393] K. Xu, G. Zhong, and X. Zhuang. Actin, spectrin, and associated proteins form a periodic cytoskeletal structure in axons. *Science*, 339(6118):452–456, 2013.

[394] M. Yamane, T. Matsuda, T. Ito, Y. Fujio, K. Takahashi, and J. Azuma. Rac1 activity is required for cardiac myocyte alignment in response to mechanical stress. *Biochemical and Biophysical Research Communications*, 353:1023–1027, 2007.

[395] K. Yangjin, J. Hyejin, and H. Othmer. The role of the tumor microenvironment in glioblastoma: A mathematical model. *IEEE Transactions on Biomedical Engineering*, 64:519–527, 2017.

[396] M. Yoshigi, E. Clark, and H. Yost. Quantification of stretch-induced cytoskeletal remodeling in vascular endothelial cells by image processing. *Cytometry Part A*, 55A:109–118, 2003.

[397] T. Yuan, M. Fairchild, A. Perkins, and G. Tanentzapf. Analysis of integrin turnover in fly myotendinous junctions. *Journal of Cell Science*, 123:939–946, 2010.

[398] A. Zemel, I. Bischofs, and S. Safran. Active elasticity of gels with contractile cells. *Physical Review Letters*, 97:128103, 2006.

[399] J. Zhang and J. Rychlewski. Structural tensors for anisotropic solids. *Archives of Mechanics*, 42(3):267–277, 1990.

[400] L. Zhang, C. Kahn, H.-Q. Chen, N. Tran, and X. Wang. Effect of uniaxial stretching on rat bone mesenchymal stem cell: Orientation and expressions of collagen types I and III and tenascin-C. *Cell Biology International*, 32:344–352, 2008.

[401] L. Zhang, C. Strouthos, Z. Wang, and T. Deisboeck. Simulating brain tumor heterogeneity with a multiscale agent-based model: Linking molecular signatures, phenotypes and expansion rate. *Mathematical and Computer Modelling*, 49:307–319, 2009.

[402] Y. Zhang, K. Abiraman, H. Li, D. M. Pierce, A. V. Tzingounis, and G. Lykotrafitis. Modeling of the axon membrane skeleton structure and implications for its mechanical properties. *PLoS Computational Biology*, 13(2):e1005407, 2017.

[403] S. Zhao, A. Suciu, T. Ziegler, J. Moore, E. Bürki, J.-J. Meister, and H. Brunner. Synergistic effects of fluid shear stress and cyclic circumferential stretch on vascular endothelial cell morphology and cytoskeleton. *Arteriosclerosis, Thrombosis, and Vascular Biology*, 15:1781–1786, 1995.

[404] J. Zheng, P. Lamoureux, V. Santiago, T. Dennerll, R. E. Buxbaum, and S. R. Heidemann. Tensile regulation of axonal elongation and initiation. *Journal of Neuroscience*, 11(4):1117–1125, 1991.

[405] Q.-S. Zheng. On transversely isotropic, orthotropic and relative isotropic functions of symmetric tensors, skew-symmetric tensors and vectors. Part I: two dimensional orthotropic and relative isotropic functions and three dimensional relative isotropic functions. *International Journal of Engineering Science*, 31(10):1399–1409, 1993.

[406] Y. Zhong, D. Kong, L. Dai, and B. Ji. Frequency-dependent focal adhesion instability and cell reorientation under cyclic substrate stretching. *Cellular and Molecular Bioengineering*, 4:442–456, 2011.

[407] C. Zhu. Mechanochemistry: A molecular biomechanics view of mechanosensing. *Annals of Biomedical Engineering*, 42:388–404, 2014.

[408] C. Zhu, Y. Chen, and L. Ju. Dynamic bonds and their roles in mechanosensing. *Current Opinion in Chemical Biology*, 53:88–97, 2019.

[409] J.-H. Zhu, C.-L. Chen, S. Flavahan, J. Harr, B. Su, and N. Flavahan. Cyclic stretch stimulates vascular smooth muscle cell alignment by redox-dependent activation of Notch3. *American Journal of Physiology - Heart and Circulatory Physiology*, 300:H1770–H1780, 2011.

[410] A. Zielinski, C. Linnartz, C. Pleschka, G. Dreissen, R. Springer, R. Merkel, and B. Hoffmann. Reorientation dynamics and structural interdependencies of actin, microtubules and intermediate filaments upon cyclic stretch application. *Cytoskeleton*, 75:385–394, 2018.

Appendix A

Analytical Characterisation of Bifurcations

In this Appendix, we provide details about the bifurcations discussed qualitatively in Sections 3.1.4 and 3.3.2. In particular, the following Proposition can readily be proved to characterise analytically the type of bifurcations which are observed for the strain energy defined by Eq. (3.140). The result can however be immediately extended to an energy in the form of Eq. (3.21).

Proposition A.1. *The differential equation* (3.129)*, with* $\mathcal{W}'(\theta)$ *given by* (3.143)*, presents a pitchfork bifurcation with* r *as a bifurcation parameter at each point*

$$(\theta_0, r_0) = \left(\frac{\pi}{2} + k\pi, \frac{1}{\rho}\right), \quad k \in \mathbb{Z}, \tag{A.1}$$

$$(\theta_1, r_1) = (k\pi, \rho), \quad k \in \mathbb{Z}, \tag{A.2}$$

where ρ *is defined in* $(3.148)_3$*, provided that* $1/\rho, \rho \neq 0$*. Moreover, the bifurcations are supercritical if* $\mathcal{K}$ *defined in* (3.147) *is positive and subcritical if* $\mathcal{K}$ *is negative.*

Proof. We recall that if a one-parameter family of one-dimensional fields $f(\theta, r)$ (sufficiently regular) satisfies the following conditions:

$$f(\theta^*, r) = 0 \quad \forall r, \tag{A.3}$$

$$\partial_\theta f(\theta^*, r^*) = 0, \qquad \partial^2_{\theta\theta} f(\theta^*, r^*) = 0, \tag{A.4}$$

$$\partial^2_{\theta r} f(\theta^*, r^*) \neq 0, \qquad \partial^3_{\theta\theta\theta} f(\theta^*, r^*) \neq 0, \tag{A.5}$$

then the associated dynamical system undergoes a pitchfork bifurcation at (θ^*, r^*). In the case we are considering, we have

$$f(\theta,r) = -\frac{1}{\eta}\mathcal{W}'(\theta) = -\frac{\varepsilon^2}{\eta}\left\{[A\xi(\theta,r) - B(r+1) + C]\xi_\theta(\theta,r)\right\}, \tag{A.6}$$

recalling Eqs. (3.143) and (3.144). We remark that, since in the remainder of the proof we will need to consider also r as a variable, we have employed the notation $\xi(\theta,r)$ to explicitly underline that ξ is also a function of r. Accordingly, we denote by ξ_θ and ξ_r its partial derivatives with respect to θ and r, respectively.

We start from $(\theta_0, r_0) = \left(\frac{\pi}{2} + k\pi, \frac{1}{\rho}\right)$ and show that the previous conditions (A.3), (A.4), (A.5) are satisfied. First of all, we have

$$f\left(\frac{\pi}{2} + k\pi, r\right) = 0 \qquad \forall r$$

since $\xi_\theta(\pi/2, r) = 0 \ \ \forall r$ and hence the first condition (A.3) holds. Secondly, we get

$$\partial_\theta f(\theta,r) = -\frac{\varepsilon^2}{\eta}\left\{A\xi_\theta(\theta,r)^2 + [A\xi(\theta,r) - B(r+1) + C]\xi_{\theta\theta}(\theta,r)\right\} \tag{A.7}$$

from which, taking into account that

$$\xi_\theta(\theta,r) = -(1+r)\sin 2\theta \quad \text{and} \quad \xi_{\theta\theta}(\theta,r) = -2(1+r)\cos 2\theta\,,$$

we obtain

$$\partial_\theta f\left(\frac{\pi}{2} + k\pi, \frac{1}{\rho}\right) = -2\frac{\varepsilon^2}{\eta}\left(1 + \frac{1}{\rho}\right)\left[-B\left(1 + \frac{1}{\rho}\right) + C\right] = 0, \tag{A.8}$$

observing that $-B(1+\rho) + C\rho = 0$. Moreover,

$$\begin{aligned}\partial_{\theta\theta} f\left(\frac{\pi}{2} + k\pi, \frac{1}{\rho}\right) &= -\frac{\varepsilon^2}{\eta}\left\{3A\xi_\theta(\theta,r)\xi_{\theta\theta}(\theta,r) + [A\xi(\theta,r) - B(1+r) + C]\xi_{\theta\theta\theta}(\theta,r)\right\}_{|(\theta_0,r_0)} \\ &= -\frac{\varepsilon^2}{\eta}\left[-B\left(1 + \frac{1}{\rho}\right) + C\right]\xi_{\theta\theta\theta}\left(\frac{\pi}{2} + k\pi, \frac{1}{\rho}\right) = 0 \end{aligned} \tag{A.9}$$

for the same reason as before. Hence, the conditions given in Eq. (A.4) are satisfied as well. Finally,

$$\partial^2_{\theta r} f\left(\frac{\pi}{2}+k\pi,\frac{1}{\rho}\right) = -\frac{\varepsilon^2}{\eta}\left[-2B\left(1+\frac{1}{\rho}\right)\right] = 2\frac{\varepsilon^2}{\eta}C \neq 0$$

since we assumed $C > 0$. The last condition to be verified reads

$$\begin{aligned}\partial^3_{\theta\theta\theta} f\left(\frac{\pi}{2}+k\pi,\frac{1}{\rho}\right) &= -\frac{\varepsilon^2}{\eta}\left[12A\left(1+\frac{1}{\rho}\right)^2 + 8B\left(1+\frac{1}{\rho}\right)^2 - 8C\left(1+\frac{1}{\rho}\right)\right] \\ &= -\frac{\varepsilon^2}{\eta}12A\left(1+\frac{1}{\rho}\right)^2 \neq 0 \end{aligned} \tag{A.10}$$

since $A \neq 0$ – otherwise the oblique equilibrium does not exist – and $\rho \neq -1$, since $\mathcal{K} \neq 0$, having observed that $\xi_{\theta\theta\theta}(\theta, r) = 4(1+r)\sin 2\theta$ and $\xi_{\theta\theta\theta\theta}(\theta) = 8(1+r)\cos 2\theta$. We conclude that all the conditions for a pitchfork bifurcation are satisfied; furthermore, we notice that the type of pitchfork bifurcation depends on the sign of A, namely on the sign of $\mathcal{K}$: if $A > 0$ the bifurcation is supercritical, since the third derivative is always negative, while if $A < 0$ the bifurcation is subcritical.

We now exploit the previous calculation to show that the system displays a pitchfork bifurcation also at each point $(\theta_1, r_1) = (k\pi, \rho)$. In particular, we immediately have

$$f(k\pi, r) = 0 \qquad \forall r\,.$$

Then, by substituting into (A.7),

$$\partial_\theta f(k\pi,\rho) = 2\frac{\varepsilon^2}{\eta}(1+\rho)[A(1+\rho) - B(1+\rho) + C] = 0$$

since $(1+\rho)(A-B)+C = 0$. The following condition is

$$\partial^2_{\theta\theta} f(k\pi,\rho) = -\frac{\varepsilon^2}{\eta}[A(1+\rho) - B(1+\rho) + C]\xi_{\theta\theta\theta}(k\pi,\rho) = 0$$

for the same reason above. Finally,

$$\partial^2_{\theta r} f(k\pi,\rho) = 2\frac{\varepsilon^2}{\eta}(1+\rho)(A-B) = 2 - \frac{\varepsilon^2}{\eta}C \neq 0$$

and

$$\partial^3_{\theta\theta\theta} f(k\pi,\rho) = -\frac{\varepsilon^2}{\eta} 12A(1+\rho)^2 \neq 0$$

if $A \neq 0$ and $\rho \neq -1$. Therefore, the system undergoes a pitchfork bifurcation also at $(\theta_1, r_1) = (k\pi, \rho)$: again, such bifurcations are supercritical if $A > 0$ and subcritical if $A < 0$. □

It is also possible to show that, if we instead consider an energy given by Eq. (3.154), then the system exhibits saddle-node bifurcations.

Proposition A.2. *The differential equation* (3.129)*, with* $\mathcal{W}'(\theta)$ *given by* (3.155)*, presents a saddle-node bifurcation with* r *as a bifurcation parameter at each point* (θ^*, r^*) *such that*

$$\theta^* = \frac{1}{2}\arctan \sqrt[3]{2\gamma} + k\frac{\pi}{2}, \tag{A.11}$$

and

$$\frac{1}{1+r^*} = \frac{1}{2}\left[1 \pm \frac{1}{\mathcal{K}\left(1+\sqrt[3]{4\gamma^2}\right)^{3/2}}\right], \tag{A.12}$$

where γ *is defined in Eq.* (3.158).

Proof. We recall that if a one-parameter family of one dimensional fields $f(\theta, r)$ (sufficiently regular) satisfies the following conditions:

$$f(\theta^*, r^*) = 0, \qquad \partial_\theta f(\theta^*, r^*) = 0 \tag{A.13}$$

$$\partial_r f(\theta^*, r^*) \neq 0, \qquad \partial^2_{\theta\theta} f(\theta^*, r^*) \neq 0, \tag{A.14}$$

then the associated system undergoes a saddle-node bifurcation at (θ^*, r^*). In this case, we need to consider

$$f(\theta, r) = -\frac{1}{\eta}\mathcal{W}'(\theta) = \left\{[A\xi(\theta, r) - B(r+1) + C]\xi_\theta(\theta) + K_{\|s}(r^2-1)(\cos^2\theta - \sin^2\theta)\right\}.$$

Again, we have emphasized explicitly the dependence of ξ on r, which here is a variable and not a fixed parameter. Since, as we verified before, (θ^*, r^*) are equilibrium points for

the system, it follows $f(\theta^*, r^*) = 0$. Then, we have that

$$\partial_\theta f(\theta^*, r^*) = -\frac{\varepsilon^2}{\eta} C(1+r^*)^2 \cos^2 2\theta^* \left[\frac{1}{\mathcal{K}} \tan^2 2\theta^* - \frac{1}{\mathcal{K}} + \frac{1}{\mathcal{K}} \frac{\sin 2\theta^*}{\sin 2\theta^* + 2\gamma \cos 2\theta^*} (1 - 2\gamma \tan 2\theta^*) \right]$$
$$= -\frac{\varepsilon^2 C}{\eta \mathcal{K}} (1+r^*)^2 \cos^2 2\theta^* \left[\sqrt[3]{4\gamma^2} - 1 + \frac{1 - 2\gamma\sqrt[3]{2\gamma}}{1 + \sqrt[3]{4\gamma^2}} \right] = 0, \tag{A.15}$$

where we have used Eqs. (A.11)–(A.12). We move on to the third condition and calculate

$$\partial_r f(\theta^*, r^*) = -\frac{\varepsilon^2}{\eta} \Big\{ -\sin 2\theta^* \left[2A(1+r^*)\cos^2\theta^* - 2B(1+r^*) + C \right] + 2r^* K_{\|s} \cos 2\theta^* \Big\}$$
$$= -\frac{\varepsilon^2}{\eta} C \cos 2\theta^* \{2\gamma + \tan 2\theta^*\} = -\frac{\varepsilon^2}{\eta} C \frac{(-1)^k (2\gamma + \sqrt[3]{2\gamma})}{\sqrt{1 + \sqrt[3]{4\gamma^2}}} \neq 0,$$

where $k \in \mathbb{Z}$ and in the second equality we have taken into account that, at equilibrium, $[A(1+r^*)\cos^2\theta^* - B(1+r^*) + C]\sin 2\theta^* = (r^* - 1)K_{\|s} \cos 2\theta^*$. Finally, we compute

$$\partial^2_{\theta\theta} f(\theta^*, r^*) = -\frac{\varepsilon^2}{\eta} \Big\{ 6A(1+r^*)^2 \sin 2\theta^* \cos 2\theta^*$$
$$+ 4(1+r^*)\sin 2\theta^* \left[A(1+r^*)\cos^2\theta^* - B(1+r^*) + C \right]$$
$$+ 4K_{\|s}(1 - r^{*2}) \cos 2\theta^* \Big\}$$

which, using again the equilibrium condition, gives

$$\partial^2_{\theta\theta} f(\theta^*, r^*) = -\frac{\varepsilon^2}{\eta} \left[6A(1+r^*)^2 \sin 2\theta^* \cos 2\theta^* \right] \neq 0. \tag{A.16}$$

Therefore, we conclude that all the conditions are satisfied and the system undergoes a saddle-node bifurcation at each point (θ^*, r^*). □